National Library of Canada
Acquisitions and Bibliographic Services Branch
395 Wellington Street
Ottawa, Ontario
K1A 0N4

Bibliothèque nationale du Canada
Direction des acquisitions et des services bibliographiques
395, rue Wellington
Ottawa (Ontario)
K1A 0N4

Your file Votre référence

Our file Notre référence

NOTICE

The quality of this microform is heavily dependent upon the quality of the original thesis submitted for microfilming. Every effort has been made to ensure the highest quality of reproduction possible.

If pages are missing, contact the university which granted the degree.

Some pages may have indistinct print especially if the original pages were typed with a poor typewriter ribbon or if the university sent us an inferior photocopy.

AVIS

La qualité de cette microforme dépend grandement de la qualité de la thèse soumise au microfilmage. Nous avons tout fait pour assurer une qualité supérieure de reproduction.

S'il manque des pages, veuillez communiquer avec l'université qui a conféré le grade.

La qualité d'impression de certaines pages peut laisser à désirer, surtout si les pages originales ont été dactylographiées à l'aide d'un ruban usé ou si l'université nous a fait parvenir une photocopie de qualité inférieure.

Canada

PHOTON EMISSIONS FROM ION BEAM - TARGET GAS COLLISIONS

IN A MASS SPECTROMETER

AND

THE THERMOCHEMISTRY OF ORGANIC FREE RADICALS AND CATIONS

by Paul Michael Mayer, B.Sc.(Hons)

A thesis submitted to the
School of Graduate Studies and Research

In partial fulfillment of the requirements for the degree of
Doctor of Philosophy

In the Ottawa-Carleton Chemistry Institute
Department of Chemistry, University of Ottawa
Ottawa, Ontario, Canada

August 1994

Candidate	Supervisor
Paul Michael Mayer	Prof. John L. Holmes

ISBN 0-612-00544-5

Canada

UNIVERSITÉ D'OTTAWA
UNIVERSITY OF OTTAWA

To Mom and Dad

and

Teresa, Chris and John

Abstract

This thesis represents the culmination of four years of research into two aspects of gas phase ion chemistry. The first was an attempt to obtain information on internal excitation in polyatomic projectile - target gas collisions in a mass spectrometer. Knowledge of internal excitation is critical to the interpretation of collision induced dissociation (CID) mass spectra. A novel collision cell was designed for a VG ZAB-2F sector mass spectrometer which permitted the detection and analysis of photon emissions from keV projectile - target gas collisions. Early experiments performed in the second field-free region of the mass spectrometer (sec. 4.2) involved the analysis of emitted light with a series of wavelength cutoff filters. Histographic emission spectra were obtained for three $C_2,H_4,O^{+\bullet}$ ions and two $C_2,H_5,Cl^{+\bullet}$ ions. The spectral characteristics were found to be indicative of ion structure. This led to the development of a more elaborate apparatus in the third field-free region of the ZAB which enabled the aquisition of monochromated emission spectra (sec. 4.3).

The emission spectra obtained for 8 keV $N_2^{+\bullet}$, $O_2^{+\bullet}$ and $CO_2^{+\bullet}$ projectile ions with the target gases He, N_2, O_2 and CO_2 showed that a) collisional excitation of the ions was a vertical process, b) considerable translational kinetic energy was converted into internal energy in the collisions (up to 22 eV) and c) the observed emissions relate to the relative geometries of the ground and excited states of the ions. Histographic spectra for these three projectiles obtained with 18 target gases exhibited definite trends. The abundance of fragment ions in the collision induced dissociation mass spectra of $N_2^{+\bullet}$ and $CO_2^{+\bullet}$ was found to increase linearly with emission intensity, indicating that fragmentation was the

result of electronic excitation in the ions.

Monochromated collision induced emission (CIE) spectra were also obtained from 8 keV polyatomic ion - He, Ar target gases for the first time. Three $C_2,H_4,O^{+\bullet}$ isomers oxirane$^{+\bullet}$, acetaldehyde$^{+\bullet}$ and vinyl alcohol$^{+\bullet}$ along with their fragment ions $CO^{+\bullet}$, HCO^+, CH_3^+ and CH_3CO^+ were studied. Emissions were found to be from electronically excited atomic and diatomic fragments, C (3s $^1P^0$), O^+ (4p $^2D^0$), $H^\bullet$ (n=4), $HO^\bullet$ (A $^2\Sigma^+$), HC^+ (B $^1\Delta$) and HC (A $^2\Delta$). The spectra provided the first quantitative information on internal energy deposition in these polyatomic projectile - target gas collisions. Most of the excited state products were formed by 6-14 eV excitation in the $C_2,H_4,O^{+\bullet}$ precursor ions. No emissions due to excitations of less than 6 eV were detectable. Two correlations were observed when these emission spectra were compared to the CID mass spectra of the ions. The $HO^\bullet$ (A $\rightarrow$ X) emission band increased in intensity as the abundance of the $C_2H_3^+$ counterion increased in the CID mass spectra, indicating that the fragmentation process involves the formation of $HO^\bullet$ (A). On the other hand, as the O^+ peak in the CID spectra decreases, the O^+ emission band in the CIE spectra increased.

The CIE spectra of two $C_2,H_5,Cl^{+\bullet}$ isomers $CH_3CH_2Cl^{+\bullet}$ and $CH_3ClCH_2^{+\bullet}$ and their fragment ions CCl^+ and $^+CH_2Cl$ were also obtained. The results were similar to those for the $C_2,H_4,O^{+\bullet}$ ions. It was clear from comparisons to the CID mass spectra that the excited state fragments were not formed directly from the $C_2,H_5,Cl^{+\bullet}$ precursors but from a series of consecutive fragmentations. Excitation of the precursor may have resulted in fragmentation to many highly excited products which continued to fragment until only excited atomic and diatomic species remained. It was these final products that we see in

the CIE spectra.

The appearance energy (AE) technique employing monoenergetic electron impact ionization was used to determine the heats of formation of many organic free radicals and cations. The following $\Delta_f H^\circ_{298}$ data were obtained for oxygen containing free radicals (all values ± 3 kcal mol^{-1}): $^{\bullet}CH_2CH_2OH$, -13.5 kcal mol^{-1}; $CH_3\dot{C}HOH$, -14.5 kcal mol^{-1}; $^{\bullet}CH_2CH_2CH_2OH$, -16.0 kcal mol^{-1}; $^{\bullet}CH_2CH(OH)CH_3$, -23.0 kcal mol^{-1}; $^{\bullet}CH_2C(OH)(CH_3)_2$, -35.2 kcal mol^{-1}; $CH_3\dot{C}HCH_2OH$, -18.8 kcal mol^{-1}; $(CH_3)_2\dot{C}OH$, -25.6 kcal mol^{-1}; $HO\dot{C}HCH_2OH$, -52.6 kcal mol^{-1}; $^{\bullet}CH_2C(O)OH$, -61.6 kcal mol^{-1}; $^{\bullet}CH_2C(O)OCH_3$, -57.5 kcal mol^{-1}; $^{\bullet}CH_2OCH_2CH_3$, -10.6 kcal mol^{-1}; $^{\bullet}C(O)OH$, -46.0 kcal mol^{-1}; $^{\bullet}C(O)OCH_3$, -39.9 kcal mol^{-1}; $HOO^{\bullet}$, 3.5 kcal mol^{-1}; $(CH_3)_3COO^{\bullet}$, -25.2 kcal mol^{-1}; $HC(O)O^{\bullet}$, -37.7 kcal mol^{-1}; $CH_3C(O)O^{\bullet}$, -51.7 kcal mol^{-1}.

An investigation was made of the effect of -OH substitution on C-H bond strengths in alcohols. The -OH group was found to decrease 1° C-H bond strengths by 10, 5 and 3 kcal mol^{-1} when substituted α (on the C atom in the C-H bond), β (one C atom removed from the C-H bond) and γ (two C atoms removed from the bond) to the bond respectively. The effect on 2° C-H bonds was only 2 kcal mol^{-1} for a β-OH group. Substitution on the free radical centre in these -OH containing free radicals was found to obey the general additivity rules for neutral molecules.

A review was made of the degree of charge delocalization in -CN substituted radical cations. Semi-empirical calculations showed that the -CN group acted primarily as an inductive electron withdrawing group in radical cations, carrying very little positive charge. The -CN group was found to raise the ionization energy of molecules compared

to -H independent of the nature of the rest of the molecule (containing saturated, double and triple bonds or aromatic ring). The heats of formation of the -CN containing radical cations were 43 ± 3 kcal mol^{-1} higher than their -H substituted analogues in all cases. These results were consistent with an inductive electron withdrawing cyano group which does not participate in the charge distribution of the ions.

Little information was available for even electron -CN substituted cations and their corresponding free radicals. We determined the $\Delta_f H°_{298}$ of the three cation $^+CH_2CN$, $CH_3{}^+CHCN$ and $(CH_3)_2{}^+CCN$, 291 ± 2 kcal mol^{-1}, 263 ± 2 kcal mol^{-1} and 236 ± 2 kcal mol^{-1} respectively. These values were used in isodesmic reactions to determine the degree of π-delocalization of the charge in the cations. The only ion in which π-delocalization was found to be significant was $^+CH_2CN$. Methyl substitution on this ion decreased π-delocalization leaving the -CN group to act primarily as an inductive electron withdrawing group.

A detailed mass spectrometric and thermochemical investigation of three C_2,H_2,N^+ isomers, $^+CH_2CN$, $^+CH_2NC$ and $HCCHN^+$ was carried out. It was found that the C_2,H_2,N^+ ions formed from dissociative ionization of CH_3CN, CH_3NC and 1-H-1,2,3-triazole were indistinguishable while that from ICH_2CN was unique. The AE values and resulting $\Delta_f H°_{298}(C_2,H_2,N^+)$ obtained from these four precursors led to the conclusion that $^+CH_2CN$ was obtained only from ICH_2CN, giving a $\Delta_f H°_{298}(^+CH_2CN)$ = 291 ± 2 kcal mol^{-1}, while the other three precusors yield the cyclic ion, having a $\Delta_f H°_{298} \leq 272$ kcal mol^{-1}.

Acknowledgements

I would like to thank the people who made this thesis possible: Prof. John L. Holmes, my supervisor, for giving me these projects to work on (I can't think of a better way to spend a Ph.D.) and teaching me how to critically evaluate my own work; Prof. John B. Westmore (Univ. of Manitoba) for introducing me to mass spectrometry over three summers and also showing me the meaning of scientific credibility; John Krause, lab manager, teacher and all around crazy guy; Clem Kazakoff, for all of those morning coffee chats; Sander Mommers, for teaching me so much about the instruments, putting up with my stupidity, and being able to fix anything, anytime. I would also like to express my gratitude to the students and post-docs I worked beside over the last seven years (no particular order): Martine Bissonette, Martin Sirois, David Harnish, Hongwen Chen, Christiane Aubry, Yan An, Jill MacDonald, Gary Stern (Univ. of Manitoba), Dmitri Zagorevski, Yu Ran Luo, Jian Ru Cao and undergraduates Christine Rondeau, Michael Vasseur, Jean-Michel Regimbald and Sofia Ahmed.

Finally, I would like to take this opportunity to express my appreciation to Dr. Fred P. Lossing. It has been an honour to work with him, even though the instrument was a constant source of consternation. His good humour, attitude and vast experience not only in science but in the world around him was a pleasure to share. I consider myself lucky to know him.

Where would a scientist be without food on his plate. The Natural Sciences and Engineering Research Council of Canada has financially supported my over the last seven years with summer research awards and post-graduate scholarships.

Contents

		page
Abstract		ii
Acknowledgements		vi
Contents		vii
List of Tables		x
List of Figures		xii
List of Abbreviations		xvi
Chapter 1	Some Preliminary Remarks	1
Chapter 2	Instrumentation	4
2.1 Introduction		4
2.2 The VG ZAB-2F Mass Spectrometer		4
2.2.1 The ion source of the ZAB-2F		6
2.2.2 Ion beam focussing lens assembly		10
2.2.3 The magnetic sector: momentum analysis		10
2.2.4 The second field-free region (2FFR)		13
2.2.5 The electrostatic sector: energy analysis		16
2.2.6 The third field-free region (3FFR)		18
2.2.7 Apparatus for analyzing photon emissions from projectile - target gas collisions		22
2.3 Monoenergetic Electron Impact Appearance Energy Apparatus		28
2.3.1 The electron energy selector		28
2.3.2 Ion extraction and analysis		30
References		32
Chapter 3	Experimental Description	33
3.1 Introduction		33
3.2 Types of Ions in the Mass Spectrometer		33
3.2.1 Source generated ions		33

3.2.2 Metastable ions 35

3.3 Conventional Experiments Performed on the VG ZAB-2F 35
3.3.1 Mass-analysed ion kinetic energy spectrometry (MIKES) 35
3.3.2 Collision induced dissociation (CID) mass spectrometry 37
3.3.3 Kinetic energy release (KER) measurements 38
3.3.4 Charge stripping (CS) mass spectrometry 41
3.3.5 Neutralization - reionization (NR) mass spectrometry 41

3.4 Aquiring Emission Spectra from Projectile - Target Gas Collisions 42
3.4.1 2FFR experiments 42
3.4.2 3FFR experiments 43

3.5 Appearance Energy Determinations 47
3.5.1 The basic relationship 47
3.5.2 Reverse activation energy 48
3.5.3 Temperature and kinetic shift effects 50
3.5.4 Competitive dissociations 53
3.5.5 Experimental procedure 55

References 57

Chapter 4 Photon Emissions from keV Projectile Ion - Target Gas Collisions 59

4.1 Introduction 59

4.2 2FFR Experiments 62
4.2.1 Introduction 62
4.2.2 Results and Discussion 62

4.3 3FFR Experiments 66
4.3.1 Introduction 66
4.3.2 Emissions from $N_2^{+\bullet}$ - target gas collisions 66
4.3.3 Emissions from $O_2^{+\bullet}$ - target gas collisions 87
4.3.4 Emissions from $CO_2^{+\bullet}$ - target gas collisions 99
4.3.5 Information from the $N_2^{+\bullet}$, $O_2^{+\bullet}$ and $CO_2^{+\bullet}$ emission spectra 110
4.3.6 Emissions from isomeric $C_2,H_4,O^{+\bullet}$ - target gas collisions 115
4.3.7 Information from $C_2,H_4,O^{+\bullet}$ CIE spectra 133
4.3.8 Emissions from isomeric $C_2,H_5,Cl^{+\bullet}$ - target gas collisions 138
4.3.9 Information from $C_2,H_5,Cl^{+\bullet}$ CIE spectra 151
4.3.10 Conclusion 154

References 155

Chapter 5 Organic Free Radical and Cation Thermochemistry 162

5.1 Introduction 162
5.2 Oxygen - Containing Organic Free Radicals 162
5.2.1 Introduction 162
5.2.2 Results and Discussion 162
5.2.3 Thermochemical conclusions 173

5.3 Cyano - Substituted Radical Cation Thermochemistry 175
5.3.1 Introduction 175
5.3.2 Experimental 178
5.3.3 Results and Discussion 178
5.3.4 Thermochemical conclusions 195

5.4 Cyano - Substituted Even Electron Cations 196
5.4.1 Introduction 196
5.4.2 Results and Discussion 197
5.4.3 Thermochemical conclusions 208

Appendix for 5.4: Mass Spectrometry of C_2,H_2,N^+ Ions 211

References 223

Claims to Original Research 229

List of Tables

		page
Table 3.4.1	Target Gases Used in CIE Experiments	46
Table 4.3.1	Observed Target Gas Emissions in Figs 4.3.1 a-d	71
Table 4.3.2	Observed Transitions in Figs 4.3.7 a-d	89
Table 4.3.3	Relative Intensities of Peaks in the He CID Mass Spectrum of Three $C_2H_4O^{+\bullet}$ Ions	135
Table 4.3.4	Relative Intensities of Peaks in the He CID Mass Spectrum of Two $C_2H_5Cl^{+\bullet}$ Ions	153
Table 5.2.1	Experimentally Determined Appearance Energies, AE, of Counter Ions, Y^+, from Precursors, RY; Calculated $\Delta_fH^\circ_{298}$ of Product Radicals, $R^\bullet$, (estimated uncertainty ± 3 kcal mol^{-1}), and Bond Strengths, D(R-H).	163
Table 5.2.2	Lowest Energy Alternative Processes Producing Counter Ions, Y^+.	167
Table 5.2.3	A Comparison of Bond Strengths of Hydroxy Substituted (position with respect to the bond in question) Alkyl Radicals, $R^\bullet$, With Those From the Corresponding Alkyl Radical, $A^\bullet$.	173
Table 5.3.1	Distribution of Charge in $R\text{-}CN^{+\bullet}$ as Calculated by MNDO.	179
Table 5.3.2	-CN Substitution in Saturated Radical Cations.	180
Table 5.3.3	-CN Substitution in Double Bond Containing Radical Cations.	183
Table 5.3.4	-CN Substitution in Triple Bond Containing Radical Cations.	184
Table 5.3.5	-CN Substitution in Benzene Ring Containing Radical Cations.	186
Table 5.3.6	Thermochemistry of -H, -Cl, -Br, -I and -CN Substituted Acetyl Radicals and Ions.	194
Table 5.4.1	$\Delta_fH^\circ_{298}(^\bullet CH_2CN)$ Derived from Kinetic Measurements.	199
Table 5.4.2	Appearance Energy Determinations for the Formation of $^+CH_2CN$ from CH_3CN.	200

Table 5.4.3 Determination of $\Delta_f H°_{298}(^{\bullet}CH_2CN)$ from AE Measurements. 202

Table 5.4.4 Summary of Results for -CN Substituted Free Radicals and Even Electron Cations. 209

List of Figures

page

Figure 2.2.1. Modified BEE geometry VG ZAB-2F mass spectrometer at the University of Ottawa. 5

Figure 2.2.2. Ion source of the ZAB-2F. 7

Figure 2.2.3. Magnetic sector. 11

Figure 2.2.4. Second field-free region (2FFR). 14

Figure 2.2.5. Electrostatic sector (ESA). 17

Figure 2.2.6. Third field-free region (3FFR). 19

Figure 2.2.7. 3FFR collision cell. 21

Figure 2.2.8. Collision cell for observing emissions from ion beam - target gas collisions in the 2FFR. 23

Figure 2.2.9. Schematic diagram of the 3FFR region for studying emissions from ion beam - target gas collisions and a detailed schematic drawing of the observation cell. 24

Figure 2.2.10. Schematic diagram of filter box assembly in the 3FFR. 27

Figure 2.3.1. Appearance energy apparatus. 29

Figure 3.2.1. Simplified potential energy surface of a molecular ion. 36

Figure 3.3.1. Examples of typical peak shapes in MIKE and CID mass spectra. 40

Figure 3.4.1. Calibration of monochromator system. 45

Figure 3.5.1. Dissociation of an ion $RY^{+\bullet}$ to $R^{\bullet} + Y^{+}$ involving a reverse energy barrier, ε_r and its relationship to $AE(Y^{+})$. 49

Figure 3.5.2. Appearance energy curves for the IE of water and the AE of m/z 43 from $CH_3C(O)CH_2CH_2OH$. 56

Figure 4.2.1. CIE spectra obtained for three $C_2H_4O^{+\bullet}$ isomers using He and O_2 target gases in C2 and OC. 63

Figure 4.2.2. He CIE spectra, C2, of two $C_2,H_5,Cl^{+\bullet}$ isomers. 65

Figure 4.3.1. $N_2^{+\bullet}$ - target collision induced emission spectra (in-OC) a) He, b) N_2, c) O_2 and d) CO_2. 75-78

Figure 4.3.2. Potential energy diagram of N_2 and $N_2^{+\bullet}$. 79

Figure 4.3.3. Expanded view of the $\Delta\upsilon = 0$ band of the $N_2^{+\bullet}$ ($B \rightarrow X$) transition. 80

Figure 4.3.4. $N_2^{+\bullet}$ - target collision induced emission spectra (in-PC) a) He, b) N_2, c) O_2 and d) CO_2. 81-84

Figure 4.3.5. Plot of total photon counts over the spectral range 180-680 nm vs target gas ionization energy for $N_2^{+\bullet}$ projectiles. 85

Figure 4.3.6. Plot of total photon counts over the spectral range 180-680 nm vs relative fragment ion, N^+, abundance in the CID spectrum of $N_2^{+\bullet}$ with the 18 target gases listed in Table 3.4.1. 86

Figure 4.3.7. $O_2^{+\bullet}$ - target collision induced emission spectra (in-OC) a) He, b) N_2, c) O_2 and d) CO_2. 92-95

Figure 4.3.8. $O_2^{+\bullet}$ - CO_2 (in-PC) collision induced emission spectrum. 96

Figure 4.3.9. Plot of total photon counts over the spectral range 180-680 nm vs target gas ionization energy for $O_2^{+\bullet}$ projectiles. 97

Figure 4.3.10. Plot of total photon counts over the spectral range 180-680 nm vs relative fragment ion, O^+, abundance in the CID spectrum of $O_2^{+\bullet}$ with the 18 target gases listed in Table 3.4.1. 98

Figure 4.3.11. $CO_2^{+\bullet}$ - target collision induced emission spectra (in-OC) a) He, b) N_2, c) O_2 and d) CO_2. 102-105

Figure 4.3.12. High resolution spectrum of the $CO_2^{+\bullet}$ ($B \rightarrow X$) transition from $CO_2^{+\bullet}$ - He (in-OC) collisions. 106

Figure 4.3.13. $CO_2^{+\bullet}$ - He (in-PC) collision induced emission spectrum. 107

Figure 4.3.14. Plot of total photon counts over the spectral range 180-680 nm vs target gas ionization energy for $CO_2^{+\bullet}$ projectiles. 108

Figure 4.3.15. Plot of total photon counts over the spectral range 180-680 nm vs relative fragment ion, C^+, O^+ and $CO^{+\bullet}$, abundance in the 109

CID spectrum of $CO_2^{+\bullet}$ with the 18 target gases listed in Table 3.4.1.

Figure 4.3.16. Fragment ion peaks in the helium CID mass spectra of $N_2^{+\bullet}$, $O_2^{+\bullet}$ and $CO_2^{+\bullet}$. 113

Figure 4.3.17. $CO^{+\bullet}$ collision induced emission spectra (in-OC) a) He and b) Ar 119,120

Figure 4.3.18. HCO^+ collision induced emission spectra a) He (in-OC), b) He (in-PC), c) He (in-PC) - higher resolution and d) Ar (in-OC). 121-124

Figure 4.3.19. CH_3^+ - He (in-OC) collision induced emission spectrum. 125

Figure 4.3.20. oxirane$^{+\bullet}$ collision induced emission spectra a) He (in-OC), b) Ar (in-OC) and c) Ar (in-PC). 126-128

Figure 4.3.21. acetaldehyde$^{+\bullet}$ collision induced emission spectra (in-OC) a) He and b) Ar. 129,130

Figure 4.3.22. vinyl alcohol$^{+\bullet}$ collision induced emission spectra (in-OC) a) He and b) Ar. 131,132

Figure 4.3.23. $CCl^{+\bullet}$ - He (in-OC) collision induced emission spectrum. 141

Figure 4.3.24. CH_2Cl^+ collision induced emission spectra a) He (in-OC), b) He (in-PC), c) Ar (in-OC) and d) Ar (in-PC). 142-145

Figure 4.3.25. $CH_3CH_2Cl^{+\bullet}$ collision induced emission spectra a) He (in-OC), b) Ar (in-OC) and c) Ar (in-PC). 146-148

Figure 4.3.26. $CH_3ClCH_2^{+\bullet}$ collision induced emission spectra (in-OC) a) He and b) Ar. 149,150

Figure 5.3.1. Plot of IE vs 1/n for saturated radical cations with substituent -H, -CN, -Cl, -Br and -I. 182

Figure 5.3.2. Plot of IE vs substituent for triple bond containing radical cations with either -H or -CN substituent. 185

Figure 5.3.3. Plot of IE vs sbustituent for aromatic ring containing radical cations with either para-H or para-CN substituent. 189

Figure 5.4.1. 2FFR CID mass spectra of source generated C_2,H_2,N^+ ions from 214

precursor molecules I-IV.

Figure 5.4.2. NR mass spectra of source generated C_2,H_2,N^+ ions from precursor molecules I-IV. 215

Figure 5.4.3. 3FFR He CID mass spectra of m/z 40 recovery ions in 2FFR NR mass spectra of source generated C_2,H_2,N^+ ions from precursor molecules I-IV. 216

Figure 5.4.4. 3FFR He CID mass spectra of m/z 40 ions in 2FFR MIKE spectra of metastable precursor ions from precursor molecules I-IV. 219

List of Abbreviations

AE	- appearance energy
ARMS	- angle resolved mass spectrometry
B	- denotes a magnetic sector
CID	- collision induced dissociation
CIE	- collision induced emission
CS	- charge stripping
Da	- Dalton (atomic unit of mass)
E,ESA	- denotes an electrostatic sector
FFR	- denotes a field-free region
$\Delta_f H^\circ_{298}$	- heat of formation at 298K under standard conditions (1 atm)
IE	- ionization energy
MIKES	- mass-analyzed ion kinetic energy spectrometry
MS	- mass spectrometry
NR	- neutralization - reionization
OC	- observation cell
PC	- post-collision cell
TES	- translational energy spectroscopy
UV	- ultra-violet wavelength region
VIS	- visible wavelength region
VUV	- vacuum ultra-violet

Chapter 1

Some Preliminary Remarks

Gas phase ion chemistry, as the name implies, is the science of understanding the chemistry (bond making and breaking) of organic, inorganic and organometallic species (molecules, ions and radicals) in the gas phase. Interest lies in the unimolecular structural rearrangements and bond dissociations of ions and neutrals as well as the more classical chemistry of bimolecular reactions, etc. Many techniques are employed to study the chemistry of gas phase ions and neutrals over a wide variety of conditions. The most popular is mass spectrometry. Mass spectrometry as a technique extends into almost every field of science, probably more so than any other. An example to illustrate this can be found in the subject headings in the publication "Mass Spectrometry Bulletin" , a monthly offering of The Royal Society of Chemistry, Thomas Graham House, Science Park, Milton Road, Cambridge, U.K.. It attempts to list all publications which are associated with mass spectrometry. The headings are: instrument design and techniques, isotope studies, mass measurement, chemical analysis, general organic chemistry, organic mass spectrometry, natural products, drugs and pharmacology, clinical studies, general biochemistry, polymer chemistry, organometallic, inorganic, fossil fuels, geochemistry, environmental, electron impact ionization, photoionization, nonreactive ion processes, reactive ion processes, ion/molecule reactions, clusters, electron spectroscopy, neutral particles, surface phenomena, solid state studies, thermodynamics and reaction kinetics.

Mass spectrometry as a technique started with the identification of the isotopes of the elements (information in the next two paragraphs is from "Mass Spectrometry" 2nd ed,

by H.E. Duckworth, R.C. Barber and V.S. Venkatasubramanian, Cambridge University Press, Cambridge, 1986). J.J. Thomson (1913) used his positive ray parabolae to determine that cations of the elements can have different masses, or isotopes. F.W. Aston (1919), at Cambridge, made the first mass spectrograph to separate and enrich the isotopes of the elements. It focussed the positive ions to increase resolving power. A.J. Dempster (1918), a Canadian working at the University of Chicago, built a semi-circular analyzer which focussed a beam of ions with a magnetic field. Mass spectrometry started to move from the separation of isotopes to the determination of atomic mass. It was during the 1930's in particular, and with the work of K.T. Bainbridge, that many atomic masses were determined accurately for the first time.

The modern sector mass spectrometer (which employs magnets and energy analyzers) was born from the derivation of trajectory equations for ions in magnetic and electric fields. R. Herzog, J.H.E. Mattauch, E.G. Johnson and A.O. Nier were particularly influential on the design of sensitive high resolution mass spectrometers. Since World War II mass spectrometry has moved in several directions. Higher resolution has always been a goal and two, three, four and even five sector mass spectrometers are manufactured. Alternatives to the sector instrument have been developed to suit a wide variety of special conditions, samples and desired physico-chemical information. They include time-of-flight, quadrupole, ion trap and ion cyclotron resonance instruments. Mass spectrometry has also moved from its beginnings in atomic mass measurement to a fundamental tool in gas phase ion chemistry.

The reader will notice from the title that this thesis consists of what seem to be

two very different lines of investigation. However, they are both intimately related to gas phase ion chemistry in different ways. The first part of the title, photon emissions from ion beam - target gas collisions, concerns the application of a technique common to collision spectroscopy to the study of gas phase ion chemistry. It is the first attempt to study the collisions between polyatomic projectiles and a target gas by examining light emissions from electronically excited collision products. As will be discussed in Chapter 4, it represents the first non mass-spectral investigation of the role of internal excitation in polyatomic projectile - target gas collisions, a technique that has been used in mass spectrometry and gas phase ion chemistry for over 25 years. A critical part of collision-based studies is the energies of the reactants, products and intermediates. Since the intermediates and products of the collision induced processes are atoms, free radicals, molecules and cations (even and odd electron), their energies, and in particular their heats of formation need to be known. The field of gas phase thermochemistry is a long studied area of chemistry. However, our knowledge of the thermochemistry of transient species such as free radicals and cations is limited. The second half of this thesis concerns the measurement of gas phase organic free radical and cation heats of formation using the appearance energy technique. The experimental results are primarily for oxygen-containing carbon centred free radicals, but a discussion of the influence of the cyano group on the thermochemistry of radicals and even and odd electron cations is also presented. In essence, this thesis joins the old and the new and demonstrates the importance of not only pushing a field to the limits of existing technology but also of continuing to pursue more traditional lines of investigation when they can contribute.

Chapter 2

Instrumentation

2.1 Introduction

In this chapter, the components of the instruments used to complete the work presented in this thesis are described. Two instruments were used, a Vacuum Generators ZAB-2F sector mass spectrometer of BEE geometry (magnetic sector followed by two electrostatic sectors) for both standard gas phase ion chemistry and collision induced emission spectroscopy, and the electron monochromator/quadrupole apparatus for appearance energy determinations. The details of the experimental procedures will be discussed in Chapter 3.

2.2 The VG ZAB-2F Mass Spectrometer

The components and ion optics of the ZAB mass spectrometer have been published by the manufacturers [1] but the instrument at the University of Ottawa has undergone several significant modifications over the past 12 years and hence it will be described in detail in this thesis. A general schematic diagram of the instrument is shown in Fig. 2.2.1. Shown is the present three sector mass spectrometer of BEE geometry. Prior to November 1992, only the first two sectors were available and have been described elsewhere [2]. The third, along with the shown third field-free region (3FFR) was added to enhance the versatility of the instrument. The unique features which make it important to the work reported in this thesis will be discussed.

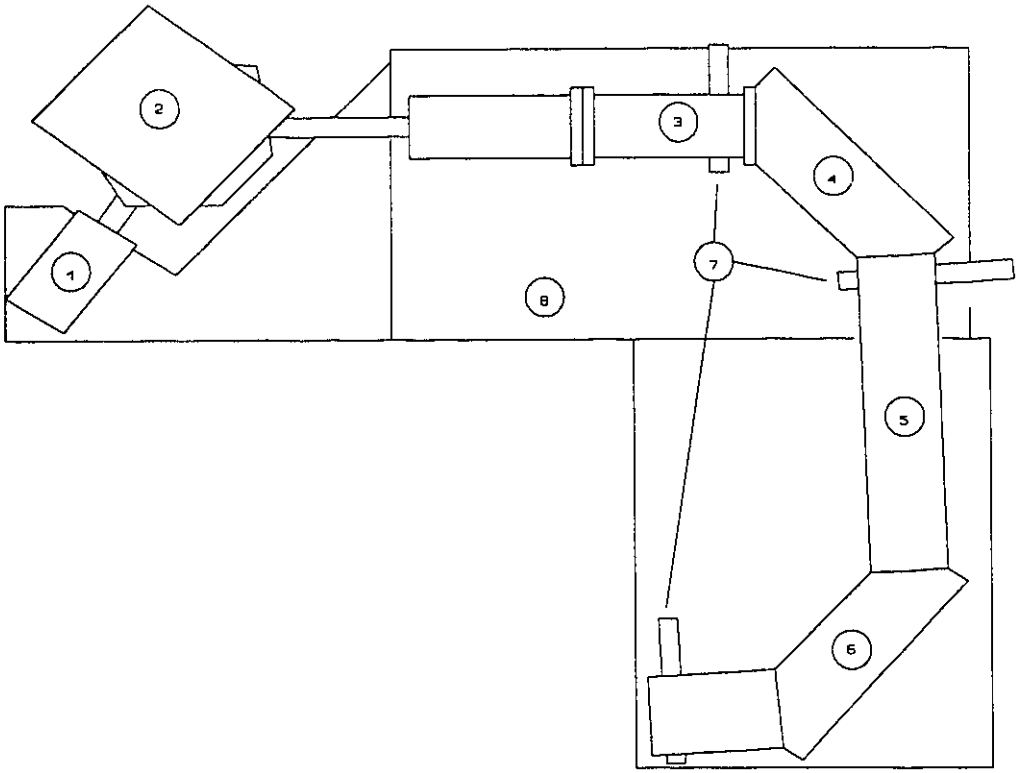

Fig. 2.2.1. Modified BEE geometry VG ZAB-2F mass spectrometer at the University of Ottawa, 1. ion source, 2. magnet, 3. second field-free region (2FFR), 4. electrostatic analyzer 1 (ESA 1), 5. third field-free region (3FFR), 6. electrostatic analyzer 2 (ESA 2), 7. detector assemblies, 8. mass spectrometer bench.

2.2.1 The ion source of the ZAB-2F

A mass spectrometer's ion source is, as the name implies, the part of the instrument where the ions to be studied are made. Fig. 2.2.2 shows a schematic diagram of the ion source assembly on the ZAB. The dimensions are roughly correct, though some licence has been taken for the sake of clarity. In the left column the components are shown separated when in reality they are stacked together into a single block approximately 20 mm tall. Gaseous samples are introduced into the ionization chamber which consists of the space inside the ion source between the source base (5) and cover (11) surrounded by the block (7), via any of the three inlet ports in the ion source block (7):

a) solids probe/CI gas inlet (8) - the solids probe has a ceramic tip in which a small glass tube, typically the lower 1 cm of a conventional melting point tube, is inserted. The solids probe is pushed into the ion source housing via a differentially pumped vacuum lock and the tip inserted into the inlet (8). The tip can be heated and sample which sublimes off the solid inside the glass tube enters the ionization chamber. Also, gas samples can be introduced through this inlet via a variable leak valve located exterior to the ion source housing, which in turn is connected to the gas cylinder containing the sample.

b) liquids septum inlet (9) - liquids can be introduced with a microlitre syringe into a heated metal drum reservoir (typically held at 100-140 °C). Vapours from the liquid then pass through a glass capillary approximately 10 cm long and leak into the ionization chamber via this inlet.

c) Granville-Phillips™ septum inlet (10) - A Granville-Phillips™ variable leak valve is

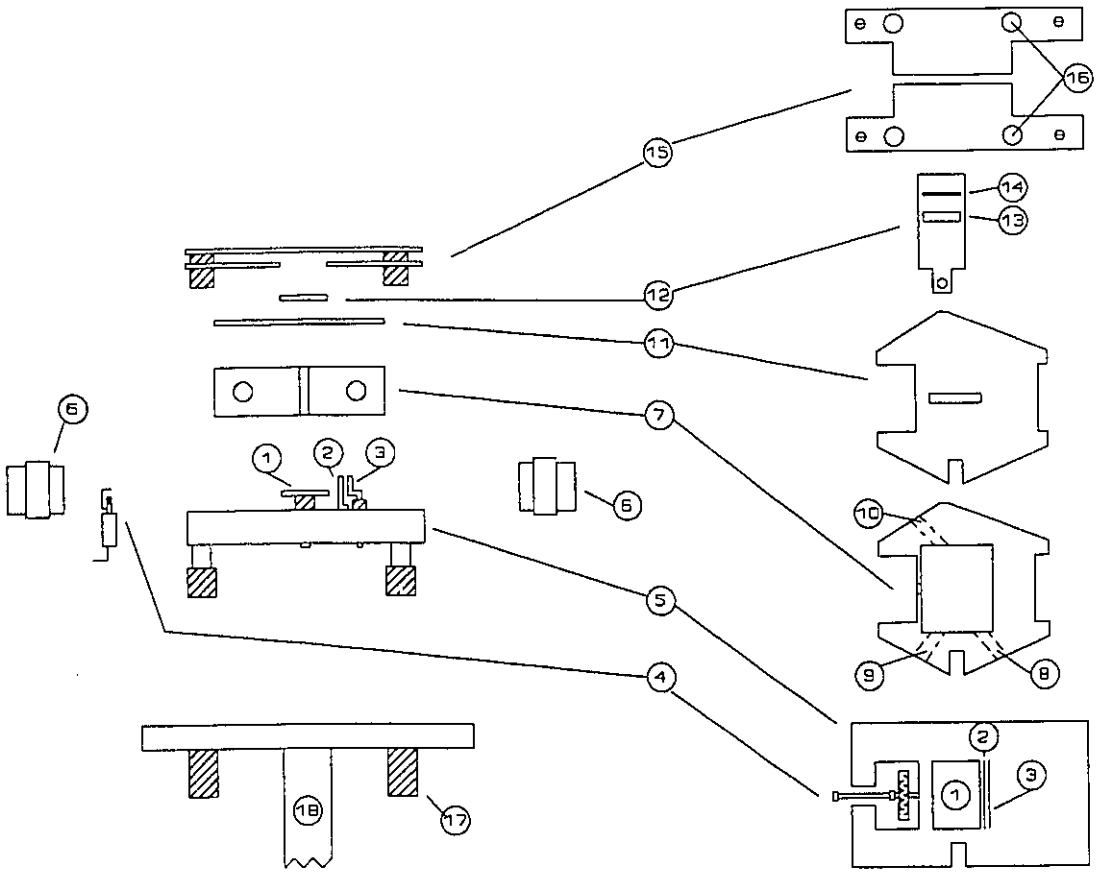

Fig. 2.2.2. Ion source of the ZAB-2F, 1. repeller electrode, 2. grounded plate, 3. trap electrode, 4. filament support and wire coil, 5. ion source base, 6. magnet, 7. ion source block, 8. CI gas inlet/solids probe inlet, 9. liquids septum inlet, 10. Granville Phillips™ septum inlet, 11. source cover, 12. variable source slit, 13. electron impact slit, 14. chemical ionization slit, 15. preliminary beam focus, 16. ion source alignment holes, 17. ceramic electrical insulators, 18. ion source support.

used to permit vapours from volatile liquids to pass through a glass capillary approximately 10 cm in length and bleed into the ionization chamber. Samples are frozen in a glass pot, pumped down to about 0.01 mbar (1 Pa) and allowed to thaw. The process is referred to as "degassing". Degassing is performed at least once and commonly 2-3 times if the sample warrants it due to the presence of air or other volatile impurity. This inlet system allows volatiles to be introduced into the ionization chamber without heating the sample, a process which may cause the premature decomposition of thermally unstable compounds.

Once inside the ionization chamber, the gaseous molecules of the sample are exposed to an electron beam emanating from the filament (4). The filament is a small coil of Rhenium wire through which is passed roughly 2.5 amps of current. The thermally ejected electrons are accelerated toward the ion source block by a variable potential difference with respect to the source block (usually +50 to +100 V but values as low as +5 V are possible). The electrons pass through a small hole in the source block and travel across the ionization chamber to the electron trap (3), positive with respect to the source block, where the current can be monitored. Two magnets (6) at opposite ends of the source, parallel to the path of the electrons, provide sufficient magnetic field to cause the electrons to supposedly take a spiral path through the ionization chamber, increasing the time they spend there, thus increasing the chance that a molecule/electron encounter will occur.

Any neutral species which are produced in the above processes are lost to the differential pumping system. Anions produced by electron capture are accelerated into the

base of the ion source (5) by the positive potential difference applied to the entire source assembly (typically 8000 V with respect to the grounded source housing). Cations formed are pushed out of the ionization chamber by the repeller electrode (1) which is typically positive with respect to the source block by a few volts. The ions pass through the slit in the source cover (11), through either the EI (13) or CI (14) slit, and are accelerated toward the magnetic analyzer due to the 8000 V potential applied to the source assembly (5,7,11,12). The importance of the adjustable EI/CI slit (12) follows.

Under normal electron impact ionization conditions the slit used (13) is wide and allows the maximum number of ions to leave the source to give the greatest sensitivity. However, it is possible to form ions another way, a process referred to as chemical ionization (CI). A relatively large pressure of a reagent gas (ex. methane, methylpropane, ammonia) is introduced into the source via inlet (8) together with a trace pressure of the sample. Electron impact ionization will occur predominantly with the reagent gas, A, due to its large excess. The ionized reagent, $A^{+\bullet}$, undergoes bimolecular reactions with A to form species such as AH^+. The protonated reagent molecules can react with the sample molecule, M, to produce adduct ions such as MH^+ (also MNH_4^+ using ammonia). These sample molecule adducts are termed "pseudo-molecular ions" since they differ from normal molecular ions ($M^{+\bullet}$) but still contain the intact molecular structure. These pseudo-molecular ions tend to survive to the detector without dissociating. To achieve the relatively large source pressures needed to perform CI (~ 10^{-3} - 10^{-2} mbar or 0.1-1 Pa), the ionization chamber needs to be as closed as possible. The CI slit (14) is much narrower than the EI slit and allows the pressure inside the ionization chamber to be

raised without tripping the differential pumping system's safety relay.

Once the ions leave the ionization chamber, they are accelerated to zeV translational kinetic energy (T) (z = number of charges, e = atomic unit of charge in Coulombs and V = potential difference in volts; T(eV) = zeV) by the potential applied between the source block and housing. The beam is focussed toward the lens assembly by two plates (15) which are about -1 kV with respect to the source block and independently variable.

2.2.2 Ion beam focussing lens assembly

The focussing lens is located immediately after the ion source and consists of some 27 independently and co-variable electrodes in a space roughly 5 cm long. As the beam of ions passes through the lens, voltages applied to the plates affect its path. Independently adjusting the potentials applied to the components of the lens allows the investigator to better collimate the beam for improved transmission through the rest of the instrument. A focussing lens assembly is also present in both the second and third field free regions (see secs 2.2.4 and 2.2.6).

2.2.3 The magnetic sector: momentum analysis

Once focussed, the ion beam travels through a short region which is free of electric and magnetic fields called, appropriately, the first field-free region. It then enters the magnetic sector (Fig. 2.2.3). The magnetic sector consists of two parallel electromagnets (1) surrounding an iron core. The ion beam travels through the flight tube (3) perpendicular to the direction of the imposed magnetic field. The path of an ion travelling orthogonal to a magnetic field is described by a simple mathematical

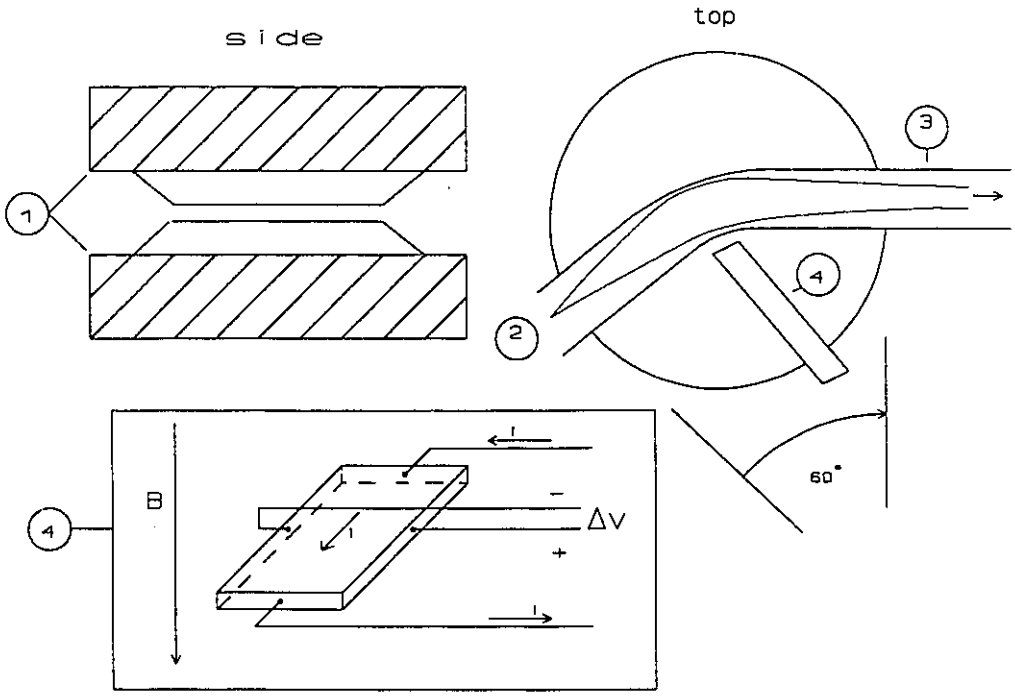

Fig. 2.2.3. Magnetic sector, 1. electromagnet coils, 2. ion beam path, 3. flight tube, 4. Hall probe.

relationship:

$$r = mv/Bze \qquad (I)$$

where r is the radius of curvature of the path of the ion, m is the ion's mass, v is the velocity, B is the magnetic field strength and z and e are as described in section 2.2.1. The ZAB-2F has a magnetic sector with a fixed radius of curvature of 30 cm [1]. So,

$$mv = Brze \qquad (II)$$

Changing the value of B selectively passes ions of particular values of mv, momentum, through the magnetic sector. From sec. 2.2.1 it was seen that the ions are given zeV translational kinetic energy upon exiting the ionization chamber.

$$zeV = \tfrac{1}{2}mv^2 \qquad (III)$$

$$v = (2zeV/m)^{\frac{1}{2}} \qquad (IV)$$

So, eq. (II) becomes,

$$m/z = B^2r^2e/2V \qquad (V)$$

In other words, ions with a particular mass-to-charge ratio, m/z, can be selectively passed through the magnetic sector by appropriate choice of a value of B.

Ions then travel to the second focal point of the magnetic sector situated in the second field-free region (2FFR) of the instrument, Fig. 2.2.1. The strength of the magnetic field is controlled by varying the current through the electromagnet coils (1). It is monitored by a Hall probe (4) whose function is based on the Hall effect. The inset in Fig. 2.2.3 shows the fundamental principles of the Hall probe. A strip of metal is placed orthogonal to the magnetic field flux (shown as the downward arrow to the left of the diagram) and a current, i, is driven through it, again orthogonal to the magnetic field. The

magnetic field applies a force to the charge carriers (electrons) in the metal strip normal to both the current direction and magnetic field flux, causing them to drift to one edge. This migration produces a potential difference, ΔV, across the strip, proportional to the magnetic field strength for a given value of i, which can be measured and monitored.

Ions which dissociate inside the magnetic field yield product ions which will not have the proper momentum to be focussed at the second focal point. Product neutrals are not affected by the magnetic field and will travel in a straight line path until they encounter a surface.

2.2.4 The second field-free region (2FFR)

The momentum-selected ion beam passes through the second field-free region of the instrument (Fig. 2.2.1) on its way to the electrostatic sector. An expanded view of the 2FFR can be found in Fig. 2.2.4. A more detailed discussion has been presented elsewhere [3]. The dimensions in Fig. 2.2.4 are not to scale but rather for schematic clarity. The entire 2FFR is shown in the lower part of the figure as a profile from above while an expanded view of the experimental components in the region is shown from the side in the upper part of the figure. The beam traverses five areas in the experimental section of the 2FFR:

a) Collision Cell, C1 (1) - A collision cell consists of a 2-3 cm long block of steel through which a 2 mm groove is cut. The beam passes through the cell via this groove. A collision (target) gas can be introduced into the groove, prompting projectile - target gas collisions. A more detailed discussion of collision events and experiments will be presented in the next two chapters. The differential pumping in the region produces a

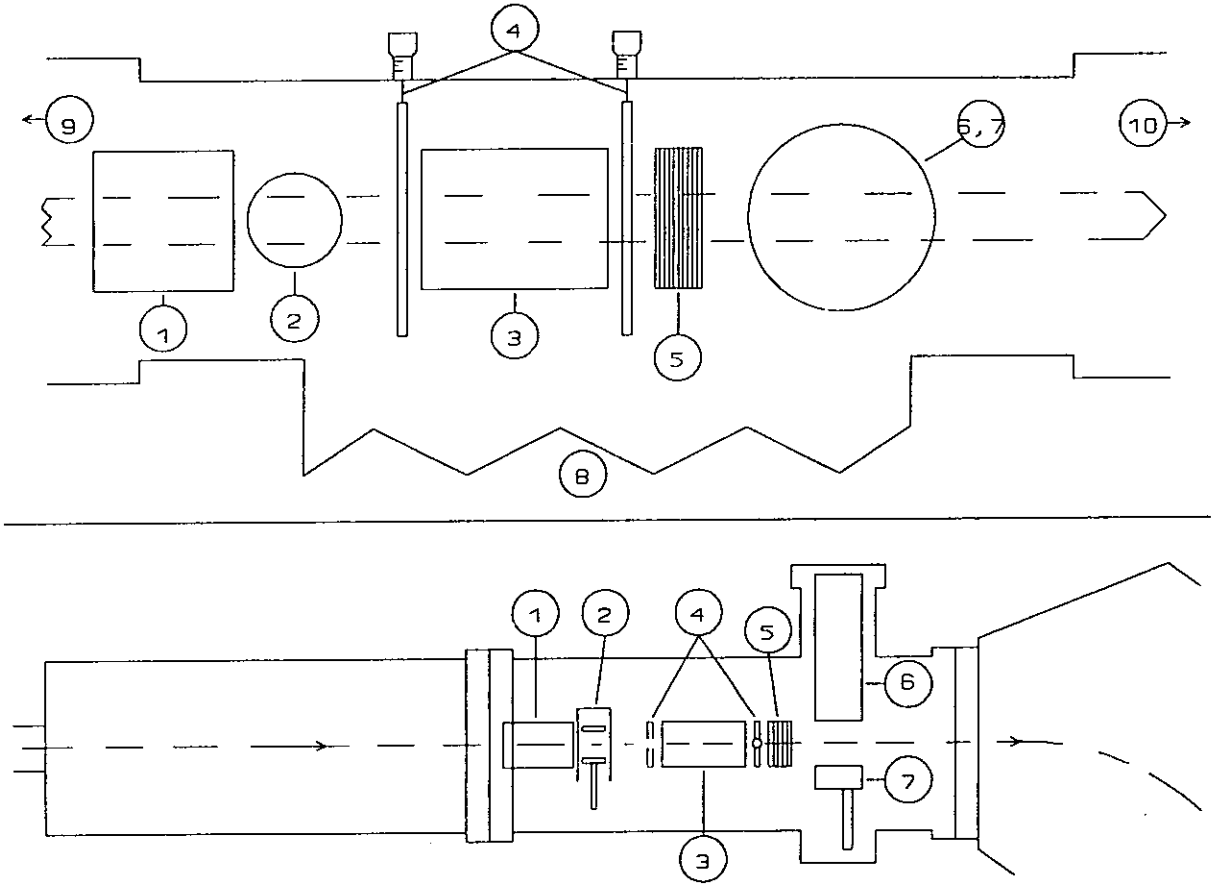

Fig. 2.2.4. Second field-free region (2FFR), 1. collision cell C1, 2. beam deflector electrode, 3. collision cell C2, 4. y-axis beam collimating slits, 5. focussing lens assembly, 6. single focussing detector electron multiplier, 7. single focussing detector conversion dynode, 8. diffusion pump stack, 9. to magnetic sector, 10. to electrostatic sector.

pressure gradient between the cell and the surroundings preventing the gas from spreading throughout the region. Once through C1 the beam passes the ion beam deflector electrode.

b) Beam Deflector Electrode (2) - A potential difference can be applied between the electrodes on either side of the ion beam deflecting charged projectiles out of the beam path.

c) Collision Cell, C2 (3) - Situated at the second focal point of the magnetic sector and the entrance focal point of the first electrostatic sector is the original (manufacturer installed) collision cell. It is the same as C1 except 1.0 cm longer. On either side of the cell are y-axis (horizontal plane) beam collimating slits (4) used to improve the selectivity of the projectiles entering C2.

d) Focussing lens assembly (5) - The ion beam passes through a focussing lens assembly similar in function and design to that described in sec. 2.2.2. The lens allows the investigator to steer the beam into electrostatic analyser 1 (ESA 1).

e) Detector (6,7) - Finally, the beam passes on to the single focussing detector assembly (6,7). The detector consists of an electron multiplier, EM (6), on one side of the ion beam and an electrode, called the conversion dynode (7), on the other. A high voltage (kV) is applied to the dynode causing the beam to be attracted onto its surface. The high energy surface collisions eject electrons from the dynode which are accelerated by a potential difference across to the EM where they are monitored. For most applications, the single focussing detector is not used and the ion beam is allowed to traverse the ESA.

To monitor the pressure inside the mass spectrometer, an ionization gauge is used. It acts like an ion source in that gas molecules pass over a filament and become ionized.

The ions then are attracted to a counter electrode and the resulting current obtained is proportional to the number of gas molecules passing over the filament. The reponse current is then calibrated to give a reading of pressure. The field-free regions and sectors of the mass spectrometer are kept at 10^{-8} mbar (~ 1 x 10^{-6} Pa).

2.2.5 The electrostatic sector: energy analysis

Once the ions complete transit of the 2FFR they enter an electrostatic sector, Fig. 2.2.1 and Fig. 2.2.5. The sector consists of two curved parallel plates between which is applied a potential difference producing an electric field of strength E. Transmission of an ion through the sector is governed by the following relationships:

$$\tfrac{1}{2}mv^2 = \tfrac{1}{2}zeEr \qquad \text{(VI)}$$

and from eq. III this becomes

$$2zeV = zeEr$$

giving

$$r = 2V/E \qquad \text{(VII)}$$

The two ESA sectors on the ZAB each have a radius of curvature, r, of 38 cm. Adjusting the potential across the ESA plates allows ions of selected translational kinetic energy to pass through and be focussed, at which point a detector assembly is present to monitor the ion flux. Note in eq. VII that neither the mass nor charge of the ion is present. So, ions with one, two, three, etc. charges, accelerated by a potential, V, will pass through the ESA at a common value of E. An ion with +1 charge accelerated across a potential difference of 8000 V will have 8 keV translational kinetic energy and be focussed by the ESA by a field of E_1. An ion with +2 charges will have 16 keV translational energy but

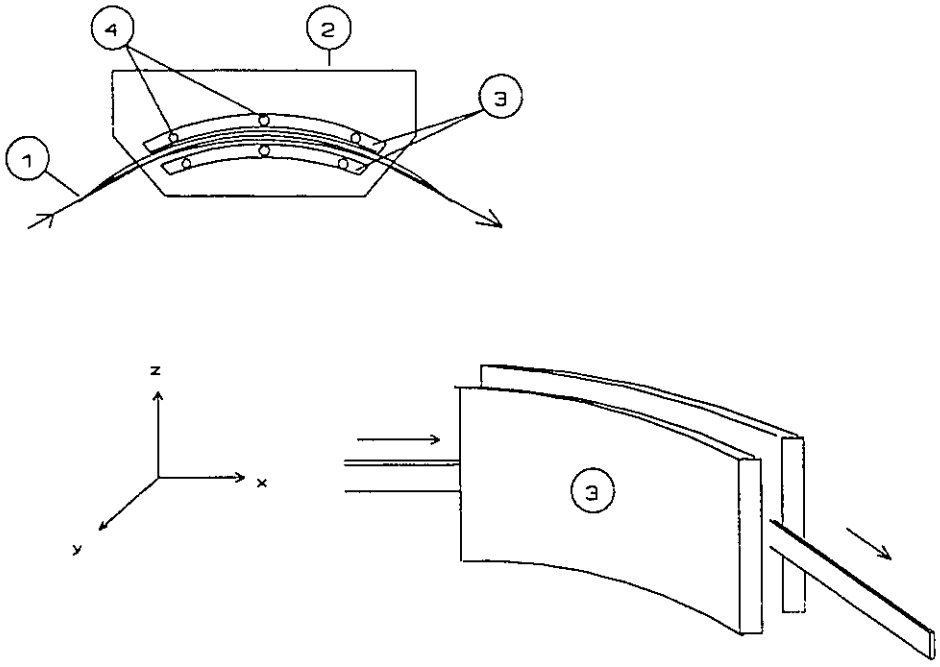

Fig. 2.2.5. Electrostatic sector (ESA), 1. ion beam path, 2. ESA housing, 3. curved steel plates, 4. positioning points.

will experience a field strength equivalent to $2E_1$ at the same values of accelerating and ESA potential difference as the singly charged ion.

As with the magnetic sector, product ions and neutrals from ion dissociations inside the sector will not pass through the ESA.

2.2.6 The third field-free region (3FFR)

After traversing the first ESA, the ion beam travels through the third field-free region (3FFR), Fig. 2.2.6. The 3FFR was manufactured by VG Analytical (Manchester) and delivered in the fall of 1992. It consists of a 1 metre long box differentially pumped by 2 six-inch diffusion pumps and ending in a second ESA. The lower part of Fig. 2.2.6 shows the complete 3FFR. An expanded view of the experimental region is in the upper portion of the figure.

The ion beam is focussed by the first ESA at the y-axis beam collimating slits (1). There, it can be detected by the double focussing detector assembly (2,3). The detector consists of a photomultiplier tube (PMT (2)) coupled with a conversion dynode (3). A high voltage applied to the dynode pulls the ion beam toward it and the resulting keV collision of the beam with the dynode surface causes electrons to be ejected. A potential difference between the dynode and the PMT accelerates the electrons across the gap to impinge on a scintillant material which emits photons detected by the PMT. When the detector is turned off, the ion beam passes on through a focussing lens assembly (4). This lens focusses the beam gradually down to the end of the 3FFR to the primary focus of the second ESA at the y-axis slit (11). As the now near parallel ion beam passes through the 3FFR experiments can be performed on it. Presently, the region contains three normal

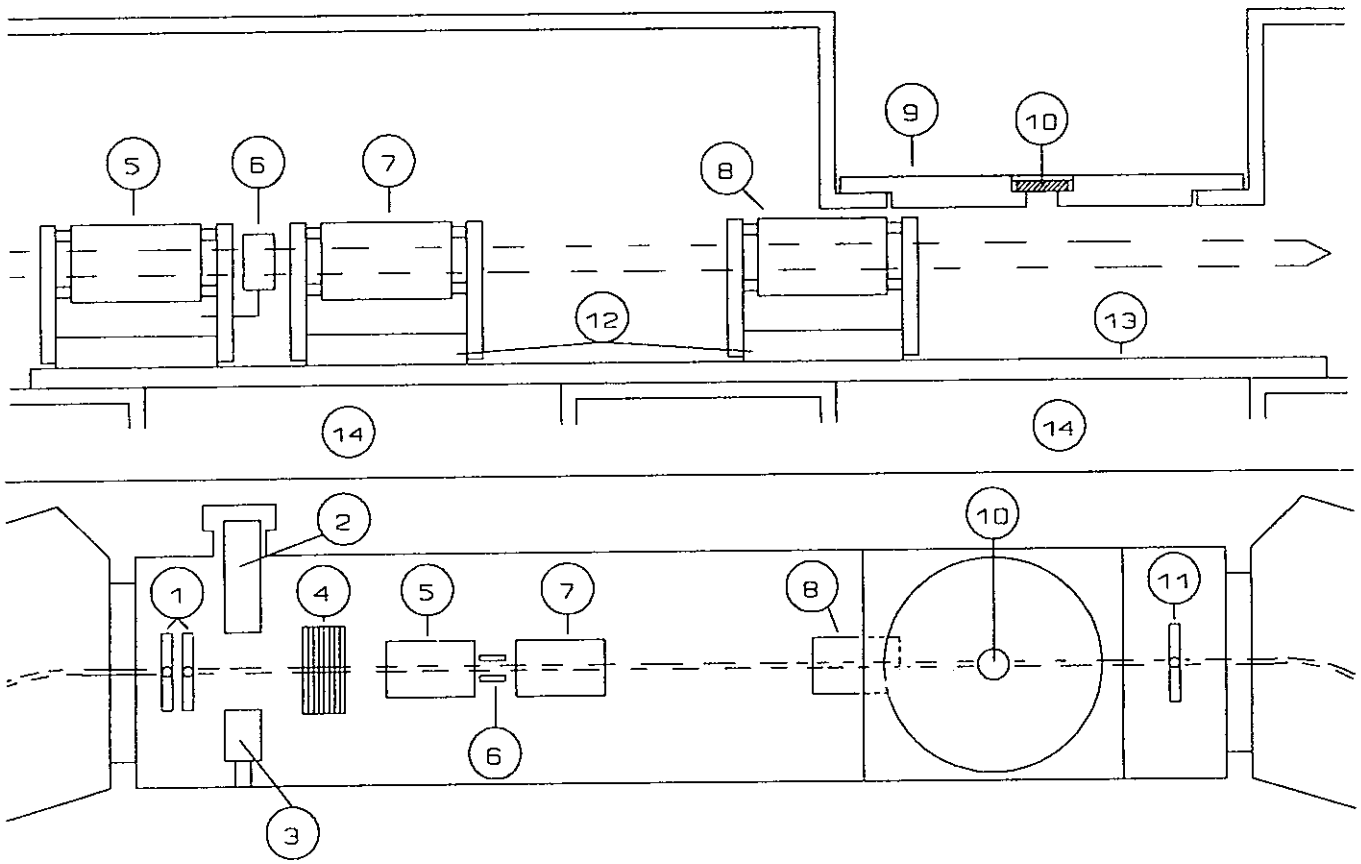

Fig. 2.2.6. Third field-free region (3FFR), 1. y-axis beam collimating slits, 2. photomultiplier tube, 3. conversion dynode, 4. focussing lens assembly, 5. collision cell, 6. deflector electrodes, 7. collision cell, 8. collision cell, PC, 9. window flange, 10. optical window, 11. y-axis beam collimating slit, 12. collision cell boats, 13. two parallel optical rails, 14. diffusion pump stacks.

collision cells (5,7,8) mounted on boats (12) which can be moved anywhere along a pair of optical rails (13) running along the bottom of the 3FFR box housing. The collision cells in the 3FFR were designed during the thesis work. A scale diagram of a cell assembly can be found in the upper portion of Fig. 2.2.7. The assembly is held together by four threaded rods each passing through a glass tube running the length of the cell. This electrically isolates the cell body (1) allowing it to be floated by several hundred volts with respect to the grounded end plates (2). The end plates prevent the field generated by a charged cell from penetrating into the surrounding region, defocussing the ion beam. The first cell in the region has a pair of plate electrodes extending from its exit end plate, insulated from the rest of the cell. A potential difference applied between the elctrodes may be used to deflect projectile ions out of the beam path.

Near the end off the 3FFR is a zone designed for the study of radiation emitted by projectile - target gas collisions. It consists of an indented housing and a flange (9) which is capable of holding a transparent window (10). The details of the apparatus used for this work follows in the next section.

Passage of the ion beam through the second ESA to the triple focussing detector assembly (exactly the same as the double focussing assembly) is governed by the same rules and equations as presented for the first ESA, sec. 2.2.5.

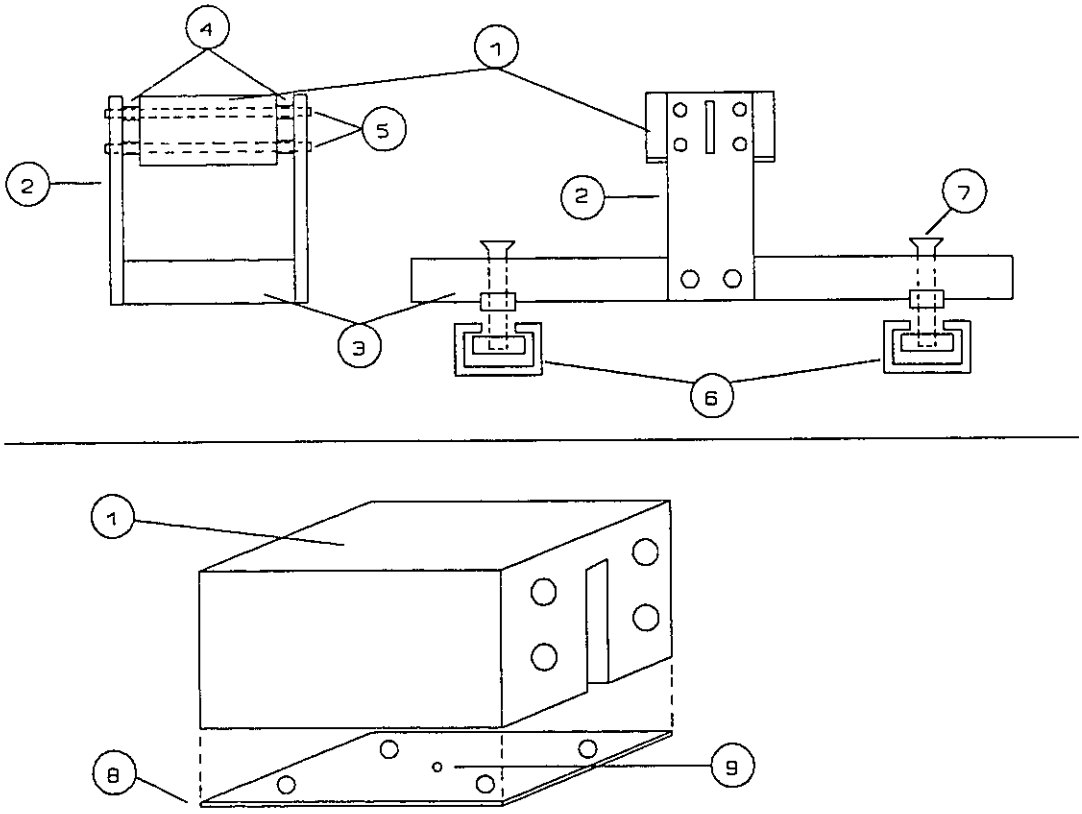

Fig. 2.2.7. 3FFR Collision cell, 1. collision cell body, 2. end plates, 3. mounting boat, 4. ceramic electrical insulators, 5. glass tubing, 6. optical rails, 7. boat - rail fastening bolts, 8. cell body bottom plate, 9. target gas inlet hole.

2.2.7 Apparatus for analyzing photon emissions from projectile - target gas collisions

The apparatus described in this section for the detection and analysis of photon emissions from projectile - target gas collisions were developed during the course of study of this thesis. Experiments prior to November 1992 were performed in the 2FFR of the ZAB-2F (Fig. 2.2.4). With the installation of the 3FFR and second ESA, a new apparatus was developed which allowed monochromated emission spectra to be obtained (3FFR experiments).

a) 2FFR experiments - The only place available to attempt a study of photon emissions from collisionally activated ion beams was the region occupied by the single focussing detector (Fig. 2.2.4, (6)). A novel collision cell / PMT housing assembly was designed to fit into the flange which normally held the detector EM (Fig. 2.2.8). A collision cell (1) was mounted with one side wall next to a quartz window (2). The inside of the cell was highly polished to increase the reflection of light through the window. Light exiting the cell travels down a polished tube (ID 20 mm) (3) before exiting the 2FFR housing flange (4). Attached exterior to the flange was an adapter (5) which could hold a rectangular bar having a series of holes into which the wavelength cutoff filters (Newport Inst. Canada, Nepean, Ontario) were glued.

b) 3FFR experiments - This apparatus is illustrated in Fig. 2.2.9. The observation cell (OC) is located in the 3FFR (Fig. 2.2.6) underneath the quartz window (fused silica - WU-25 Optikon Corp., Waterloo, Ontario), allowing the analyzing device to be brought within 30 mm of the ion beam. Collisions can be performed in the OC and emissions

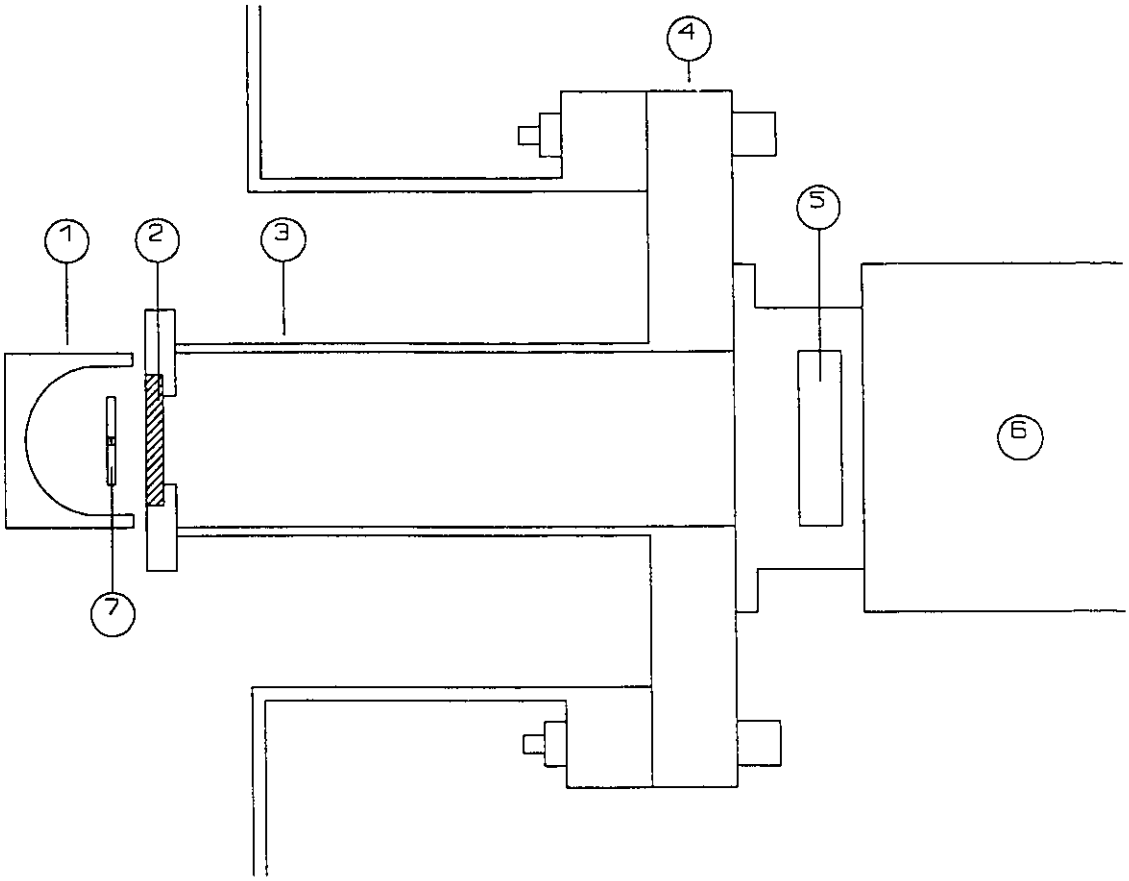

Fig. 2.2.8: Collision cell for observing emissions from ion beam - target gas collisions in the 2FFR, 1. collision cell with polished, semicylindrical interior, 2. quartz window, 3. polished tube, 4. vacuum flange, 5. filter bar adaptor, 6. photomultiplier housing, 7. ion beam, out of page.

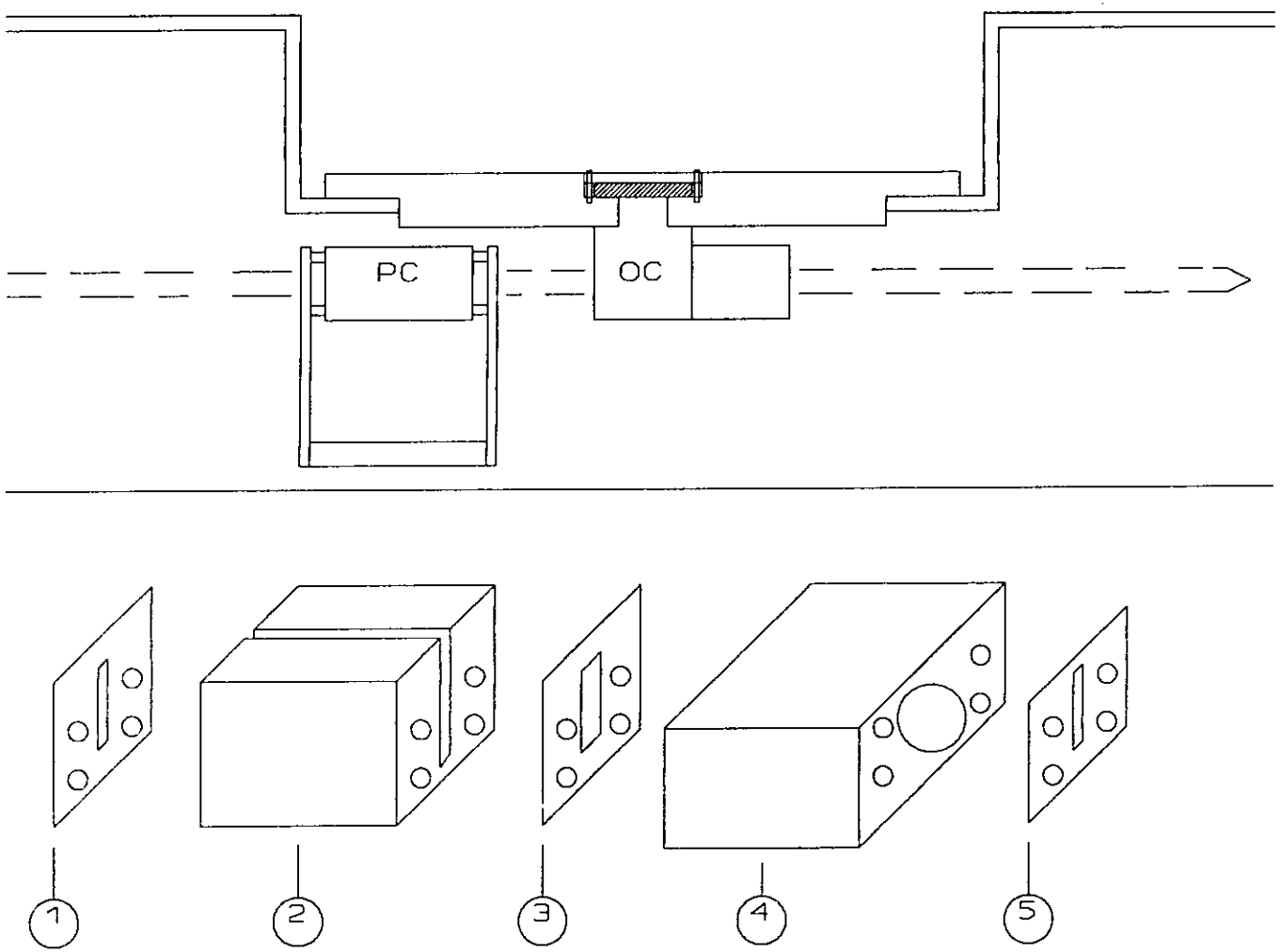

Fig. 2.2.9. Schematic diagram of the 3FFR region for studying emissions from ion beam -target collisions and detailed schematic drawing of observation cell, OC, 1. entrance slit, 2. standard collision cell, 3. intermediate slit, 4. absorber cell, 5. exit slit.

from excited ions and target directly observed (in-cell observations); the time window of observation being 0.00 - 0.09 μs with 8 keV $N_2^{+\bullet}$, but will depend on the mass and translational energy of the projectile ion. Situated before the OC is a moveable collision cell, PC (see also Fig. 2.2.6). Collisions performed in this cell allow the analysis of emissions from the ion beam without interference from target gas emissions. However, the lifetimes of states studied is limited to long-lived metastable states. These experiments will be referred to as post-collision observations. It was discovered in the early experiments that photons were emitted from metal surfaces when struck by keV ions. While the normal ion beam passing through the observation cell did not cause metal surface emissions, it is known that ion beam - target gas collisions scatter ions from the beam path. It was a potential problem that these scattered ions would cause interfering metal surface emissions. The observation cell was designed to prevent this (lower portion of Fig. 2.2.9). The standard cell (2) has a 3 mm groove and attaches directly underneath the window. To prevent scattered ions from impinging on the exit slit, a wide intermediate slit (3) is situated between the standard cell and the absorber cell (4). The absorber cell consists of a cylindrical chamber blackened with Aqua-Dag™. This is followed by a standard exit slit (5). Photons emitted when the scattered ions hit the final, narrow exit slit are absorbed in the absorber cell and do not make it back into the standard cell and through the window to the detector. Tests have shown that this cell arrangment successfully eliminates interfering metal surface photon emissions.

The entrance slit of a scanning wavelength monochromator (Acton SpectraPro 275, 27.5 cm focal length, 1200 groove/mm holographic grating) was positioned over the OC

and used to wavelength resolve light emitted in it. A cooled PMT (Thorn EMI 9635QB, 180-680 nm range, Products For Research Cooler, TE 182TSRF), attached to the exit slit of the monochromator, was used to monitor the wavelength resolved emissions. The details of their use will be described in Chapter 3.

The second type of experiment reported for the 3FFR apparatus is one in which the light emitted by long-lived excited state species in the OC was analyzed by wavelength cutoff filters (see sec. 2.2.7a). The filters were glued into a filter bar similar to the one used in the 2FFR experiments. A schematic diagram of the apparatus used to manipulate the filters in a light-tight environment is shown in Fig. 2.2.10.

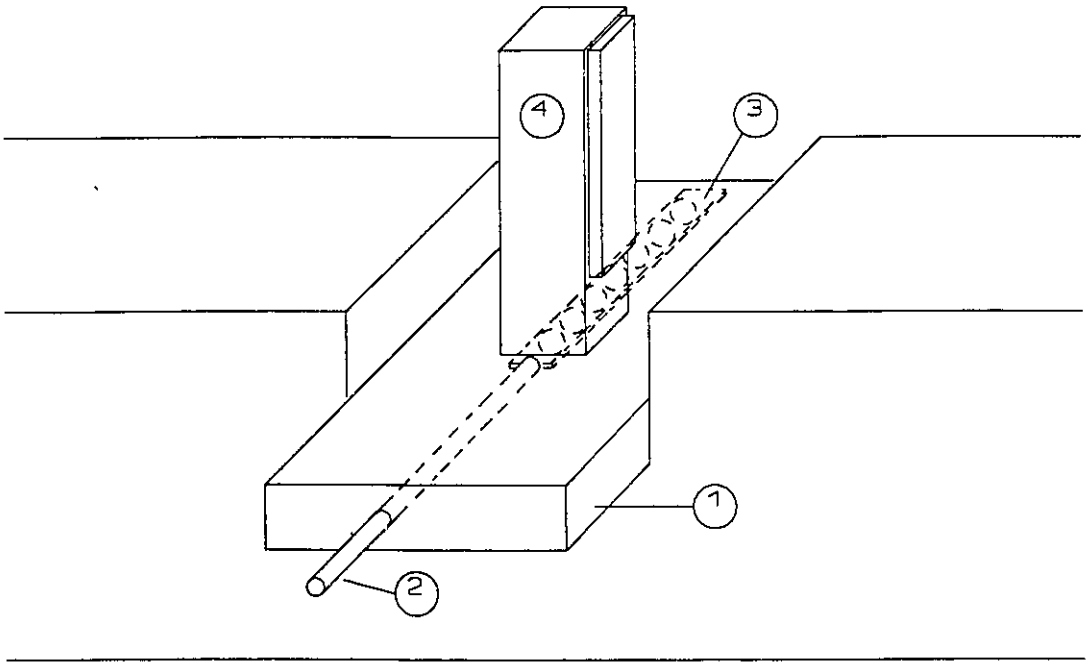

Fig. 2.2.10. Schematic diagram of filter box assembly in the 3FFR, 1. aluminum, light tight box, 2. push-pull rod, 3. filter bar, 4. cooled PMT housing.

2.3 Monoenergetic Electron Impact Appearance Energy Apparatus

For the past 25 years, Dr. Fred P. Lossing has been measuring electron impact appearance energies (AEs) using a custom designed and manufactured electron energy selector which produces electron beams of precisely known energy (±0.02 eV). A detailed description of the components of the apparatus and its characteristics has been published [3]. It is the only such instrument in the world and after 25 years is still responsible for most of the new organic cation and free radical heats of formation reported in the literature. It is only through the determination, skill and good humour of Fred Lossing that this apparatus has remained functional and relevant. It has been an honour to work so closely with him on the instrument.

2.3.1 The electron energy selector

A schematic diagram of the double hemispherical electron energy selector and ion source is shown in Fig. 2.3.1. Electrons are ejected from a tungsten filament (1) and accelerated through the electron gun (2) toward the base plate (3) which supports the assorted components. The electrons pass through a 0.36 mm diameter hole at the end of the gun and enter the first stage hemispherical analyzer (4). The analyzer consists of two concentric hemispheres supported on the base plate by electrical insulators. A variable potential difference can be applied between the two hemispheres to guide the electrons through the selector. The energy spread of the beam causes the image of the entrance aperture to be spread out into a ribbon which falls on the exit aperture of this first selector. Only electrons which fall onto a 5 mm diameter hole in the base plate will then pass through to the second hemispherical analyzer (5). The trajectory of the electrons

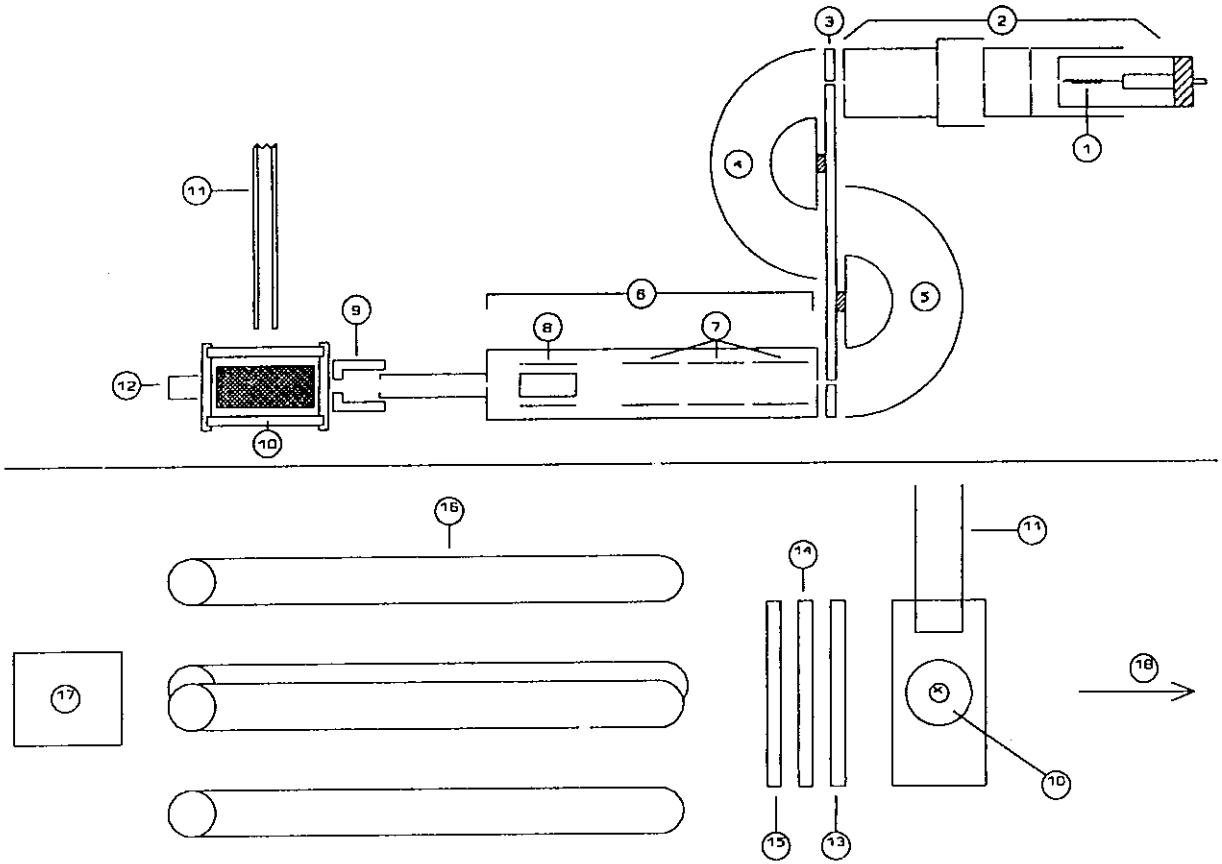

Fig. 2.3.1. Appearance energy apparatus, 1. filament, 2. electron gun, 3. base plate, 4. first double-hemispherical analyzer, 5. second double-hemispherical analyzer, 6. beam collimator, 7. cylindrical deflectors, 8. quadruplate deflector, 9. energy contoller electrode, 10. ion source, 11. sample inlet, 12. electron trap, 13. ion extractor electrode, 14. field adjustor electrode, 15. focussing electrode, 16. Ultek Quad-250 mass analyzer, 17. electron multiplier, 18. to vacuum system.

through the second analyzer, geometrically identical to the first, is 90° with respect to the first analyzer. Electrons which fall on a 0.36 mm hole at the end of the second analyzer pass on to the collimator (6). The collimator is a set of cylindrical lenses (7) and quadruplate deflector (8) which focus the now spatially selected beam (which has a narrow energy spread) onto the energy controller (9) and the ion source (10). The energy controller electrode accelerates/decelerates the electrons to the desired energy (5.8-30 eV) without significantly altering the energy spread of the beam. Sample is introduced into the ion source (10) by a glass inlet system (11). The ion source consists of a cylindrically arranged, gold-plated platinum mesh with a gold plated trap on one end (12). Electrons entering the ion source bombard sample molecules and are collected at the trap. The voltages applied to each of the roughly 20 independently variable components must be adjusted so as to produce both good energy selection and sufficient electron flux to perform an experiment. This operation is largely an art form since changing a potential in one place requires readjustment and fine tuning of all the others.

2.3.2 Ion extraction and analysis

The lower portion of Fig. 2.3.1 shows the ion extraction and quadrupole analyser system. In this view, the electron beam from the collimator is traveling into the page at the "x". Ions formed in the source are extracted by a negative potential of 6-10 V on the ion extractor electrode (13). A field-adjustor electrode (14) and focus plate (15) serve to guide the ions into the quadrupole mass analyzer (16), an Ultek Quad-250. Mass-selected ions are detected by an electron multiplier (17) and the signal fed to a Victoreen "Femtometer" vibrating reed amplifier. The resulting amplified signal is fed to an IBM-

XT computer where it is digitised and stored. The computer also controls the energy controller electrode. The experimental procedure for measuring an appearance energy will be described in Chapter 3.

References - Chapter 2

1. R.P. Morgan, J.H. Beynon, R.H. Bateman and B.N. Green, Int. J. Mass Spectrom. Ion Phys., 28 (1978) 171.

2. J.L. Holmes, A.A. Mommers, J.K. Terlouw and C.E.C.A. Hop, Int. J. Mass Spectrom. Ion Proc., 68 (1986) 254.

3. K. Maeda, G.P. Semeluk and F.P. Lossing, Int. J. Mass Spectrom. Ion Phys., 1 (1968) 395.

Chapter 3

Experimental Description

3.1 Introduction

In this chapter the chemistry taking place in the mass spectrometer and appearance energy apparatus will be discussed. The types of ions and the processes generating them will be described. The experimental procedures employed in this thesis to study these species will follow.

3.2 Types of Ions in the Mass Spectrometer

3.2.1 Source generated ions

Sample molecules encountering the electron beam in the ion source are affected in several ways: a) ionization, b) excitation followed by radiative and non-radiative relaxation and dissociation and c) electron capture. Molecules which are electronically, vibrationally and rotationally excited by the impact of an electron may emit a photon(s), dissociate or non-radiatively decay back to their ground state. These events are not studied by mass spectrometry since no ions are created and the neutral molecules and radicals are simply pumped away. Electron capture to create radical anions is possible in the ionization chamber. However, the probability of capturing an electron from the electron beam is small relative to the other two processes. Furthermore, the primary dissociation process of a radical anion is electron loss, which is not usually interesting from a mass spectrometric point of view except as a means for generating neutral beams. The process

of primary importance to mass spectrometry is electron impact (EI) ionization. A sample molecule, M, may have an electron(s) removed from it by the electron beam. The resulting radical cation is called a molecular ion, $M^{+\bullet}$, and can undergo three different processes. The molecular ions may be generated in the lower vibrational levels of their ground electronic state and the ions will remain intact and be detected, provided the electronic state is non-dissociative. If vibrationally excited ground state $M^{+\bullet}$ ions are formed, some of the ions may unimolecularly dissociate into a neutral, R (a molecule or free radical) and a cation, Y^+ (odd or even electron respectively):

$$M^{+\bullet} \rightarrow R + Y^+$$

These fragments may dissociate further by themselves or be excited by the electron beam prompting their ionization and/or dissociation. These are the processes usually associated with the production of a mass spectrum. A third process involves the formation of electronically excited $M^{+\bullet}$ ions. These ions may dissociate and contribute to the mass spectrum or they may relax back to the ground state via radiative or non-radiative processes. The optical spectroscopy of electron impact excited molecules and ions has been widely studied and the reader is directed to the work of J.P. Maier [1] for examples of the type of information obtained. It is important to remember that for a given sample, the investigator presently has almost no way of knowing exactly what is occuring in the ionization chamber. This fact will become important when the possibility is explored of the participation of source generated electronically excited molecular ions in the collision induced emission experiments (Chapter 4).

3.2.2 Metastable ions

Ions (molecular or source generated fragment) which dissociate between the ion source and detector are called **metastable ions**. An excellent discussion of the characteristics of metastable ions was published by Cooks et. al. [2] and remains the authoritative source for describing their properties. Only a brief description will be given here. Whether an ion dissociates in the ion source, survives to the detector or dissociates along the way depends on the population of the excited vibrational and rotational modes upon electron impact. A simplified representation of this is shown in Fig. 3.2.1. Electron impact ionization may yield molecular or fragment ions with densely populated states near the dissociation threshold. These ions may survive to exit the ion source prior to dissociation. Since the lifetimes of these metastable ions is considerably longer than that of a vibration, they will be able to rearrange to lower energy structures. The last stable species residing in a potential well prior to dissociation is called the **reacting configuration**. Depending on the internal energy distribution of the metastable ion there may be different dissociation processes which are able to compete to different extents.

3.3 Conventional Experiments Performed on the VG ZAB-2F

3.3.1 Mass-analyzed ion kinetic energy spectrometry (MIKES) [2]

It is possible to obtain a mass spectrum of the product ions from the dissociation of a metastable mass selected ion. In the 2FFR or 3FFR of the ZAB (Fig. 2.2.1), the unimolecular fragments, Y^+ and R, of the mass selected metastable ion RY^+ will, by the

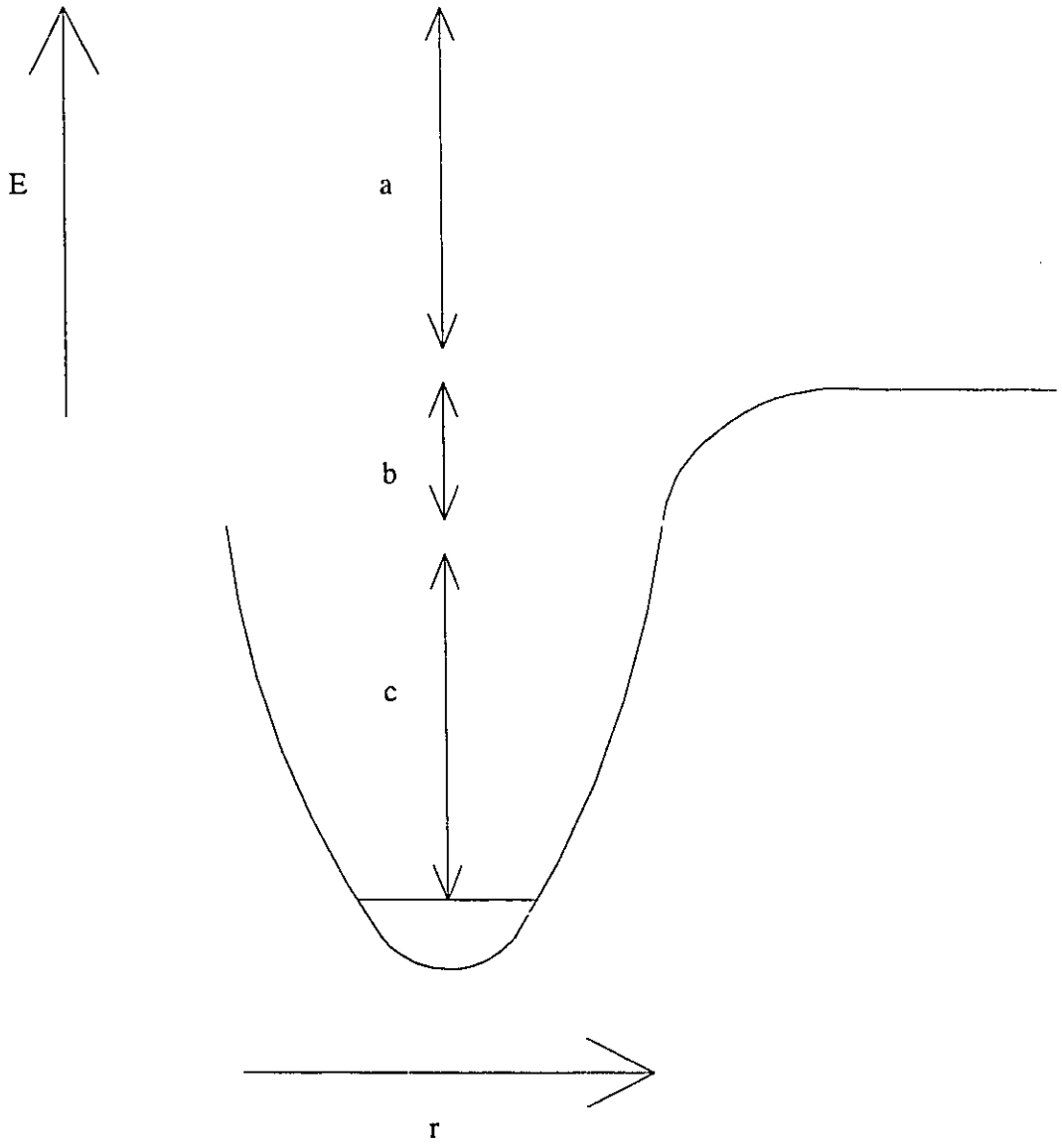

Figure 3.2.1. Simplified potential energy surface of a molecular ion showing energy characteristics of ions formed in the ion source, a) source fragmentation, b) metastable ions fragmenting to products outside the ion source and c) stable ions surviving to the detector. E is increasing energy and r increasing internuclear distance.

conservation of energy principle, have lower translational kinetic energy than their precursor:

$$zT_{Y+} = \tfrac{1}{2}m_{Y+}v \; ; \; zT_R = \tfrac{1}{2}m_R v \; ; \; zT_{RY+} = \tfrac{1}{2}m_{RY+}v$$

Thus we find

$$T_{Y+} = (m_{Y+} / m_{RY+})T_{RY+} \text{ and } T_R = (m_R / m_{RY+})T_{RY+}$$

By scanning the ESA (sec. 2.2.5) to pass ions of lower translational energy, the fragment ions will sequentially pass through to the detector. The final ion abundance vs kinetic energy spectrum is converted to an ion abundance vs fragment m/z spectrum by the above relationships.

3.3.2 Collision induced dissociation (CID) mass spectrometry [3,4]

A collision induced dissociation (CID) mass spectrum of a mass selected ion is obtained by introducing a target gas into a collision cell in one of the field-free regions of the ZAB (Figs 2.2.4, 2.2.6). The amount of target gas is controlled by monitoring the reduction in ion beam flux. The ionization gauges in the field-free regions of the mass spectrometer (sec. 2.2.4) will respond differently to gases of different ionization energy, IE. To obtain the same "pressure" reading on the gauge, considerably more of a gas such as helium, which has a high IE (24 eV), will have to be introduced into the mass spectrometer compared to a gas such as O_2 (IE = 12 eV). Thus, to perform collision experiments under the same real conditions, target gases are introduced to achieve the same percentage ion beam reduction (guaranteeing the same number and types of collisions) and not to give the same pressure reading. Experiments are typically performed under single collision conditions. If the ion beam is reduced to 90% of its pre-cell flux,

the probability of a projectile encountering more than one target gas atom or molecule on its way through the collision cell is extremely small. As the pressure in the collision cell is increased, this probability increases, until multiple collision conditions are achieved. The resulting CID mass spectrum, obtained and analyzed in the same way as a MIKE spectrum, contains peaks due to ions formed in all possible unimolecular dissociation processes for that ion. A more detailed discussion of the fundamental principles behind a CID is presented in Chapter 4.

3.3.3 Kinetic energy release (KER) measurements [2]

In a unimolecular dissociation internal energy of the precursor ion (electronic, vibrational and rotational) may be converted isotropically into translational kinetic energy of the departing fragments. This phenomenon is called kinetic energy release (KER). The result of x-axial (i.e. along the beam path) KER is the observation of fragment ion peaks in the MIKE or CID spectra which are wider in kinetic energy spread than the precursor ion peak. In a CID, however, this spread is complicated by collisional scattering and so KER is most often discussed only for peaks in MIKE spectra. If the mass spectrometer is operated under conditions of high resolution, obtained by narrowing the y-axis beam collimating slits throughout the instrument, the width of the fragment ion peak is indicative of this kinetic energy release. Often this release is due to a reverse activation barrier, ε_r, for the dissociation. The guiding rule-of-thumb for the correlation between the measured KER and ε_r is a) a large barrier (i.e. a large ε_r) results in a large measured KER and b) a small measured KER means that the barrier is likely small. Note that the inverse of each statement is not necessarily true. There is no well established, quantitative

correlation between the two either. The measured value for the KER is typically expressed as the value at half-height of the fragment ion peak, $T_{0.5}$, and is calculated by the following equation:

$$T_{0.5,Y+}\ (\text{meV}) = \frac{m_{RY+}^2(\Delta V_{0.5,Y+}^2 - \Delta V_{0.5,RY+}^2)}{16\times(8)m_{Y+}m_R}$$

where m stands for the mass of the respective species, $\Delta V_{0.5}$ is the full width energy spread of the fragment and precursor ion peaks at half height and (8) represents the typically 8 keV translational kinetic energy of the precursor. The resulting $T_{0.5}$ is in meV.

There are several characteristic peak shapes expected in a MIKE or CID spectrum (Fig. 3.3.1). The simplest is one with a near Gaussian profile (a Maxwell-Boltzmann distribution of released kinetic energy) which is similar to the main beam profile, Fig. 3.3.1a. It results when a single dissociation process produces the fragment ion. As the average KER increases and the distribution changes to one exhibiting a low probability for small KER, the peak will change from a Gaussian to a flat-topped profile and eventually to a dished-top profile, Fig. 3.3.1b. There is no physico-chemical significance to the dished-top profile, rather it results from z-axial discrimination in the instrument. The entrance ports to the magnetic and ESA sectors have a limited z-axis (vertical axis of the ion beam) height. As the isotropically distributed KER increases, some of the ions receiving it in the z-axis direction will be lost. This results in relatively fewer ions being detected near the peak centroid (since their x-axis kinetic energy is equal to the original precursor x-axis kinetic energy).

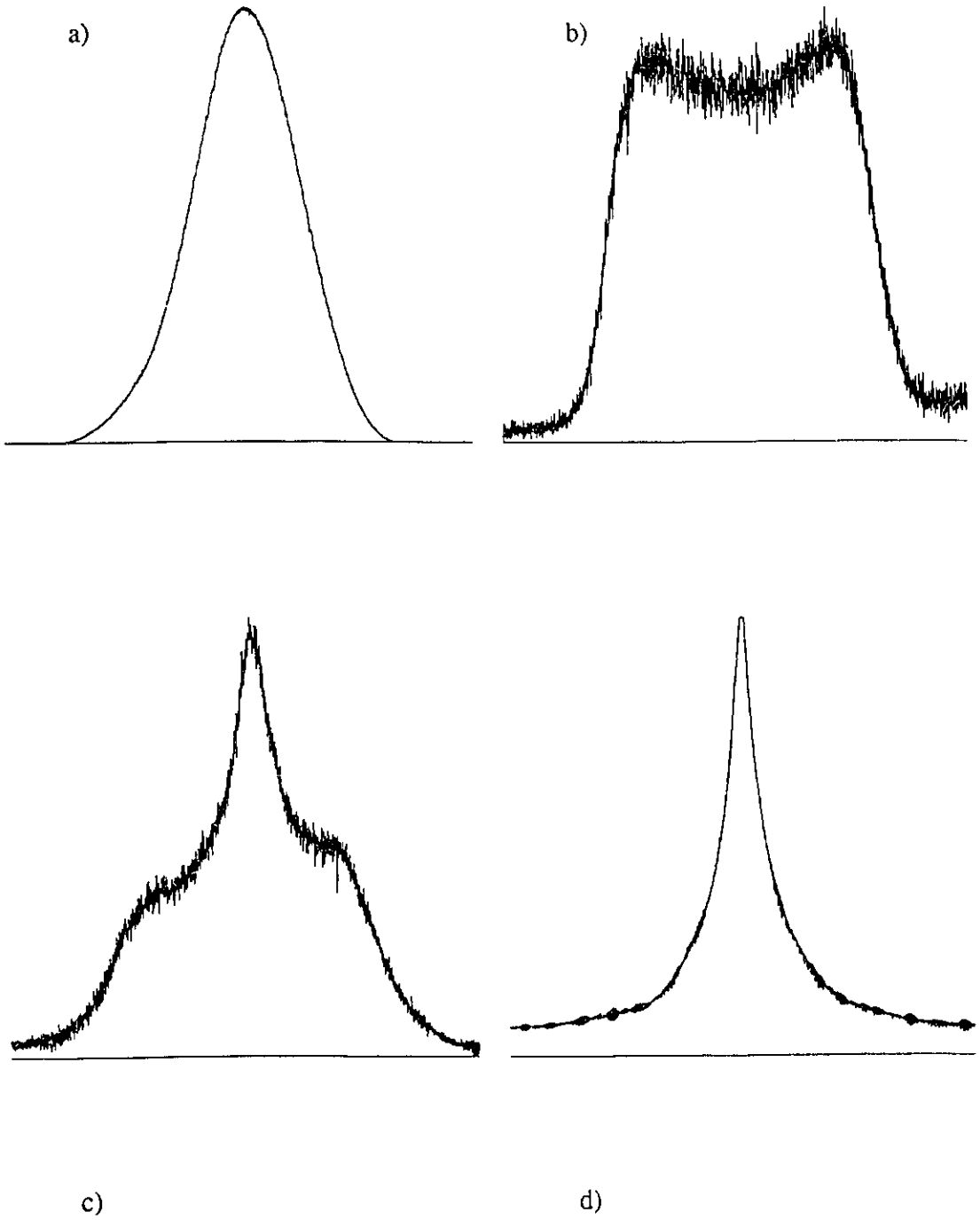

Figure 3.3.1. Examples of typical peak shapes in MIKE and CID mass spectra, a) Gaussian, b) dished-top, c) composite, d) due to dissociation from a continuum of internal states.

If there is more than one dissociation process producing a fragment ion (either from structurally different precursor ions or from multiple pathways from the same precursor), each with a different KER, a composite peak results, Fig. 3.3.1c. The two peaks are superimposed giving the net peak a non-Gaussian appearance. If the fragment ion is formed in a dissociation from a continuum of states of the precursor (such as one which is excited into the vibrational continuum above its dissociation threshold), a non-Gaussian peak with a gently sloping profile may be obtained, Fig. 3.3.1d. These peak shapes will become significant in Chapter 4 when a CID is examined more closely.

3.3.4 Charge stripping (CS) mass spectrometry [5]

In the collision process an electron can be stripped off the projectile ion, RY^+, to form a dication, RY^{2+}. Charge stripping can also occur from fragment ions. The resulting doubly charged ions will have roughly the same translational kinetic energy as the singly charged precursor and hence traverse the ESA with an apparent translational energy one-half that of the true value (see sec. 2.2.5, eq. VI). The peaks are characteristically of low abundance and narrow. Their measured energy width is half of the main beam width for the same reason that they are observed at half their kinetic energy, and since there is no KER in their formation.

3.3.5 Neutralization - reionization (NR) mass spectrometry [6]

Examination of the 2FFR and 3FFR of the ZAB-2F reveals a set of two collision cells separated by a deflector electrode in each, Fig. 2.2.4 (1-3) and Fig. 2.2.6 (5-7). To study neutrals in a mass spectrometer, a neutralization - reionization (NR) experiment can be performed. When a low IE target gas is introduced into the first cell, charge transfer

between the projectile ion and the target can occur. A potential is then applied across the deflector which deflects charged species out of the beam path. The neutrals formed in the first collision cell (from charge transfer and the neutral fragments from CID) can pass through the deflector into the second collision cell. A target gas in the second cell re-ionizes the neutrals and induces their CID. The final product ions are analyzed in the same way as the other experiments discussed above. The most common target gases are xenon (for neutralization) and oxygen (for re-ionization).

3.4 Analyzing Emissions from Projectile - Target Gas Collisions

3.4.1 2FFR experiments

The introduction of the 2FFR observation cell, OC, described in sec. 2.2.7(a) and Fig. 2.2.8 meant that collision gas could be introduced into any of the (then three) collision cells in the 2FFR (C1 and C2 were described in sec. 2.2.4) and emissions observed in the observation cell.

The emission signal was obtained primarily by photon counting but also by analogue monotoring of the current from the PMT (Thorn EMI 9635QB, 180-680 nm), Fig. 2.2.8(6). A photon counter (Princeton Applied Research Model 1121 Discriminator Control Unit and Model 1112 Photon Counter/Processor) was employed to measure the light flux for a 10 second interval when each filter was introduced between the quartz window and the PMT. The difference between measurements with successive filters corresponded to the total observed radiation in each spectral region. Eight regions could be selected using seven wavelength cutoff filters. Stray light and dark current for each filter were eliminated from the readings by taking the difference between the

measurements obtained with the ion beam on and off. The resulting spectra are histographs of the emission over the spectral range detected by the PMT (180-680 nm).

3.4.2 3FFR experiments

The 3FFR experiments were usually performed with sufficient target gas pressure in the OC or the PC (Fig. 2.2.9) to attenuate the ion beam to 60% of its pre-cell flux (unless otherwise stated). Monochromated emission spectra were obtained by analogue monitoring of the current from the PMT. In order to eliminate the contribution from noise spikes, which were a very common interference in these experiments, the current from the PMT was sampled as follows. The monochromator was instructed to step to the desired wavelength and the data aquisition program (Mommers Technology Inc., Ottawa, Ontario) sampled the PMT response current 100 times leaving 50 msecs between each reading. The probability of a noise spike of 1 msec duration overlapping a reading was approximately 1/50 and it would be averaged with 99 good readings. This allowed the spectra to be acquired, as the noise content was dramatically reduced. However, it resulted in long aquisition times, with approximately 5 seconds per point on a spectrum. Photon counting did not result in any improvement in either signal-to-noise or accumulation time in the present system. The low light levels and the characteristics of the PMT made counting unattractive. Counting was however used for the filter experiments described below. The resolution used for the monochromated spectra depended on the signal-to-noise of the features in each spectrum. The entrance and exit slits of the monochromator were set to 0.15, 0.5, 1, 2 or 3 mm depending on the sensitivity required. The full width at half maximum, FWHM, of an atomic line as a function of these slit widths was 0.5,

1.0, 2.0 nm, 5.5 nm and 10 nm respectively. Calibration of the monochromator was performed using the 404 nm, 435.6 nm and 545 nm mercury emission lines from the overhead fluorescent lamps in the laboratory (Fig. 3.4.1). The system was found to be -0.5 nm off of the spectroscopic values for these lines. However, this discrepancy was insubstantial for most of the emission spectra obtained since their resolution and step size resulted in uncertainties greater than ± 0.5 nm. Where this -0.5 nm error was significant it has been corrected for in the figures in Chapter 4. The emission spectra reported in Chapter 4 were not corrected for the varying response of the detection system with wavelength (due to the transmission charateristics of the quartz window and monochromator and the PMT quantum efficiency over the spectrum). The spectrum between 180-190 nm was omitted from the figures in secs. 4.3.2-8 because the transmission cutoff of the quartz window lies in this region.

For the filter experiments, collisions were performed the PC (Fig. 2.2.9) with sufficient target pressure to achieve 50% beam transmission, and light emitted in the OC was analyzed by the cutoff filters and the same cooled PMT (Fig. 2.2.10). A photon counter (Princeton Applied Research Model 1121 Discriminator Control Unit and Model 1112 Photon Counter/Processor) was employed to measure the light flux for a 60 second interval when each filter was introduced between the fused silica window and the PMT. The difference between measurements with successive filters corresponded to the total observed radiation in each spectral region. Eight regions could be selected using seven wavelength cutoff filters. Stray light and dark current for each filter were eliminated from the readings by taking the difference between the photon counts obtained with the ion

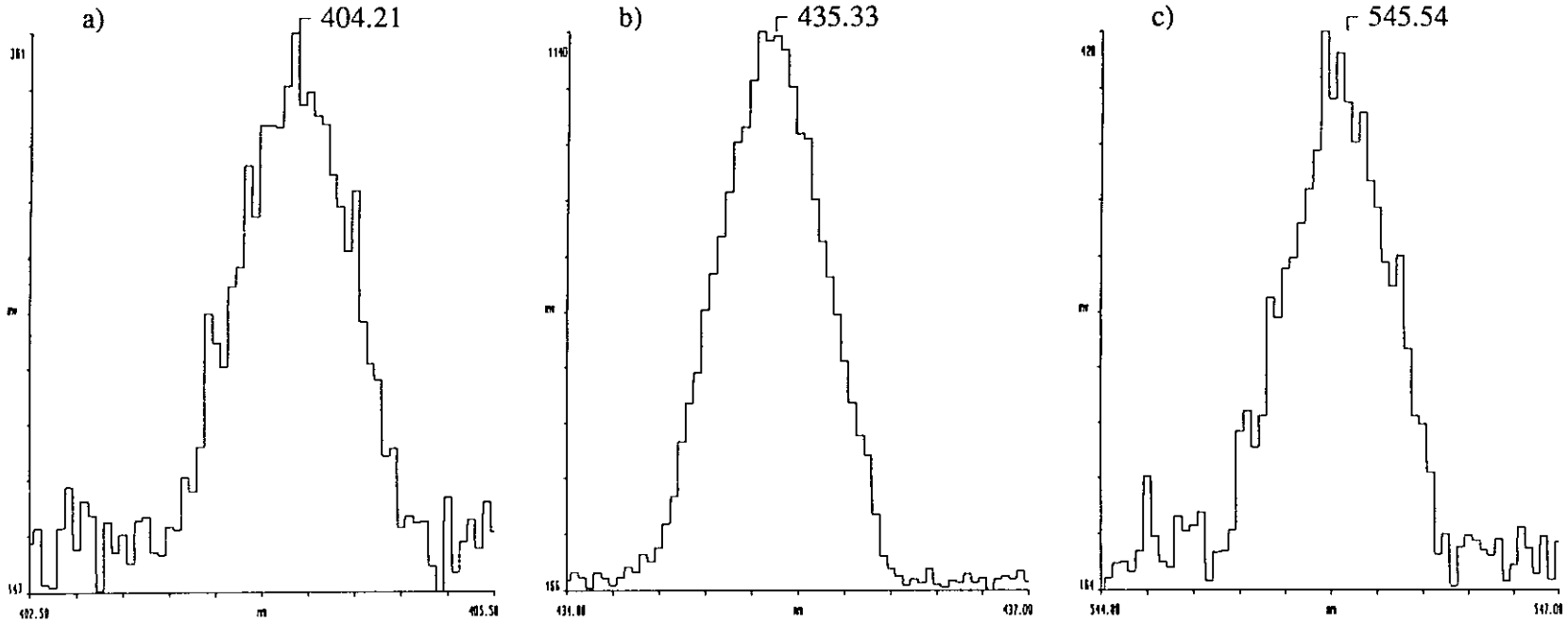

Fig. 3.4.1. Calibration of monochromator system a) mercury line at 404.65 nm, b) mercury line at 435.83 nm and c) mercury line at 546.07 nm. 0.25 mm slit widths, 0.05 nm step size, 4 scan average.

beam on and off. Eighteen different targets were used, covering a range of nine ionization energy (IE) values, Table 3.4.1.

Table 3.4.1

Target Gases Used in CIE Experiments

Target	IE[a] (eV)
He	24.59
Ar	15.76
N_2	15.58
Kr	14.00
CO	14.01
CO_2	13.77
Xe	12.13
O_2	12.07
CH_3CN	12.19
CF_2Br_2	11.07
C_2H_5Cl	10.97
CS_2	10.07
2-C_3H_7I	9.18
Tetrahydropyran	9.25
$(CH_3)_2NH$	8.23
3,4-Dihydro-2,H-pyran	8.34
CH_3SSCH_3	7.4
$(CH_3)_2NNH_2$	7.28

a. ref. 112.

All compounds used in this study were commercially obtained and of high purity (>99.9%). Helium, nitrogen, oxygen, carbon dioxide and argon were obtained from Air Products and were all +99.9999% pure.

3.5 Appearance Energy Determinations

3.5.1 The basic relationships

Two types of ionization energies are frequently discussed, vertical and adiabatic. A vertical ionization energy, IE_v, is obtained when the ionization process occurs with no geometry change, i.e., on a time scale much less than a vibration. This is the IE measured by photoionization since the absorption of a photon is a fast process. An adiabatic ionization energy, IE_a, is the energy difference between a molecule in its ground vibrational level and the molecular ion in its ground vibrational level. Electron impact ionization usually yields IE_a unless the geometries of the molecule and molecular ion are dramatically different [7]. The ionization energy of a molecule, IE(RY), can be measured by determining the appearance energy, AE, of the molecular ion, $AE(RY^{+\bullet})$, i.e., the threshold for the appearance of the molecular ion with increasing electron energy.

$$RY + e^- \rightarrow RY^{+\bullet} + 2e^-$$

$$AE(RY^{+\bullet}) = IE(RY) = \Delta_f H^\circ_{298}(RY^+) - \Delta_f H^\circ_{298}(RY)$$

The AE of an fragment ion is defined as the lowest energy of ionizing particle (electron or photon) required to detect the ion from a dissociative ionization process from a precursor molecule.

$$RY + e^-(h\nu) \rightarrow RY^{+\bullet} + 2e^-(1e^-) \rightarrow R^\bullet + Y^+ + 2e^-(1e^-)$$

The AE of Y^+ is taken as the enthalpy of the overall process:

$$AE(Y^+) = \Delta_f H^\circ_{298}(R^\bullet) + \Delta_f H^\circ_{298}(Y^+) - \Delta_f H^\circ_{298}(RY) \qquad (I)$$

with the departing electron assigned a heat of formation of 0 kcal mol^{-1}. From the above equation it is evident that knowing $AE(Y^+)$, $\Delta_f H^\circ_{298}(RY)$ and one of the other heats of

formation allows the fourth term to be evaluated. In the studies presented in Chapter 5, the value of primary interest is the free radical heat of formation:

$$\Delta_f H^\circ_{298}(R^\cdot) = \Delta_f H^\circ_{298}(RY) + AE(Y^+) - \Delta_f H^\circ_{298}(Y^+)$$

The appearance energy method for determining radical or ion heats of formation requires that the desired ion-radical pair be formed by a process that does not have a significant kinetic shift or reverse energy barrier (see secs 3.4.2 and 3.4.3). Otherwise, the simple relationship can only yield an upper limit for the radical heat of formation. A simple bond cleavage in a molecular ion is usually chosen to produce the ion-radical pair because such dissociations predominantly meet these criteria.

e.g.(Table 5.1.1, (1)) $CH_3C(O)CH_2CH_2OH^{+\cdot} \rightarrow CH_3CO^+ + {}^\cdot CH_2CH_2OH$

Each of the potential problems associated with the appearance energy technique will now be discussed in detail.

3.5.2 Reverse activation energy

As discussed in sec. 3.3.3 a unimolecular dissociation may have a significant reverse energy barrier, ε_r (Fig. 3.5.1). If this is the case, the measured threshold AE of an ion Y^+ will be the enthalpy of the dissociative ionization plus the reverse energy barrier:

$$AE(Y^+) = \Delta_f H^\circ_{298}(R^\cdot) + \Delta_f H^\circ_{298}(Y^+) + \varepsilon_r - \Delta_f H^\circ_{298}(RY)$$

Since there is no method of determining ε_r quantitatively, dissociations must be chosen which have low ε_r values. Measuring the KER of the dissociation on the ZAB (sec. 3.3.3) will give an indication of the importance of the reverse barrier. A narrow peak ($T_{0.5} < 20$ meV) should be associated with an ε_r which is within the experimental error inherent in

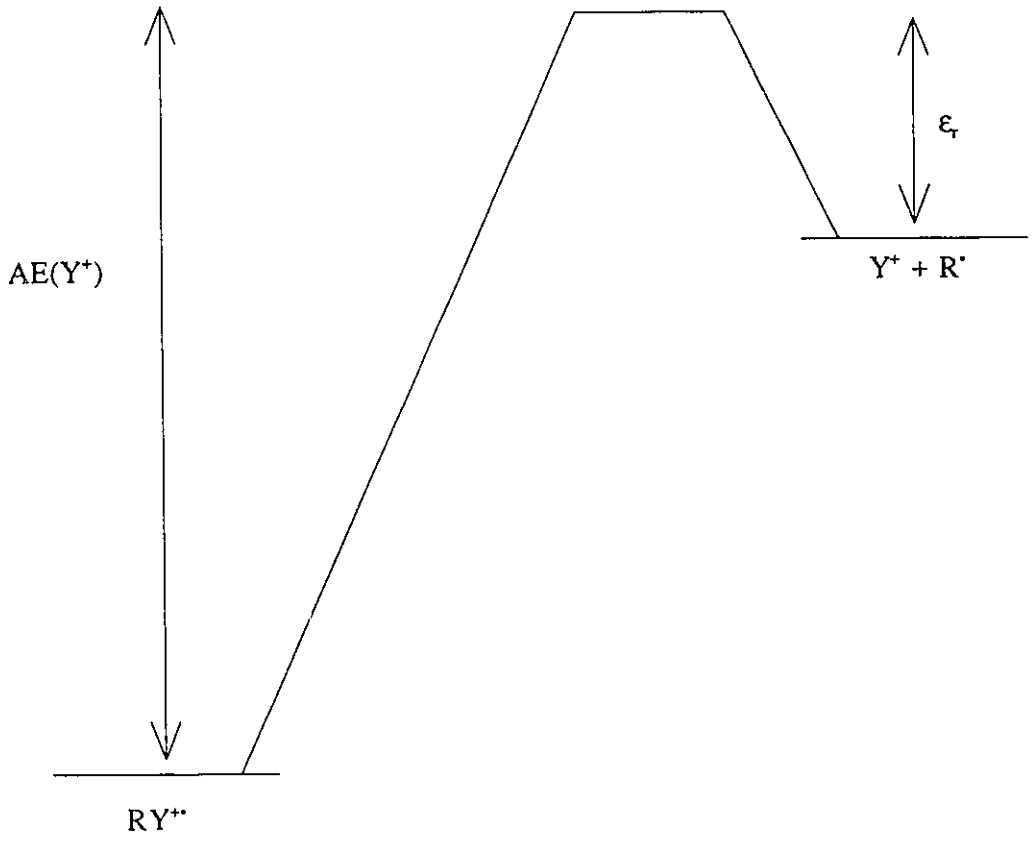

Figure 3.5.1. Dissociation of an ion $RY^{+\bullet}$ to $R^{\bullet} + Y^{+}$ involving a reverse energy barrier, ε_r and its relationship to $AE(Y^{+})$.

eq. (I).

3.5.3 Temperature and kinetic shift effects

Another more subtle problem concerns the temperature applicable to the product ion and radical. This has been considered in detail for photoionization thresholds by Traeger and McLoughlin [8], following earlier work by Chupka [9]. The basic difficulties are (a) how to identify the meaningful onset energy and (b) how to correct this energy for the contribution towards the activation process from the molecules' initial thermal internal energy. For photoionization experiments this is achieved (a) by the linear extrapolation to zero of a selected post-threshold portion of the ion yield vs photon energy curve, and equating this energy, $AE_{expmt}(Y^+)$, to $AE_0(Y^+)$ (the zero Kelvin enthalpy change for the reaction, ΔH°_0) minus that fraction of the internal (thermal) energy, E_i, which is effective in the dissociation. If the desired product enthalpies of formation are for 298 K, then $AE_{298\ expmt}(Y^+)$ can be derived from an experiment conducted at that temperature. It has been assumed [8,9] that all the rotational and vibrational energy of the precursor molecule, RY (at 298 K), is operative in the decomposition of the transition state and so E_i can be evaluated from the usual thermodynamic heat capacity terms. The final equation [8], in terms of the appearance energy $AE_{298\ expmt}(Y^+)$ is given by

$$AE_{298\ expmt}(Y^+) = \Delta_f H^\circ_{298}(Y^+) + \Delta_f H^\circ_{298}(R^\bullet) - \Delta_f H^\circ_{298}(RY)$$
$$-\{ \int_0^{298} Cp(Y^+) + \int_0^{298} Cp(R^\bullet) - 5/2\ RT\} \qquad (II)$$

or for example, if the heat of formation of the radical is desired,

$$\Delta_f H^\circ_{298}(R^\bullet) = AE_{298\ expmt}(Y^+) + \Delta_f H^\circ_{298}(RY) - \Delta_f H^\circ_{298}(Y^+) +$$
$$\{ \int_0^{298} Cp(Y^+) + \int_0^{298} Cp(R^\bullet) - 5/2\ RT\} \qquad (III)$$

where $Cp(Y^+)$ and $Cp(R^\cdot)$ are the molar heat capacities of the products and 5/2 RT is the term related to the translational energy deficit of the products [8].

This approach was clearly justified for a number of small molecules e.g. NH_3 and H_2O [8], where the full inclusion of internal energies was required to give a satisfactory standard $\Delta_f H^\circ_{298}$ for the fragment ions, using the selected extrapolated photoionization AE values. The choice of the linear portion of the latter often appears to be straightforward [8], but in some cases (e.g. the photoionization AE for $C_7H_7^+$ ions from toluene [10]), may appear somewhat arbitrary.

If the threshold energies chosen in the electron impact experiments have the same significance as those for photodissociation, they should be corrected by adding to them the terms in braces in eq. (II), before calculating a $\Delta_f H^\circ_{298}$ value for a product ion or neutral (eq. III). Linear extrapolation of our energy selected electron impact AE curves is not possible. A small part of their curvature at the foot arises from the electron energy distribution (typically ca 50 meV at half width) a feature much amplified in the calibrant curve. It should be noted that, unlike the calibrant ionization energy (IE) plot which is linear over a short range, the AE curves for the polyatomics contain a large number of unresolved discontinuities arising from a multitude of vibrational states. It is worth emphasising that, unlike thresholds measured with electrons having the wide energy spread typical of those from a normal ion source filament, the thresholds reported here do not depend significantly on the sensitivity at which the ions are detected, i.e. further data accumulation does not lead to ever lower values for the AE.

We are not convinced that the measured electron impact appearance energy

represents a threshold lower than the correct value by an energy equal to the sum of the heat capacity terms in eq. II. Indeed for polyatomic ions, we question that all or even a major fraction of the internal thermal energy participates in the activation process. If the fragmentation products are at 0K, the derived uncorrected $\Delta_f H^\circ_{298}$ values for many EI experiments reported elsewhere would all be too low by as much as 5 kcal mol^{-1} or more (in eq. III the 0K correction increases the $\Delta_f H^\circ_{298}$ of the radical (or ion)). See, for example, the recent values [11] for $\Delta_f H^\circ_{298}(C_2H_5^\cdot)$ which are independent of precursor molecule size and very close to the accepted value obtained by a variety of other methods. A further example is the observed threshold energy for the products, ionized but-2-ene and acetaldehyde, from the dissociative ionization of hexanal [12]. For this nineteen atom molecule the calculated AE using 298 K $\Delta_f H^\circ_{298}$ values, 9.87 eV, was very close to the observed value 9.89 eV.

In a recent study of ionization energies [13], particular attention was paid to the possible "tailing" of the energy selected electron impact IE threshold curves as a result of "hot bands" (i.e. the effect of thermally populated, low-lying excited states of the molecule), but none appeared in those experiments even at the highest sensitivity.

The question of kinetic shift for simple bond cleavages which involve metastable molecular ions, has also been considered [14]. For the loss of the halogen atom from ionized phenyl chloride, bromide and iodide the residual kinetic shift in the limiting rate constant range appropriate to the present AE measurements, ca 10^3 s^{-1}, was small indeed, less than 0.2 eV for the worst case, C_6H_5Cl, where the average kinetic energy released in the μs time scale ($k \approx 10^5 - 10^6$ s^{-1}) was also the largest, ca 0.09 eV. For phenyl iodide

the corresponding values were <0.1 eV and 0.048 eV. Thus the non inclusion of a kinetic shift term appears justifiable for simple bond cleavages having no reverse energy barrier and, if metastable, only small average kinetic energy releases (say ≤ 0.05 eV). Only three of the reactions in the present study were metastable processes, and for reactions 9, 12 and 16 the average kinetic energy releases were all less than 0.05 eV ($T_{0.5}$ < 20 meV).

The inclusion of the remaining correction in eq. II, for translational energy loss (1.5 kcal mol^{-1} at 298 K) should only be made if the other correction factors can be identified and quantified. Our experience to date indicates that for polyatomic systems the effects essentially cancel out. Without clear evidence for the degree of participation of internal (thermal) energies in polyatomic ion fragmentations and its relationship with the measured threshold, we argue that no correction is better than one incorrectly identified and applied. The effects of kinetic shift, internal energy and the 5/2 RT term operate in opposite directions; the first being added to the appearance energy and the latter two subtracted. Therefore, in this work no numerical value has been given to this unquantified source of possible error.

3.5.4 Competitive dissociations

For the larger precursor molecules used in this study, there is the possibility that there may be alternative reaction pathways which form the desired fragment ion, processes which may be thermochemically equivalent to, or even more favourable than, the simple bond cleavage. For this to be so, the desired neutral fragment formed by the simple bond cleavage must be capable of being subdivided into chemically reasonable radicals and molecules. For example, consider a molecular ion, $M^{+\bullet}$, which shows a

prominent $[M-C_3H_7O^{\bullet}]^+$ peak in its normal mass spectrum. Instead of the single loss of an intact $C_3H_7O^{\bullet}$ radical, the sequential losses of $C_3H_5^{\bullet}$ and H_2O (or vice versa), CH_4 and $C_2H_3O^{\bullet}$, $CH_3^{\bullet}$ and C_2H_4O, etc. could in principle be involved. The normal mass spectrum must therefore be inspected for the necessary intermediate m/z values corresponding to any of the above alternative fragmentation routes. The examination of metastable ion mass spectra provides useful additional information, in that they can confirm the precursor ion - fragment ion relationships. In order to determine if an alternative pathway is thermochemically competitive, there are two energy terms which must be taken into account. These are (a) the sum of the heats of formation of all neutral intermediates and (b) whether the energy barrier for any reaction in an alternative pathway exceeds the observed threshold for the desired reaction. It is convenient at this point to define a value, δ, which is the difference, $\Sigma[\Delta_fH^\circ_{298}(\text{neutral intermediates})] - \Delta_fH^\circ_{298}(\text{radical fragment})$. If the sum of the enthalpies of the proposed neutral intermediates exceeds the $\Delta_fH^\circ_{298}$(radical fragment) obtained from the measured AE, then δ is positive and the alternative channel cannot compete. If δ is zero or negative, then the alternative pathway could in principle compete with the simple bond cleavage. It is then necessary to determine if the energy barrier for the alternative pathway exceeds the observed threshold (case (b) above). An example is the production of the 3-hydroxypropyl radical, $^{\bullet}CH_2CH_2CH_2OH$, from ionized 5-hydroxypentan-2-one ((6), Table 5.1.1). Loss of H_2O and $C_3H_5^{\bullet}$ yield a δ value of -2.9 kcal mol^{-1}. It was necessary, therefore, to measure the appearance energy of the intermediate ion, $[C_5H_{10}O_2 - H_2O]^{+\bullet}$, m/z 84. The result showed that the minimum energy barrier for the alternative pathway was greater than that for the desired reaction by at least

0.4 eV.

3.5.5 Experimental procedure

The AE of an ion is measured by plotting the yield of the ion vs impacting electron energy over a range of 0.80 eV which includes the threshold. Signal averaging is employed to identify the very small ion fluxes near the threshold. The AE is identified as the onset of the ion yield. This AE is calibrated by measuring the IE of water, which is present in the ion source together with the sample, immediately before and after the AE measurement. This process is repeated until consistent results are obtained, usually two or three times. An example of the thresholds observed is given in Fig. 3.5.2. The sample, 4-hydroxybutan-2-one, upon ionization dissociates into the acetyl cation, CH_3CO^+ (m/z 43) and the 2-hydroxyethyl radical, $HOCH_2CH_2^{\bullet}$. The measured AE (m/z 43), 10.08 eV was corrected against the water standard by adding 0.12 eV (Table 5.2.1, 1). Typically, the measured IE (H_2O) is found to be lower than the true value, 12.60 eV [14], by 0-2 eV. This is due to contact potentials in the monochromator shifting the real potential experienced by the electrodes from that which is applied to them. For cases where an ion with m/z 18 is formed from the sample itself, with an AE lower than the measured IE of the water calibrant, the IE of Krypton is used as the calibrant. It was not necessary to use Kr in the work presented here.

All but one of the precursor molecules used in the AE experiments discussed in this thesis were of the highest purity obtainable from commercial sources. Isocyanomethane (see Appendix for 5.4) was synthesised by a published route [16].

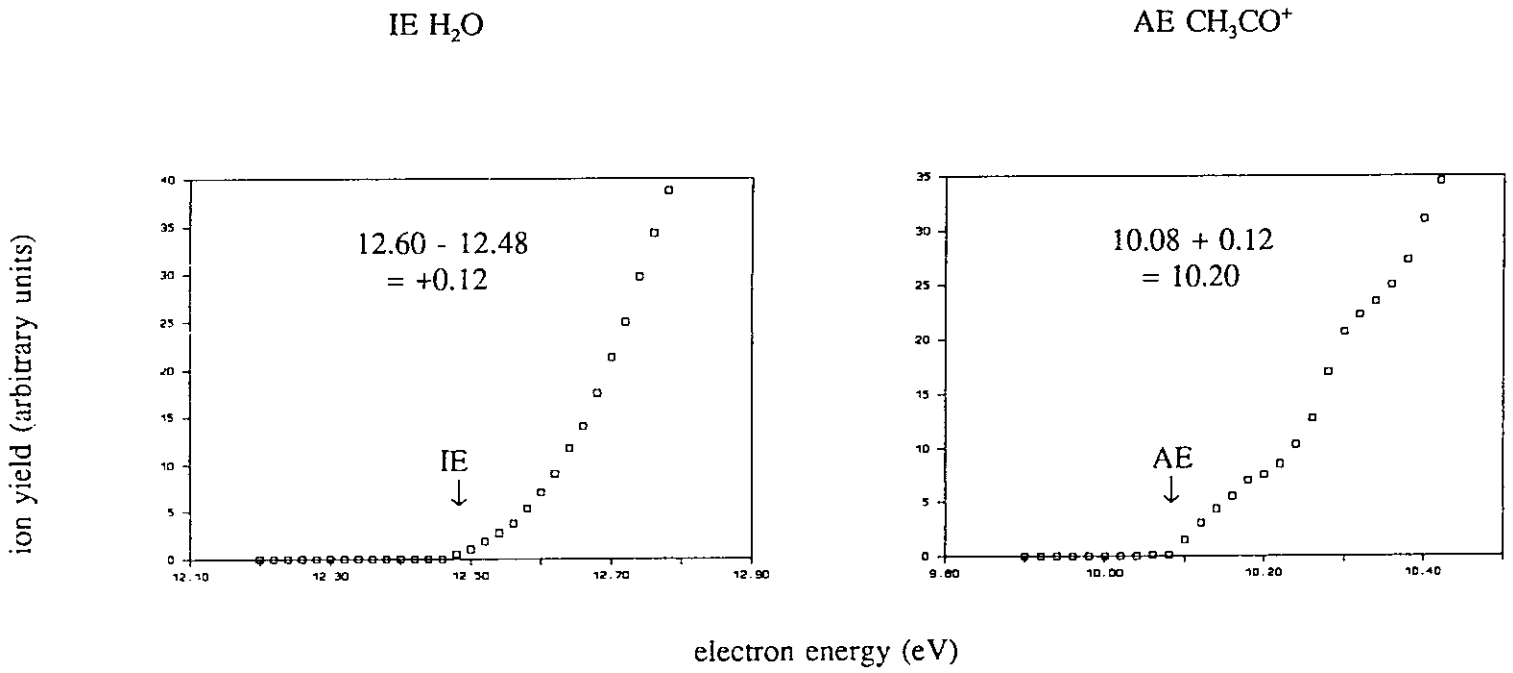

Figure 3.5.2. Appearance energy curves for the IE of water (12.60 eV [14]) and the AE of m/z 43 from $CH_3C(O)CH_2CH_2OH$ (Table 5.2.1, 1)

References - Chapter 3

1. J.P. Maier, Chem. Soc. Rev., 17 (1988) 45.

2. R.G. Cooks, J.H. Beynon, R.M. Caprioli and G.R. Lester, Metastable Ions, Elsevier Sci. Pub. Co., 1973.

3. F.W. McLafferty, R. Kornfeld, W.F. Haddon, K. Levsen, I. Sakai, P.F. Bente III, S.-C. Tsai and H.D.R. Schuddemage, J. Am. Chem. Soc., 95 (1973) 3886.

4. R.G. Cooks in Collision Spectroscopy, ed. R.G. Cooks, Plenum Press, N.Y., 1978, Ch.7.

5. R.G. Cooks, J.H. Beynon and T. Ast, J. Am. Chem. Soc., 94 (1972) 1004.

6. D.O. Danis, C. Wesdemiotis and F.W. McLafferty, J. Am. Chem. Soc., 105 (1983) 7454.

7. J.D. Morrison in MTP International Review of Science - Mass Spectrometry, ed. A. Maccoll, University Park Press, Baltimore, 1972, Ch. 2.

8. J.C. Traeger and R.G. McLoughlin, J. Am. Chem. Soc., 103 (1981) 3647.

9. W.A. Chupka, J. Chem. Phys., 54 (1971) 1936.

10. J.C. Traeger and R.G. McLoughlin, Int. J. Mass Spectrom. Ion Phys., 27 (1978) 319; see also, J.M. Buschek, J.J. Ridal and J.L. Holmes, Org. Mass Spectrom., 23 (1988) 543.

11. J.L. Holmes, F.P. Lossing and A. Maccoll, J. Am Chem. Soc., 110 (1988) 7339.

12. J.L. Holmes, J.K. Terlouw and F.P. Lossing, J. Phys. Chem., 80 (1976) 2860.

13. J.L. Holmes and F.P. Lossing, Org. Mass Spectrom., 26 (1991) 537.

14. P.C. Burgers and J.L. Holmes, Int. J. Mass Spectrom. Ion Proc., 58 (1984) 15.

15. S.G. Lias, J.E. Bartmess, J.F. Liebman, J.L. Holmes, R.D. Levin and W.G. Mallard, J. Phys. Chem. Ref. Data, 17 Suppl. 1 (1988).

16. J. Casanova Jr., R.E. Schuster and N.D. Werner, J. Chem. Soc. (1963) 4280.

CHAPTER 4

Photon Emissions From keV Projectile Ion - Target Gas Collisions

4.1 Introduction

Over the past 30 years, the nature of the excitation and dissociation processes occuring in projectile - target gas collisions has been studied by fundamental collision spectroscopists. The techniques used include i) investigations of the relationship between internal energy deposition in a collision and the angle at which the projectile is scattered from its original trajectory, ii) studying the loss of translational kinetic energy of the projectile when a portion of it is converted into internal energy and iii) analyzing photon emissions from vibronically excited projectile and target species formed in the collision. These studies have been performed over a wide range of collision energies (thermal - MeV). The incentive for much of this work was the understanding of interstellar phenomena, the development of new lasers and the understanding of the fundamentals of the fusion process. Thus, the species which have been studied have been predominantly atomic, diatomic and triatomic projectiles and target gases.

Gas phase ion chemistry in general and mass spectrometry in particular are primarily concerned with the behaviour of polyatomic projectile ions. One of the most important sources of information about these polyatomic ions is a collision induced dissociation (see 3.3.2 for experimental procedure). Collision induced dissociation (CID) as a technique in mass spectrometry has developed significantly over the past 20 years. It has been used to probe ion and neutral fragmentation pathways and to identify

structurally isomeric ions [1,2]. Essentially, a small fraction of the projectile ion's translational kinetic energy is converted into internal energy (rotational, vibrational and electronic) of the projectile and target gas prompting the projectile to dissociate. Many ingenious collision based methods have been described, e.g. charge stripping [3], charge reversal [4], neutralization-reionization [5] and surface induced dissociation [6]. However, the understanding of the fundamental processes occuring during the collision between a polyatomic projectile and a target gas has not progressed rapidly, i.e. how much energy is converted from translational kinetic energy to internal energy and how is it distributed between rotational, vibrational and electronic energy? This lack of undertanding often hinders the interpretation of the CID mass spectrum, so efforts have been made to understand these collision events.

Examining mass spectral changes with various parameters such as target ionization energy, target gas pressure and projectile translational energy has provided some qualitative information on the internal energy deposition in the projectile and target in keV collisions [7-9]. Attempts have been made to quantify the energy deposited into the polyatomic projectile. The mass spectrometric techniques employed have mirrored the techniques mentioned above employed by collision spectroscopists. Angle-Resolved Mass Spectrometry (ARMS) [10-14] attempts to relate the angles at which polyatomic ions are scattered by a collision to the internal energy deposited in the ion and target by observing the change in relative peak intensities in the CID mass spectrum as a function of scattering angle. However, at the small scattering angles studied, 0-3°, the experiment is complicated by the KER in the ion's fragmentation [15-20]. It was shown by the group

of J.H. Beynon [19,20] that while the contribution to the scattering angle due to KER can be numerically separated out, the ancilliary information required (including vibrational frequencies) is seldom available for polyatomic cations. It was concluded that ARMS would never yield quantitative information on the excitation in polyatomic ions in the collision event. A more precise technique is high resolution Translational Energy Spectroscopy (TES) [21-23]. In TES, the translational energy lost by the projectile in a non-momentum transfer collision is assumed to be equal to the internal energy deposited into the projectile and/or target. Minor peaks at energies slightly lower in translational energy than the main ion beam result from energy losses which can be correlated with electronic excitation in the projectile and/or target. The technique was always plagued by poor energy resolution [ex. 24,25] but Hamdan and Brenton's [23] double energy analyzing instrument is capable of excellent energy resolution for a mass spectrometer (±0.01 eV). TES can be used to study projectile ions of a multitude of origins. However, it is limited to the study of charged species since they must be focussed and analyzed by ESAs (see sec. 2.2.5). Also, although the resolution of Hamdan and Brenton's instrument is excellent for a mass spectrometer, it is rather poor from a spectroscopic point of view (as high as ± 3 nm, but more typically, their resolution corresponds to ± 10 - 15 nm). This lack of resolution means that assigning peaks in the TES spectrum to excitations in the polyatomic projectile ion beams is difficult due to the variety of possible excitations. For this reason, TES studies have focussed on atomic and diatomic charged projectiles for which excellent spectroscopic data may already be available.

We have decided to approach the problem with the third technique from collision

spectroscopy. Analyzing the light emissions from polyatomic projectile - target gas collisions should yield information about the excitation and dissociation of the projectile. This approach has the advantage over TES of the ability of studying any projectile beam, charged or neutral, as well as having much better spectroscopic resolution, allowing vibronic transitions to be identified more easily. This chapter describes the development of this pursuit.

4.2 2FFR Experiments

4.2.1 Introduction

In order to test the feasibility of observing emissions from polyatomic projectile ions, histographic spectra were obtained for several isomeric ions of mass spectrometric interest using the apparatus described in sec. 2.2.7a. Spectra were analyzed for distinguishing features that may be useful in identifying mass spectrometrically similar ion structures. Three $C_2,H_4,O^{+\bullet}$ ions and two $C_2,H_5,Cl^{+\bullet}$ isomers were chosen.

4.2.2 Results and Discussion

The 8 keV collision induced emission (CIE) spectra for three $C_2,H_4,O^{+\bullet}$ isomers can be found in Fig. 4.2.1. Oxirane$^{+\bullet}$ and acetaldehyde$^{+\bullet}$ ions were generated by EI on the respective neutral molecules and vinyl alcohol$^{+\bullet}$ was formed from dissociative ionization of cyclobutanol [26]. The spectra were obtained for both C2 and OC collision events using sufficient target gas pressure to reduce transmission of the ion beam to 80% of its pre-cell flux. The problem with OC collision experiments was that target gas emissions

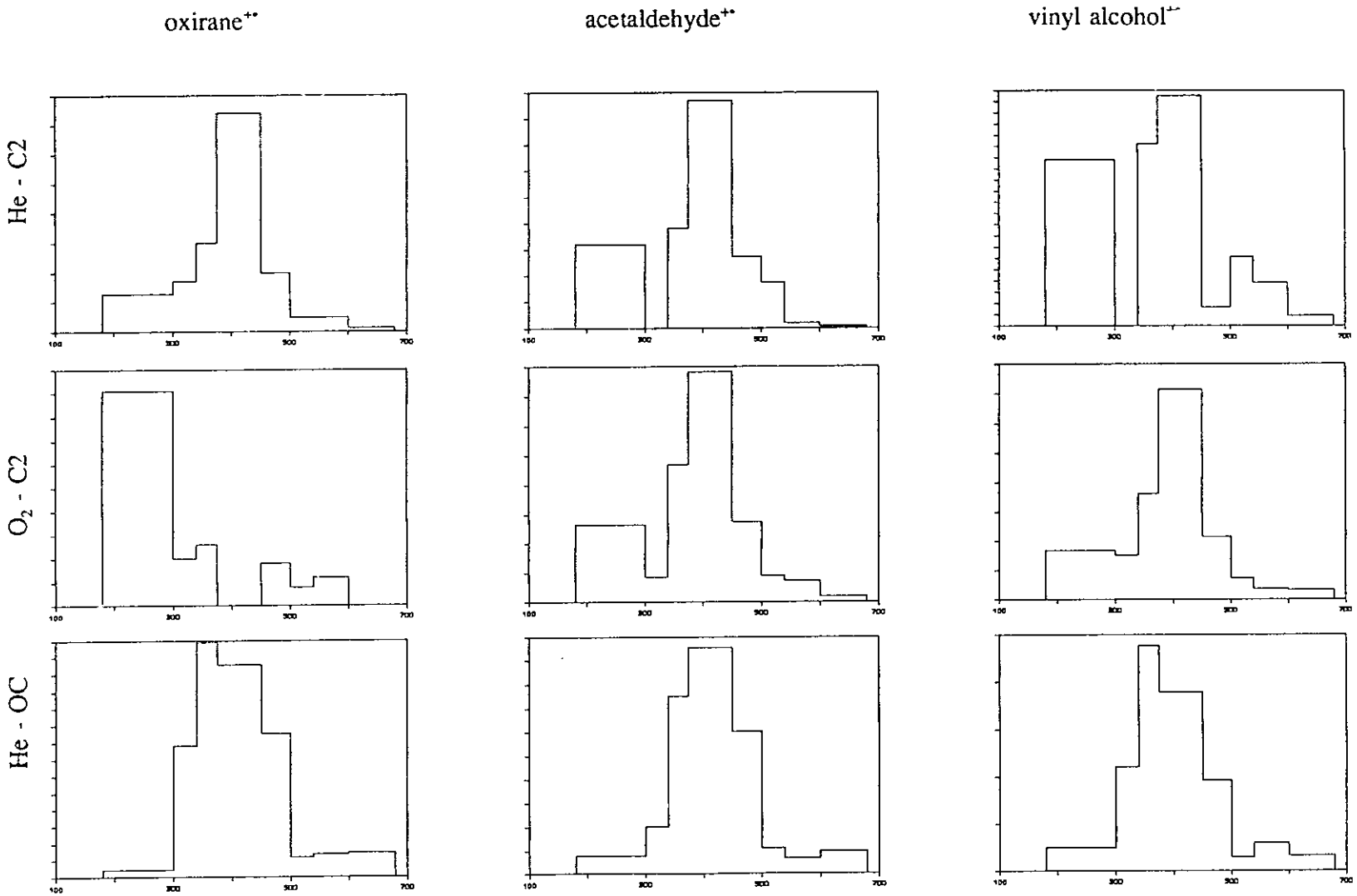

Fig. 4.2.1. CIE spectra obtained for three $C_2,H_4,O^{+\bullet}$ isomers using He and O_2 target gases in C2 and OC. Emission intensity in arbitrary units, wavelength range 180-680 nm.

overlap with ion beam emissions to an unknown extent. However, for comparison they are included in Fig. 4.2.1. There are two trends in the spectra which can be examined separately. Each of the three isomers exhibits pronounced differences between their C2 and OC spectra, indicating that the nature of the emitting species changes during the transit from C2 to the OC. Also, the spectra for the isomers are structure specific. This indicates that there may be different emitting species, both parent and products, for each isomer. The He CID mass spectra, while distinguishable, contain mainly the same ions in varying relative abundances (see Table 4.3.3 and [26]).

The CIE spectra of two $C_2,H_5,Cl^{+\bullet}$ ions were also obtained, Fig. 4.2.2. The bonding in the two structures is very different with $CH_3ClCH_2^{+\bullet}$ displaying a divalent halogen atom. However, their respective He CIE spectra are similar save for a stronger component for the $CH_3ClCH_2^{+\bullet}$ in the spectral region 180-300 nm. Their He and O_2 CID spectra (Table 4.3.4 and [27]) differ in a change in the relative intensities of peaks corresponding to the fragment ions $C_2H_4^{+\bullet}$ and $C_2H_5^{+}$, the latter being more intense for $CH_3ClCH_2^{+\bullet}$.

These results underline one potential use of this type of experiment, the unequivocal identification of ion structure. However, the lack of resolution means the exact nature of the emitting species remains unknown. These results have been published [28,29] in slighly different format. The success of these preliminary experiments led to the development of apparatus which would enable the aquisition of spectra with a scanning wavelength monochromator.

$CH_3CH_2Cl^{+\bullet}$ - He in C2

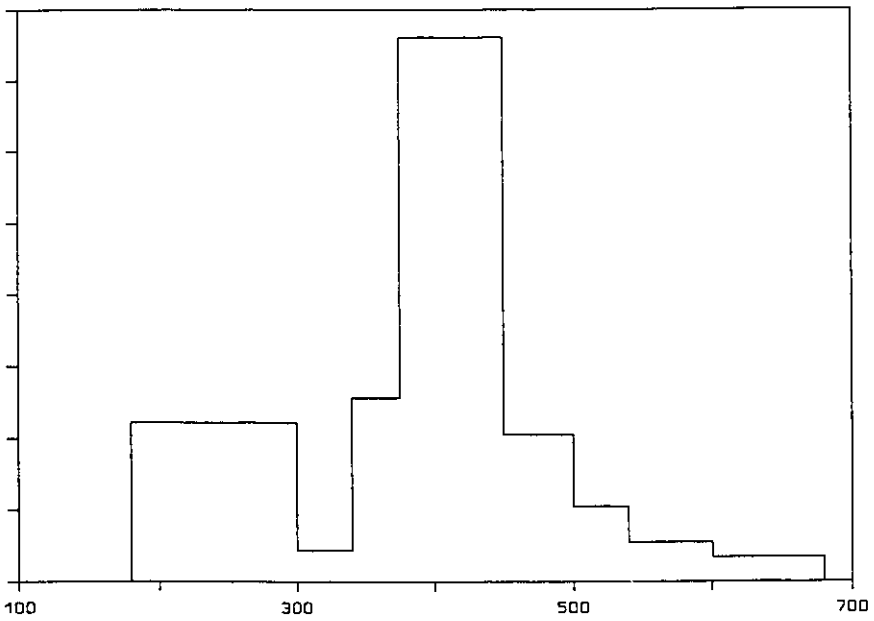

$CH_3ClCH_2^{+\bullet}$ - He in C2

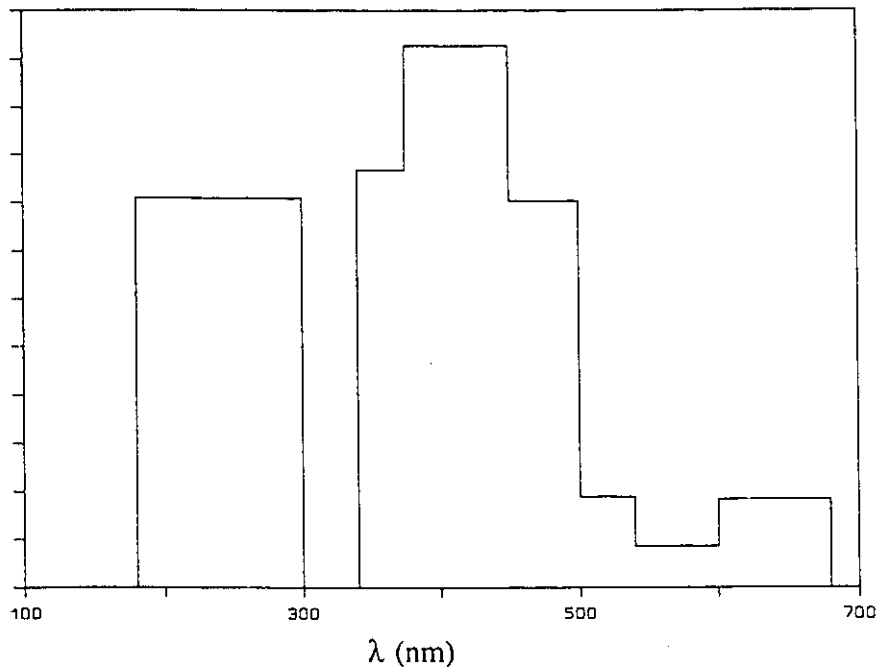

Fig. 4.2.2. He CIE spectra, C2, of two $C_2,H_5,Cl^{+\bullet}$ isomers. Emission intensity in arbitary units.

4.3 3FFR Experiments

4.3.1 Introduction

In this section are reported the analysis of the resolved emission spectra obtained upon collision of 8 keV $N_2^{+\bullet}$, $O_2^{+\bullet}$ and $CO_2^{+\bullet}$ ions with He, N_2, O_2 and CO_2 targets, as well as qualitative trends in emission obtained with 14 other targets. The apparatus and procedure used was described in secs 2.2.7b and 3.4.2. It is the first example of this type of optical experiment using a commercial, analytical mass spectrometer. The above three ions were chosen so that comparisons could be made with an extensive literature. Also, the electronic states of the ions and their corresponding neutrals and fragments are well known.

A series of polyatomic ions were also studied. The CIE spectra of three $C_2,H_4,O^{+\bullet}$ isomers and two $C_2,H_5,Cl^{+\bullet}$ isomers and their fragments were obtained with He and Ar target gases to determine the nature of the emitting species, something which was not possible with the histographic spectra discussed earlier. The results are discussed in relation to the CID characteristics of the ions studied.

4.3.2 Emissions from $N_2^{+\bullet}$ - target gas collisions

The $N_2^{+\bullet}$ ion beam

The $N_2^{+\bullet}$ ion beam was generated by electron impact (EI) on N_2 using 50-60 eV electrons and a typical ion flux of 0.5 - 1.0 nA was obtained. The possibility exists that excited $N_2^{+\bullet}$ ions are generated which have lifetimes sufficiently long for them to participate in the collision experiment. Maier [30] presented the relative abundance of $N_2^{+\bullet}$

$X\ ^2\Sigma_g^+$, $A\ ^2\Pi_u$ and $B\ ^2\Sigma_u^+$ states under various EI conditions. Under the conditions used in the present study, considerable $N_2^{+\bullet}$ $A\ ^2\Pi_u$ would be formed in the ion source, up to 60%, with ~ 13% being in the $B\ ^2\Sigma_u^+$ state. The $A\ ^2\Pi_u$ state has a long halflife (τ = 16 μs) whereas any $B\ ^2\Sigma_u^+$ state formed will decay rapidly (τ = 0.07 μs). The 8 keV $N_2^{+\bullet}$ ions studied here are 12.8 μs old by the time they enter the OC and hence only the most stable $X\ ^2\Sigma_g^+$ and $A\ ^2\Pi_u$ state species will participate in the CIE process. Unfortunately, although the electron energy could be reduced to 20 eV to help eliminate $N_2^{+\bullet}$ $A\ ^2\Pi_u$ in the ion beam [30], the ion flux obtained at that energy was too small to obtain a spectrum.

Moran et. al. [31] studied reactions between ≤ 3.5 keV $N_2^{+\bullet}$ ions with N_2 target molecules at various electron energies. Collisions took place at least 7.11 μs after excitation of $N_2^{+\bullet}$ in the ion source and evidence for $N_2^{+\bullet}$ $A\ ^2\Pi_u$ participation was found. However, if $N_2^{+\bullet}$ $A\ ^2\Pi_u$ was a significant fraction of the ion flux, $N_2^{+\bullet}$ ($A\ ^2\Pi_u \rightarrow X\ ^2\Sigma_g^+$) emissions might be expected in the absence of target gas. No photons could be detected without the presence of target gas, even with only the bare PMT. Hence, we conclude that $N_2^{+\bullet}$ $A\ ^2\Pi_u$ makes up a negligible fraction of the ion beam in these experiments.

Metastable $N_2^{+\bullet}$ ions dissociating to form N^+ and $N^\bullet$ in the 3FFR may also contribute to the spectrum. The MIKES spectrum of these $N_2^{+\bullet}$ ions showed that N^+ and $N^\bullet$ comprised only 0.0026% of the total ion flux and hence the contributions of these unimolecularly generated fragments can be ignored under the present conditions of sensitivity.

In-cell observations : ion beam emissions

The emission spectra over the wavelength range 190-680 nm obtained from $N_2^{+\bullet}$ - He, N_2, O_2 and CO_2 collisions are shown in Figs 4.3.1a-d. Spectral assignments were assisted by using data obtained over smaller wavelength ranges employing greater signal averaging than was used for the full spectra, to improve signal-to-noise. A common feature observed in Figs 4.3.1a-d was assigned to the $\Delta\upsilon$ = +2, +1, 0, -1, -2 vibrational transition sequences in the $N_2^{+\bullet}$ ($B\ ^2\Sigma_u^+ \rightarrow X\ ^2\Sigma_g^+$) electronic transition [32]. The $C\ ^3\Pi_u \rightarrow B\ ^3\Pi_g$ second positive system in N_2 [32] appeared when N_2 and O_2 were the targets (Figs 4.3.1b,c), however, strong target emissions masked this progression when CO_2 was used as the collision agent. The lower IE target O_2 produced the most abundant N_2 emissions as well as the $\Delta\upsilon$ = -3 vibrational sequence in the $N_2^{+\bullet}$ ($B \rightarrow X$) transition, Fig. 4.3.1c. Also present in the spectra are narrow bands attributable to the N^+ transitions 3d $^3F^0 \rightarrow$ 3p ^3D and/or 3d $^3P^0 \rightarrow$ 3p ^3S (500 nm, Figs 4.3.1a-c) and the 3p $^3D \rightarrow$ 3s $^3P^0$ transition (568.3 nm, Fig 4.3.1a) [33]. A potential energy diagram for N_2 and $N_2^{+\bullet}$ is shown in Fig. 4.3.2.

Nitrogen has proved to be a popular target to study collision induced excitation and charge exchange because the electronic excited states have been so well characterized. There have been several studies in which the emission spectrum resulting from keV projectile - N_2 target collisions were obtained [34-39], but only one in which $N_2^{+\bullet}$ was the projectile [40]. All of the studies measured the cross sections of the various emission bands detected. Common to all experiments was the observation of the $N_2^{+\bullet}$ ($B\ ^2\Sigma_u^+ \rightarrow X\ ^2\Sigma_g^+$) $\Delta\upsilon$ = +2, +1, 0, -1, -2 progression, a feature of the present results with all four targets. Doering [40] performed 1-10 keV $N_2^{+\bullet}$ projectile experiments with N_2 as the target

and observed primarily the $N_2^{+\bullet}$ ($B\ ^2\Sigma_u^+ \rightarrow X\ ^2\Sigma_g^+$) progression, as well as the first and second positive systems of N_2. In $N_2^{+\bullet}$ - N_2, we observed the second positive system of N_2. Doering also reported several N^+ emissions. We have identified one of these, N^+ ($3d\ ^3F^0 \rightarrow 3p\ ^3D$, 500 nm, Fig. 4.3.1b).

A common conclusion from all these studies was that the vibrational distribution in the $\Delta\upsilon$ = +2, +1, 0, -1, -2 bands of the $B\ ^2\Sigma_u^+ \rightarrow X\ ^2\Sigma_g^+$ transition can be described by a Franck-Condon excitation process. In other words, since the geometries of the ground and excited $N_2^{+\bullet}$ states are similar, Fig. 4.3.2, excitation and emission favor the observation of the low vibrational energy level transitions (0-0, 1-1, 1-0 etc). This is seen in the present spectra where the band maxima coincide with the low vibrational transitions (ex. Fig. 4.3.3). This is not observed from low eV collisions. There have been several CIE studies of $N_2^{+\bullet}$ over the translational energy range of 1-1000eV [38,41-48]. The emissions observed ranged from $N_2^{+\bullet}$ ($B\ ^2\Sigma_u^+ \rightarrow X\ ^2\Sigma_g^+$) for the higher energy, harder collisions, to N_2 ($C\ ^3\Pi_u \rightarrow B\ ^3\Pi_g$) in $N_2^{+\bullet}$ collisions with alkali atoms [46] and other species of low IE.

Much Translational Energy Spectroscopy, TES, work has been done on keV $N_2^{+\bullet}$ - target collisions [49-51 - $N_2^{+\bullet}$ projectile; 52-56 - N_2 target]. Peaks due to various energy losses have been assigned to N_2 and $N_2^{+\bullet}$ excitations depending on the particular system studied. Recent TES studies [50,51] identified the Meinel system of $N_2^{+\bullet}$, $A\ ^2\Pi_u \leftarrow X\ ^2\Sigma_g^+$, resulting from collisions between $N_2^{+\bullet}$ and Ar, N_2, O_2 and NO. Only minor peaks were attributed to the $N_2^{+\bullet}$ ($B\ ^2\Sigma_u^+ \leftarrow X\ ^2\Sigma_g^+$) system. We did not observe any peaks related to the Meinel system of $N_2^{+\bullet}$, but it does occupy a spectral region in which our detection system is relatively inefficient (550-1770nm [32]). Moreover, the TES energy loss peaks

are due to excitation of the $N_2^{+\bullet}$ projectile whereas we study emission. The A $^2\Pi_u$ state has a long lifetime, particularly the low vibrational energy levels, as was discussed above. This may preclude the observation of most of the emissions from this state in the present experiments.

In-cell observations : target gas emissions

In each of the OC experiments shown in Fig. 4.3.1, emissions from the target gas were observed. In the case of $N_2^{+\bullet}$ - He, Fig. 4.3.1a, only minor He(I) emissions at 317.4 nm, 388.8 nm and 447.8 nm, corresponding to the common triplet emission system, can be deduced; the $\Delta\upsilon = 0$ peak of the $N_2^{+\bullet}$ (B $\rightarrow$ X) transition would mask the He(I) $3^3P \rightarrow 2^3S$ transition at 388.8nm, if present. A reason for this low yield of He emissions may be the high energy of its first excited states (2s and 2p). Energy depositions of more than 22 eV are needed in the $N_2^{+\bullet}$ - He collision in order to excite the He atom to the n=3 and 4 states and emissions from transitions to the n=2 states observed in our experiment. In the three other experiments, emissions from ionized target species and even target fragments are observed, although in the case of $N_2^{+\bullet}$ - N_2, it is impossible to separate ion and target emissions. A summary of the observed target transitions can be found in Table 4.3.1.

Table 4.3.1

Observed Target Gas Emissions in Figs. 4.3.1a-d

System	Transition			λ(nm)	ref.
$N_2^{+\bullet}$ - He	-see text				
	He (I)	$4^3P \rightarrow 2^3S$		318.7	33
		$3^3P \rightarrow 2^3S$		388.8	
		$4^3D \rightarrow 2^3P$		447.1	
$N_2^{+\bullet}$ - N_2	-see text				
	N_2	$C\ ^3\Pi_u \rightarrow B\ ^3\Pi_g$	$\Delta\upsilon =$ +2	295-298	32
			+1	310-315	
			0	330-337	
	$N_2^{+\bullet}$	$B\ ^2\Sigma_u^+ \rightarrow X\ ^2\Sigma_g^+$	$\Delta\upsilon =$ +2	329-331	32
			+1	355-358	
			0	385-391	
			-1	417-429	
			-2	451-471	
			-3	508-523[a]	
$N_2^{+\bullet}$ - O_2					
	$O_2^{+\bullet}$	$A\ ^2\Pi_u \rightarrow X\ ^2\Pi_g$		190 →	70
	O^+	$3d\ ^4F \rightarrow 3p\ ^4D^0$		407	33,74
		$3p\ ^4P^0 \rightarrow 3s\ ^4P$		434.6	
		$3p\ ^2D^0 \rightarrow 3s\ ^2P$		440.7	
$N_2^{+\bullet}$ - CO_2					
	$CO_2^{+\bullet}$	$B\ ^2\Sigma_u^+ \rightarrow X\ ^2\Pi_g$		287-290	94
		$A\ ^2\Pi_u \rightarrow X\ ^2\Pi_g$	$\Delta\upsilon =$ +4	305	91-93
			+3	314	
			+2	324-330	
			+1	337-338	
			0	350-351	
			-1	367	
			-2	389	
			-3	412.5	
			-4	438	

a. only present when O_2 the target.

Post-collision observations

When the collision events take place in PC and emissions are observed in OC, the long lived emitting states derived only from the ion beam are studied. The post-collision emission experiments were performed with PC placed 1 cm from the observation cell. The excited states which will be observed must have total lifetimes of at least 0.05 μs. In addition to monochromated spectra of $N_2^{+\bullet}$ emissions after collisions with the above four target gases, histographic spectra involving 18 targets were obtained using the wavelength filters, Table 3.4.1, in order to get a better understanding of the general trends in emission.

The spectra obtained from post-collision observations are much weaker than those from in-OC collision observations. Hence, the resolution possible in these experiments was limited. However, the spectra were relatively straightforward to interpret. The $N_2^{+\bullet}$ ($B \rightarrow X$) transition was observed in each of the four spectra, Figs 4.3.4a-d. However, there was a noticable shift in the relative intensities of the vibrational transition bands, $\Delta\upsilon = +1$ being relatively more intense than was observed in the in-OC experiments, Figs 4.3.4a-d. Weak N_2 ($C \rightarrow B$) bands are also present, Figs 4.3.4b-d, providing insight into the origin of the peaks in Fig. 4.3.4b. The $N_2^{+\bullet}$ projectile contributes at least part of both the $N_2^{+\bullet}$ ($B \rightarrow X$) and N_2 ($C \rightarrow B$) emission peaks in that spectrum.

There are some weak CO_2^+ emissions evident in Fig. 4.3.4d indicating that some target leaks through from PC into OC. However, the spectrum is not simply a weak twin of Fig. 4.3.1d and hence most of the emissions must be from excited state species formed in $N_2^{+\bullet}$ - CO_2 collisions in the PC. Appearing in each of the four spectra is a peak at 249

nm which is absent in the previous experiments. It can be assigned to the N^+ ($4p\ ^1S \rightarrow 2s2p\ ^1P^0$) transition [33] or it may form part of a progression in N_2^{+*} or N_2 extending into the VUV [32], but since only one peak is present it is impossible unequivocally to identify its origin.

It has been demonstrated by mass spectrometry that the degree of charge exchange between ion and target increases as the ionization energy of the target decreases, provided that the target does not get too big [7,57]. This is especially important for exothermic charge exchange processes (IE(target) < IE(neutral projectile)). However, a plot of the total observed N_2^{+*} beam emission (180-680 nm) from the filter experiments with all 18 target gases versus target IE, Fig. 4.3.5, shows that emission increases with an increase in target IE. This result was independent of spectral region, except for the region from 180-300 nm, which, if anything, decreased with increasing target IE. The results are consistent with the dominant spectral feature observed being the N_2^{+*} ($B \rightarrow X$) transition. The peaks in the 180-300 nm region of the spectra were due mainly to neutral N_2 emissions which will increase as charge exchange with the target increases.

The fragmentation of an ion during a CID experiment has been shown to generally increase with increasing target IE [7,9]. This result supported the proposal that fragmentation was a result of electronic excited state dissociation. Electronic excitation is more prominent in collisions with small, high IE targets than for large, polarizable, low IE targets [9, see also 58-61]. When the observed emission is plotted as a function of CID fragment ion abundance, Fig. 4.3.6, emission is found to increase almost linearly with increasing fragmentation. A clear relationship is observed for the spectral regions from

300-500 nm, with a slighly less direct relationship for the regions from 500-680 nm. The UV region 180-300 nm shows no connection between emission and fragmentation. These results indicate that the excited states of N_2^{+*} responsible for the formation of fragment ions and neutrals are also responsible for the emission in the 300-500 nm spectral region, i.e., B $^2\Sigma_u^+$. Another possibilty is that the predominant emitting species are the excited state fragment ions and neutrals themselves. However, the flux of these products is small and only minor peaks due to N^+ emissions are evident in the spectra in Fig. 4.3.1 and no peaks were observed in Fig. 4.3.4.

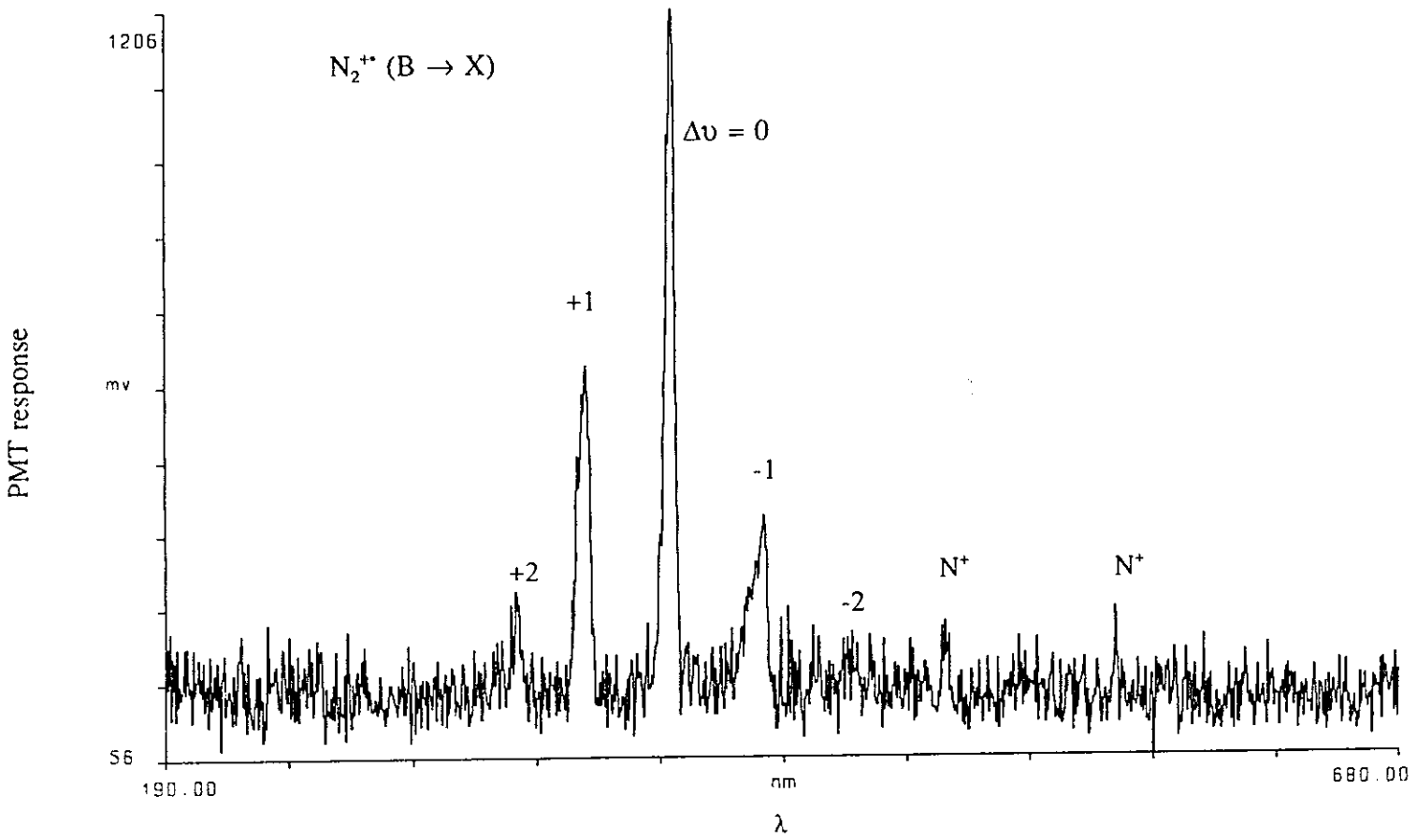

Fig. 4.3.1 a. N_2^{+*} - He (in-OC) collision induced emission spectrum. 1.0 mm slits, 0.5 nm step size, 6 scan average.

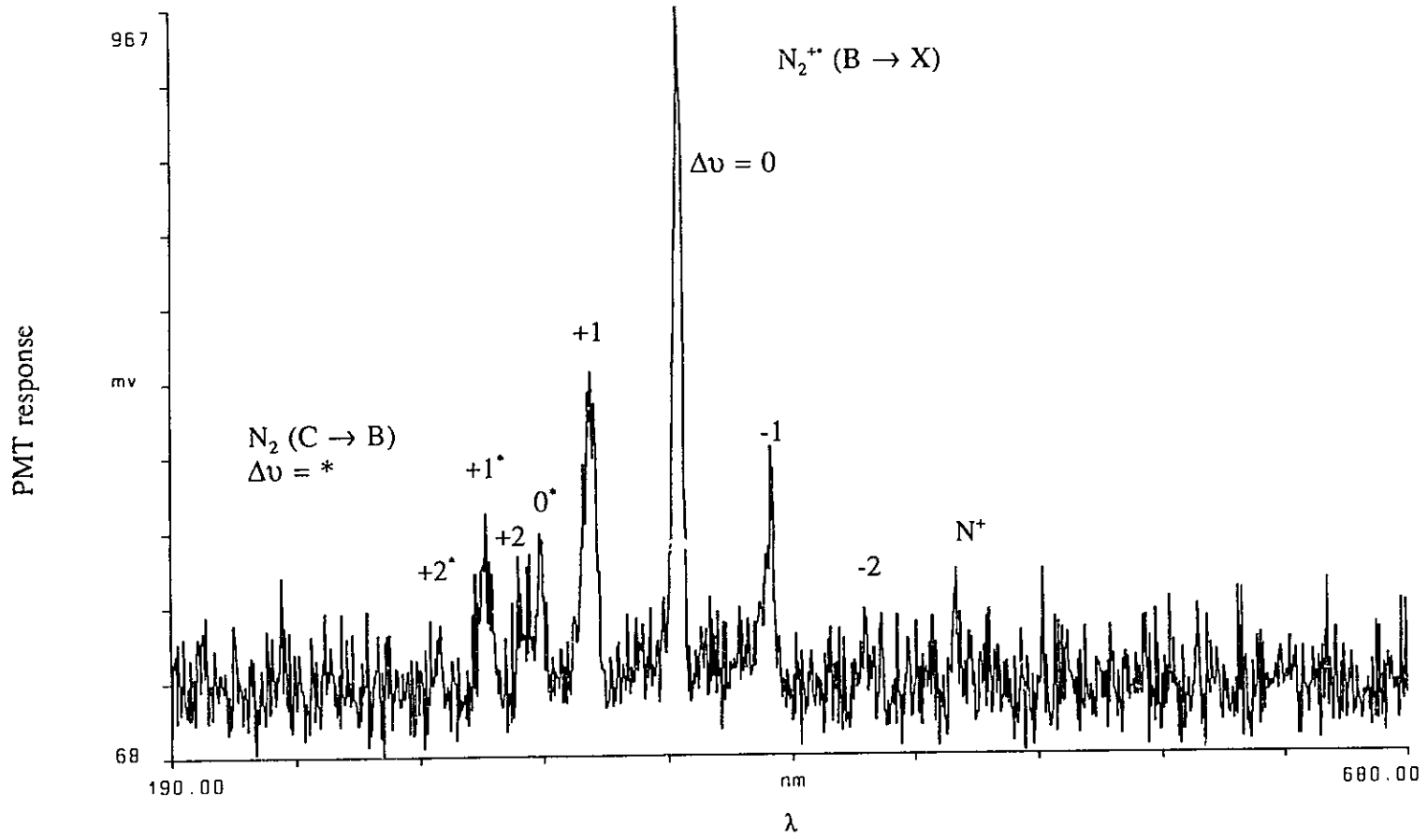

Fig. 4.3.1 b. N_2^{+*} - N_2 (in-OC) collision induced emission spectrum. 1.0 mm slits, 0.5 nm step size, 5 scan average.

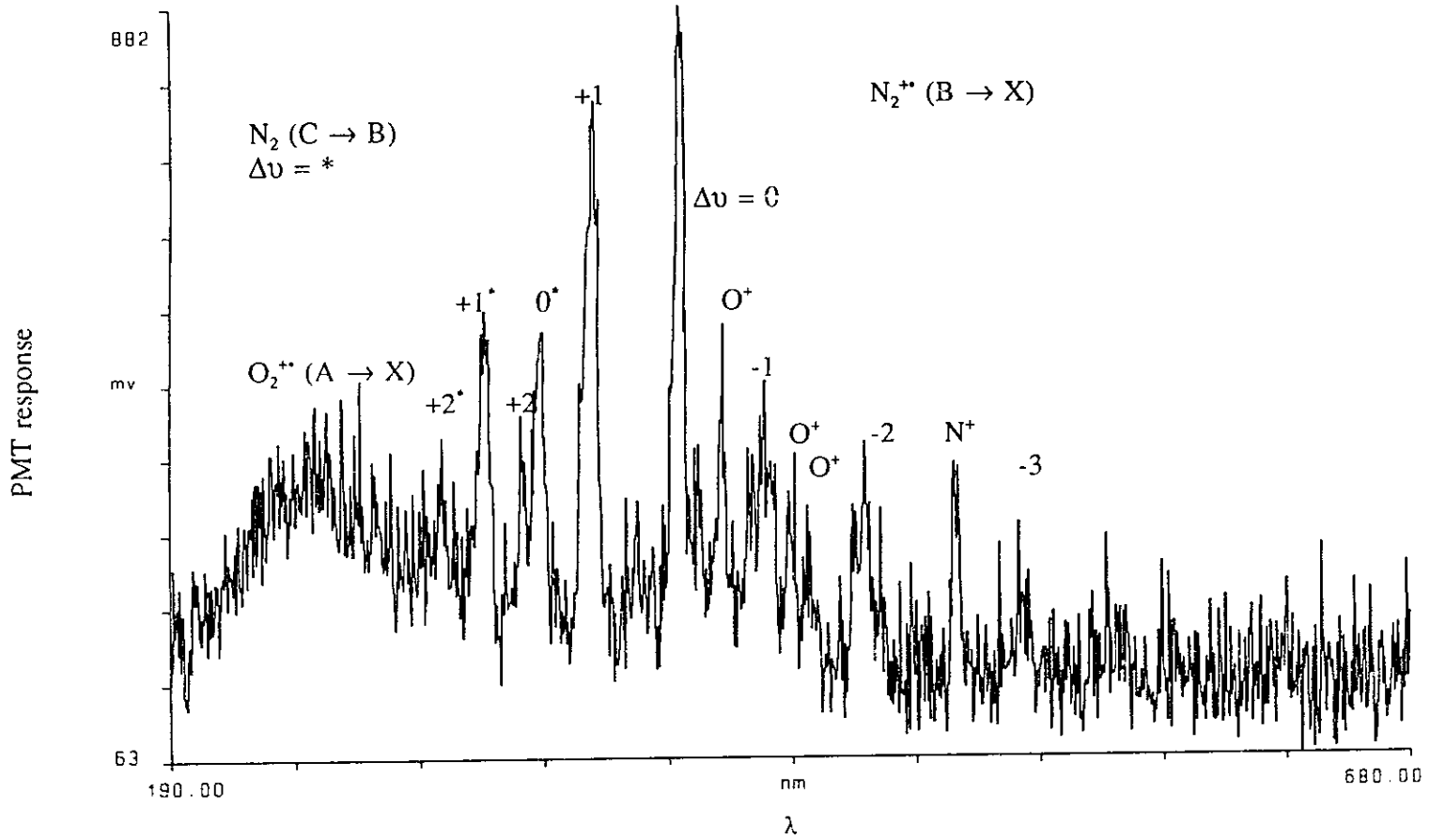

Fig. 4.3.1 c. N_2^{+*} - O_2 (in-OC) collision induced emission spectrum. 1.0 mm slits, 0.5 nm step size, 4 scan average.

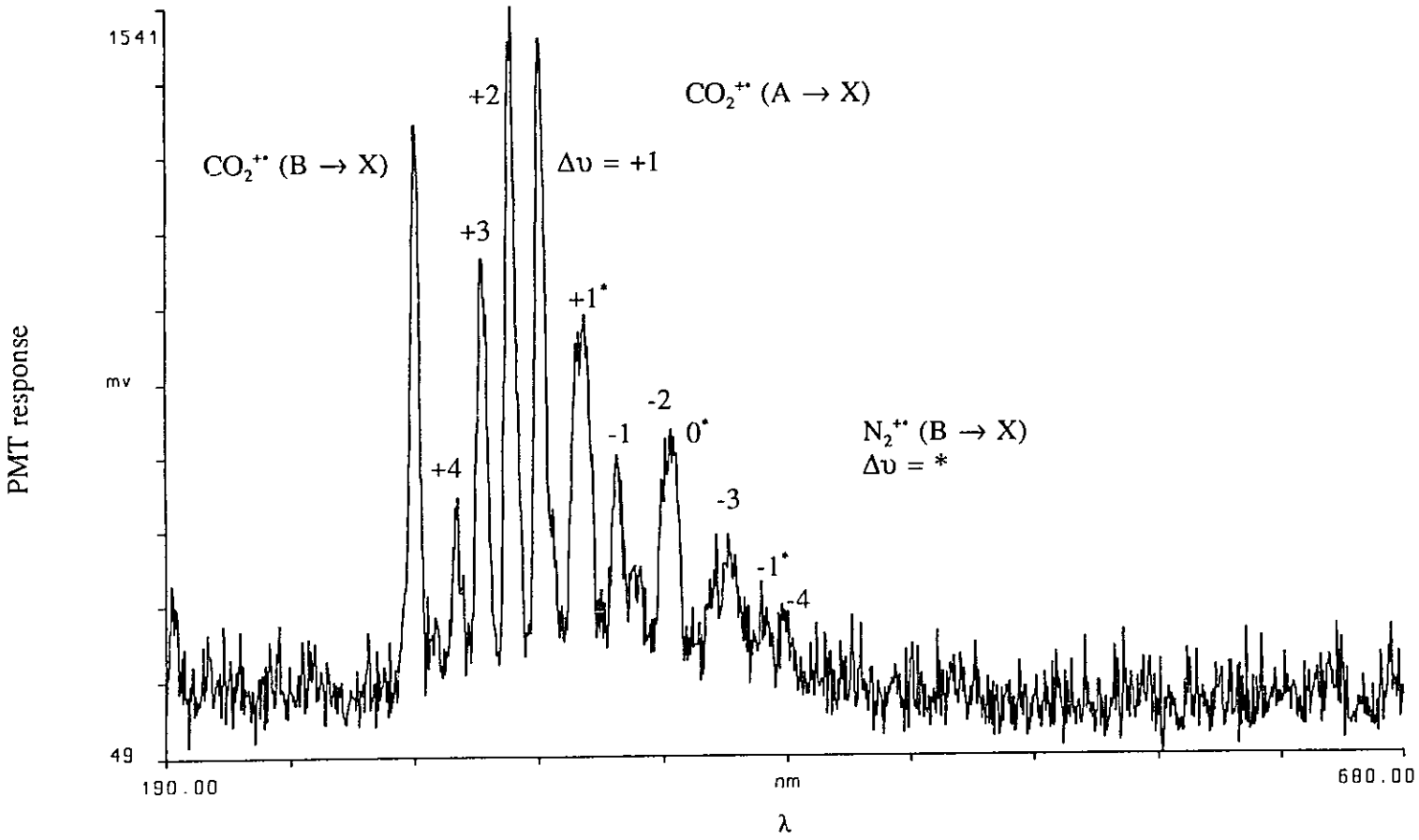

Fig. 4.3.1 d. $N_2^{+\bullet}$ - CO_2 (in-OC) collision induced emission spectrum. 1.0 mm slits, 0.5 nm step size, 4 scan average.

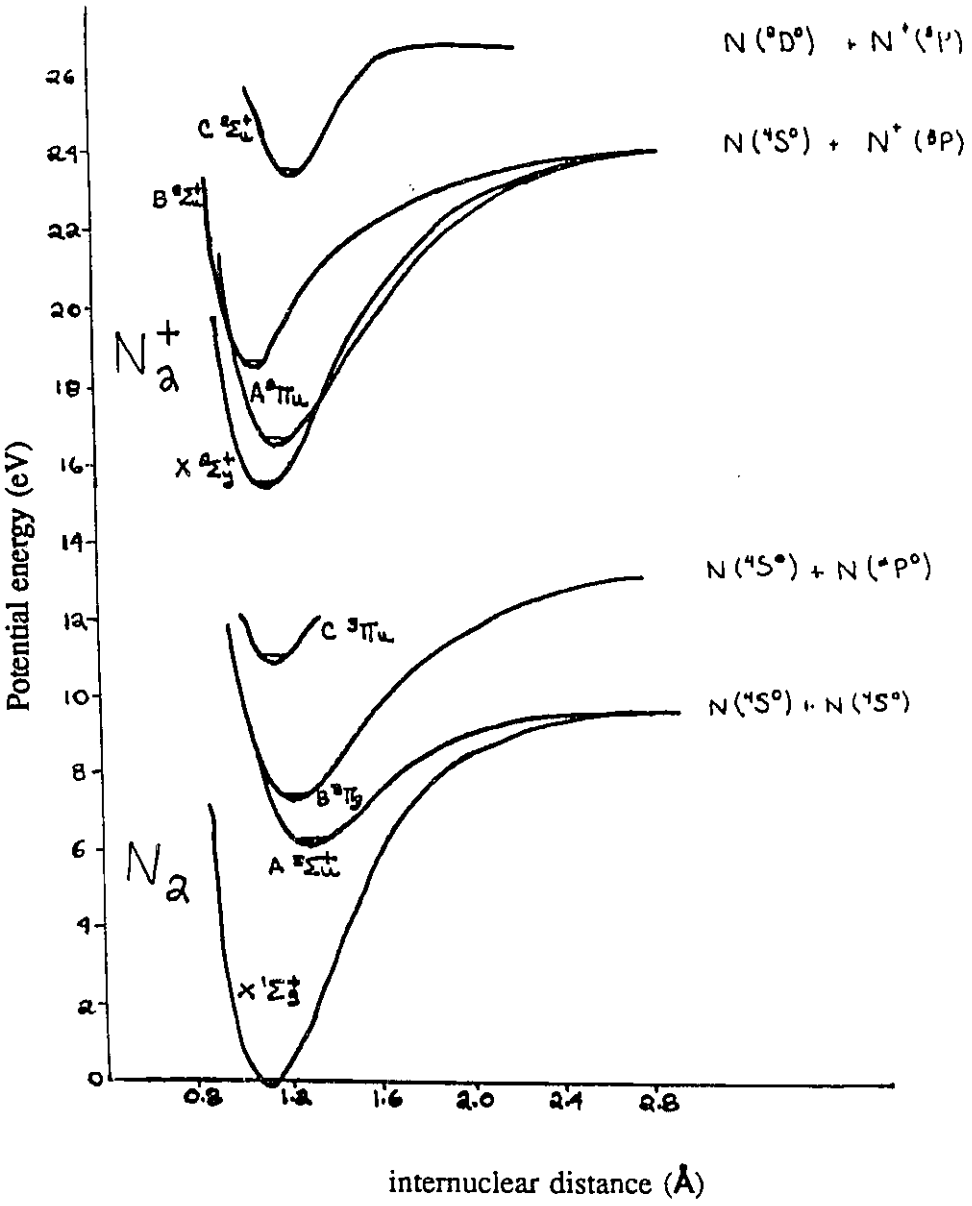

Fig. 4.3.2. Potential energy diagram of N_2 and $N_2^{+\cdot}$ [32].

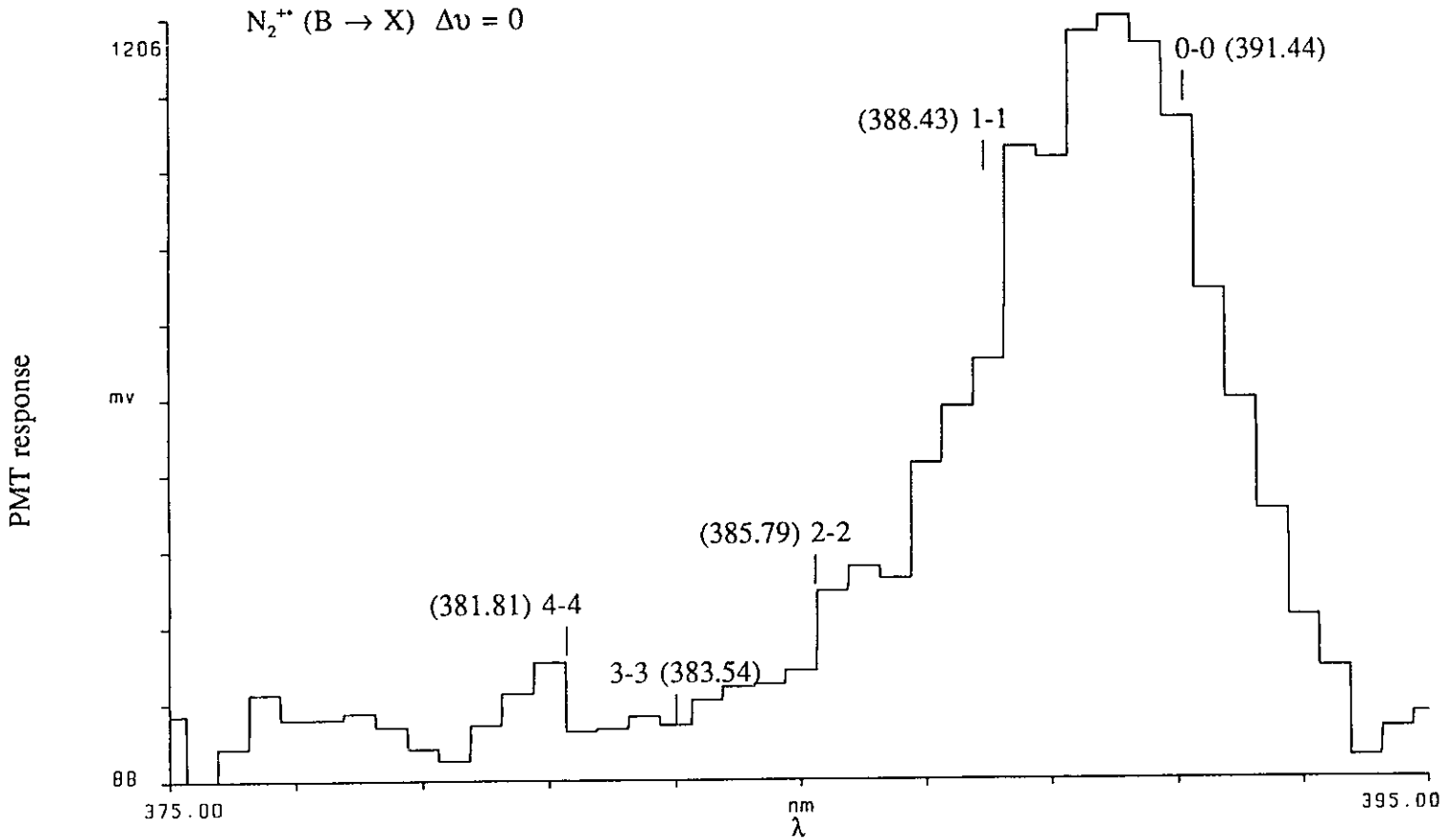

Fig. 4.3.3. Expanded view of the $\Delta\upsilon = 0$ band of the N_2^{+*} (B → X) transition in Fig. 4.3.3.a showing positions of the 0-0, 1-1, 2-2, etc. transitions. Positions corrected for -0.5 nm calibration error (see sec. 3.4.2)

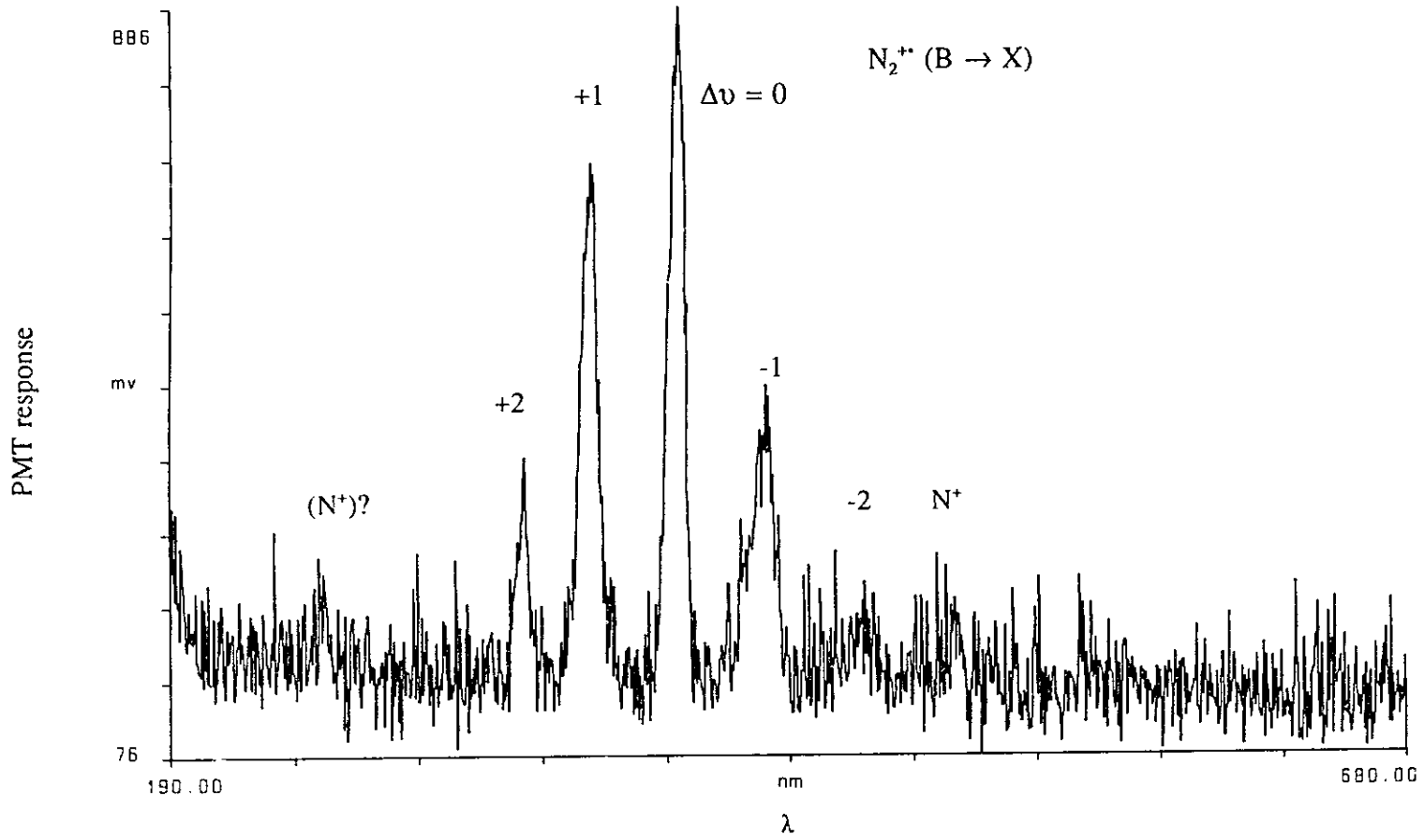

Fig. 4.3.4 a. N_2^{+*} - He (in-PC) collision induced emission spectrum. 2.0 mm slits, 0.5 nm step size, 5 scan average.

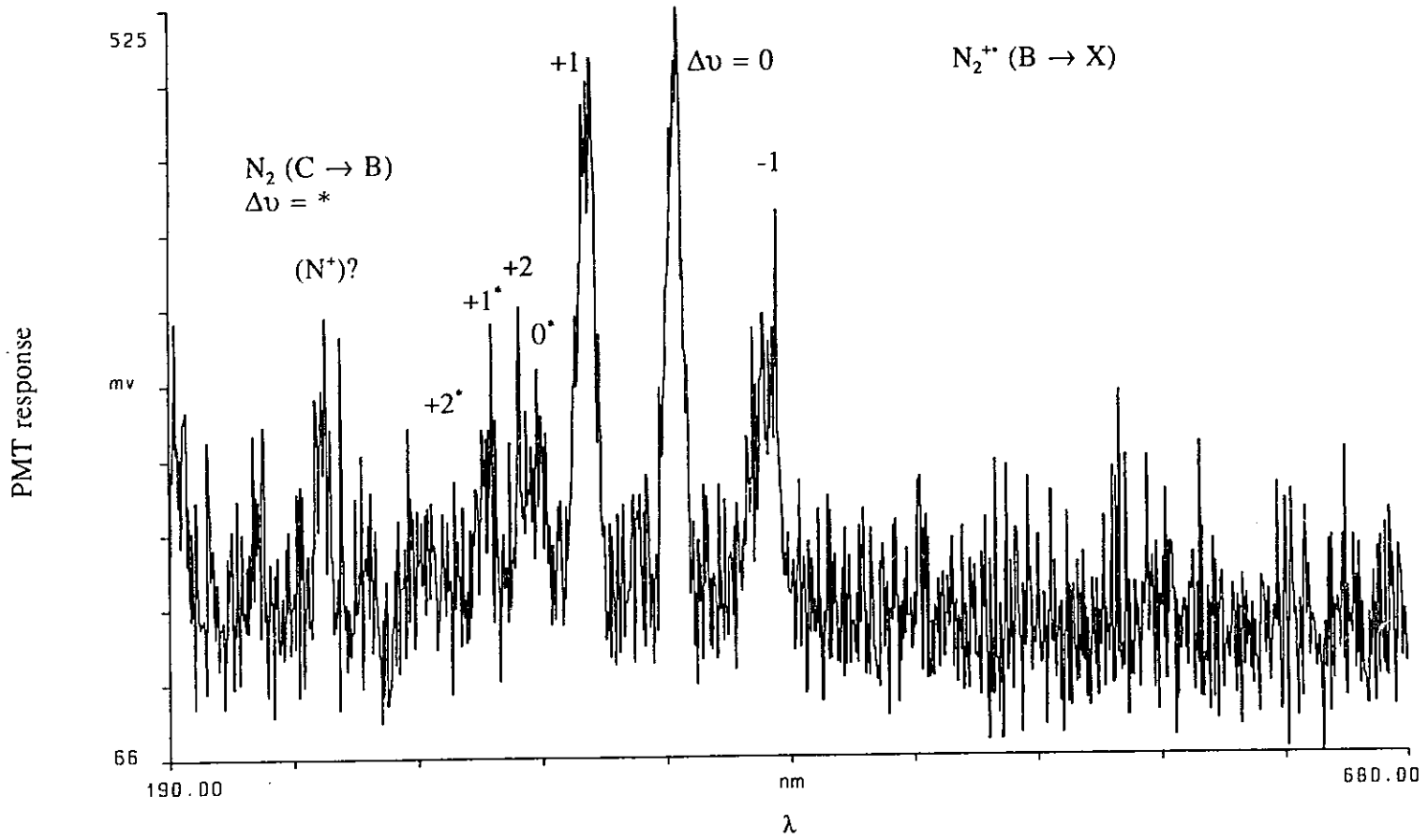

Fig. 4.3.4 b. $N_2^{+\bullet}$ - N_2 (in-PC) collision induced emission spectrum. 2.0 mm slits, 0.5 nm step size, 5 scan average.

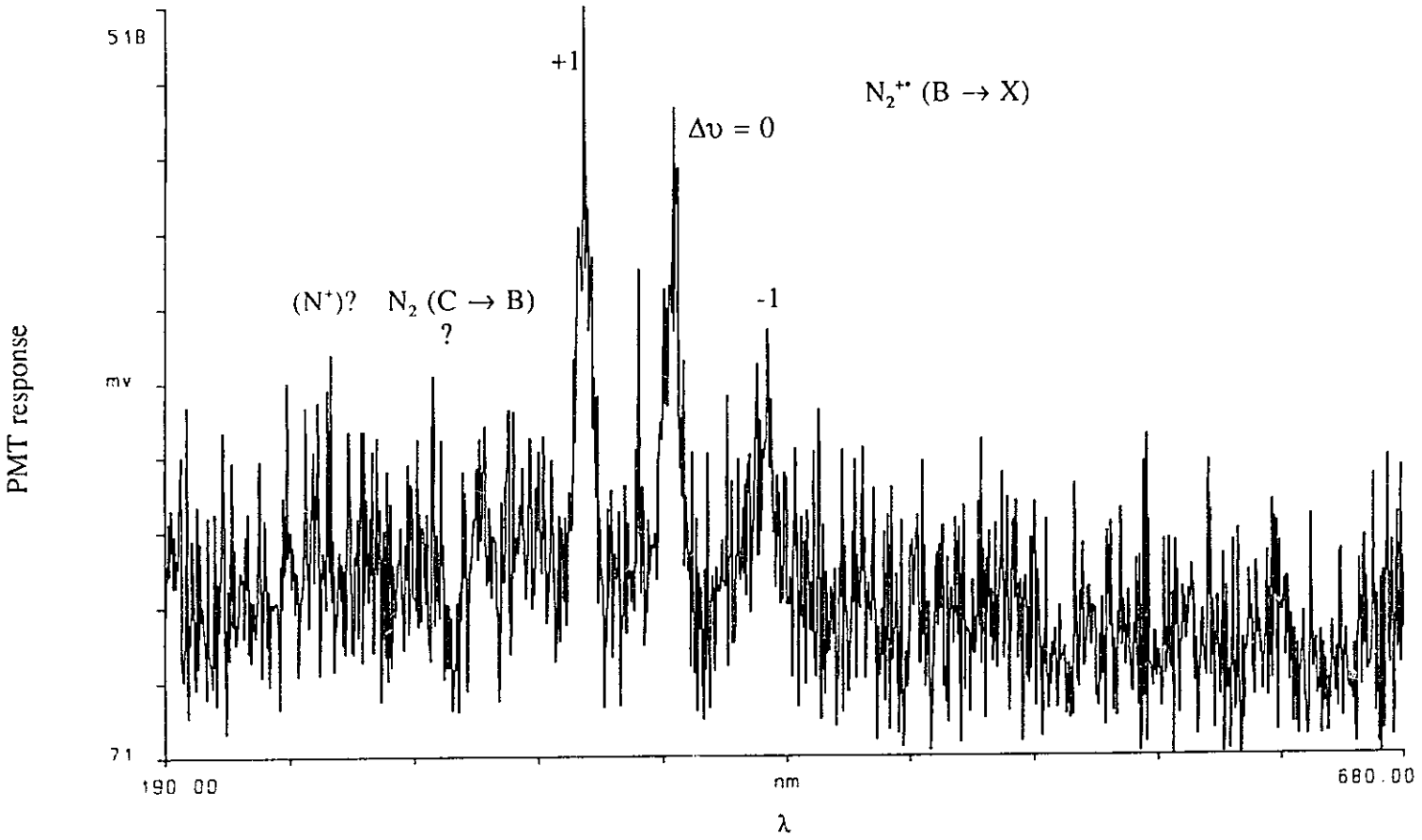

Fig. 4.3.4 c. N_2^{+*} - O_2 (in-PC) collision induced emission spectrum. 2.0 mm slits, 0.5 nm step size, 4 scan average.

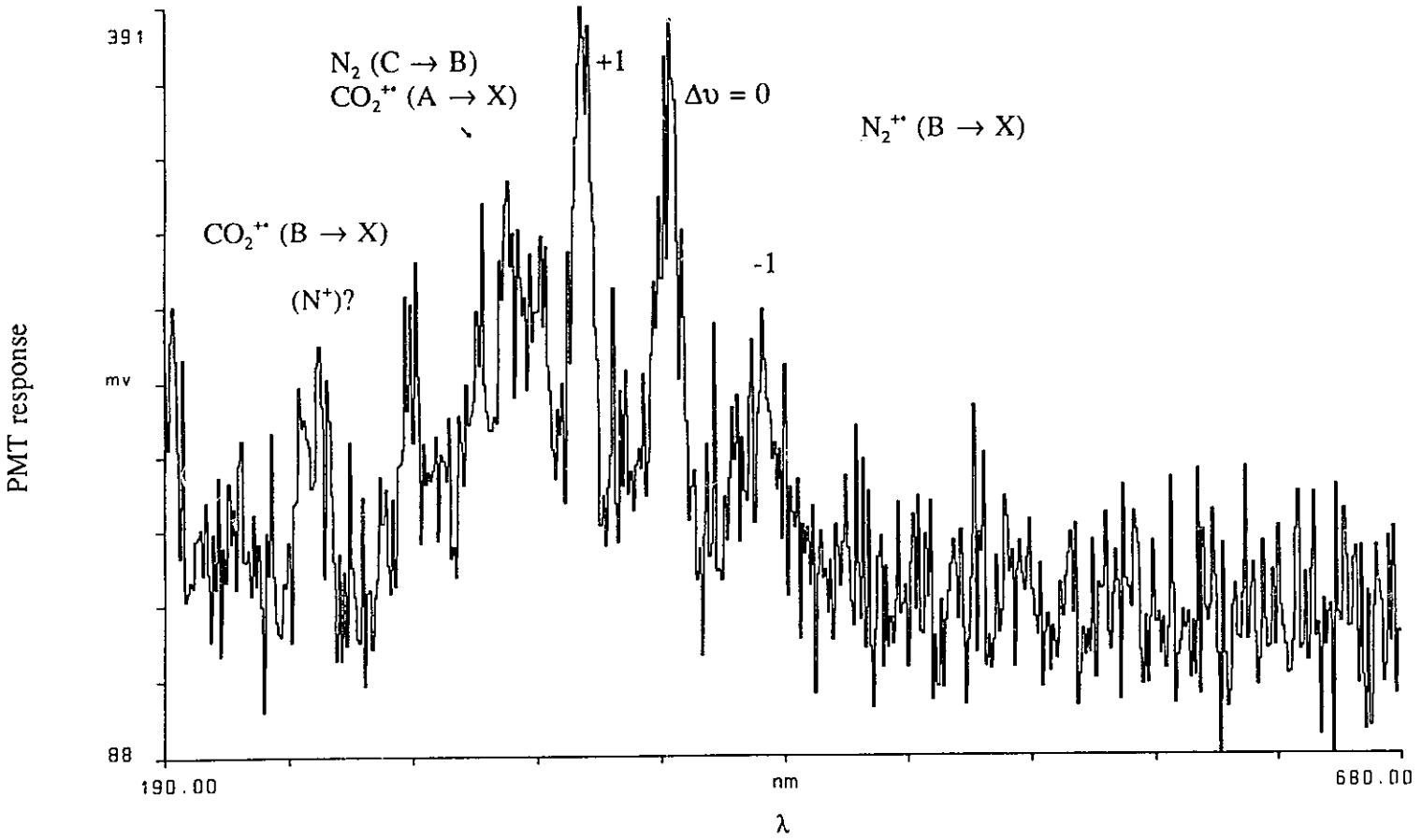

Fig. 4.3.4 d. $N_2^{+\bullet}$ - CO_2 (in-PC) collision induced emission spectrum. 3.0 mm slits, 1 nm step size, 10 scan average.

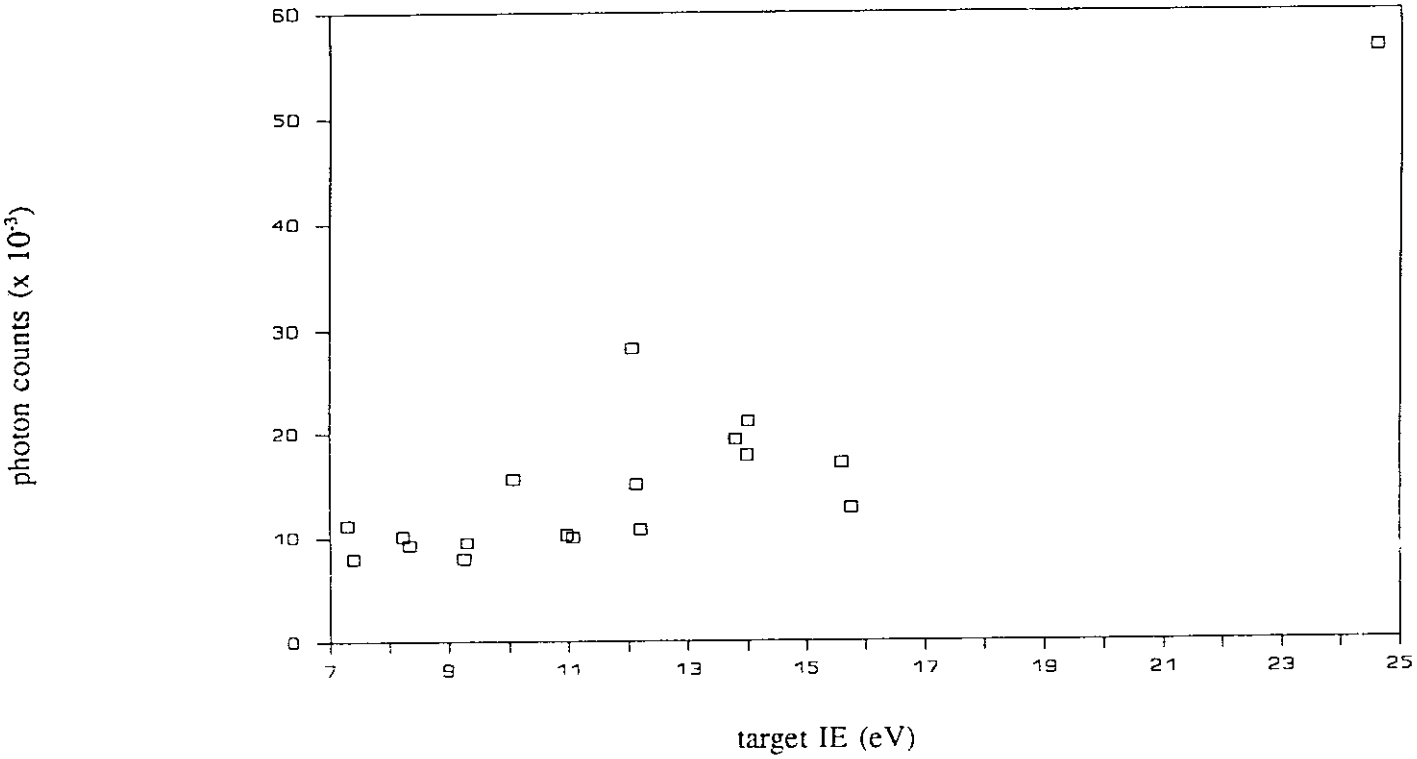

Fig. 4.3.5. Plot of total photon counts over the spectral range 180-680 nm vs target gas ionization energy for $N_2^{+\bullet}$ projectiles (see discussion of post-collision observations). Counts normalized to a common $N_2^{+\bullet}$ flux.

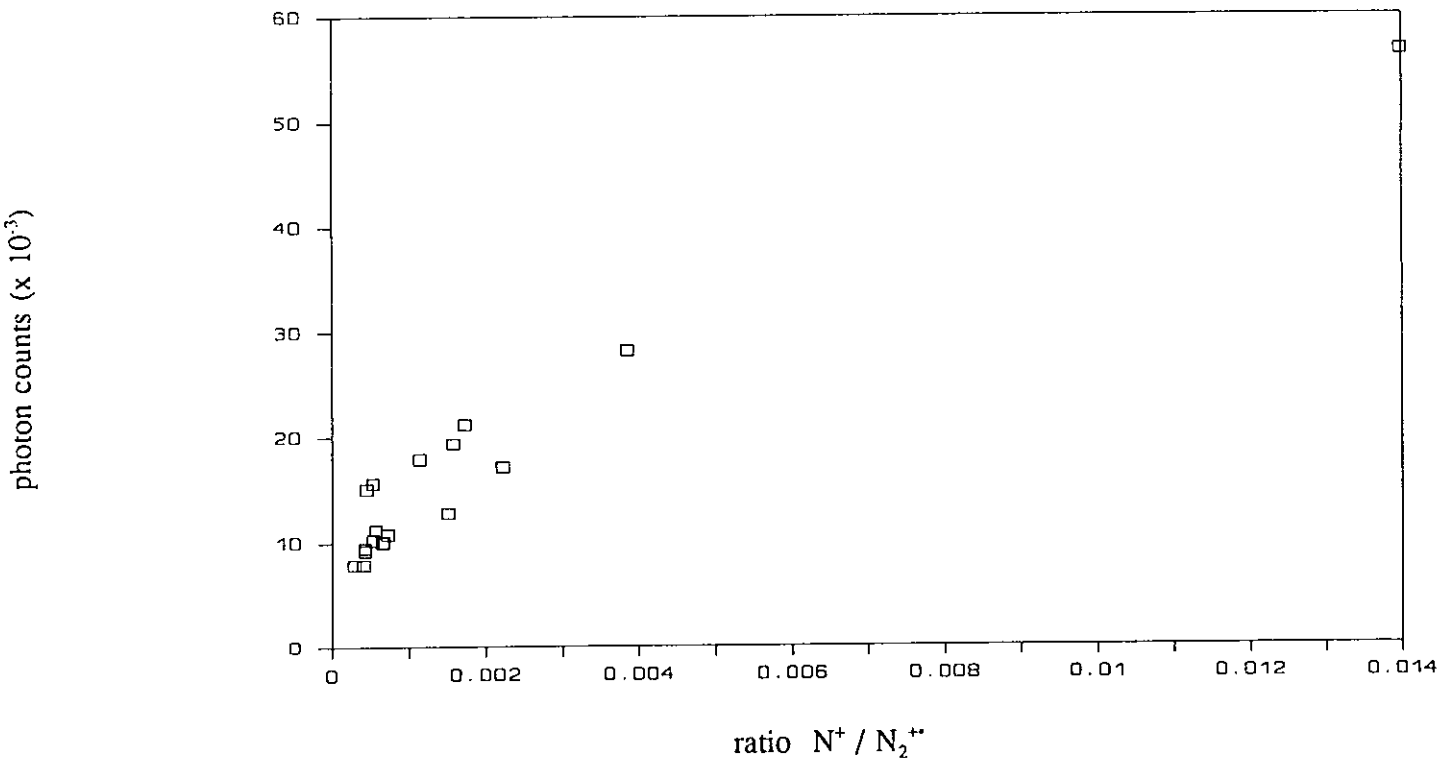

Fig. 4.3.6. Plot of total photon counts over the spectral range 180-680 nm vs relative fragment ion, N^+, abundance in the CID spectrum of $N_2^{+\bullet}$ with the 18 target gases listed in Table 3.4.1. Counts normalized to a common $N_2^{+\bullet}$ flux.

4.3.3 Emissions from $O_2^{+\bullet}$ - target gas collisions

The $O_2^{+\bullet}$ ion beam

The diatomic $O_2^{+\bullet}$ ions were formed in the ion source by 70-100 eV electron impact on O_2. Under these conditions, many states of $O_2^{+\bullet}$ are produced, including X $^2\Pi_g$, a $^4\Pi_u$, A $^2\Pi_u$ and b $^4\Sigma_g^-$ [62-64]. O'Keefe and McDonald [64] used Fourier transform mass spectrometry to determine that for 70 eV electron impact the above states are formed in the ratios 0.34, 0.30, 0.10 and 0.26 respectively. Other investigations [65-67] yielded values for the relative abundance of a $^4\Pi_u$ between 0.10 - 0.48. Formation of $O_2^{+\bullet}$ $^2\Sigma_g^-$ results in pre-dissociation [68]. The radiative lifetimes of A $^2\Pi_u$ and b $^4\Sigma_g^-$ are 0.67 μs and 1.1 μs respectively [64]. The $O_2^{+\bullet}$ ion beam is 13.7 μs old by the time it reaches the OC and the population of these two states will be negligible. The radiative lifetime of a $^4\Pi_u$ is 0.22 s [64] since the transition to the ground state is spin-forbidden. Therefore, the $O_2^{+\bullet}$ ion beam in the present experiments is composed of X $^2\Pi_g$ and a $^4\Pi_u$ species. Turner et. al. [69] determined that at 50 eV electron energy, an $O_2^{+\bullet}$ ion beam will contain 30% a $^4\Pi_u$ up to 20 μs after ionization. It is clear, then, that two electronic states of $O_2^{+\bullet}$ will participate in the present experiments. Unlike $N_2^{+\bullet}$, the long lifetime of the a $^4\Pi_u$ state precludes its spectroscopic observation.

In-cell observations : ion beam emissions

The CIE spectra obtained from 8 keV $O_2^{+\bullet}$ - He, N_2, O_2 and CO_2 collisions can be found in Fig. 4.3.7a-d. No emissions were observed from $O_2^{+\bullet}$ in the ion beam in any of

the experiments, only emissions from the fragments O^+ and O. The $O_2^{+\bullet}$ ($A\ ^2\Pi_u \rightarrow X\ ^2\Pi_g$) band in Fig. 4.3.7c was present whenever O_2 was the target (see also Figs 4.3.1c and 4.3.11c) and hence was assigned to the O_2 target and not the $O_2^{+\bullet}$ in the ion beam. A list of all observed transitions is given in Table 4.3.2. Compare these results with those of $N_2^{+\bullet}$ in section 4.2. The lack of $O_2^{+\bullet}$ emissions is indicative of the relatively shallow potential energy surfaces of the excited states and their displaced geometry with respect to the ground state [70]. Franck-Condon excitation results in vibrational excitation leading to dissociation. No studies involving optical emissions or translational energy loss from $O_2^{+\bullet}$ projectile - target collisions could be found for comparison.

In-cell observations : target gas emissions

Each of the four spectra in Fig. 4.3.7 exhibit target gas emissions. A list of the target emissions is given in Table 4.3.2. The transitions observed are virtually identical with those found for $N_2^{+\bullet}$ projectiles, Table 4.3.1. Interestingly, when N_2 was the target, few ion beam emissions were observed. It is clear that reversing projectile and target does not make for a complementary experiment (compare Figs. 4.3.1c and 4.3.7c). Studies of the optical emissions from projectile - O_2 collisions from the literature [71-73 - keV projectiles; 41,74,75 - eV projectiles] report both the $O_2^{+\bullet}$ ($b\ ^4\Sigma_g^- \rightarrow a\ ^4\Pi_u$) first negative system and ($A\ ^2\Pi_u \rightarrow X\ ^2\Pi_g$) second negative system along with O^+ and O emissions. The $A\ ^2\Pi_u \rightarrow X\ ^2\Pi_g$ system increased in prominance as the energy of the projectile increases. No emissions due to the $b\ ^4\Sigma_g^- \rightarrow a\ ^4\Pi_u$ first negative system in $O_2^{+\bullet}$ were observed in our experiments. TES studies of keV projectile - O_2 collisions [50,51,56,76-84] attribute peaks

Table 4.3.2

Observed Transitions in Figs 4.3.7a-d.

System		transition	λ(nm)	ref.
$O_2^{+\cdot}$ - He	He	see Table 4.3.1		
	O	$4p\ ^5P \rightarrow 3s\ ^5S^0$	395	33
		$7d\ ^5D^0 \rightarrow 3p\ ^5P$	465.5	
	O^+	$3p'\ ^2D^0 \rightarrow 3s\ ^2P$	243-245	33
		$3p\ ^2P^0 \rightarrow 3s\ ^2P$	395-398	
		$3d\ ^4F \rightarrow 3p\ ^4D^0$	407	
		$3p\ ^4P^0 \rightarrow 3s\ ^4P$	432-437	
		$3p\ ^2D^0 \rightarrow 3s\ ^2P$	441	
		$3p'\ ^2F^0 \rightarrow 3s'\ ^2D$	459	
		$3p\ ^4D^0 \rightarrow 3s\ ^4P$	464-469	
		$3d\ ^4P \rightarrow 3p\ ^4S^0$	489	
$O_2^{+\cdot}$ - N_2	$N_2^{+\cdot}$	$B \rightarrow X$ see Table 4.3.1		
	N_2	$C \rightarrow B$ see Table 4.3.1		
	N^+	$3d\ ^3F^0 \rightarrow 3p\ ^3D$	500	33
$O_2^{+\cdot}$ - O_2	$O_2^{+\cdot}$	$A \rightarrow X$	190 →	70
	O	$4p\ ^5P \rightarrow 3s\ ^5S^0$	395	33
		$7d\ ^5D^0 \rightarrow 3p\ ^5P$	465.5	
	O^+	$3d\ ^4P \rightarrow 3p\ ^4D^0$	386-393	33
		$3p\ ^2P^0 \rightarrow 3s\ ^2P$	395-398	
		$3d\ ^4F \rightarrow 3p\ ^4D^0$	407	
		$3d'\ ^2G \rightarrow 3p'\ ^2F^0$	418.5	
		$3p\ ^4P^0 \rightarrow 3s\ ^4P$	432-437	
		$3p'\ ^2F^0 \rightarrow 3s'\ ^2D$	459	
		$3p\ ^4D^0 \rightarrow 3s\ ^4P$	464-469	
$O_2^{+\cdot}$ - CO_2	$CO_2^{+\cdot}$	$B \rightarrow X$ see Table 4.3.1		
	$CO_2^{+\cdot}$	$A \rightarrow X$ see Table 4.3.1		
	O	$7d\ ^5D^0 \rightarrow 3p\ ^5P$	465.5	33
	O^+	$3d\ ^4P \rightarrow 3p\ ^4D^0$	386-393	33
		$3d\ ^4F \rightarrow 3p\ ^4D^0$	407	
		$3d\ ^4D \rightarrow 3p\ ^4P^0$	410-412	
		$3p\ ^4P^0 \rightarrow 3s\ ^4P$	432-437	
		$3p\ ^4D^0 \rightarrow 3s\ ^4P$	464-469	

to excitation of O_2 from X $^3\Sigma_g^-$ ground state to the a $^1\Delta_g$, b $^1\Sigma_g^+$, A $^3\Sigma_u^+$ and B $^3\Sigma_u^-$ excited states. Only one study [52] reported and assigned peaks to the formation of excited state $O_2^{+\bullet}$. Energy loss spectra due to impact of 1 keV $He^{+\bullet}$ ions on O_2 at large scattering angles contained peaks due to formation of $O_2^{+\bullet}$ c $^4\Sigma_u^-$, B $^2\Sigma_g^-$, b $^4\Sigma_g^-$, A $^2\Pi_u$ and a $^4\Pi_u$ states.

Post-collision observations

The $O_2^{+\bullet}$ - target systems did not yield emissions of the same magnitude as the $N_2^{+\bullet}$ experiments. Undoubtedly, since fragments make up only a small fraction of the ion beam and are responsible for the ion beam emissions discussed above, the same levels of signal cannot be expected. The effect is also seen in post-collision observation experiments where for a common ion flux, $O_2^{+\bullet}$ beam emissions are of the order of one quarter of those of the $N_2^{+\bullet}$ beam experiments. For this reason, it was possible to obtain only one post-collision emission spectrum involving $O_2^{+\bullet}$ using CO_2 as the target, Fig. 4.3.8. Evident from the figure is that the contribution of extraneous target gas emissions is not negligible.

As in section 4.3.2, correlations were sought between emission and the CID relevant parameters of target IE (Fig. 4.3.9) and fragment abundance (Fig. 4.3.10). The filter spectra were obtained with the same 18 target gases used in the $N_2^{+\bullet}$ study. However, unlike $N_2^{+\bullet}$, no clear correlation was evident in the two figures. The same result was found when each spectral region, or combination of regions, was plotted. The reason for this is probably the relatively large target gas emissions. Since the projectiles which emit in these experiments are the low yield fragment O^+ and O species, target gas

contributions are more significant than when $N_2^{+\bullet}$ was the projectile. There was more ion beam emission from the nitrogen molecular ions and so contributions to the post-collision observations of leaked target gas were less significant. Only a small degree of scatter was added to the plots in Figs 4.3.5 and 4.3.6.

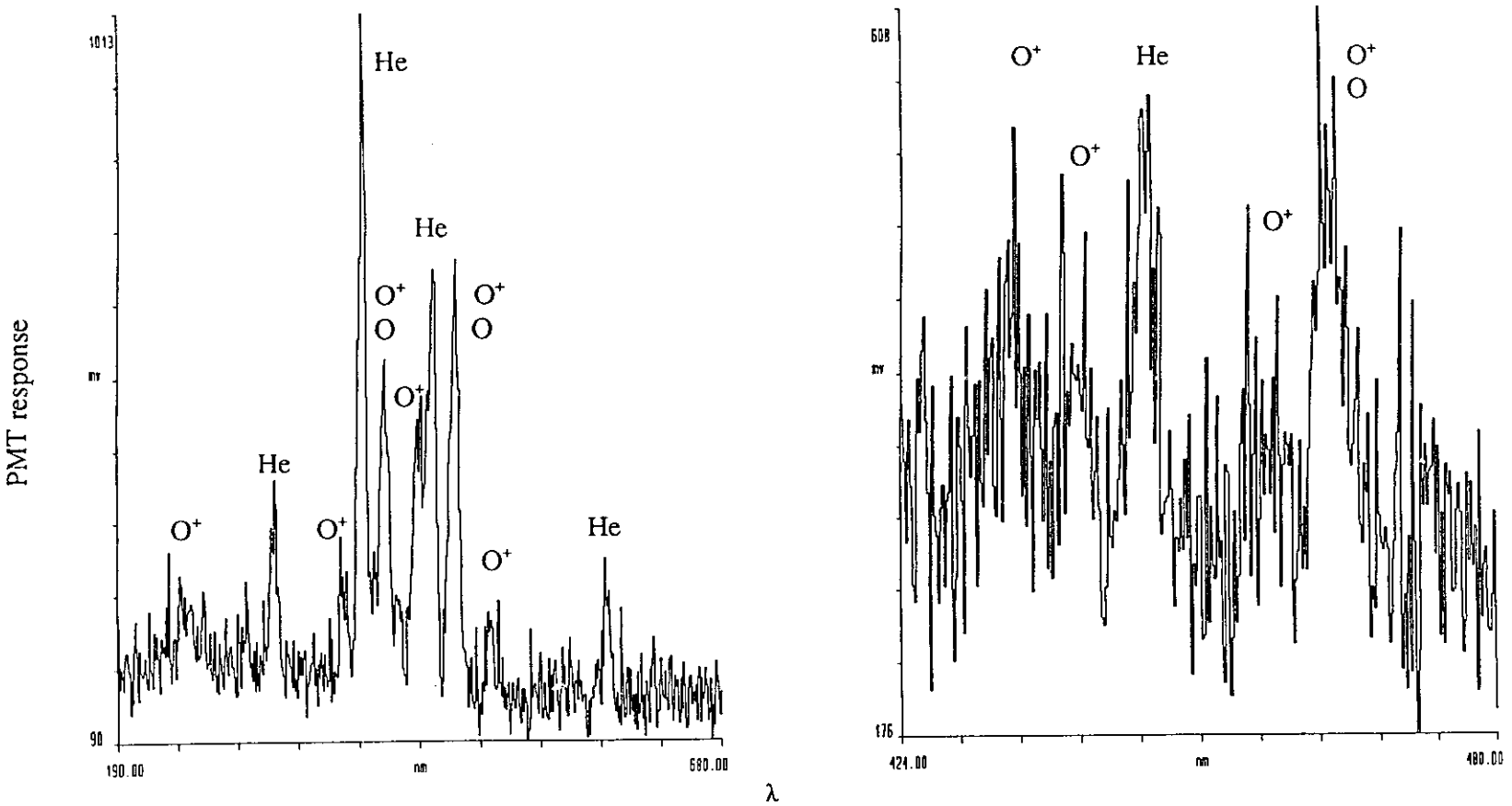

Fig. 4.3.7 a. $O_2^{+\bullet}$ - He (in-OC) collision induced emission spectrum. Left- full spectrum, 2.0 mm slits, 1 nm step size, 8 scan average and Right- 424-480 nm, 1.0 mm slits, 0.2 nm step size, 9 scan average.

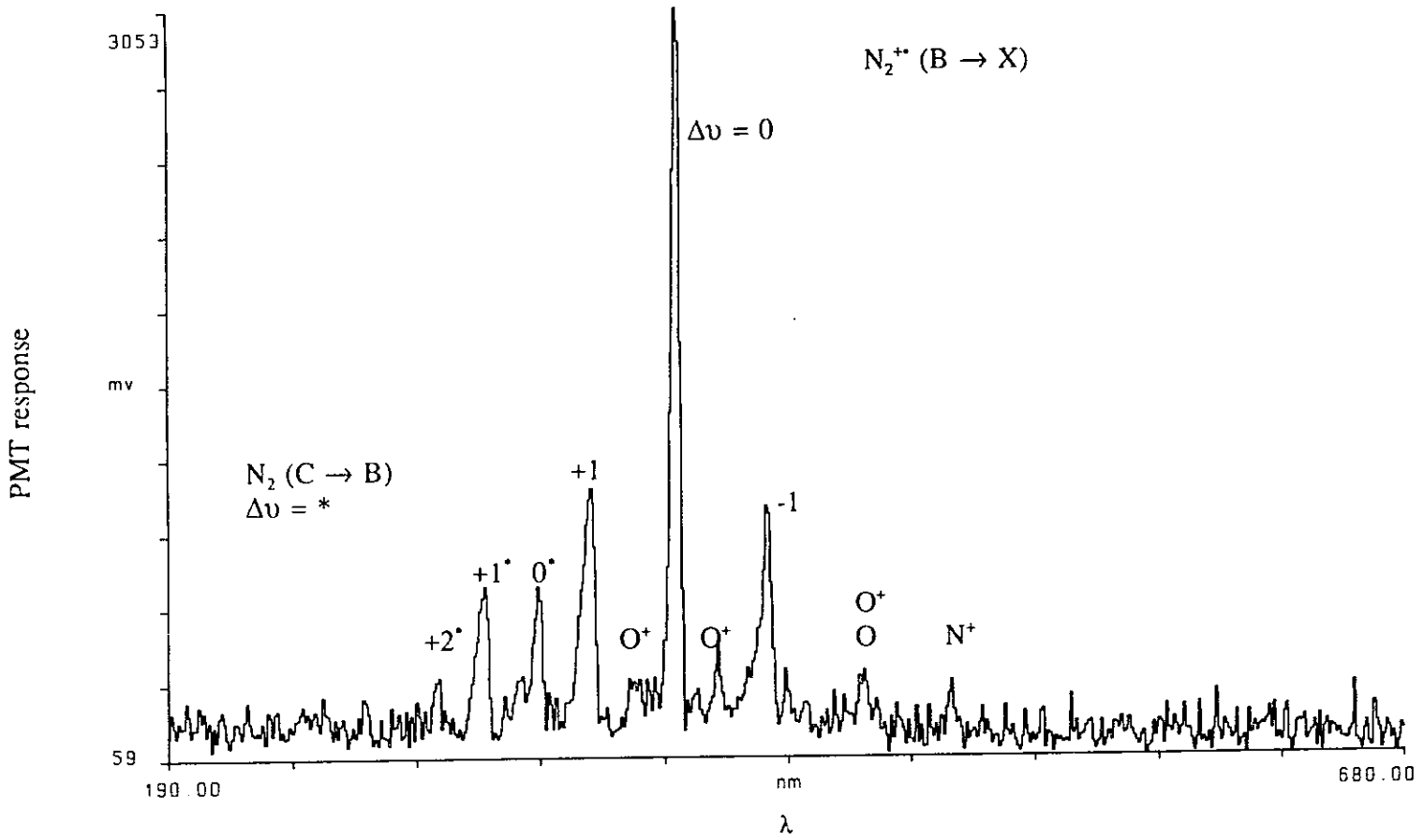

Fig. 4.3.7 b. O_2^{+*} - N_2 (in-OC) collision induced emission spectrum. 1.0 mm slits, 1 nm step size, 3 scan average.

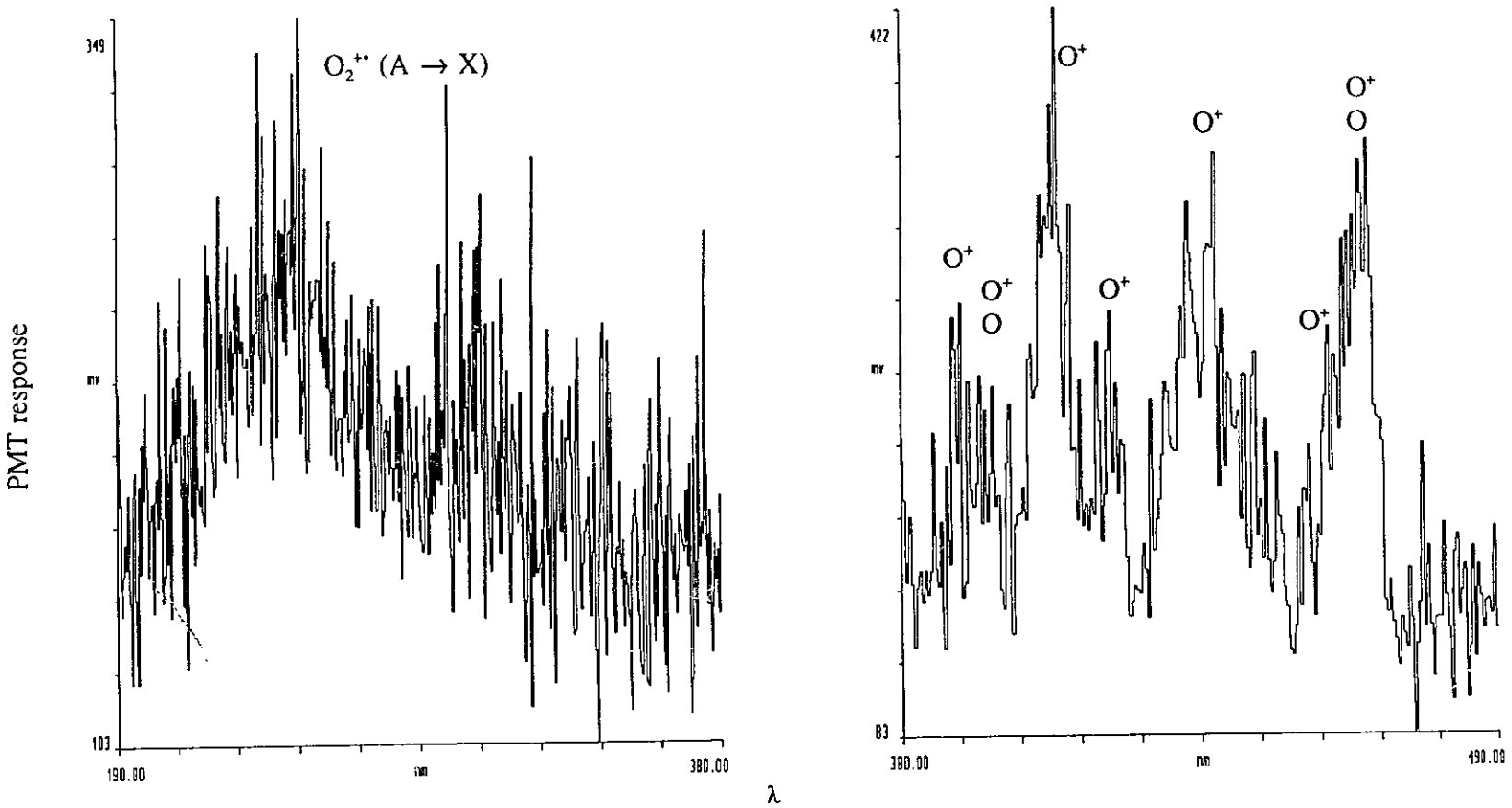

Fig. 4.3.7 c. $O_2^{+\bullet}$ - O_2 (in-OC) collision induced emission spectrum. Left- 190-380 nm and Right- 380-490 nm, Both- 2.0 mm slits, 0.5 nm step size, 6 scan average.

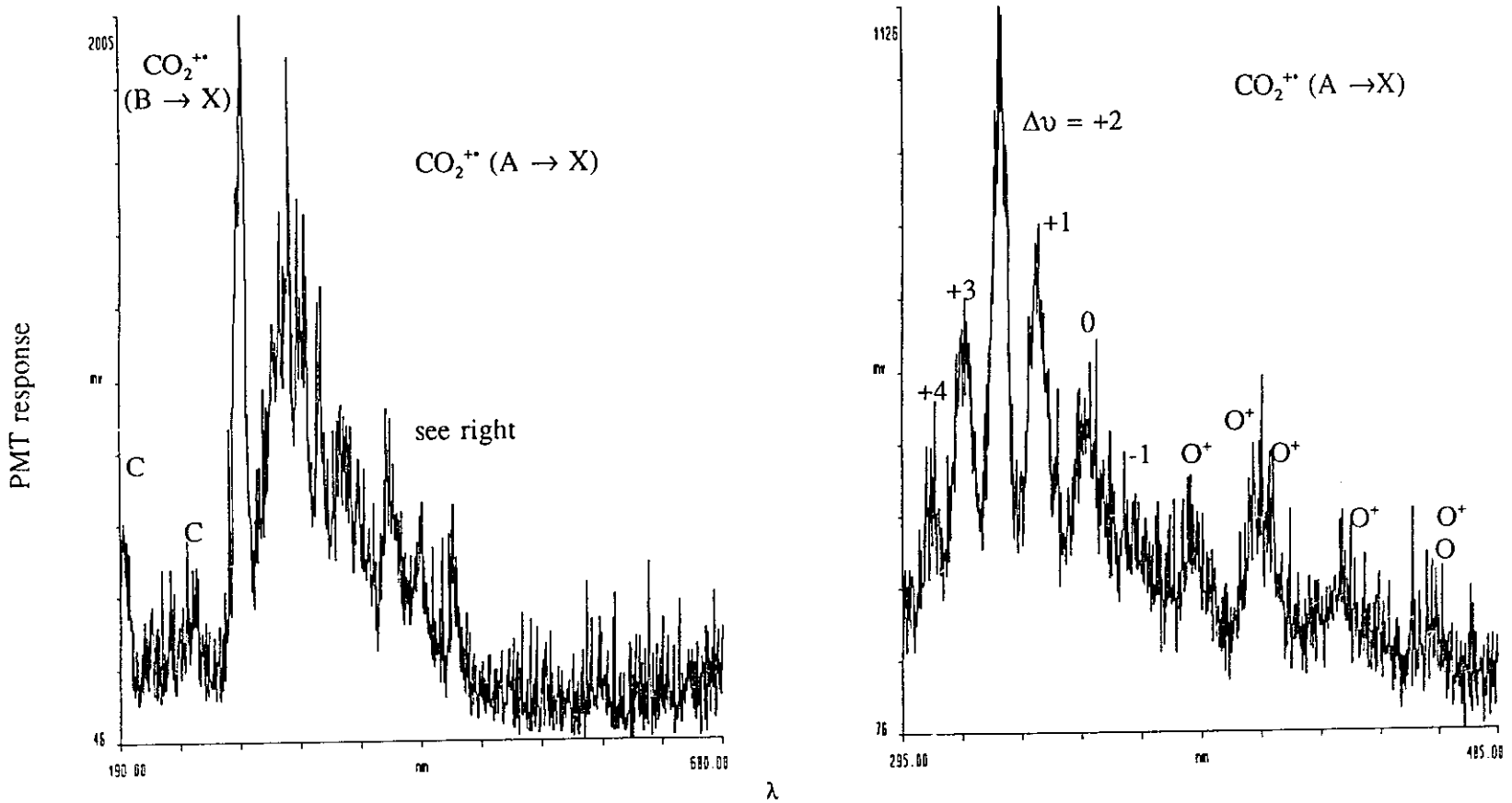

Fig. 4.3.7 d. $O_2^{+\bullet}$ - CO_2 (in-OC) collision induced emission spectra. Left- full spectrum, 3.0 mm slits, 0.5 nm step size, 1 scan and Right- 295-485 nm, 2.0 mm slits, 0.2 nm step size, 3 scan average.

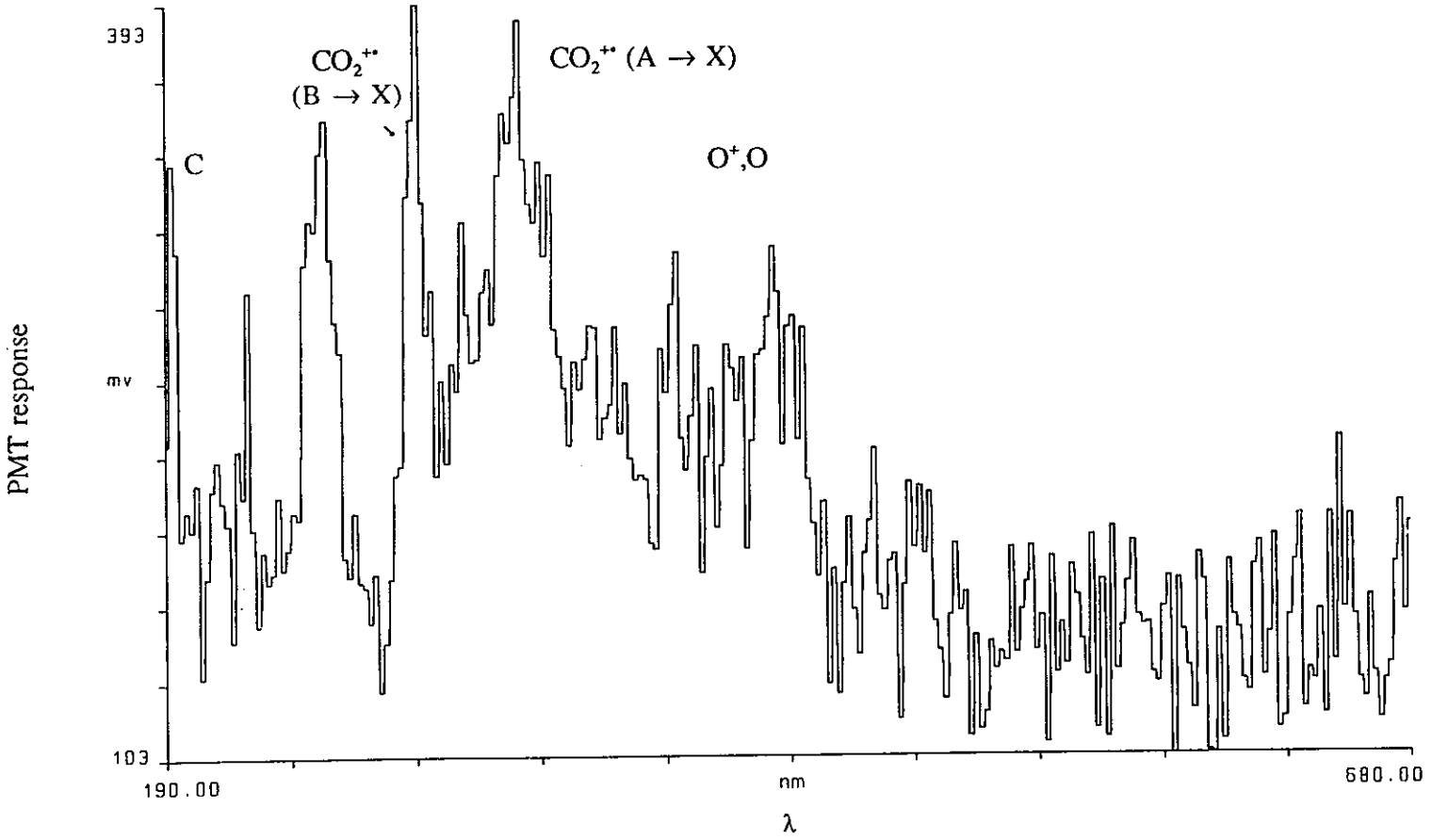

Fig. 4.3.8. $O_2^{+\bullet}$ - CO_2 (in-PC) collision induced emission spectrum. 3.0 mm slits, 2 nm step size, 10 scan average.

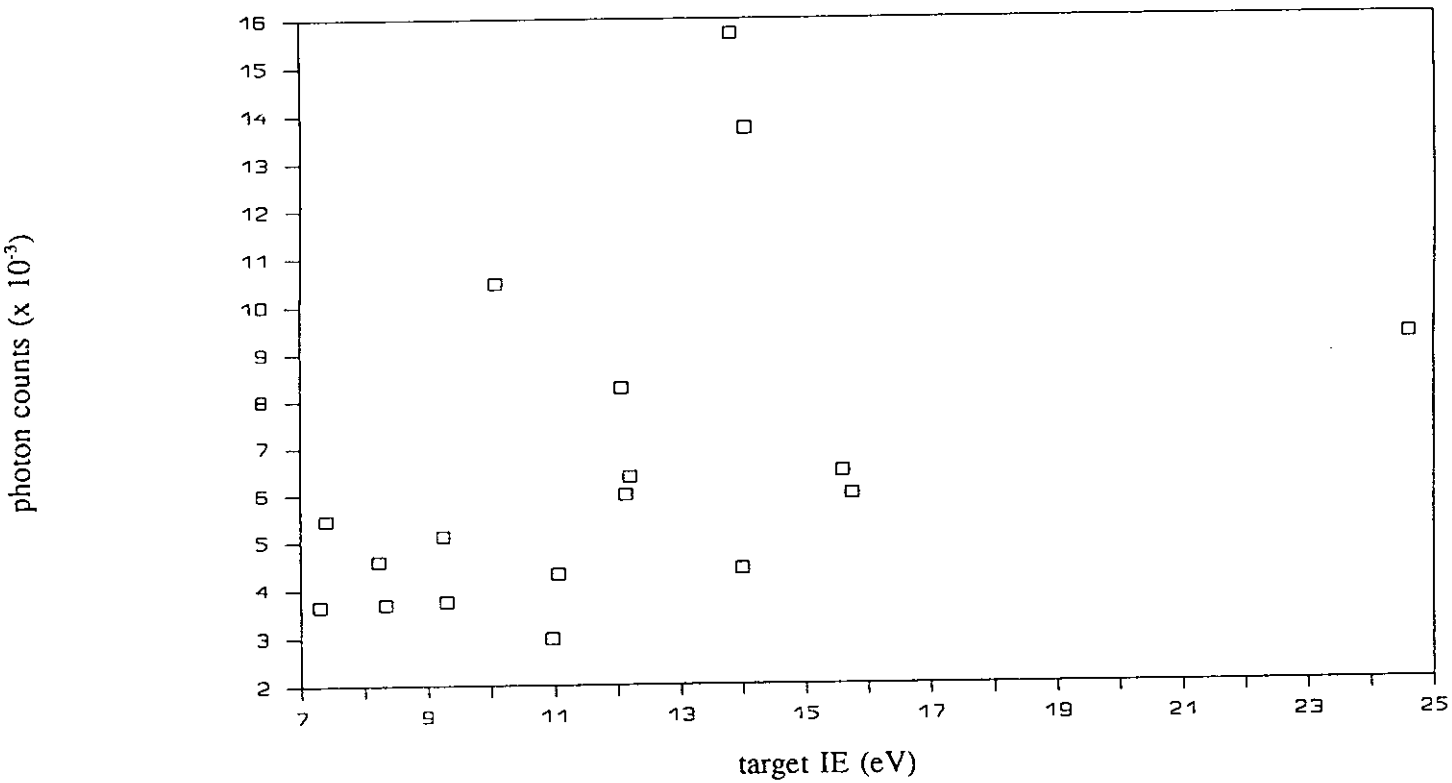

Fig. 4.3.9. Plot of total photon counts over the spectral range 180-680 nm vs target gas ionization energy for $O_2^{+\bullet}$ projectiles (see discussion of post-collision observations). Counts normalized to a common $O_2^{+\bullet}$ flux.

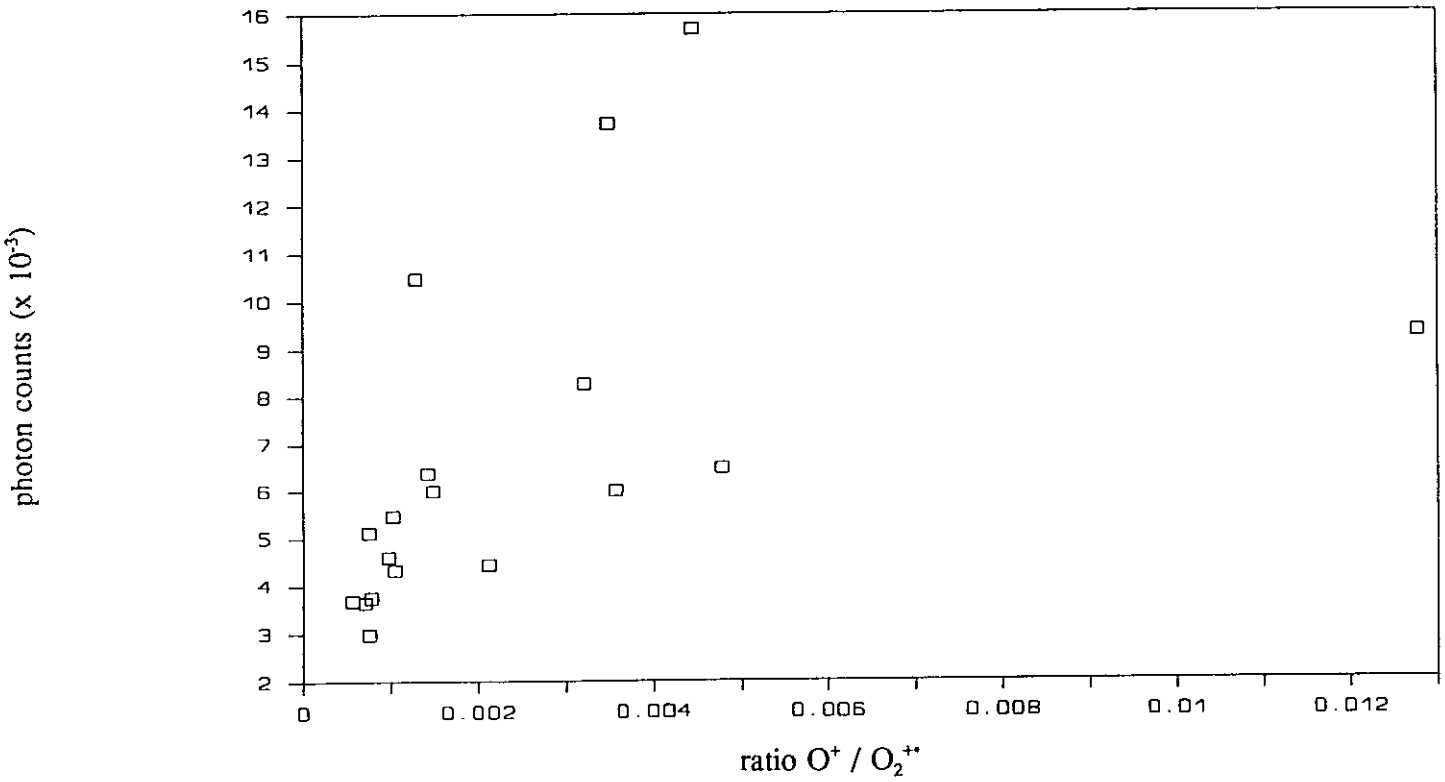

Fig. 4.3.10. Plot of total photon counts over the spectral range 180-680 nm vs relative fragment ion, O^+, abundance in the CID spectrum of $O_2^{+\bullet}$ with the 18 target gases listed in Table 3.4.1. Counts normalized to a common $O_2^{+\bullet}$ flux.

4.3.4 Emissions from $CO_2^{+\bullet}$ - target gas collisions

The $CO_2^{+\bullet}$ ion beam

Carbon dioxide ions were formed by ca 70 eV electron impact on CO_2 in the ion source. The ion is generated in the X $^2\Pi_g$, A $^2\Pi_u$, B $^2\Sigma_u^+$ and C $^2\Sigma_g^+$ states [85-90] upon electron or photon ionization. The C $^2\Sigma_g^+$ state predissociates [86] to give O^+ (^4S_u) and CO ($^1\Sigma_g^+$) and hence will not form part of the $CO_2^{+\bullet}$ ion beam. The radiative lifetimes of the A $^2\Pi_u$ and B $^2\Sigma_u^+$ states are ~116 ns [85,87,88,90] and 115 ns [85,87,89] respectively. The $CO_2^{+\bullet}$ ions require 16 μs to travel from the ion source to the CIE collision cell and thus are all predominantly in their ground state.

In-cell observations - ion beam emissions

The CIE spectra for 8 keV $CO_2^{+\bullet}$ - He, N_2, O_2 and CO_2 collisions performed in the OC are presented in Figs 4.3.11a-d. The dominant spectral features in Figs 4.3.11 a,c,d are due to $CO_2^{+\bullet}$ (B $^2\Sigma_u^+ \rightarrow$ X $^2\Pi_g$), shown under higher resolution in Fig. 4.3.12, and (A $^2\Pi_u \rightarrow$ X $^2\Pi_g$) transitions [91-94]. There are also two bands to shorter wavelengths of the B $\rightarrow$ X band at 192 nm and 247 nm which correspond to the C transitions 3s $^1P^0 \rightarrow$ 2p ^1D and 3s $^1P^0 \rightarrow$ 2p ^1S respectively [33]. The most abundant fragment ion of $CO_2^{+\bullet}$ is $CO^{+\bullet}$ and the B $^2\Sigma^+ \rightarrow$ X $^2\Sigma^+$ transition from this species is evident in Fig. 4.3.11a [95]. The $CO_2^{+\bullet}$ - He experiment was also performed with sufficient target gas pressure to achieve 90% ion beam transmission, i.e., single collision conditions (sec. 3.3.2). The CIE spectrum was identical to, but weaker than Fig. 4.3.11a, indicating that multiple collision

processes do not affect the emitting species.

There have been no previous attempts to study emissions from $CO_2^{+\bullet}$ projectile - target gas collisions. Reid [96] attributed one of two scattering profile peaks to excitation of $CO_2^{+\bullet}$ to the A $^2\Pi_u$ state. There have been several studies of optical emissions from keV projectile (usually H^+ or $He^{+\bullet}$) - CO_2 collisions [97-104]. They all report the $CO_2^{+\bullet}$ (B $\rightarrow$ X) and (A $\rightarrow$ X) transitions. The presence of fragment emissions in these experiments seems to be extremely sensitive to projectile nature and translational energy. Some spectra were reported to contain very minor emissions from $CO^{+\bullet}$ [97,98,101], C and C^+ [100,101]. Due to the moderate resolution possible in the present experiments, identifying minor peaks amidst intense $CO_2^{+\bullet}$ emissions was difficult. A double charge transfer study of OH^+ - CO_2 [105] concluded that a two step charge transfer from OH^+ to OH^- resulted in two $CO_2^{+\bullet}$ ions, one in the ground state and one in the A $^2\Pi_u$ state. In a theoretical and mass spectrometric study of ionized target gas species formed in keV H^+ - CO_2 collisions, Johnson and Parker [106] concluded that the ratio of $CO_2^{+\bullet}$ (A) to (B) formed in the charge transfer - excitation was ~ 1.2 : 1.

In-cell observations - target gas emissions

Emissions were also observed from all of the target gases except helium; $CO_2^{+\bullet}$ - N_2 collisions yielded predominantly $N_2^{+\bullet}$ (B $\rightarrow$ X) and N_2 (C $\rightarrow$ B) emissions, Fig. 4.3.11b (see Table 4.3.1). Very little remains of the $CO_2^{+\bullet}$ peaks except for the B $\rightarrow$ X band at 289 nm and the fragment peak at 192 nm. This result is similar to that observed for the $O_2^{+\bullet}$ - N_2 experiment, where no emissions from the ion beam could be elucidated,

Fig. 4.3.7b. When O_2 was the target, Fig. 4.3.11c, a weak spectrum was obtained, but one in which both $CO_2^{+\bullet}$ progressions and the $O_2^{+\bullet}$ ($A \rightarrow X$) broad band emissions are present. Naturally, it is impossible to distinguish projectile - target emissions in Fig. 4.3.11d save for the projectile fragment bands at 192 nm and 247 nm.

Post-collision observations

The monochromated spectrum of $CO_2^{+\bullet}$ - He collisions performed in PC is shown in Fig. 4.3.13. It is virtually identical to the spectrum of the same system obtained from in-OC collisions, Fig. 4.3.11a. Absent are the C and $CO^{+\bullet}$ bands due to the short lifetime of the former and weakness of the latter.

Trends in emission were sought from the filter experiments with the 18 target gases listed in Table 3.4.1 in the same manner as discussed for $N_2^{+\bullet}$ and $O_2^{+\bullet}$. A plot of the total spectral emission vs target IE, Fig. 4.3.14, shows the same trend as found for $N_2^{+\bullet}$ projectiles.

A plot of total emission vs fragment ion abundance, Fig. 4.3.15, is nearly linear, again similar to that observed for $N_2^{+\bullet}$. Plots of each spectral region vs the relative abundance of each fragment ion, C^+, O^+ and $CO^{+\bullet}$, were identical for each. This indicates that no particular fragment species is predominantly responsible for the emission in any given spectral region. Since fragment emissions are so minor in these post-collision observation experiments, it can be concluded that fragmentation occurs as a result of electronic excitation, presumably to states higher than C $^2\Sigma_g^+$.

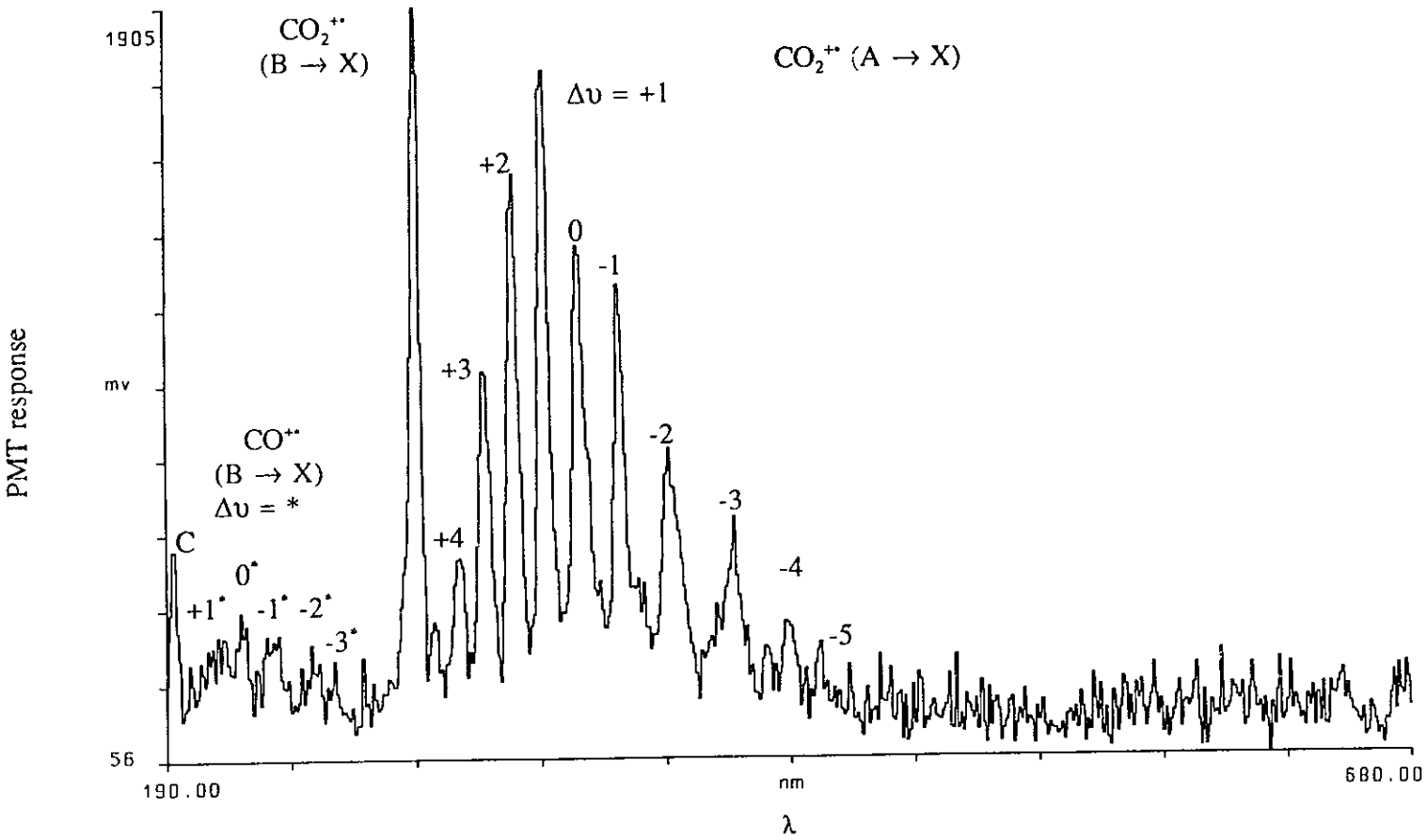

Fig. 4.3.11 a. $CO_2^{+\bullet}$ - He (in-OC) collision induced emission spectrum. 1.0 mm slits, 1 nm step size, 4 scan average.

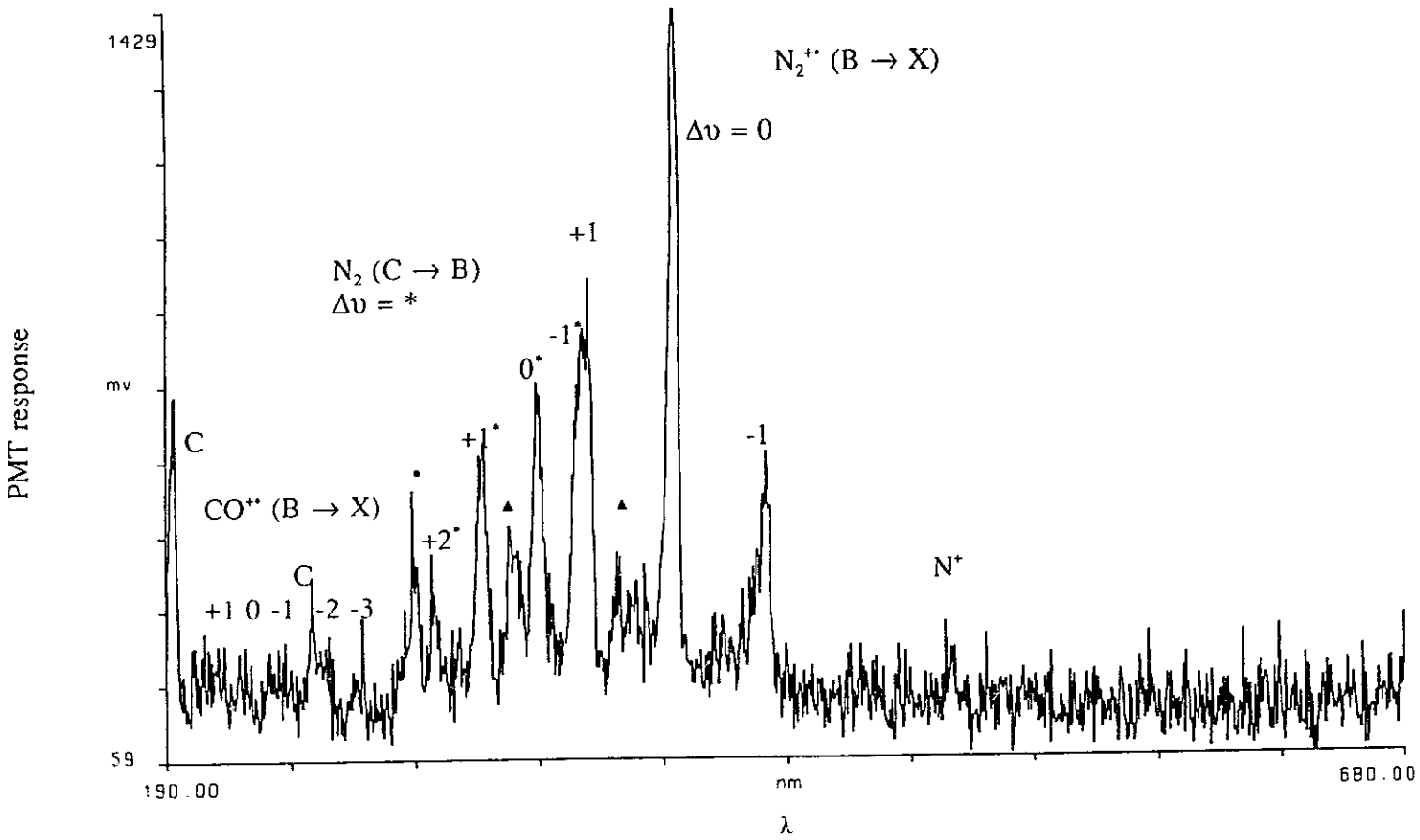

Fig. 4.3.11 b. $CO_2^{+\bullet}$ - N_2 (in-OC) collision induced emission spectrum. 1.0 mm slits, 0.5 nm step size, 4 scan average.

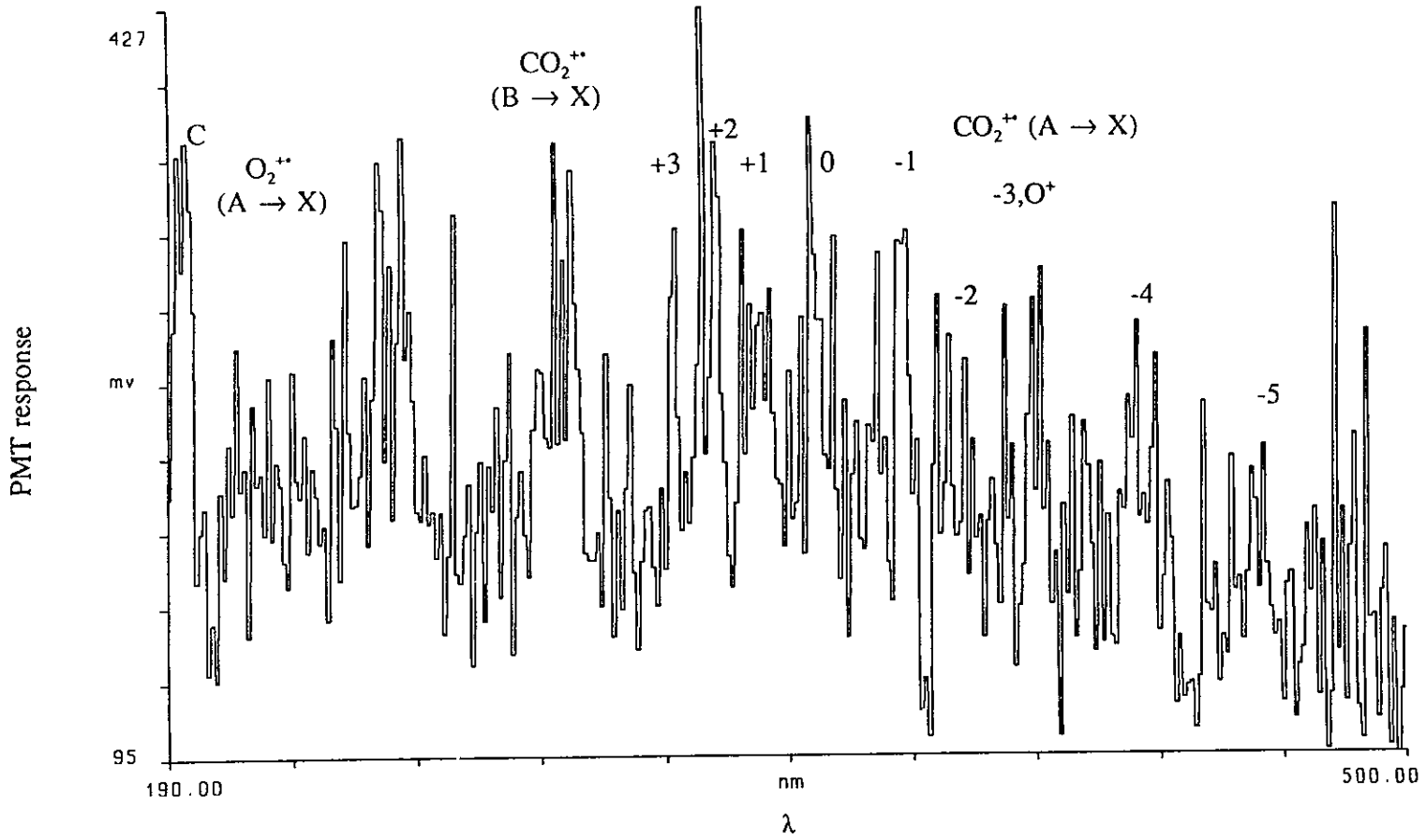

Fig. 4.3.11 c. $CO_2^{+\bullet}$ - O_2 (in-OC) collision induced emission spectrum. 2.0 mm slits, 1 nm step size, 3 scan average.

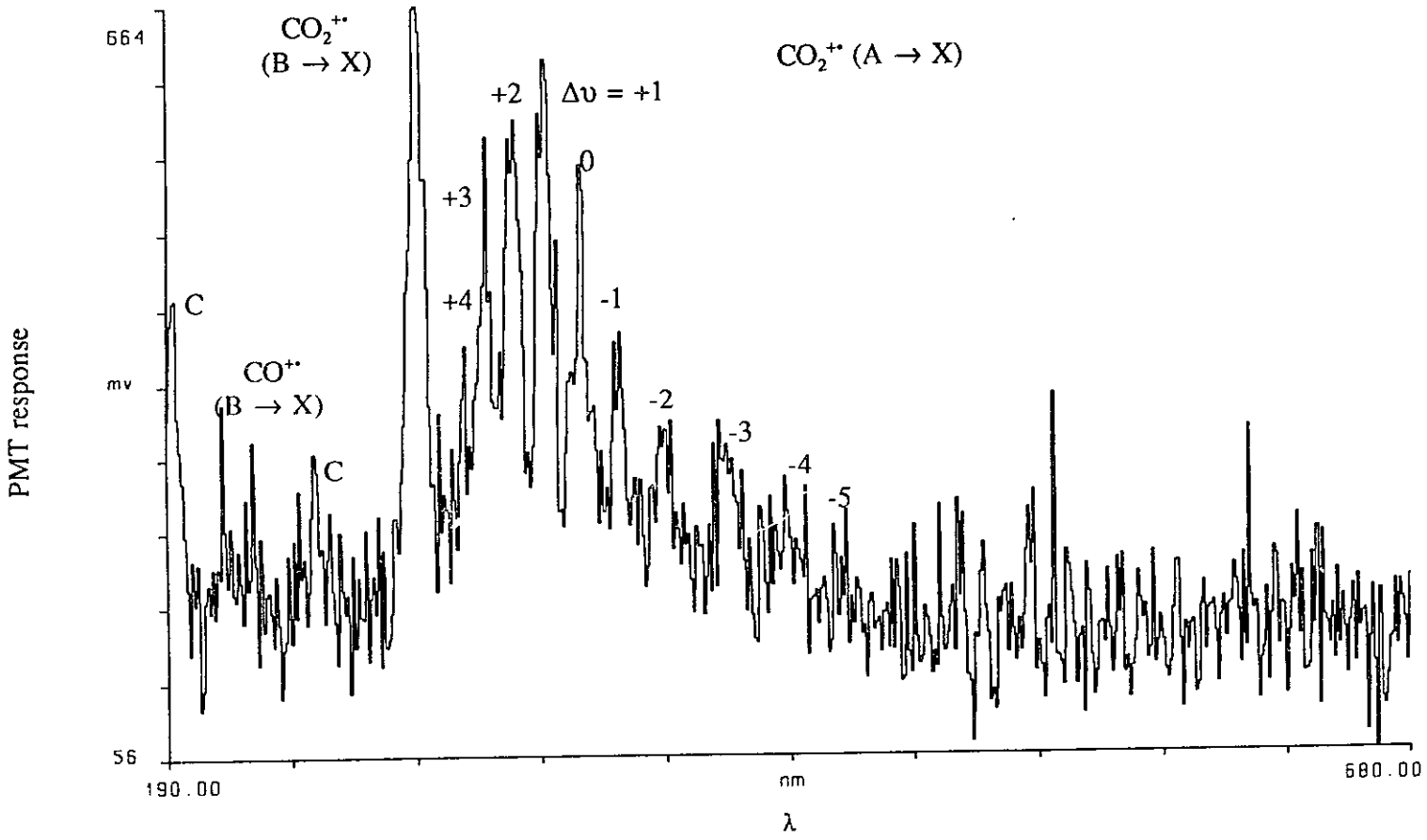

Fig. 4.3.11 d. $CO_2^{+\bullet}$ -CO_2 (in-OC) collision induced emission spectrum. 2.0 mm slits, 1 nm step size, 4 scan average.

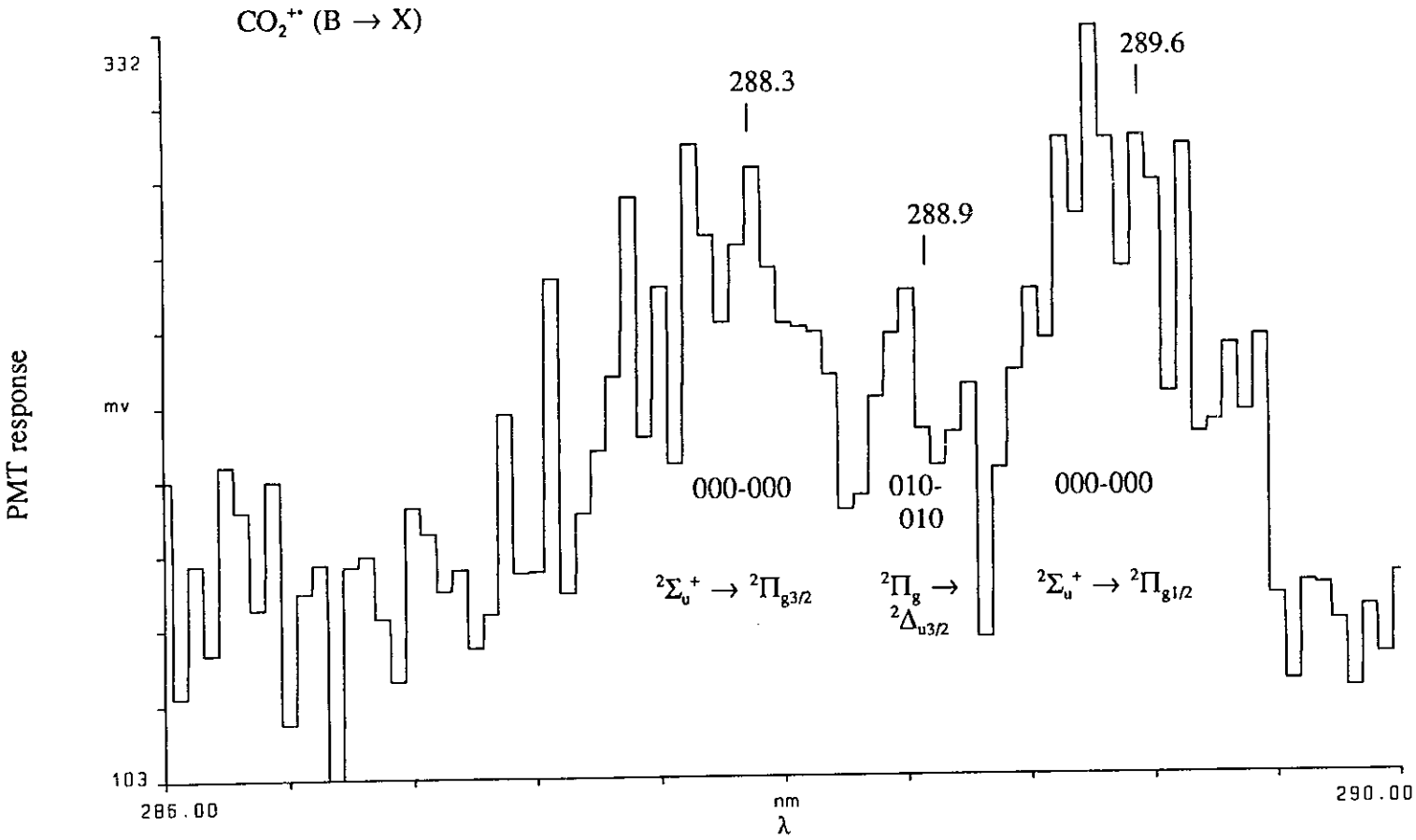

Fig. 4.3.12. High resolution spectrum of the CO_2^{+*} (B → X) transition from CO_2^{+*} - He (in-OC) collisions. 0.15 mm slits, 0.05 nm step size, 9 scan average.

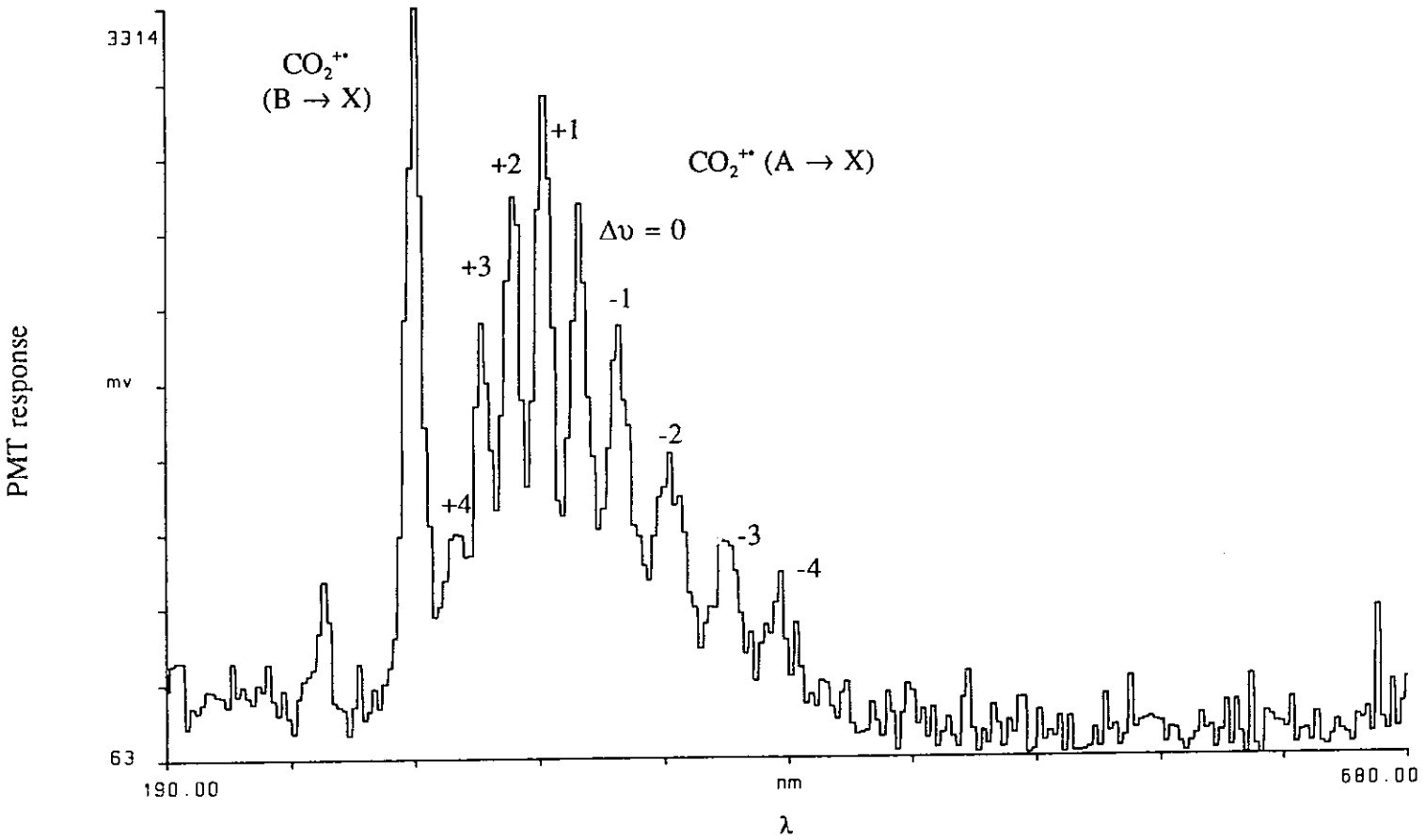

Fig. 4.3.13. $CO_2^{+\bullet}$ - He (in-PC) collision induced emission spectrum. 2.0 mm slits, 2 nm step size, 1 scan.

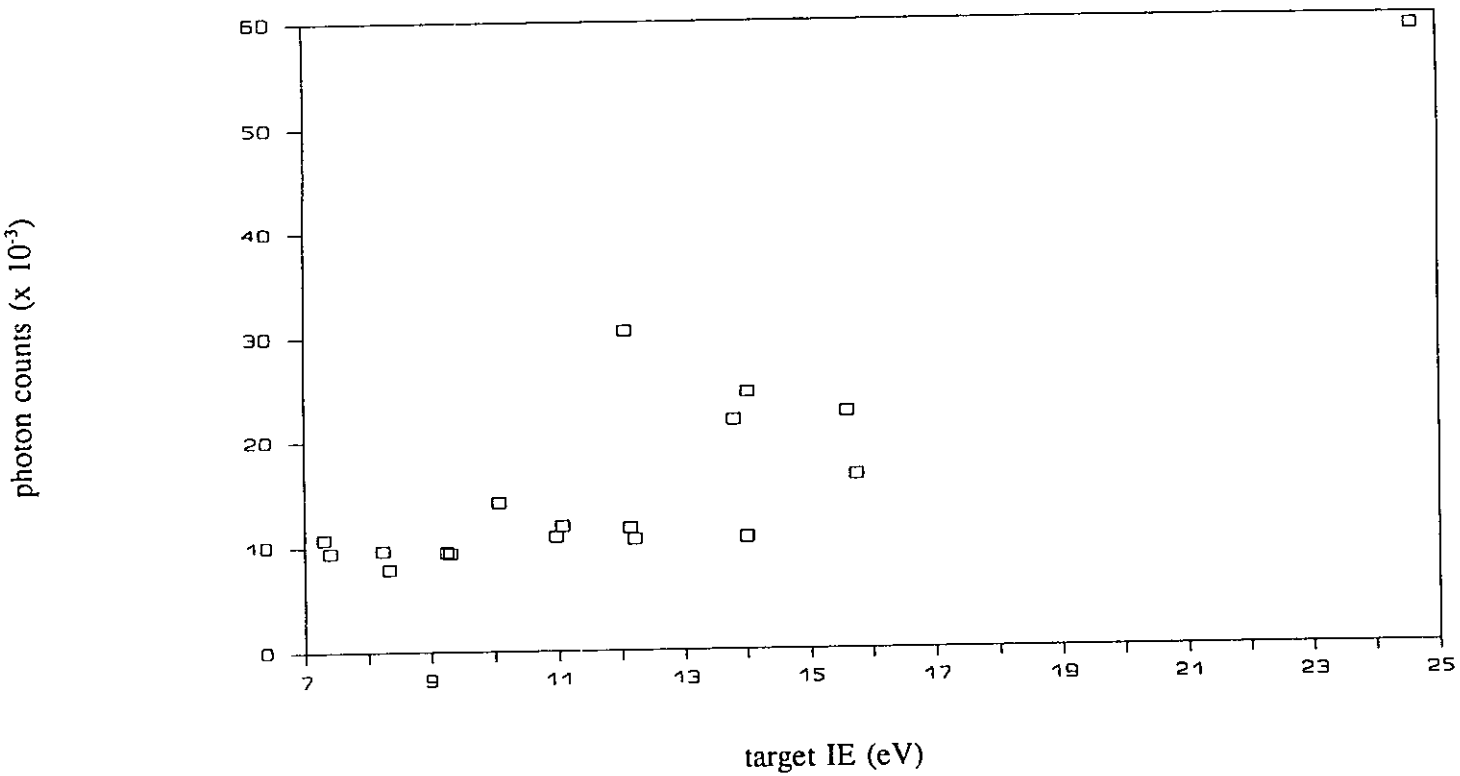

Fig. 4.3.14. Plot of total photon counts over the spectral range 180-680 nm vs target gas ionization energy for $CO_2^{+\bullet}$ projectiles (see discussion of post-collision observations). Counts normalized to a common $CO_2^{+\bullet}$ flux.

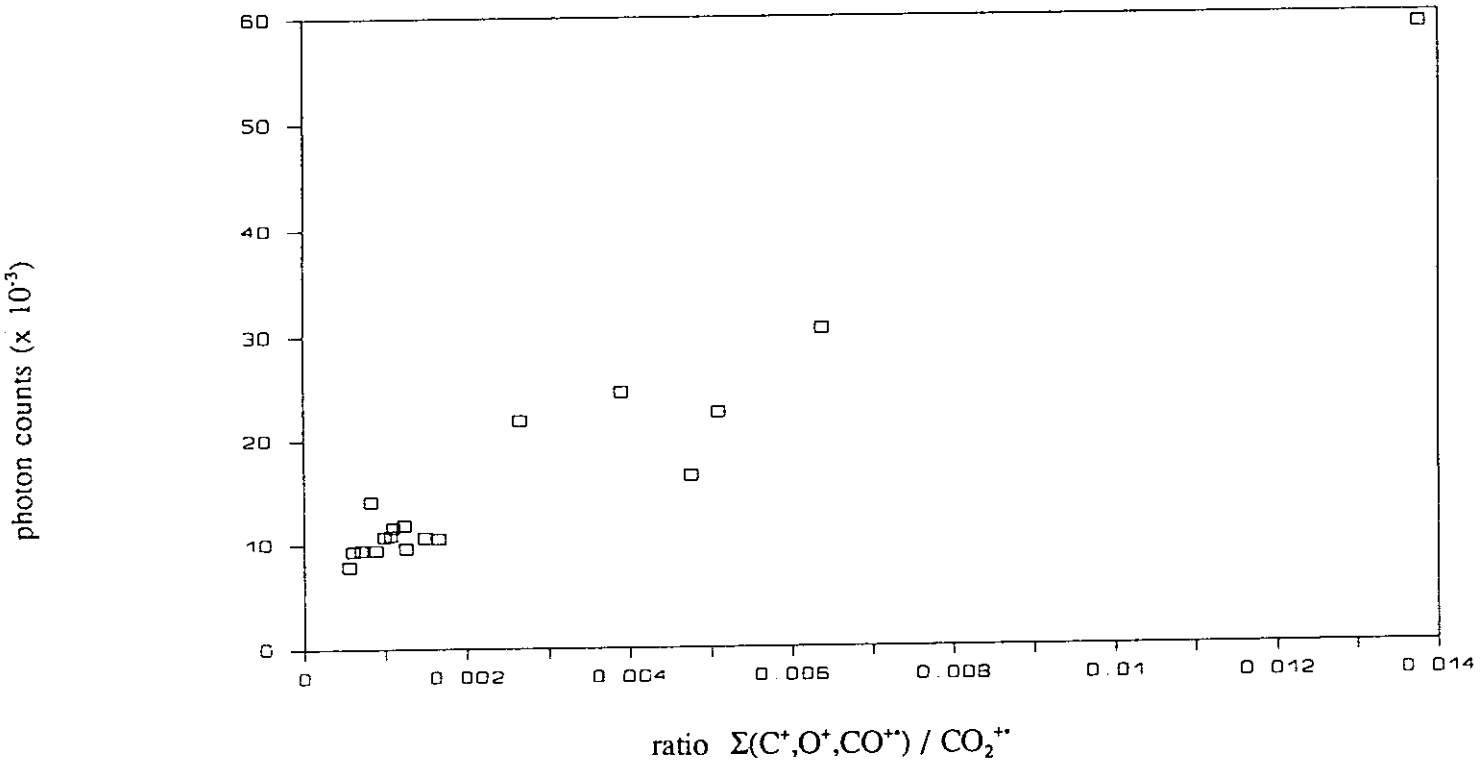

Fig. 4.3.15. Plot of total photon counts over the spectral range 180-680 nm vs relative total fragment ion, C^+, O^+ and $CO^{+\bullet}$, abundance in the CID spectrum of $CO_2^{+\bullet}$ with the 18 target gases listed in Table 3.4.1. Counts normalized to a common $CO_2^{+\bullet}$ flux.

4.3.5 Information from the $N_2^{+\bullet}$, $O_2^{+\bullet}$ and $CO_2^{+\bullet}$ emission spectra

The above collision induced emission spectra provided insight into the excitiation processes occuring in the collision cell and the origin of the fragment ion peaks in the CID mass spectra of $N_2^{+\bullet}$, $O_2^{+\bullet}$ and $CO_2^{+\bullet}$.

$N_2^{+\bullet}$

a) Energy deposition - The CIE spectra provide quantitative values for the internal energy deposition in 8 keV $N_2^{+\bullet}$ - target gas collisions. The He CIE spectrum exhibits primarily the $N_2^{+\bullet}$ ($B \rightarrow X$) transition. The $\upsilon' = 0$ level of the B state lies 3.17 eV above the $\upsilon'' = 0$ level of the ground state and emissions are observed from levels as high as $\upsilon' = 4$ (which lies 3.76 eV above the ground state). Target gas emissions can also be indicative of internal energy deposition since the conversion of translational kinetic energy to internal energy will be identical for both projectile and target. The target emissions in Fig. 4.3.1 range from nearly undetectable He lines to ionized target molecules, Table 4.3.1. When O_2 was the target, emissions were observed from $O_2^{+\bullet}$ molecules and O^+ and O fragments. The O^+ fragment emissions observed were from states up to 28.7 eV above ground state O^+. The energy deposition in O_2 required to form these states was 47.5 eV, a considerable amount of energy. If the O^+ fragments were formed after a charge transfer between $N_2^{+\bullet}$ and O_2, the charge transfer would have been endothermic by 20 eV. The formation of $O_2^{+\bullet}$ in its A state requires a charge transfer to produce N_2. The process between ground state $N_2^{+\bullet}$ and O_2 is exothermic by 3 eV. In Fig. 4.3.1c emissions are

present from both $O_2^{+\bullet}$ (A) and N_2 (C) species. The states of $O_2^{+\bullet}$ (A) responsible for the broad-band emission in Fig. 4.3.1c are up to 6.4 eV above ground state $O_2^{+\bullet}$. The N_2 (C, $\upsilon = 0$) state is 11.5 eV above ground state N_2 and 3.5 eV below the ionization energy. Neutralization of $N_2^{+\bullet}$ to N_2 (C) is actually endothermic by 8.5 eV, energy which must come from the translational kinetic energy of the projectile. Even if neutralization forms N_2 in the ground state, charge transfer resulting in $O_2^{+\bullet}$ (A) would still be endothermic by 3.4 eV. So, along with the obvious exothermic charge transfer between 8 keV $N_2^{+\bullet}$ and O_2 target gas, there are strongly endothermic contributions. When CO_2 was the target, primarily target $CO_2^{+\bullet}$ emissions were observed. The B state of $CO_2^{+\bullet}$ lies 18 eV above ground state neutral CO_2. The charge transfer with $N_2^{+\bullet}$ is only exothermic by 1 eV if ground state species are involved. As was the case with O_2, a strongly endothermic charge transfer accompanies the exothermic process in these collisions.

b) Vibrational excitation - The $N_2^{+\bullet}$ ($B \rightarrow X$) transition for in-OC collisions involving He and N_2 exhibit similar patterns in the relative intensities of the $\Delta\upsilon = +2, +1, 0, -1$ and -2 bands. When the target was changed to O_2 and CO_2, the $\Delta\upsilon = +1$ bands became relatively more intense. In addition, the $\Delta\upsilon = -3$ band was evident only when O_2 was the target. An increase in the $\Delta\upsilon = +1$ band must be due to an increased population of the $\upsilon' = 3$ level of the $N_2^{+\bullet}$ (B) state when those two targets were used. Furthermore, this increase in the $\Delta\upsilon = +1$ band was also evident in the post-collision emission spectra for all targets. An explanation may be that the transit time between the PC and the OC (~ 0.08 μs) allows vibrations in $N_2^{+\bullet}$ to occur which permit the vertical transitions originating in the $\upsilon' = 1$, 2 and 3 levels to terminate in the $\upsilon'' = 0$, 1 and 2 levels of the ground state.

c) Peak shape in the CID mass spectrum - The N^+ fragment ion from $N_2^{+\bullet}$ projectiles exhibit an interesting peak profile in the high resolution CID mass spectrum, Fig. 4.3.16a. Two distinct components are evident indicating that the fragment was formed from two different processes from the molecular ion. Since there is only one fragmentation which gives N^+, the breaking of the N≡N bond, the composite peak must be due to the dissociation of precursor ions with different internal energy content. The CIE spectra for $N_2^{+\bullet}$ show that the $N_2^{+\bullet}$ (B) state can be formed. The two components evident in Fig. 4.3.16a may be due to the dissociation of the $N_2^{+\bullet}$ X and B states.

$O_2^{+\bullet}$

a) Energy deposition - It was evident that the collisions responsible for forming the excited state products in $O_2^{+\bullet}$ - He experiments were quite severe. The He states and O^+ and O fragments produced were high in energy, requiring upwards of 23 eV and 35 eV respectively of energy deposition in ground state He and $O_2^{+\bullet}$. When other targets were used, emissions were observed from lower energy processes along with the high energy states of O^+ and O. The charge transfer reactions producing ionized target species from ground state projectiles and targets were endothermic in each case (except when O_2 was the target in which case the charge transfer was thermoneutral). The formation of excited state target ions implies an even greater endothermicity for at least some of the charge transfer processes occuring in the collision cell.

c) Peak shape in the CID mass spectrum - The fragment ion O^+ produces a peak in the CID spectrum exhibiting a profile indicative of the dissociation of the molecular ion from

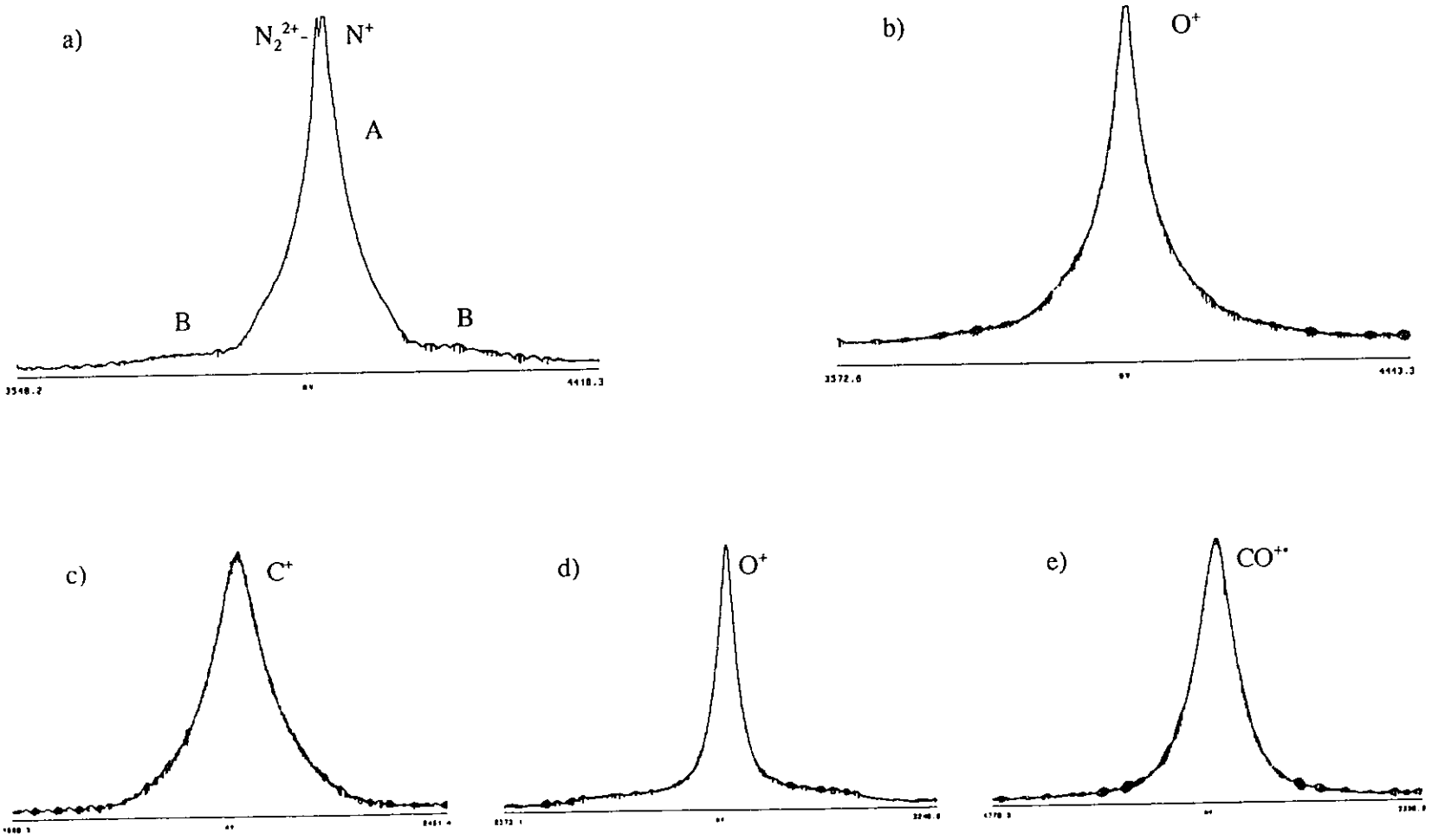

Fig. 4.3.16. Fragment ion peaks in helium CID mass spectra a) N^+ from $N_2^{+\bullet}$, b) O^+ from $O_2^{+\bullet}$, c) C^+, d) O^+ and e) $CO^{+\bullet}$ from $CO_2^{+\bullet}$. 60% ion beam transmission. C2.

a wide distribution of internal states (sec. 3.3.3), Fig. 4.3.16b. This is consistent with what is observed in the CIE spectra. A vertical excitation produces vibrationally excited $O_2^{+\bullet}$ ions. The magnitude of the possible energy deposition discussed above means that a variety of excited states can be populated. Dissociation of these states would yield the kind of peak shape shown in Fig. 4.3.16b.

$CO_2^{+\bullet}$

a) Energy deposition - Like the studies with $N_2^{+\bullet}$, most of the features observed with $CO_2^{+\bullet}$ projectiles were due to emissions from excited molecular ions. The B $\rightarrow$ X and A $\rightarrow$ X bands in the spectra represent excitation in the $CO_2^{+\bullet}$ projectile of up to 4.3 eV. Observation of the $CO^{+\bullet}$ (B $\rightarrow$ X) bands in Fig. 4.3.11a means that at least 11.2 eV can be deposited into the $CO_2^{+\bullet}$ projectiles in collisions with He. These bands decrease in prominence when the other targets are used suggesting that fewer collisions involve the conversion of this amount of energy. Carbon atoms are also formed in the 3s $^1P^0$ state which lies 8.5 eV above the ground state. Dissociation of $CO_2^{+\bullet}$ into C (3s $^1P^0$) and $O_2^{+\bullet}$ would require almost 18 eV to be converted from translational to internal energy. Target gas emissions similar to those observed for $N_2^{+\bullet}$ projectiles were also observed. Again, when N_2 was the target the dominant emitting species were N_2 and $N_2^{+\bullet}$ which was formed in the charge transfer reaction with the $CO_2^{+\bullet}$ ions. The charge transfer between ground state species is endothermic and the production of excited $N_2^{+\bullet}$ means it is even more endothermic (1 eV compared to 4.2 eV)

b) Vibrational excitation - The vibrational sequences of the A $\rightarrow$ X transition of $CO_2^{+\bullet}$

present in Figs 4.3.11a-d indicate the population of at least the $\upsilon' = 4$ level of the A state. The relative intensities of the bands was independent of target gas and time of observation (compare Figs 4.3.11a,d and 4.3.13).

c) Peak shapes in the CID mass spectrum - The three fragment ion peaks in the CID spectrum of $CO_2^{+\bullet}$ ions are shown in Figs 4.3.16c-e. The peaks due to C^+ and $CO^{+\bullet}$ are nearly Gaussian in shape while the O^+ peak is obviously composite. The dissociation of $CO_2^{+\bullet}$ can take place from the ground state or any of the excited states A, B or C. The A and B states are formed in the collision and emissions from them observed in the CIE spectra. The C state pre-dissociates into $O^+ + CO$ (see sec. 4.3.4) so emissions from this state will not be seen in the CIE spectra. The dissociation of any of these three states may be responsible for the composite peak shape in Fig. 4.3.16d.

4.3.6 Emissions from isomeric $C_2,H_4,O^{+\bullet}$ ion - target gas collisions

Collision - induced emission spectra obtained for the three $C_2,H_4,O^{+\bullet}$ isomers oxirane$^{+\bullet}$ ($CH_2CH_2O^{+\bullet}$), acetaldehyde$^{+\bullet}$ ($CH_3CHO^{+\bullet}$) and vinyl alcohol$^{+\bullet}$ (CH_2=$CHOH^{+\bullet}$) (from EI of cyclobutanol, see sec. 4.2.2) were obtained using He and Ar target gases in the OC. The sensitivity of the experiment did not allow high resolution spectra to be obtained for all three isomers. In order to narrow down the many possible emitting species, smaller fragment ions were independently studied. It is helpful to start with these smaller projectile ions and so build toward the analysis of the polyatomic $C_2,H_4,O^{+\bullet}$ ions.

$CO^{+\bullet}$ - He, Ar CIE spectra

The CIE spectrum of 8 keV $CO^{+\bullet}$ projectile - He target gas collisions in OC is shown in Fig. 4.3.17a. Clearly defined are emissions due to excited $CO^{+\bullet}$ molecular ions ($B\ ^2\Sigma \rightarrow X\ ^2\Sigma$ and possibly $A\ ^2\Pi \rightarrow X\ ^2\Sigma$ [107]) as well as the excited state fragments C ($3s\ ^1P^0 \rightarrow 1p\ ^1D$) and O^+ ($4p\ ^2D^0 \rightarrow 2p^4\ ^2P$) [33]. Target gas He lines at 317.8 nm, 388.8 nm and 447.1 nm are also present [33]. When Ar was used as the target, Fig. 4.3.17b, a host of O^+ lines as well as Ar^+ emissions (from the $4p\ ^2F$ (355 nm band) and $4p'\ ^2P^0$ (453 nm band)) [108] were identified. With this information, any future Ar, He, $CO^{+\bullet}$, C or O^+ emissions can be identified.

HCO^+ - He, Ar CIE spectra

The $CO^{+\bullet}$ system was extended by a hydrogen atom by studying HCO^+ ions formed from oxirane. The ions were also formed from methanol and acetaldehyde and the resulting CIE spectra were identical. The He CIE spectrum is shown in Fig. 4.3.18a. Along with the $CO^{+\bullet}$ ($B \rightarrow X$), C, He and O^+ emissions observed above, a set of bands corresponding to the HC ($A\ ^2\Delta \rightarrow X\ ^2\Pi$ and $B\ ^2\Sigma \rightarrow X\ ^2\Pi$) and HC^+ ($B\ ^1\Delta \rightarrow A\ ^1\Pi$ and $A\ ^1\Pi \rightarrow X\ ^1\Sigma$) emissions and the hydrogen Balmer β line ($n=4 \rightarrow n=2$) were also observed. This is in agreement with a previous study of the HCO^+ - target gas collision induced emission spectrum [109]. When the HCO^+ - He collisions were performed in the PC and emissions observed in the OC (post-collision observations), only the emissions from the diatomic species remained to any great extent, Fig. 4.3.18b,c. The time required to traverse the distance between the PC and the OC helps to separate atomic emissions which have very short lifetimes. With Ar as the target in the OC, Fig. 4.3.18d, the He

lines vanish and are replaced by Ar^+ lines which overlap the HC^+ ($B \rightarrow A$) transition.

CH_3^+ - He CIE spectrum

Methyl cation (from EI dissociative ionization of methane) - He target gas collisions produced a CIE spectrum, Fig. 4.3.19, which exhibited the C, He, H'($4 \rightarrow 2$), HC^+ ($B \rightarrow A$) and HC ($A \rightarrow X$) bands. Note the absence of the O^+ band at 284 nm. A previous optical study of high keV H^+ - CH_4 collisions [110] yielded emissions from the HC (A,B and $C \rightarrow X$) transitions as well as HC^+ ($A \rightarrow X$) and ($b\ ^3\Sigma \rightarrow a\ ^3\Pi$) transitions.

CH_3CO^+ - He, Ar CIE spectra

Acetyl ions from EI dissociation of acetone yielded in-OC CIE spectra with He and Ar target gases exhibiting the same bands as discussed above for HCO^+. However, minor peaks could not be identified and so there may well be features present which are unique to acetyl cation projectiles but which we could not assign.

Oxirane$^{+\bullet}$ - He, Ar CIE spectra

The spectrum obtained upon 8 keV oxirane$^{+\bullet}$ - He target gas collisions in the OC is shown in Fig. 4.3.20a. The spectrum was quite weak but the aforementioned C, He, H' (Balmer-β), HC ($A \rightarrow X$) and HC^+ ($B \rightarrow A$) transitions were distinguishable. With Ar as the target, Fig. 4.3.20b, most of the above features were enhanced. There was sufficient signal-to-noise in this experiment to perform the projectile - Ar collisions in the PC, and the resulting emission spectrum is shown in Fig. 4.3.20c. Only the diatomic HC^+ ($B \rightarrow$

A), HC ($A \rightarrow X$) and possibly the HC ($B \rightarrow X$) and HC^+ ($A \rightarrow X$) transitions remained together with a small contribution from C. Higher resolution spectra enabled the positive identification of C and H$^\bullet$ lines at 193 nm and 486 nm.

Acetaldehyde$^{+\bullet}$ - He, Ar CIE spectra

The in-OC He CIE spectrum of 8 keV $CH_3CHO^{+\bullet}$ projectile ions, Fig. 4.3.21a, was similar to that of oxirane$^{+\bullet}$. All the same features were present with the addition of two bands, one at ~283 nm which may be the above mentioned O^+ line (see $CO^{+\bullet}$ and HCO^+) and also a band at ~311 nm. This latter feature may be the HO$^\bullet$ ($A\ ^2\Sigma^+ \rightarrow X\ ^2\Pi$) $\Delta\upsilon$ = 0 band common to emissions from flames etc. [107]. The spectrum may include the $CO^{+\bullet}$ ($B \rightarrow X$) bands between 193-260 nm, but it is uncertain at this level of signal-to-noise.

When Ar was employed as the target, Fig. 4.3.21b, all the above features in the oxirane - He experiment were observed and the two extra bands at 283 nm and 311 nm decreased in relative intensity.

Vinyl alcohol$^{+\bullet}$ - He, Ar CIE spectra

The CIE spectrum from in-OC collisions of 8 keV CH_2=$CHOH^{+\bullet}$ projectile ions with He was slightly but significantly different from the other two isomers, Fig. 4.3.22a. The C, O^+, He and H$^\bullet$ (Balmer-β) atomic emissions were present together with the HC^+ ($B \rightarrow A$), HC ($A \rightarrow X$) and HO$^\bullet$ ($A \rightarrow X$) bands. The contribution due to the O^+ and OH$^\bullet$ bands was much more important than from either oxirane$^{+\bullet}$ or acetaldehyde$^{+\bullet}$.

The Ar CIE spectrum contained no unexpected peaks, Fig. 4.3.22b.

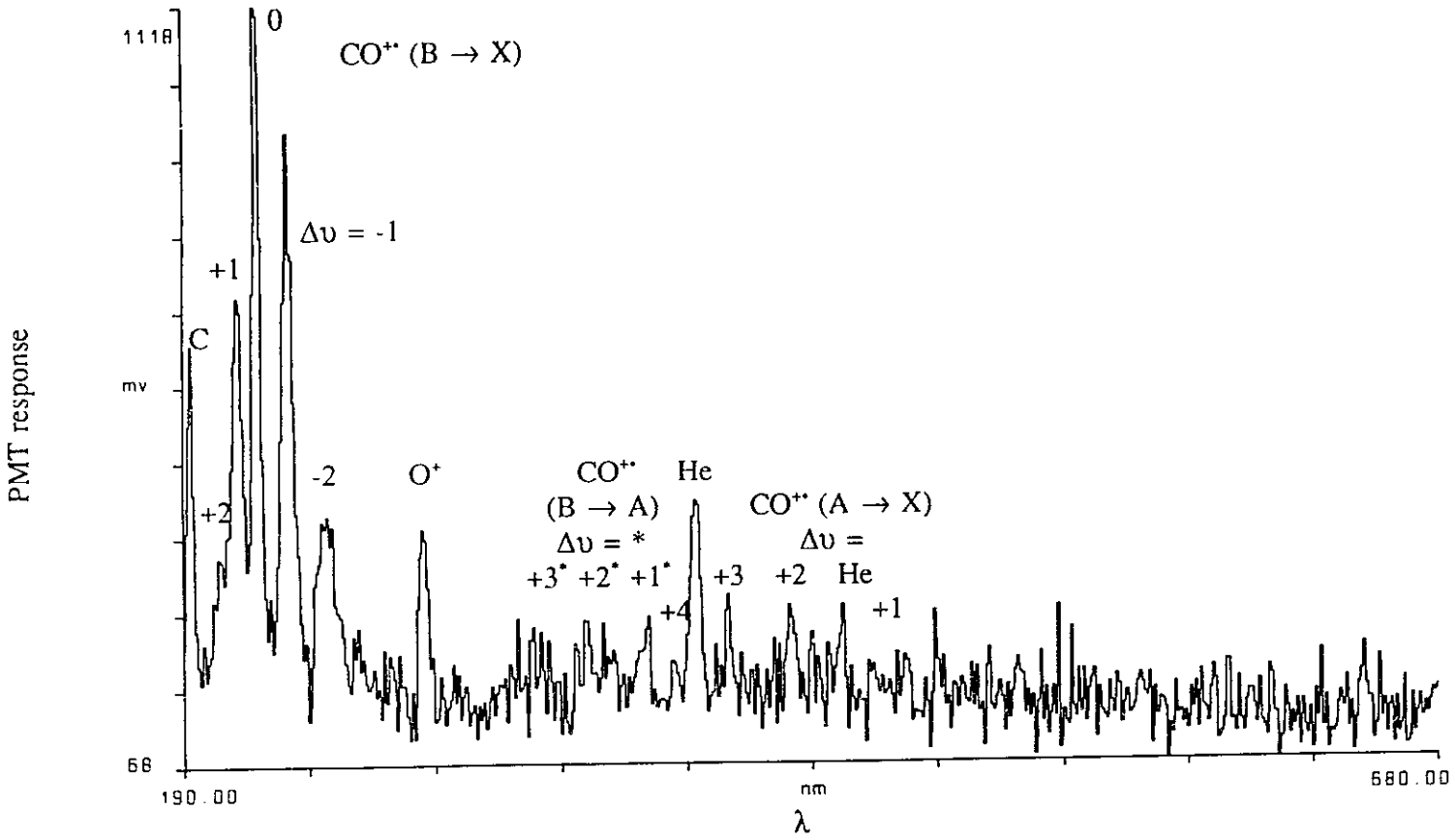

Fig. 4.3.17 a. $CO^{+\bullet}$ - He (in-OC) collision induced emission spectrum. 1.0 mm slits, 1 nm step size, 5 scan average.

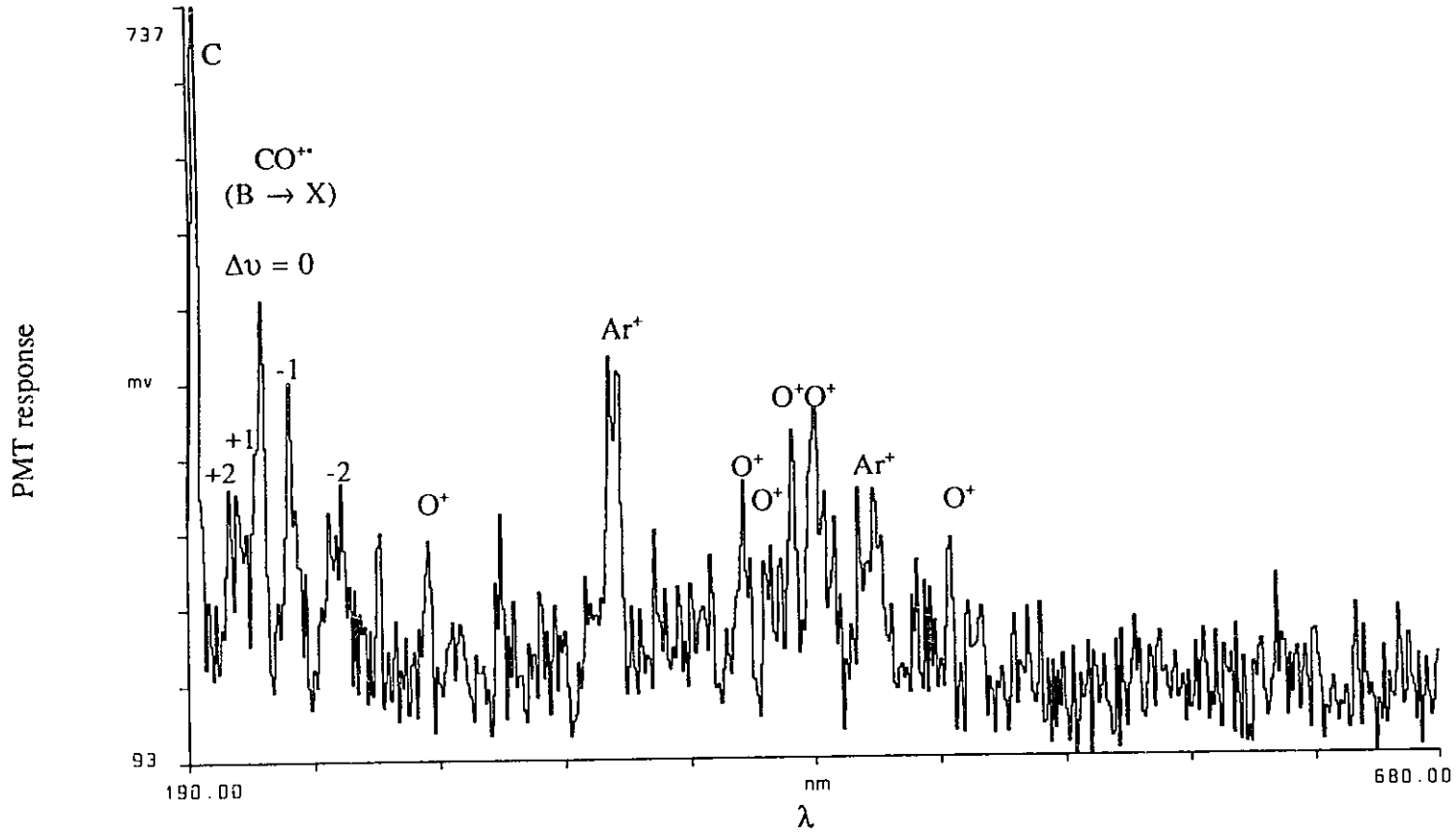

Fig. 4.3.17 b. $CO^{+\bullet}$ - Ar (in-OC) collision induced emission spectrum. 1.0 mm slits, 1 nm step size, 6 scan average.

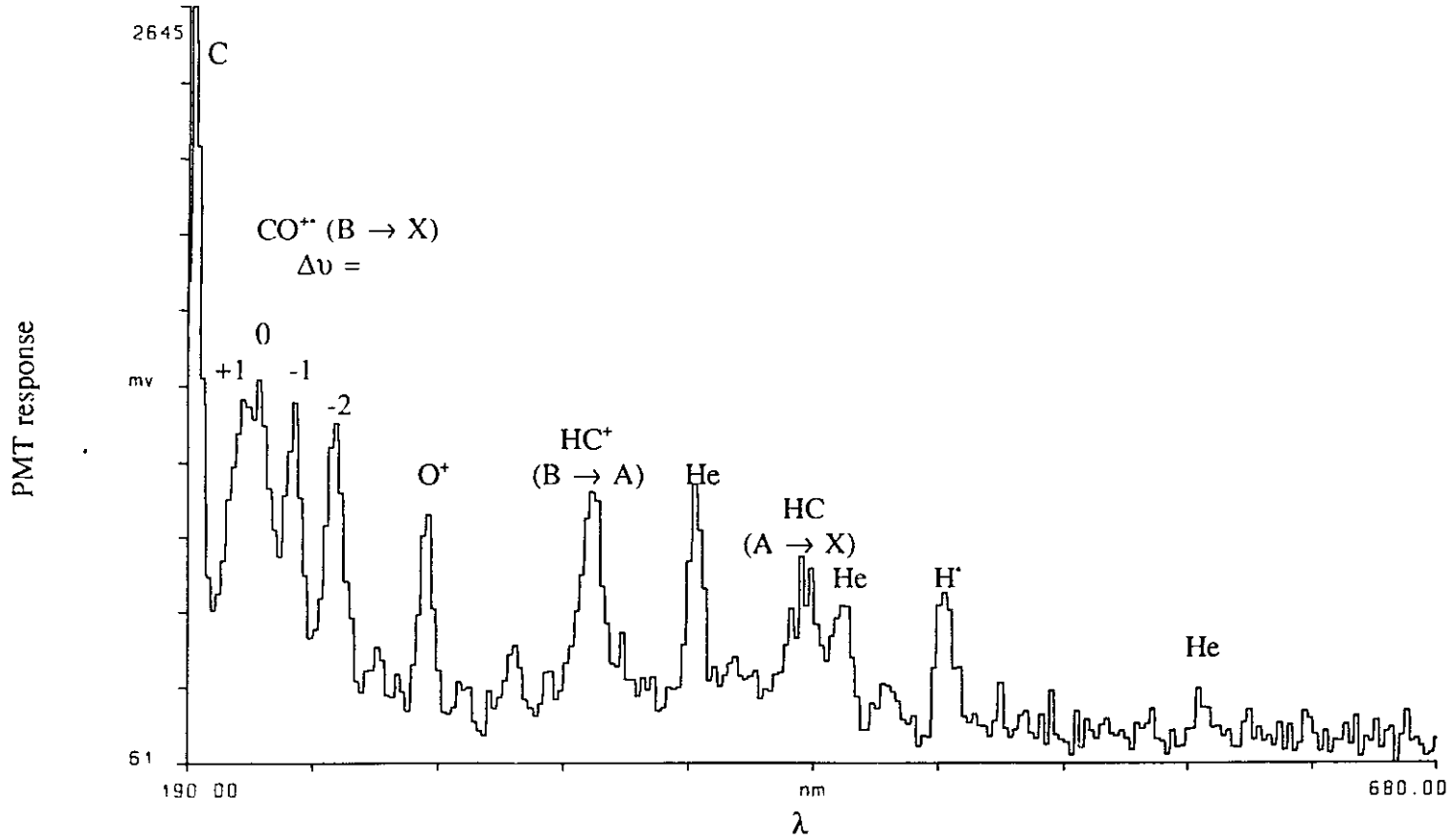

Fig. 4.3.18 a. HCO^+ - He (in-OC) collision induced emission spectrum. 2.0 mm slits, 2 nm step size, 3 scan average.

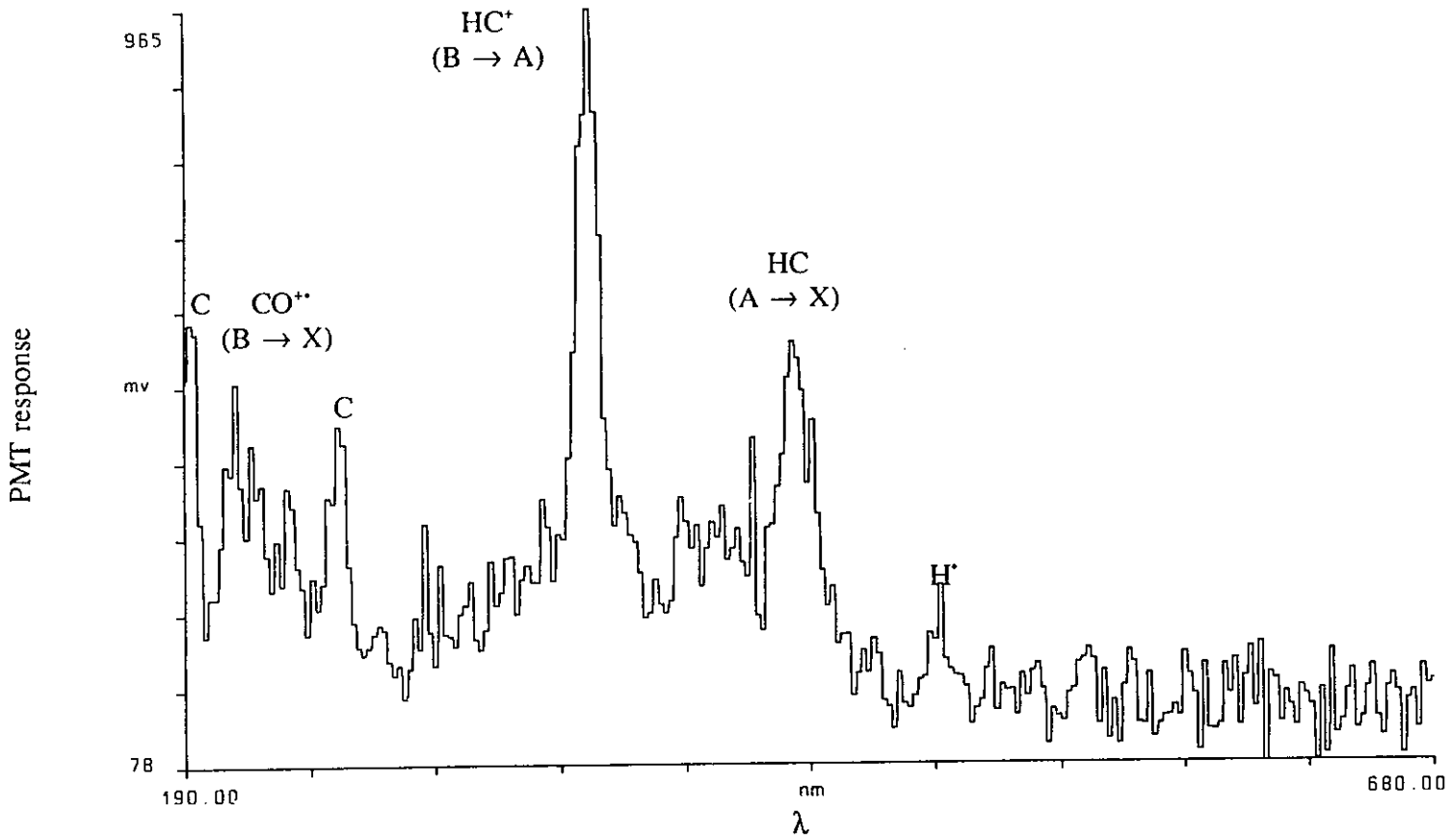

Fig. 4.3.18 b. HCO^+ - He (in-PC) collision induced emission spectrum. 2.0 mm slits, 2 nm step size, 5 scan average.

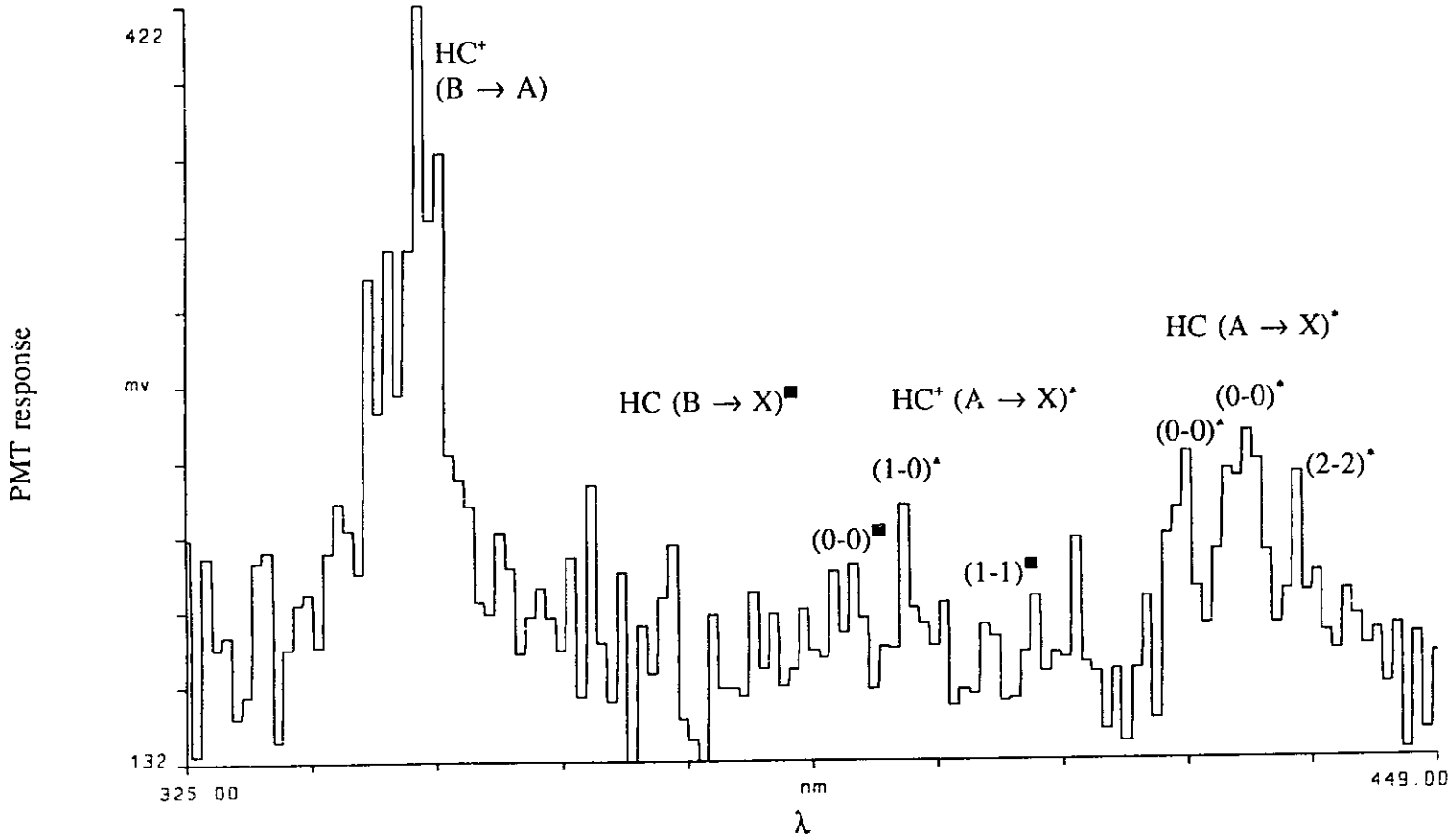

Fig. 4.3.18 c. Higher resolution HCO^+ - He (in-PC) collision induced emission spectrum. 1.0 mm slits, 1 nm step size, 14 scan average.

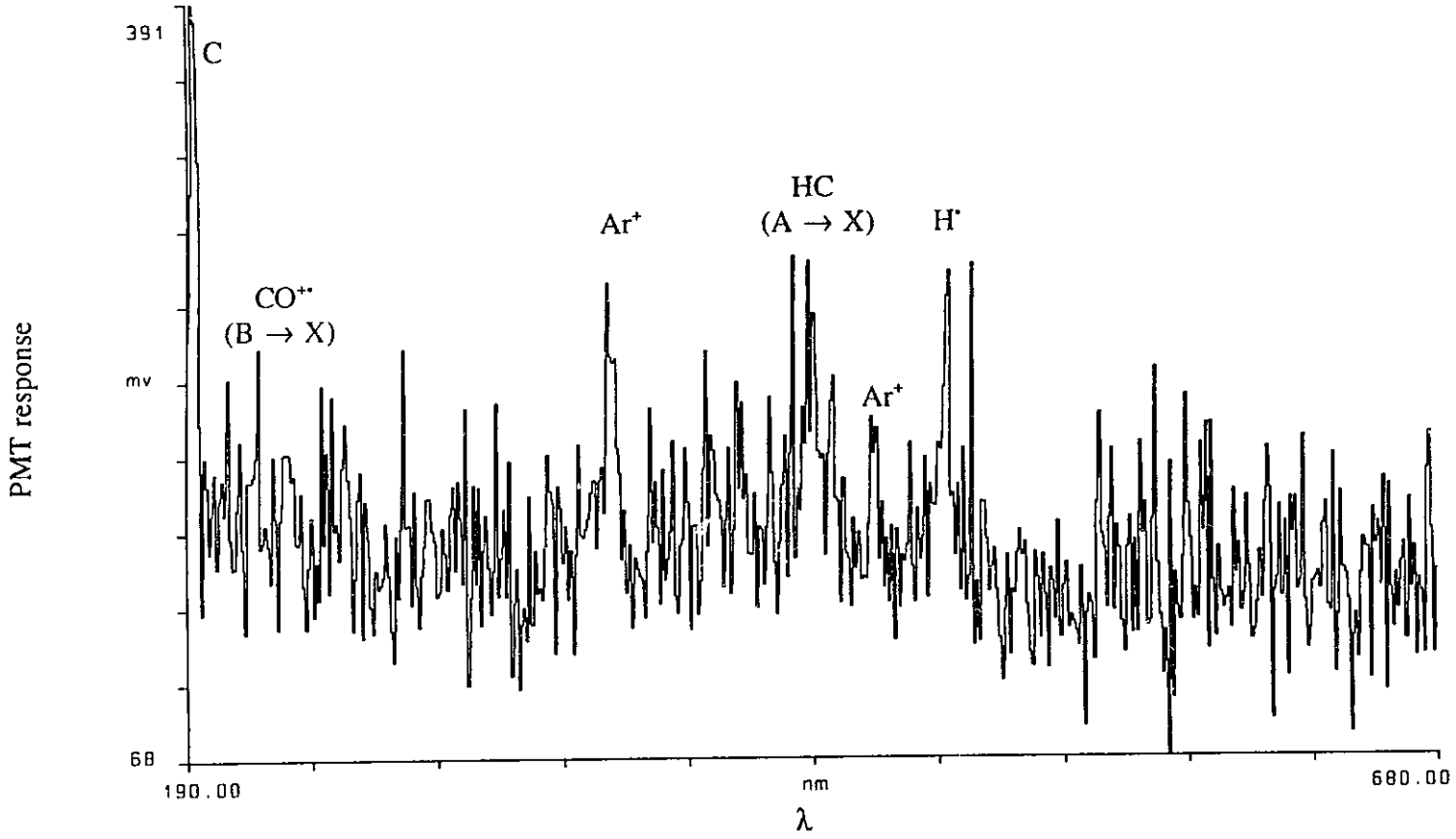

Fig. 4.3.18 d. HCO^+ - Ar (in-OC) collision induced emission spectrum. 1.0 mm slits, 1 nm step size, 8 scan average.

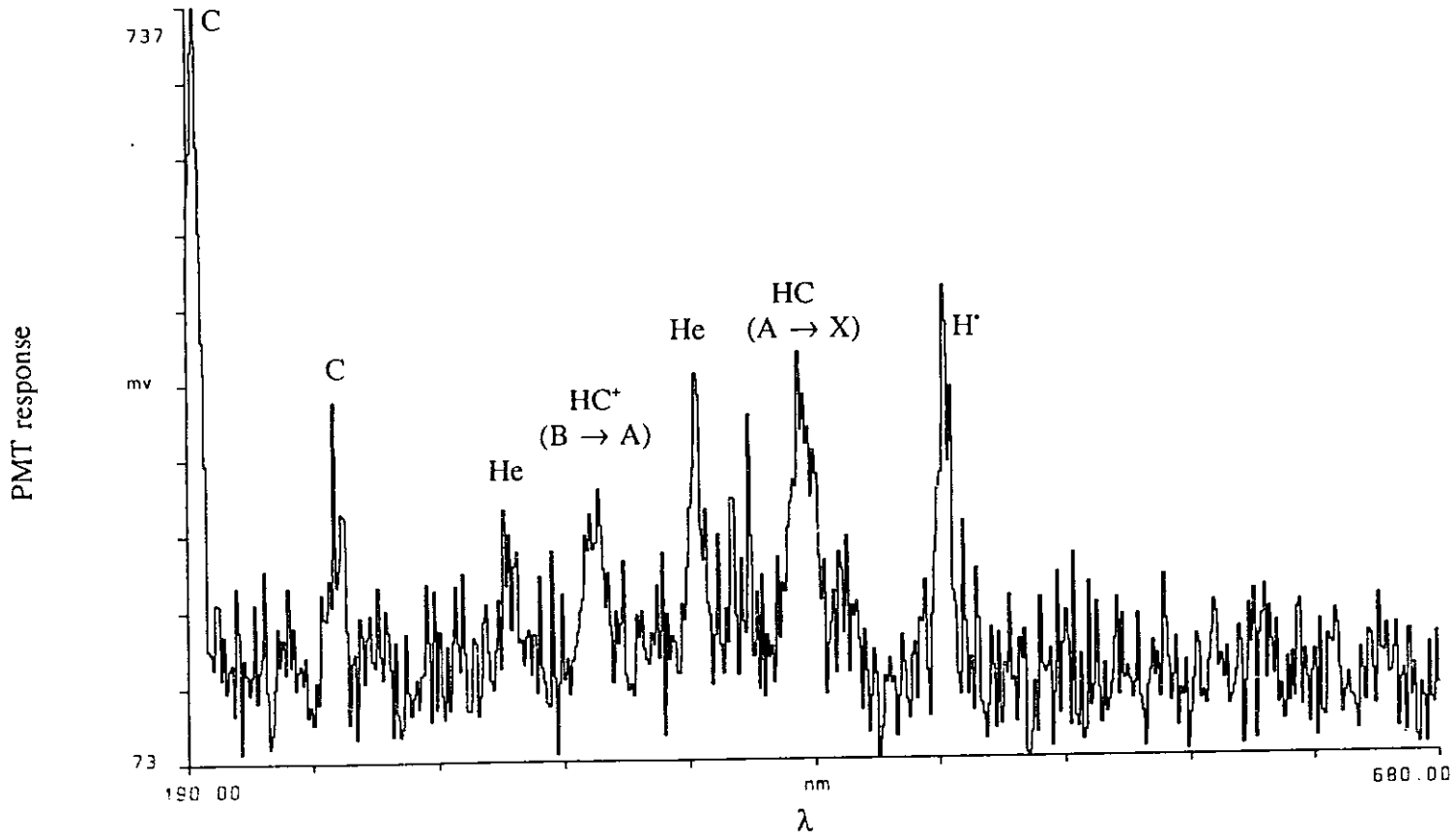

Fig. 4.3.19. CH_3^+ - He (in-OC) collision induced emission spectrum. 2.0 mm slits, 1 nm step size, 4 scan average.

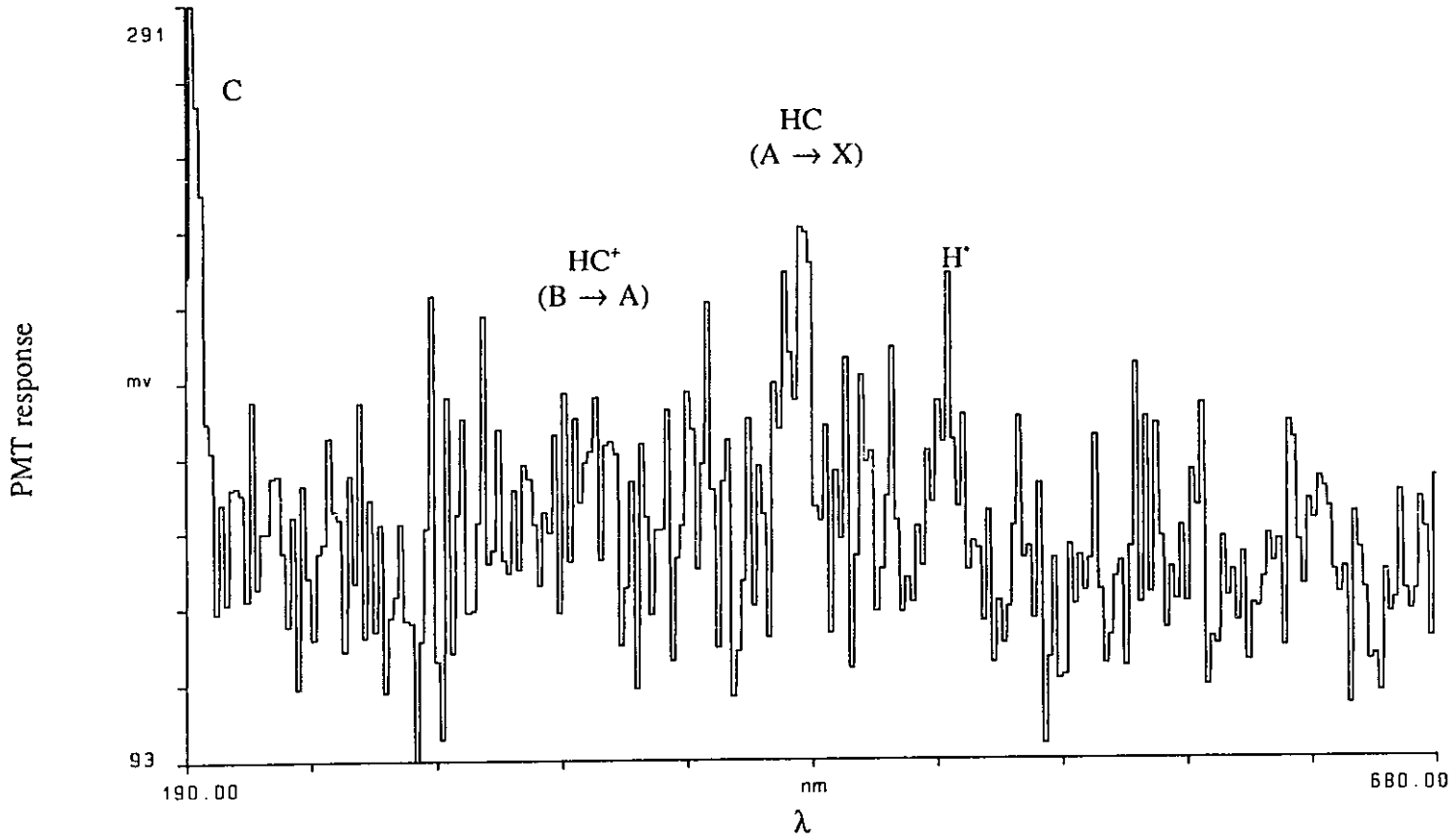

Fig. 4.3.20 a. oxirane$^{+\bullet}$ - He (in-OC) collision induced emission spectrum. 3.0 mm slits, 2 nm step size, 13 scan average.

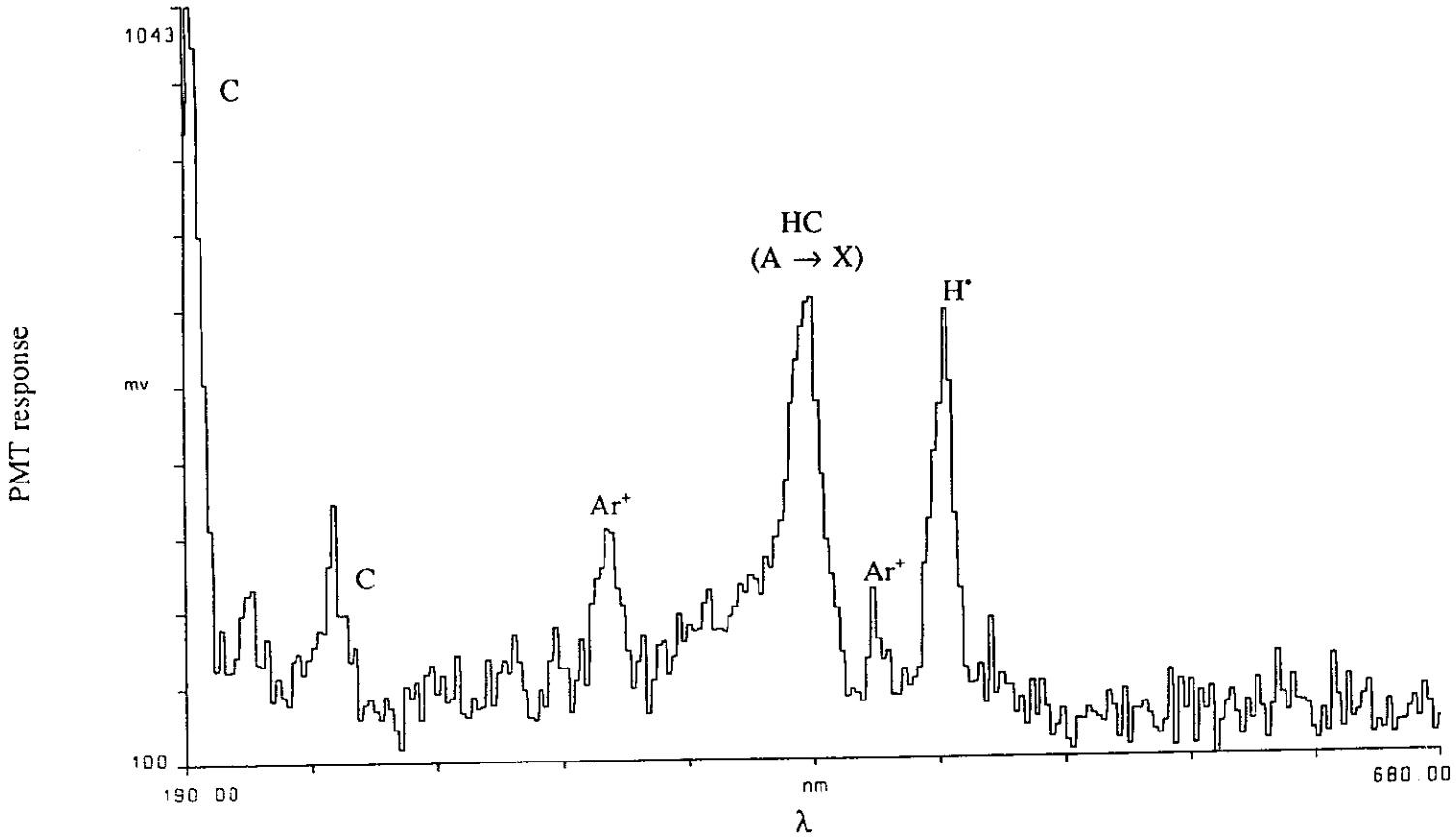

Fig. 4.3.20 b. oxirane** - Ar (in-OC) collision induced emission spectrum. 3.0 mm slits, 2 nm step size, 11 scan average.

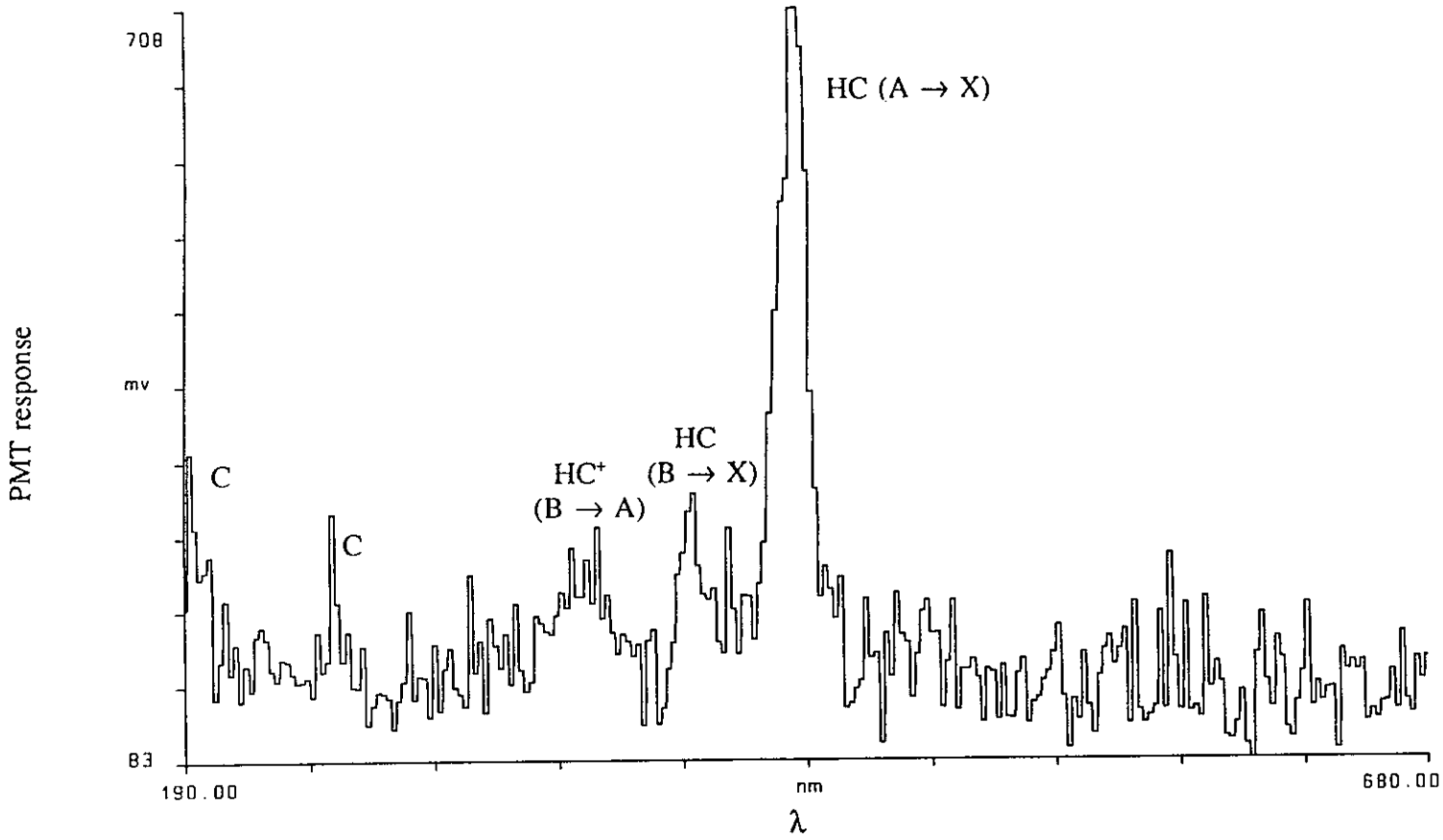

Fig. 4.3.20 c. oxirane$^{+\bullet}$ - Ar (in-PC) collision induced emission spectrum. 3.0 mm slits, 2 nm step size, 7 scan average.

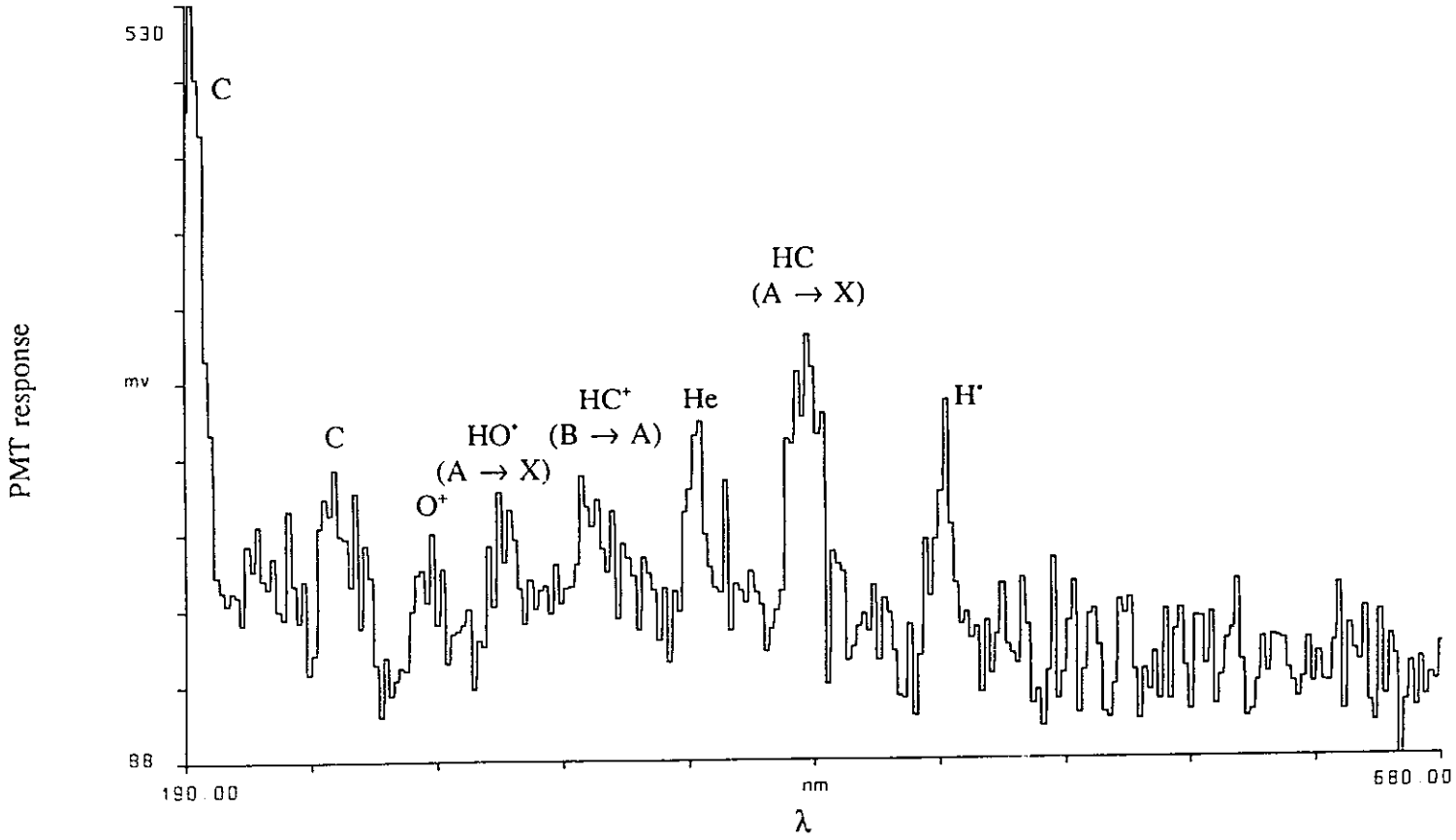

Fig. 4.3.21 a. acetaldehyde$^{+\bullet}$ - He (in-OC) collision induced emission spectrum. 3.0 mm slits, 2 nm step size, 16 scan average.

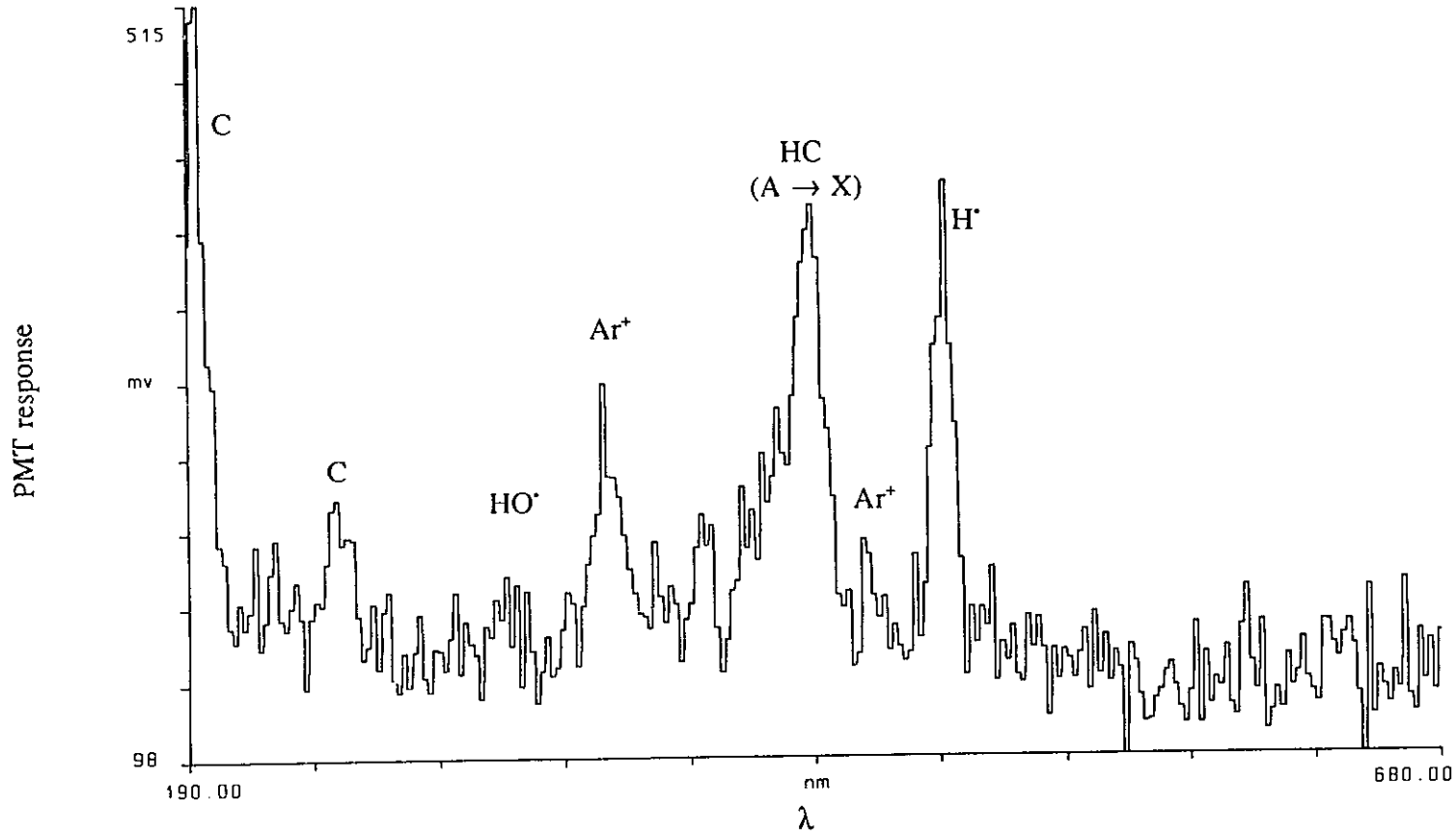

Fig. 4.3.21 b. acetaldehyde$^{+\cdot}$ - Ar (in-OC) collision induced emission spectrum. 3.0 mm slits, 2 nm step size, 14 scan average.

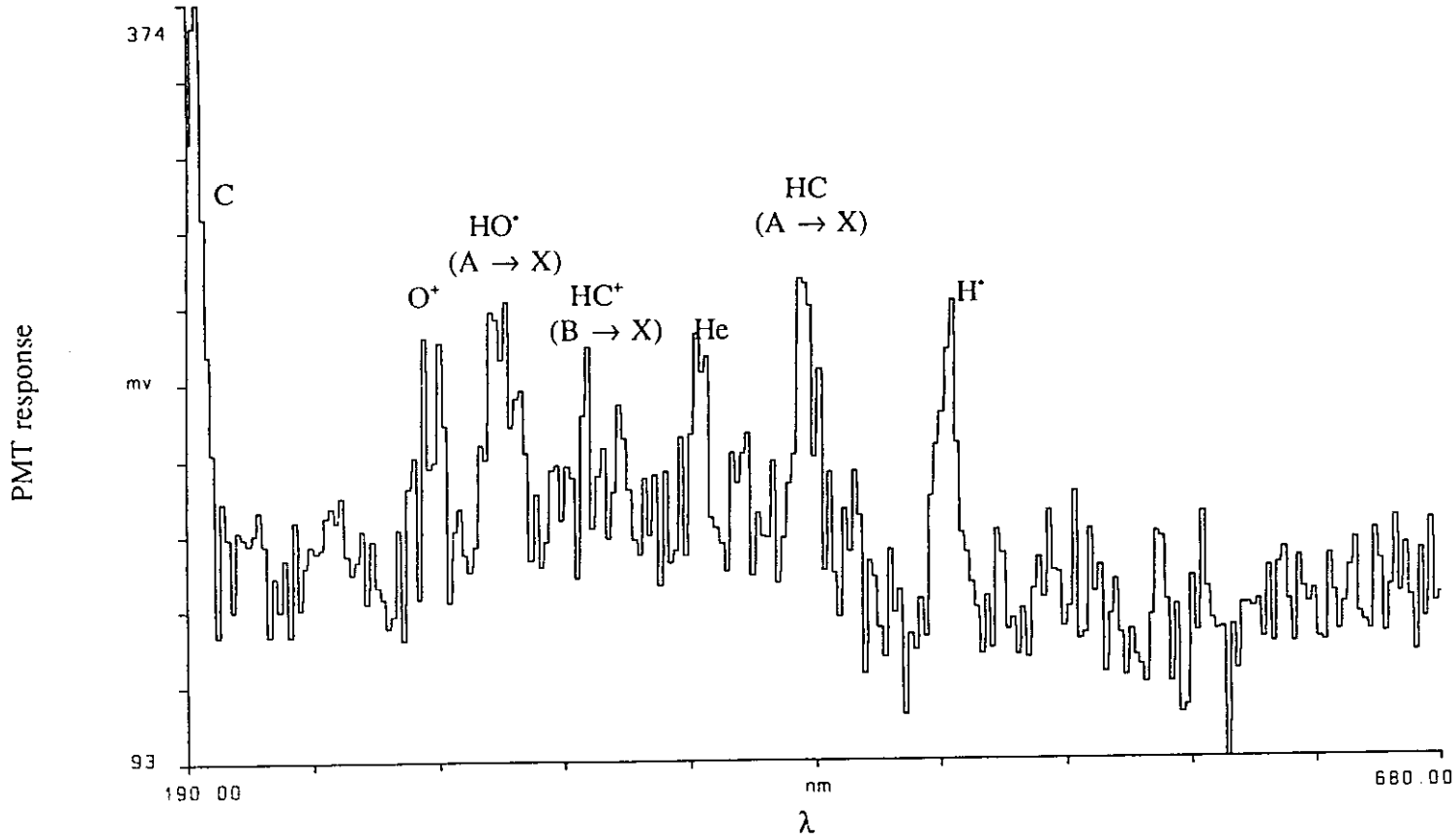

Fig. 4.3.22 a. vinyl alcohol** - He (in-OC) collision induced emission spectrum. 3.0 mm slits, 2 nm step size, 15 scan average.

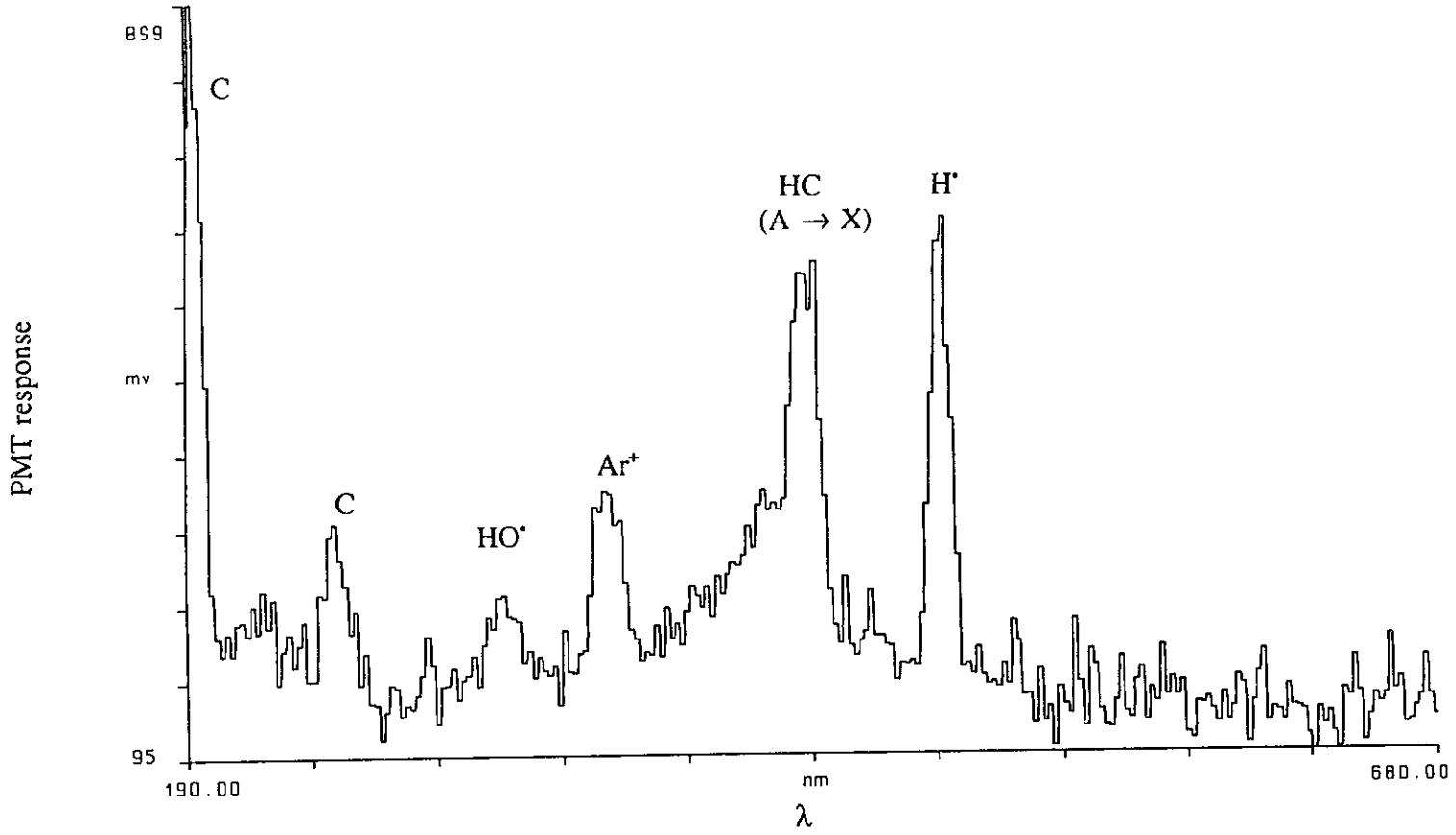

Fig. 4.3.22 b. vinyl alcohol$^{+\bullet}$ - Ar (in-OC) collision induced emission spectrum. 3.0 mm slits, 2 nm step size, 12 scan average.

4.3.7 Information from $C_2,H_4,O^{+\bullet}$ CIE spectra

The collision induced emission spectra in Figs 4.3.20-22 can provide information on the deposition of energy in these polyatomic projectile - target gas collisions. No intact molecular ion emissions were observed in these experiments, so excitation of the projectiles cannot be determined directly. It may be that when future modifications are made to the observation cell and the detection system low intensity bands due to emissions from species more complex than atomic and diatomic neutrals and ions will be observable. However, signal-to-noise in the present experiments precludes their observation. The atomic and diatomic bands in the CIE spectra do give some information on the excitation of the original $C_2,H_4,O^{+\bullet}$ ions from which they were formed.

a) Energy deposition - The excited electronic levels of oxirane, acetaldehyde and vinyl alcohol molecular ions are known from photoelectron spectroscopy [111]. The highest state observed, the E electronic state, was less than 10 eV above their respective ground states. If stable excited state molecular ions were formed in the collision event, their emissions should have been observed. The fact that these emissions were not obvious in the CIE spectra indicates that a) there are significant geometry differences between ground and excited state oxirane$^{+\bullet}$, acetaldehyde$^{+\bullet}$ and vinyl alcohol$^{+\bullet}$ and the vertical excitation process does not result in vibrationally stable excited state molecular ions (see discussion for 8 keV $O_2^{+\bullet}$ ions in sec. 4.3.3), b) a large amount of energy is being deposited in these collisions exciting the molecular ions well beyond the E electronic state resulting in the formation of electronically excited fragments and/or c) the emission is in the form of a broad band and cannot be distinguished from the background noise in the

spectra.

If the atomic and diatomic species in Figs 4.3.20-22 were formed directly upon the dissociation of excited molecular ions they yield information on the excitation occuring in the collision event. The C (3s $^1P^0$) atom, together with the counter-ion $C,H_4,O^{+\bullet}$, lies 14.4 eV above ground state oxirane$^{+\bullet}$ and similar values are obtained for acetaldehyde$^{+\bullet}$ and vinyl alcohol$^{+\bullet}$. Production of hydrogen in its n=4 state would require excitation of the three molecular ions by at least 12 eV. In order for vinyl alcohol$^{+\bullet}$ to give O^+ ions in their 4p $^2D^0$ state (30.7 eV above ground state O^+), almost 40 eV would have to be deposited.

The two diatomic emission bands common to all three isomers were the HC^+ (B $\rightarrow$ A) and HC (A $\rightarrow$ X) bands. The generation of HC^+ in its B $^1\Delta$ state (along with the counter-neutral C,H_3,O) requires ~ 13 eV of translational kinetic energy to be converted to internal energy of the precursors. Likewise, the HC (A $^2\Delta$) and C,H_3,O^+ fragments reflect an excitation of 6.3 eV. That this fragmentation requires roughly half the excitation of HC^+ (B) formation may be the reason why the HC (A $\rightarrow$ X) band was the predominant band of the two in the CIE spectra. Vinyl alcohol and acetaldehyde ions also exhibit the $HO^\bullet$ (A $\rightarrow$ X) band in their CIE spectra. The counter-ion to $HO^\bullet$ formation is $C_2H_3^+$, and the dissociation into $HO^\bullet$ (A) + $C_2H_3^+$ requires 8 eV of electronic excitation.

All but one of the emissions observed in the CIE spectra were the result of 6-14 eV being converted from translational kinetic energy to internal energy of the three molecular ions. If greater than 6 eV can be converted to internal energy then certainly less than 6 eV can be converted. However, no emissions were detected due to excitation

processes of less than 6 eV. One possible explanation is that for low eV excitation, the energy can be distributed among the many vibrational modes of these polyatomic ions (3n-6 or 15 vibrational modes). This was not possible for the simple di and triatomic ions discussed in secs 4.3.2-4 as $N_2^{+\bullet}$ and $O_2^{+\bullet}$ have only one vibrational mode and $CO_2^{+\bullet}$ has but three (the $CO_2^{+\bullet}$ ion is bent, rather than linear like neutral CO_2). These polyatomic projectiles may have rich emission spectra in the infra-red.

b) Effect of target gas - The He and Ar CIE spectra of the each isomer were very similar in the excited species which were produced, but the amounts of these species differed greatly. Using Ar as the target gas, ion beam emissions due to C, HC and $H^{\bullet}$ all became enhanced. However, the relative abundance of O^+ and $HO^{\bullet}$ in the CIE spectra of acetaldehyde$^{+\bullet}$ and vinyl alcohol$^{+\bullet}$ decreased with the introduction of Ar as the target gas. Enhancement of ion beam emissions may be due to the multitude of easily accessible excited states if Ar which can interact with the projectile ion. The exact nature of these interactions could not be determined in this study.

Also present when Ar was the target were emissions from excited state Ar^+ formed in the charge transfer with the projectile. The charge transfer reaction from ground state Ar to produce ground state oxirane is endothermic by 5.3 eV and is even more so for acetaldehyde, 5.5 eV, and vinyl alcohol, 6.6 eV. If Ar^+ was formed in the 4d ^2F state, the charge transfer reactions become even more endothermic.

c) Peak intensities in the CID mass spectra - The He and Ar CID mass spectra of the three isomers are listed in Table 4.3.3.

Table 4.3.3

Relative Intensities of Peaks in the He (Ar) CID Mass Spectra[a] of the Three $C_2,H_4,O^{+\cdot}$ Isomers

m/z	oxirane$^{+\cdot}$		acetaldehyde$^{+\cdot}$		vinyl alcohol$^{+\cdot}$	
43	23	(25)	100	(100)	100	(100)
42	8	(6)	11	(11)	26	(20)
41	0.6	(0.5)	3.6	(3)	5	(3)
40	--	(--)	0.7	(1.1)	1	(0.3)
31	0.6	(1)	--	(--)	--	(--)
30	1.6	(1.8)	0.4	(--)	3	(0.6)
29	100	(100)	53	(80)	53	(26)
28	5	(3)	6	(4)	5	(2)
27	--	(0.5)	3	(2.2)	22	(17)
26	0.6	(0.5)	6.5	(3)	19	(12)
25	--	(--)	3	(0.7)	7	(3)
24	--	(--)	0.7	(--)	1.5	(0.6)
16	3	(4)	1.5	(3)	1	(0.6)
15	14	(16)	13	(15.6)	23	(20)
14	9	(8)	6	(5.5)	9	(6.5)
13	1.3	(1)	2	(1.5)	3	(2)
12	0.4	(0.5)	0.8	(0.7)	1	(0.6)

a. helium (argon) target gas in the OC, 60% ion beam transmission - see also ref. 26

On the whole, the He and Ar CID mass spectra were similar except for changes in the intensity of the HCO^+ ion at m/z 29. It was apparent that most of the bands observed in the CIE spectra were not directly related to simple relative fragment peak intensities in the CID mass spectra. There was almost no detectable ion with m/z 31 (C loss) in the CID spectra to coincide with the large amount of excited C observed in the CIE spectra and so its unlikely to have been formed directly from the molecular ions. Ions with m/z 13 (HC^+) and m/z 30 (HC loss) were relatively minor peaks, though of similar

intensities.

Two emission bands did seem to be directly related to the CID mass spectra, the bands for O^+ (284 nm) and HO^* (312 nm). The counter-ion to HO^* formation, $C_2H_3^+$, is nearly non-existent in the CID of oxirane$^{+\bullet}$, only 3% base for acetaldehyde$^{+\bullet}$ and about 20% base for vinyl alcohol$^{+\bullet}$. It makes sense, therefore, that the HO^* emission band grows in relative intensity in the same order. On the other hand, the O^+ peak in the CID mass spectra (which may be interfered with by $CH_4^{+\bullet}$) follows the opposite trend, being most intense for oxirane$^{+\bullet}$ and least intense for vinyl alcohol$^{+\bullet}$. Producing O^+ in the 4d ^2F excited state requires 40 eV (see (a)), an energy demand which may make it a relatively less likely process for vinyl alcohol$^{+\bullet}$.

It is probable that the origin of many of the excited state species observed in the CIE spectra is not a simple one-step dissociation from the molecular ions. Collisional excitation followed by dissociation of the precursor ions may yield a wider variety of excited state fragments than is evident from the CIE spectra. These excited state fragments may themselves dissociate into smaller species until the atomic and diatomic ions and neutrals exhibited in Figs 4.3.20-22 were formed. As well, for collision processes depositing less energy into the molecular ions, polyatomic fragments which are not electronically but vibrationally excited may be formed. These are the ions observed in the CID mass spectra. Perhaps the CIE spectra represent only a small fraction of the excitation events occuring in the collision cell for polyatomic projectiles. This technique does present a new look at the processes occuring in the collision event and has provided information on the excitation events which are possible in keV polyatomic projectile -

target gas collisions, information unobtainable from experiments which rely on the interpretation of mass spectra.

4.3.8 Emissions from isomeric $C_2,H_5,Cl^{+\bullet}$ ion - target gas collisions

As with the $C_2,H_4,O^{+\bullet}$ isomers, it was helpful to start with the smaller fragment ions before attempting to interpret the CIE spectra of the two $C_2,H_5,Cl^{+\bullet}$ isomers.

CCl^+ - He CIE spectrum

The in-OC He CIE spectrum of 8 keV CCl^+ (from EI on CH_2Cl_2 in the ion source) is shown in Fig. 4.3.23. The dominant feature was the band at 237 nm which corresponds to the A $^1\Pi \rightarrow$ X $^1\Sigma^+$ transition of CCl^+ [112]. There was also a minor peak at 193 nm which was the same C emission as observed for $CO^{+\bullet}$.

CH_2Cl^+ - He, Ar CIE spectra

The chloromethyl cation (from EI on CH_2Cl_2 in the ion source) exhibits several peaks in its helium CIE spectrum, Fig. 4.3.24a. Many features are similar to those observed for the $C_2,H_4,O^{+\bullet}$ ions discussed above. The C, H* (Balmer-β), HC^+ (B $\rightarrow$ A) and HC (A $\rightarrow$ X) bands were present, along with the strong CCl^+ (A $\rightarrow$ X) transition. There were three other bands at ~ 285, 314 and 389 nm. The feature at 389 nm may be due to the HC (B $\rightarrow$ X) transition along with the HC^+ (A $\rightarrow$ X) transition. These two transitions were more intense than observed in the $C_2,H_4,O^{+\bullet}$ systems described above. When the collisions were performed in the PC, Fig. 4.3.24b, the only bands that remained in the

spectrum were the above CCl^+, HC^+, HC, C (minor) and 285 nm peaks, suggesting that the 285 nm band was not atomic and that the 314 nm band was atomic in nature.

When Argon was used as the target gas in the OC, Fig. 4.3.24c, the CIE spectrum showed considerable differences. The C, H^*, HC ($A \rightarrow X$) and Ar^+ emissions were present, but the CCl^+ ($A \rightarrow X$) band was considerably less intense than when He was the target. The two minor bands at 285 and 314 nm were still present, along with Cl^+ emissions at 384 and 479 nm (which became clearer under higher resolution) [108]. Again, when the collisions were performed in the PC, Fig. 4.3.24d, only the non-atomic bands listed above remained to any great extent.

$CH_3CH_2Cl^{+*}$ - He, Ar CIE spectra

The in-OC He CIE spectrum of 8 keV ethyl chloride ions is shown in Fig. 4.3.25a. It was a weak spectrum and only the major components are discernable. The previously observed C, H^* and HC ($A \rightarrow X$) bands are present, together with what may be the CCl^* transition at 237 nm. The poor resolution possible for this spectrum does not allow the CCl^+ band to be positively identified. There are possibly several other features between 300 nm and 420 nm including the above observed band at 314 nm. When Ar was used as the target, Fig. 4.3.25b, there was significantly more emission allowing a higher resolution spectrum to be obtained. Similar features were observed, the CCl^+ band at 237 nm decreasing in intensity so as to be indiscernable. Post-collision observations using Ar target gas, Fig. 4.3.25c, identified the HC ($A,B \rightarrow X$) and the HC^+ ($B \rightarrow A$ and possibly $A \rightarrow X$) transitions as the dominant non-atomic emission sources. The in-OC experiment

was also performed with sufficient argon to reduce the ion flux to 80% of its pre-cell value, and a weaker CIE spectrum similar to Fig. 4.3.25b was obtained. Thus, multiple collision processes are probably not responsible for much of the observed emission.

$CH_3ClCH_2^{+\bullet}$ - He, Ar CIE spectra

The ylide ion isomer of $CH_3CH_2Cl^{+\bullet}$, $CH_3ClCH_2^{+\bullet}$ was formed from EI dissociation of $CH_3OC(O)CH_2Cl$ in the ion source [113]. Unfortunately, the in-OC He CIE spectrum of this ion, Fig. 4.3.26a, was extremely weak, owing primarily to a smaller yield of these ions being obtained from the ion source relative to ethyl chloride which is an easily introduced gas. The in-OC Ar CIE spectrum, Fig. 4.3.26b, was more easily interpreted. In many ways it was simpler than the corresponding $CH_3CH_2Cl^{+\bullet}$ spectrum. Only the two C peaks, the H^* (Balmer-β) and the HC ($A \rightarrow X$) bands were present to any extent. There may also be a small band around 308 nm which could be the same as the 314 nm band observed for CH_2Cl^+ and $CH_3CH_2Cl^{+\bullet}$.

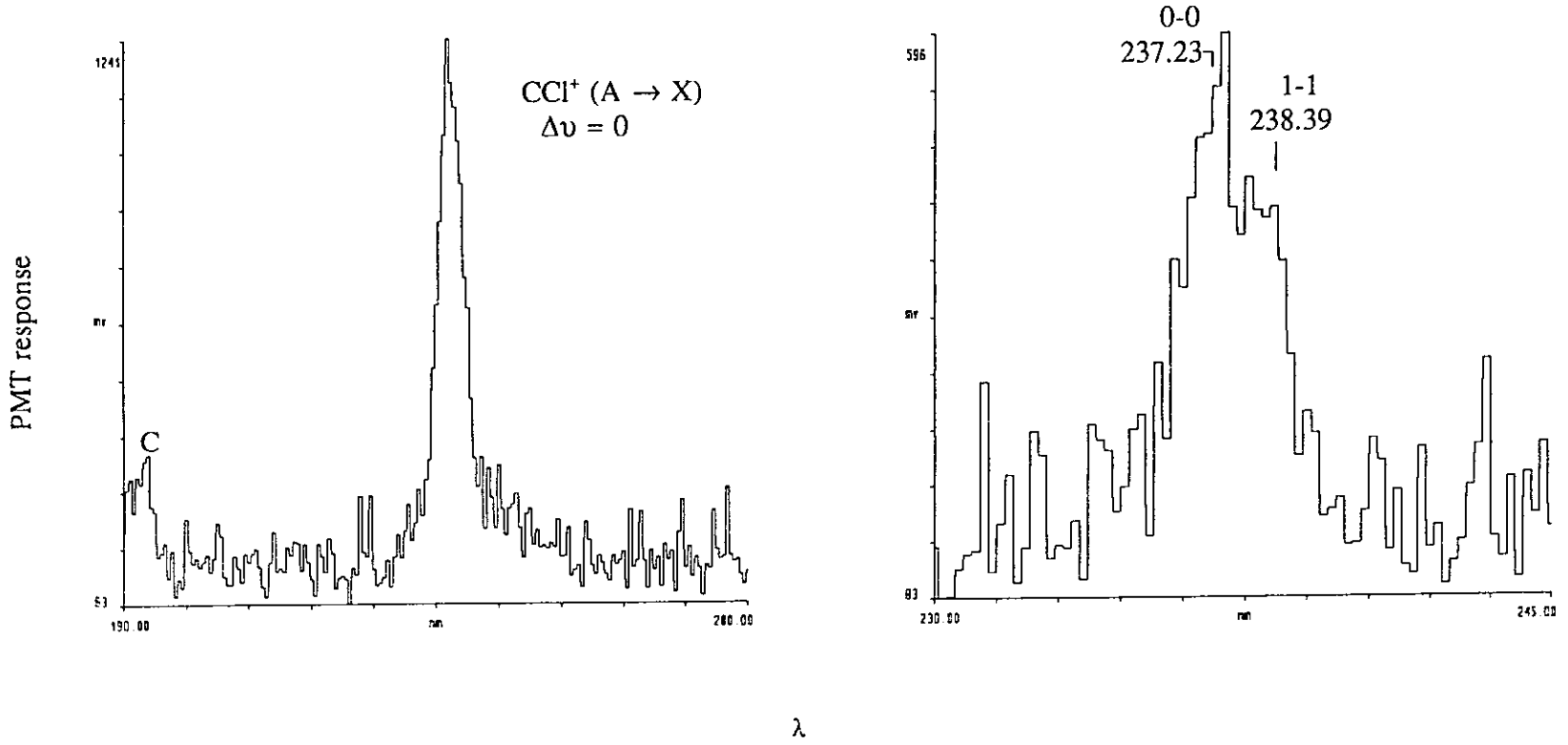

Fig. 4.3.23. CCl^+ - He (in-OC) collision induced emission spectrum. left- 1.0 mm slits, 0.5 nm step size, 3 scan average, right- 0.5 mm slits, 0.2 nm step size, 2 scan average.

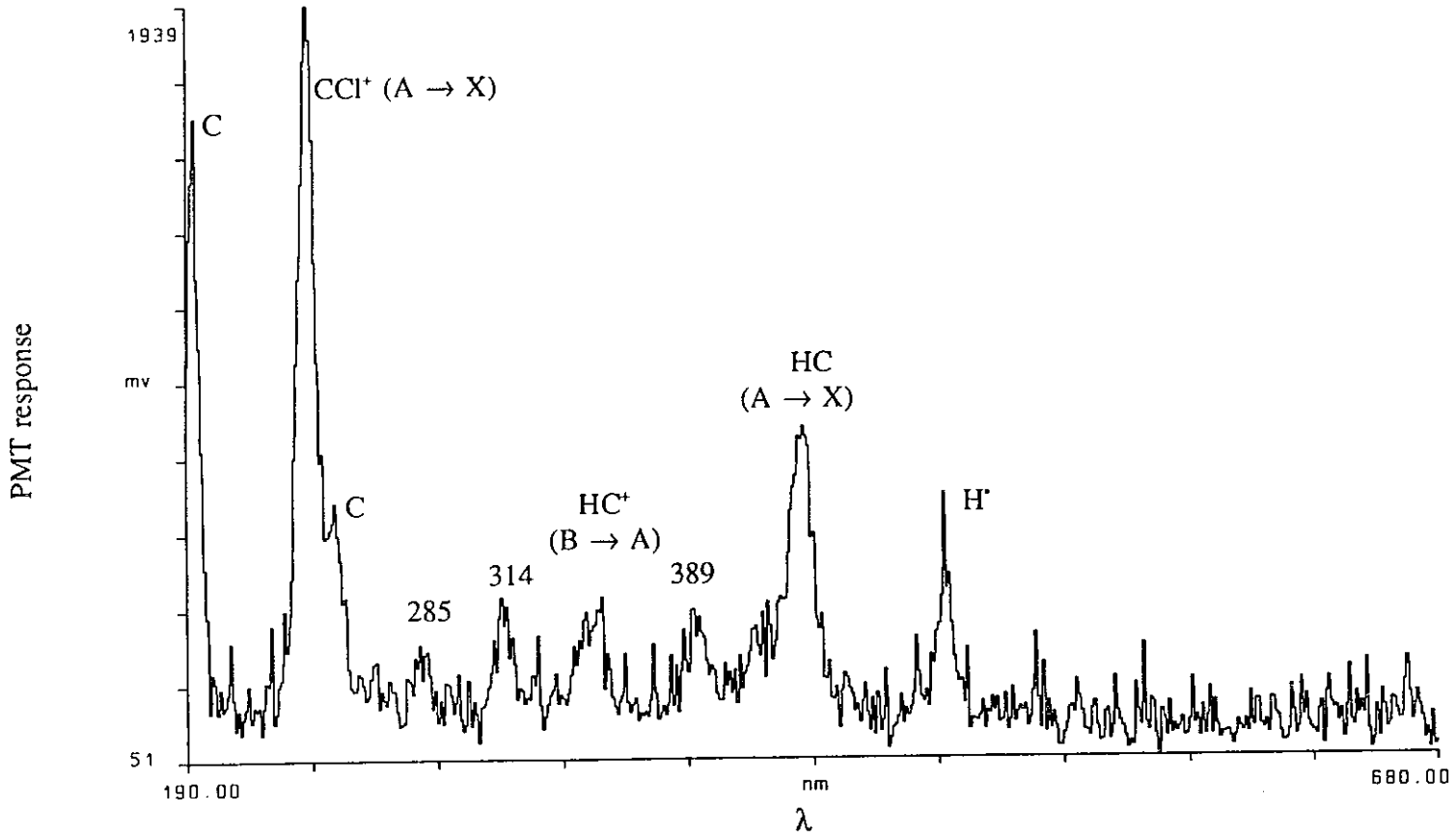

Fig. 4.3.24 a. CH_2Cl^+ - He (in-OC) collision induced emission spectrum. 2.0 mm slits, 1 nm step size, 3 scan average.

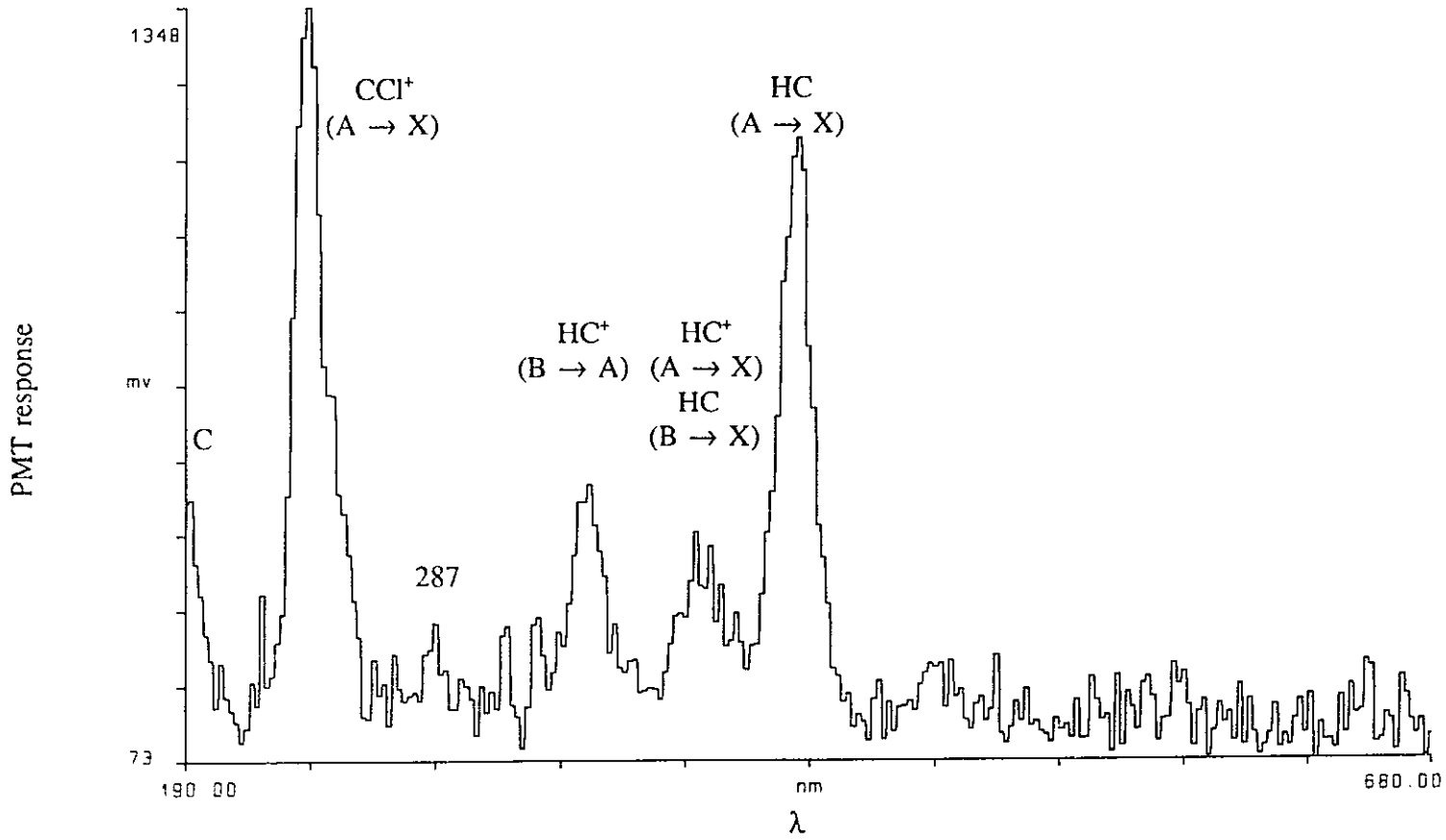

Fig. 4.3.24 b. CH_2Cl^+ - He (in-PC) collision induced emission spectrum. 3.0 mm slits, 2 nm step size, 4 scan average.

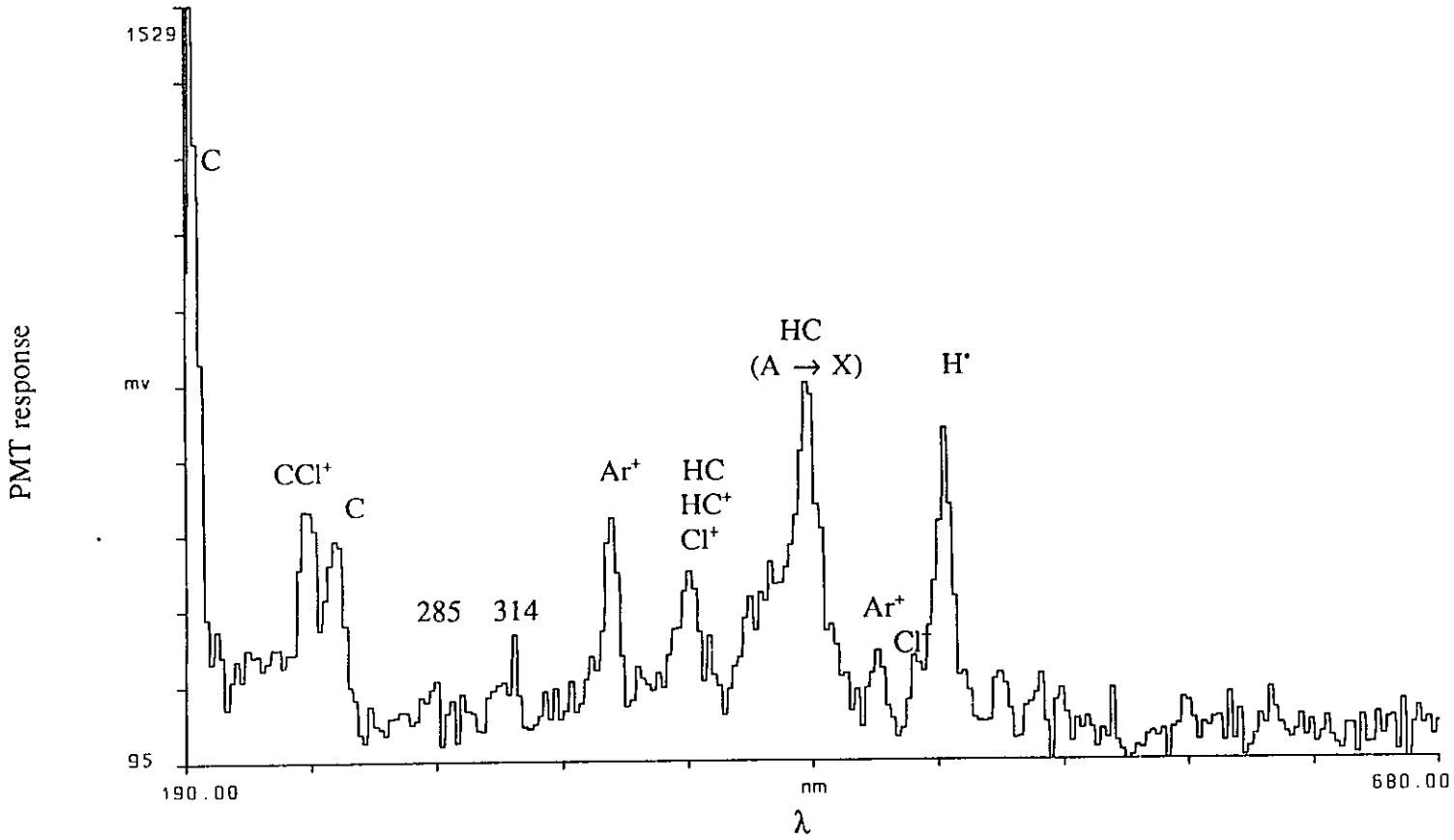

Fig. 4.3.24 c. CH_2Cl^+ - Ar (in-OC) collision induced emission spectrum. 2.0 mm slits, 2 nm step size, 8 scan average.

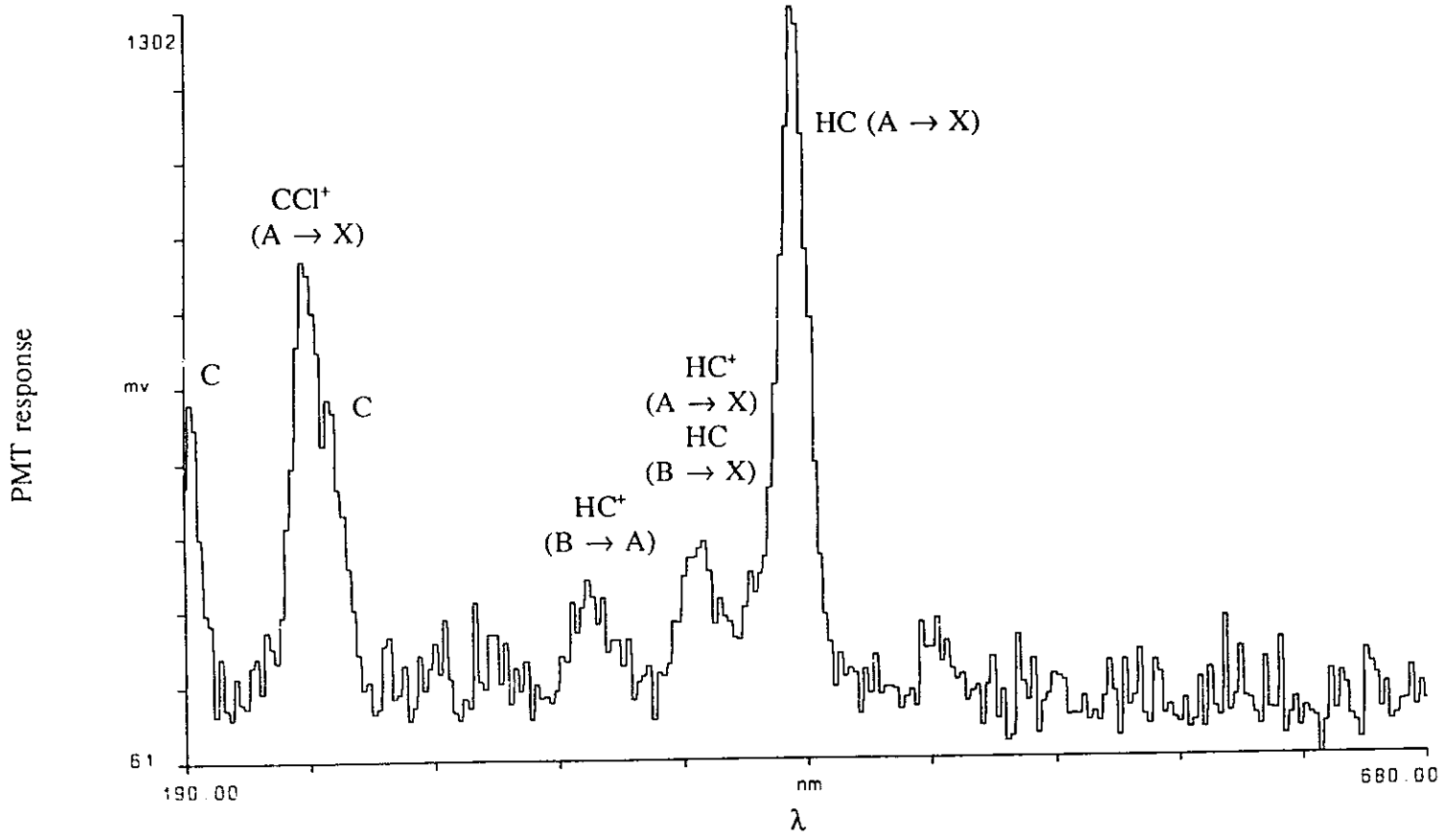

Fig. 4.3.24 d. CH_2Cl^+ - Ar (in-PC) collision induced emission spectrum. 3.0 mm slits, 2 nm step size, 4 scan average.

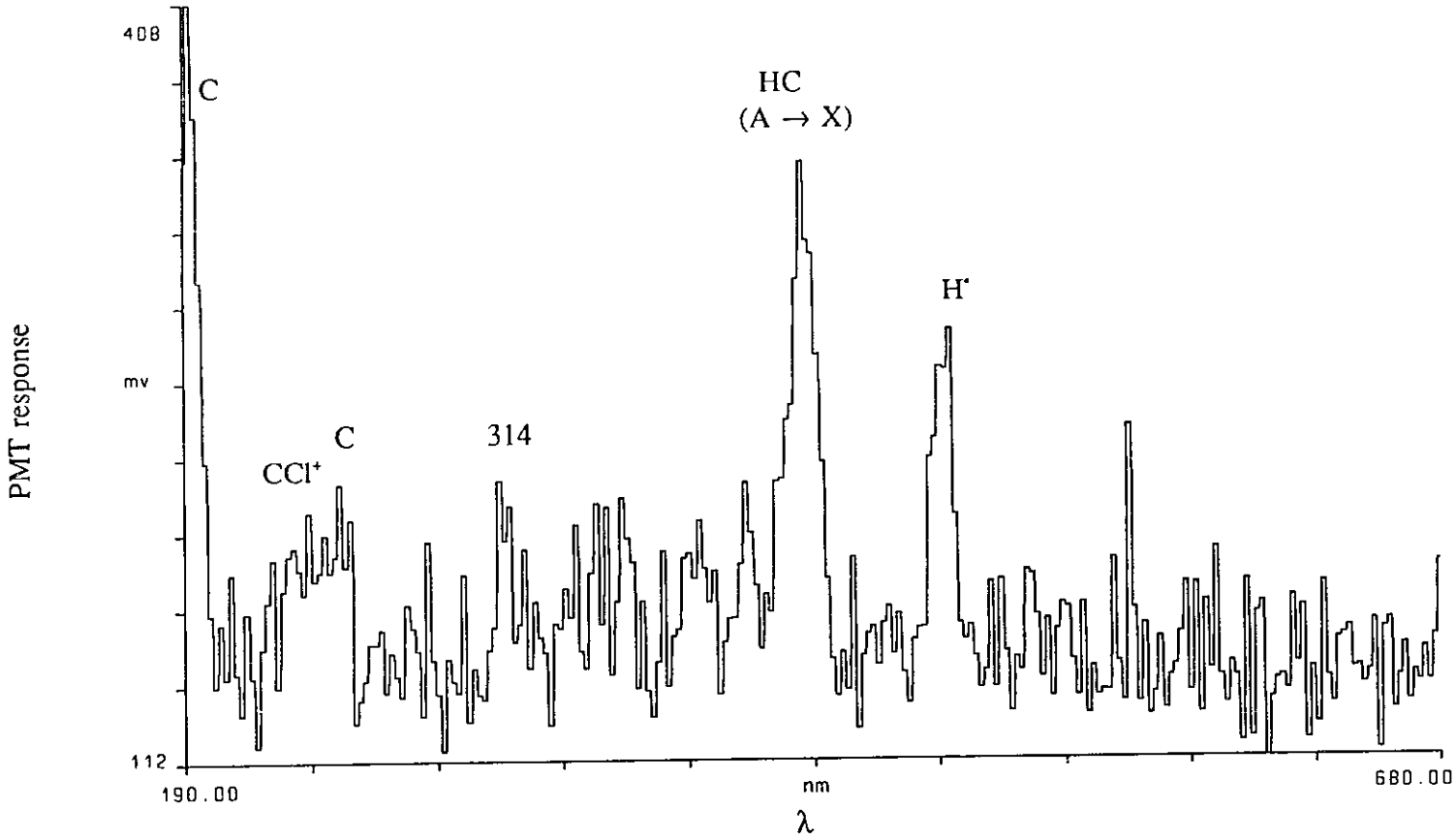

Fig. 4.3.25 a. $CH_3CH_2Cl^{+\bullet}$ - He (in-OC) collision induced emission spectrum. 3.0 mm slits, 2 nm step size, 16 scan average.

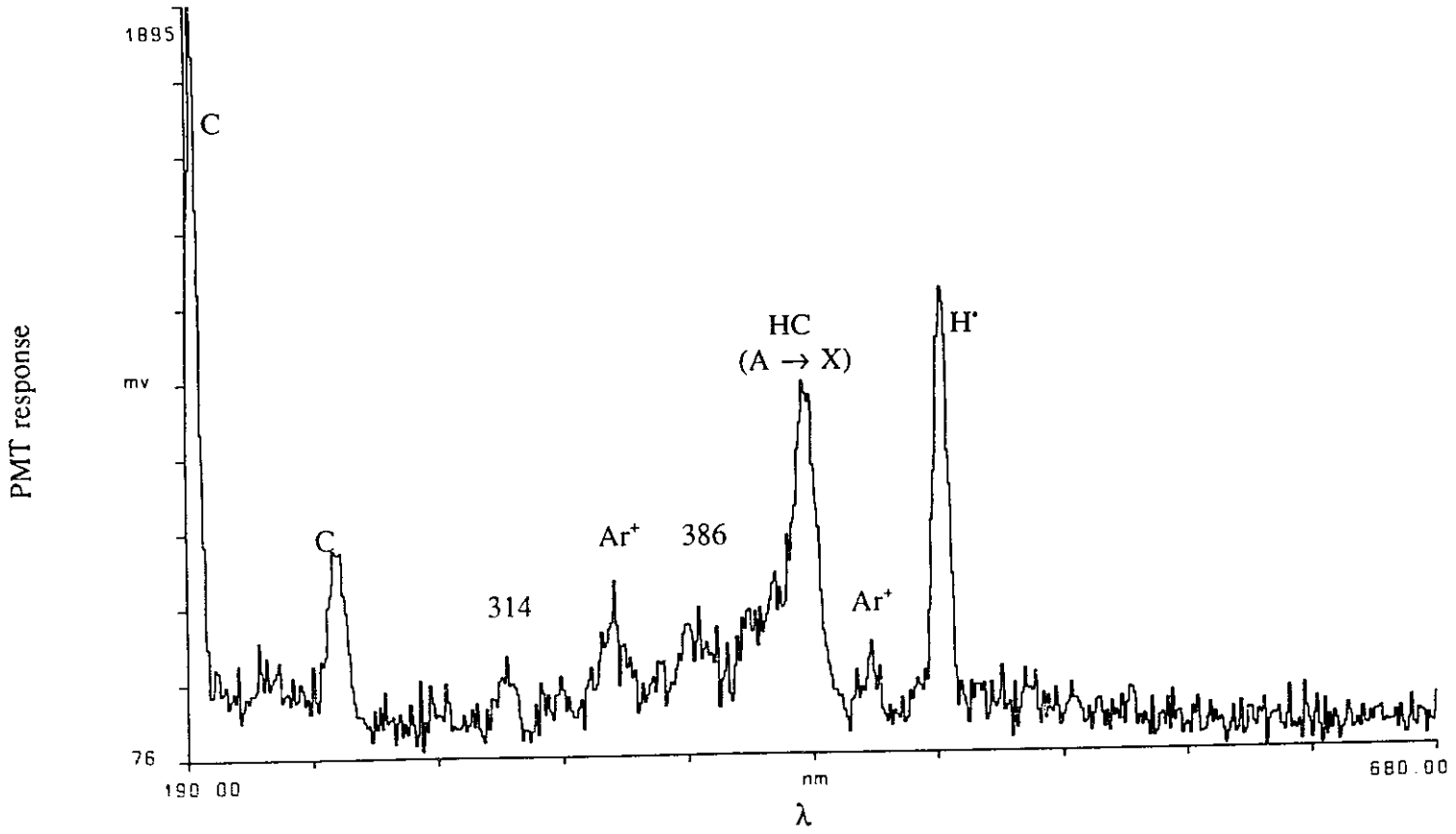

Fig. 4.3.25 b. $CH_3CH_2Cl^{+\cdot}$ - Ar (in-OC) collision induced emission spectrum. 2.0 mm slits, 1 nm step size, 5 scan average.

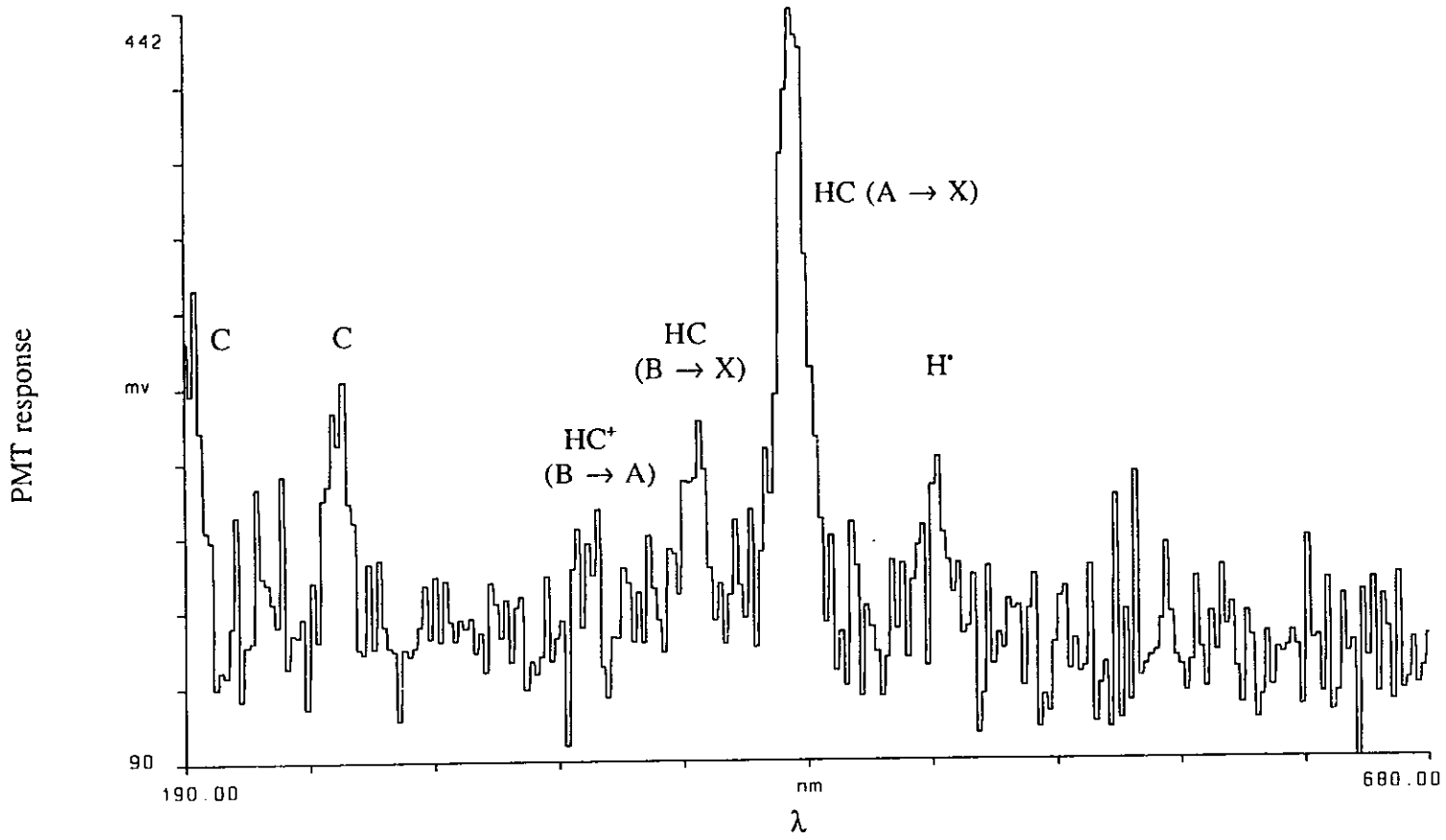

Fig. 4.3.25 c. $CH_3CH_2Cl^{+\bullet}$ - Ar (in-PC) collision induced emission spectrum. 3.0 mm slits, 2 nm step size, 11 scan average.

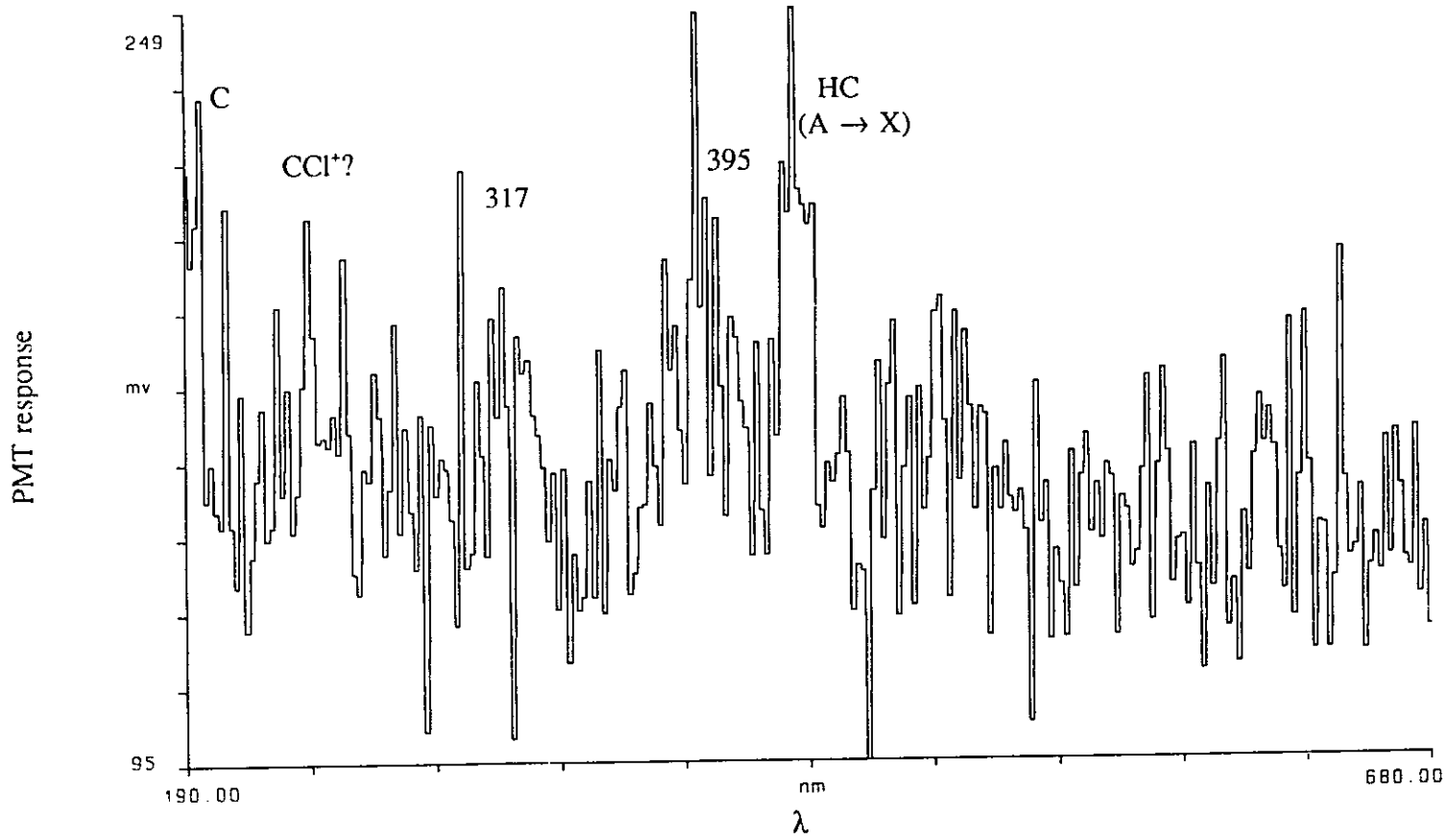

Fig. 4.3.26 a. $CH_3ClCH_2^{+\cdot}$ - He (in-OC) collision induced emission spectrum. 3.0 mm slits, 2 nm step size, 16 scan average.

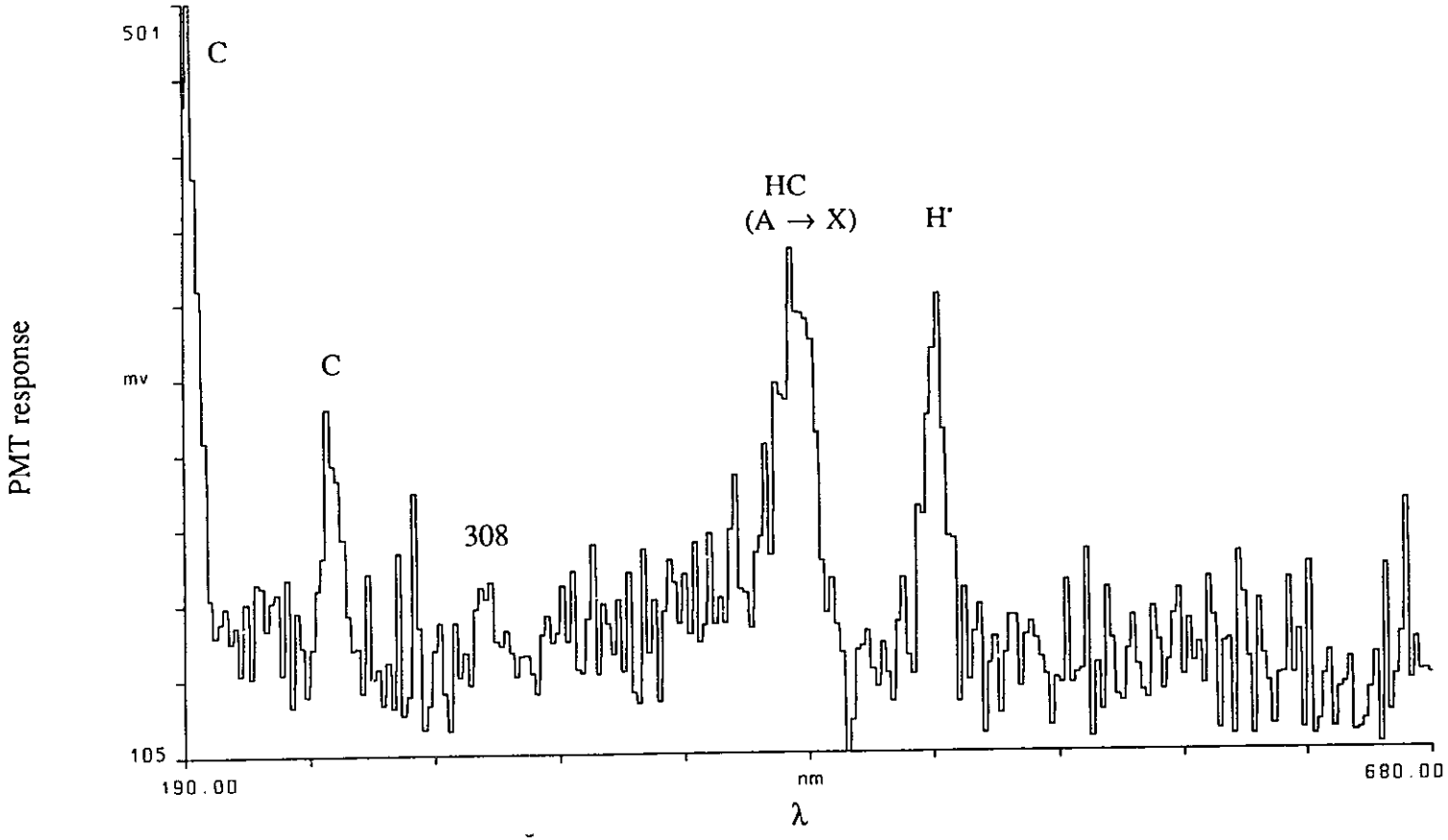

Fig. 4.3.26 b. $CH_3ClCH_2^{+\cdot}$ - Ar (in-OC) collision induced emission spectrum. 3.0 mm slits, 2 nm step size, 13 scan average.

4.3.9 Information from $C_2,H_5,Cl^{+\bullet}$ CIE spectra

As was found for the $C_2,H_4,O^{+\bullet}$ ions, all of the emissions observed in the CIE spectra of the two $C_2,H_5,Cl^{+\bullet}$ ions were from atomic and diatomic ions and neutrals. They can, however, be used to examine energy deposition in the projectile ions prior to dissociation.

a) Energy deposition - The assigned emissions in Figs 4.3.25 and 4.3.26 can be divided into atomic and diatomic ions and neutrals. The dissociation of a $C_2,H_5,Cl^{+\bullet}$ ion to form a carbon atom would require the formation of an ion of composition $C,H_5,Cl^{+\bullet}$, which could only be an ion-neutral complex involving CH_4 and HCl. Thus, it seems likely that the C (3s $^1P^0$) atom does not result from the direct dissociation of the molecular ions but rather from secondary fragmentations of smaller ions. Still, well over 8.5 eV (the energy of the 3s $^1P^0$ state in C) would have to be deposited in the molecular ions in the collision process to achieve this excited carbon atom. Hydrogen atoms in their n=4 state could be formed only after the deposition of at least 13.9 eV into the precursor ions in the collision event.

Three excited state diatomics were also identified. Two of them, HC^+ and HC, were also observed in the $C_2,H_4,O^{+\bullet}$ CIE spectra. In order to form HC (A), which is accompanied by the formation of CH_3ClH^+, ~ 7.2 eV must have been converted from translational kinetic energy to internal energy of the two precursor ions. Like carbon atom formation, HC^+ must be produced in a two step process since the neutral counterpart of composition C,H_4,Cl is a hypervalent radical. If the generation of HC^+ (B) is accompanied by CH_4 + Cl or $CH_3^\bullet$ + HCl, then at least 14 eV was deposited into the molecular ions.

Again, HC^+ (B) formation required roughly twice the energy deposition as the production of HC (A). To form CCl^+, the two isomers must eliminate CH_5, another hypervalent radical, or $H^\cdot + CH_4$. Producing CCl^+ in the A $^1\Pi$ state requires 9.8 eV.

These two isomers show that the production of the excited state atomic and diatomic species results primarily from multiple fragmentation processes. The results for the $C_2,H_4,O^{+\cdot}$ were ambiguous as to the origin of these species.

b) Effect of target gas - One difference between the CIE spectra obtained for $CH_3CH_2Cl^{+\cdot}$ and $CH_3ClCH_2^{+\cdot}$ using He and Ar target gases, aside from the enhancement of ion beam emissions with Ar, was the abundance of the CCl^+ ($A \rightarrow X$) emission band. There is evidence for this band in the He CIE spectra of both isomers, while it clearly vanishes when Ar was the target.

The same Ar^+ bands observed in the $C_2,H_4,O^{+\cdot}$ CIE spectra were present in the Ar CIE spectrum of $CH_3CH_2Cl^{+\cdot}$, Fig. 4.3.25b. The charge transfer between Ar and ethyl chloride$^{+\cdot}$ is endothermic by 4.78 eV, but will be considerably more so if Ar^+ is formed in the 4d ^{2}F state. There is no mass spectrometric evidence for the existence of stable neutral CH_3ClCH_2 [113]. Interestingly, no Ar^+ emission bands are obvious in the Fig. 4.3.26b, indicating that the charge transfer reaction to form excited Ar^+ does not occur.

c) Peak intensities in the CID mass spectra - The He and Ar CID mass spectra of the two isomers are listed in Table 4.3.4.

Table 4.3.4

Relative Intensities of the Peaks in the He (Ar) CID Mass Spectra[a] of Two $C_2,H_5,Cl^{+\cdot}$ Isomers

m/z	$CH_3CH_2Cl^{+\cdot}$	$CH_3ClCH_2^{+\cdot}$
63	5 (8)	1.4 (2)
62	1.8 (2)	0.2 (0.3)
61	1.8 (1.4)	2.5 (2)
60	1.2 (0.6)	0.5 (0.2)
59	>0 (>0)	-- (--)
51	-- (--)	0.9 (0.6)
50	-- (--)	5 (3.2)
49	23.4 (23)	100 (100)
48	4 (4)	13 (11.6)
47	4 (4)	11.6 (9)
36	1.2 (1.4)	0.9 (0.6)
35	1.8 (3.4)	0.9 (0.6)
29	100 (100)	62 (48.4)
28	84.5 (88.6)	11.6 (9)
27	26.1 (27)	5.6 (3.2)
26	10.6 (8.6)	2.3 (1)
25	2.1 (1.7)	>0 (--)
24	0.3 (0.3)	-- (--)
16	-- (--)	0.5 (--)
15	0.3 (0.1)	2.8 (1.3)
14	0.3 (0.3)	2.8 (1.3)
13	>0 (0.1)	0.5 (0.3)
12	-- (--)	0.5 (--)

a. helium (argon) target gas in the OC, 60% beam transmission - see also ref. 27.

The CID spectra of the two isomers are quite distinct, exhibiting different m/z 49 : m/z 29 peak ratios. The use of Ar as the target does not change the spectra to a significant extent. As was discussed in (a) above, it is evident that most of the atomic and diatomic emitting species observed in the CIE spectra do not result from a simple

dissociation but rather from at least two consecutive dissociations.

4.3.10 Conclusion

It has been seen that even though photon emissions from polyatomic projectile - target gas collisions are due mainly to atomic and diatomic fragments, information can be obtained concerning the amount of translational kinetic energy which is converted into internal energy during the collision event. This was one of the primary purposes for starting this investigation. Like most research, we have succeeded in creating more questions than we have answered. Experiments which deserve to be performed are a) lowering the accelerating voltage to 2 or 3 keV and examine changes in the CIE and CID spectra, b) studying ions whose neutral counterparts are unstable and examining the changes, if any, in emissions from ionized target gas species formed in charge transfer reactions and c) changing the PC-to-OC distance to investigate excited state species with longer lifetimes. Other experiments which come to mind are a) studying neutral polyatomic projectiles after neutralizing charged projectiles in the first 3FFR collision cell and deflecting away the remaining ions with the deflector electrode (Fig. 2.2.6), b) studying the CIE spectra of negative ions and c) ions formed from the dissociation of metastable precursor ions in the 2FFR. These latter experiments will require a more sensitive observation zone (OC, analyzer and detector).

These results have been or are being published [114,115,116].

References - Chapter 4

1. R.G. Cooks, in R.G. Cooks (ed), Collision Spectroscopy, Plenum Press, N.Y., 1978, Ch. 7.

2. P.J. Todd and F.W. McLafferty, in F.W. McLafferty (ed), Tandem Mass Spectrometry, Wiley-Interscience, N.Y., 1983, Ch. 7.

3. R.G. Cooks, J.H. Beynon and T. Ast, J. Am. Chem. Soc., 94 (1972) 1004.

4. T. Keough, J.H. Beynon and R.G. Cooks, J. Am. Chem. Soc., 95 (1973) 1695 and J.H. Bowie and T. Blumenthal, J. Am. Chem. Soc., 97 (1975) 2959.

5. D.O. Danis, C. Wesdemiotis and F.W. McLafferty, J. Am. Chem. Soc., 105 (1983) 7454.

6. MD. A. Mabud, M.J. Dekrey and R.G. Cooks, Int. J. Mass Spectrom. Ion Proc., 67 (1985) 285.

7. J.A. Laramee, D. Cameron and R.G. Cooks, J. Am. Chem. Soc., 103 (1981) 12.

8. C.J. Porter, R.P. Morgan and J.H. Beynon, Int. J. Mass Spectrom. Ion Phys., 28 (1978) 321.

9. M.S. Kim and F.W. McLafferty, J. Am. Chem. Soc., 100 (1978) 3279.

10. J.A. Laramee, P.H. Hemberger and R.G. Cooks, Int. J. Mass Spectrom. Ion Phys., 33 (1979) 231.

11. J.A. Laramee, J.J Carmody and R.G. Cooks, Int. J. Mass Spectrom. Ion Phys., 31 (1979) 333.

12. R.G. Cooks, Kim and J.H. Beynon, Chem. Phys. Lett., 23 (1973) 190.

13. T. Ast, D.T. Terwilliger, R.G. Cooks and J.H. Beynon, J. Phys. Chem., 79 (1975) 708.

14. P.H. Hemberger, J.A. Laramee, A.R. Hubik and R.G. Cooks, J. Phys. Chem., 85 (1981) 2335.

15. P.J. Todd, R.J. Warmack and E.H. McBay, Int. J. Mass Spectrom. Ion Phys., 50 (1983) 299.

16. R.K. Boyd, E.E. Kingston, A.G. Brenton and J.H. Beynon, Proc. R. Soc. Lond. A, 392 (1984) 59.

17. R.K. Boyd, E.E. Kingston, A.G. Brenton and J.H. Beynon, Proc. R. Soc. Lond. A, 392 (1984) 89.

18. S. Singh, M.S. Thacker, F.M. Harris and J.H. Beynon, Org. Mass Spectrom., 20 (1985) 156.

19. S. Singh, F.M. Harris, R.K. Boyd and J.H. Beynon, Int. J. Mass Spectrom. Ion Proc., 66 (1985) 131.

20. D.S. Waddell, R.K. Boyd, A.G. Brenton and J.H. Beynon, Int. J. Mass Spectrom. Ion Proc., 68 (1986) 71.

21. C.S. Enos and A.G. Brenton, Rapid Commun. Mass Spectrom., 7 (1993) 272.

22. D.P. deBruijn and J. Los, in J.F.J. Todd (ed), Adv. Mass Spectrom., Wiley and Sons, 1985, p.155.

23. M. Hamdan and A.G. Brenton, in D. Mathur (ed), Physics of Ion Impact Phenomena, Springer Series in Chemical Physics, Vol. 54, 1991, Ch. 6.

24. T. Ast, J. H. Beynon and R.G. Cooks, J. Am. Chem. Soc., 94 (1972) 6611.

25. J.H. Moore, Jr., J. Phys. Chem., 76 (1972) 1130.

26. C.C. Van de Sande and F.W. McLafferty, J. Am. Chem. Soc., 97 (1975) 4613.

27. M.C. Blanchette, J.L. Holmes and F.P. Lossing, Org. Mass Spectrom., 22 (1987) 701.

28. J.L. Holmes, P.M. Mayer and A.A. Mommers, J. Am. Chem. Soc., 113 (1991) 9405.

29. J.L. Holmes, P.M. Mayer and A.A. Mommers, Org. Mass Spectrom., 27 (1992) 537.

30. W.B. Maier II, J. Chem. Phys., 61 (1974) 3459.

31. T.F. Moran, J.B. Wilcox and L.E. Abbey, J. Chem. Phys., 65 (1976) 4540.

32. A. Lofthus and P.H. Krupenie, J. Phys. Chem. Ref. Data 6 (1977) 113 .

33. S. Bashkin and J.O. Stoner, Jr., Atomic Energy Levels and Grotrian Diagrams Vol. I, North-Holland Publishing Co., N.Y., 1975.

34. J.H. Moore, Jr. and J.P. Doering, Phys. Rev., 174 (1968) 178.

35. J.H. Moore, Jr. and J.P. Doering, Phys. Rev., 177 (1969) 218.

36. J.H. Moore, Jr. and J.P. Doering, Phys. Rev., 182 (1969) 176.

37. J.H. Birely, Phys. Rev. A., 10 (1974) 550.

38. B. Van Zyl, M.W. Gealy and H. Newmann, Phys. Rev. A, 28 (1983) 2141.

39. A. Matsumoto, T. Sano and T. Iwai, J. Phys. Soc. Jpn., 52 (1983) 1173.

40. J.P. Doering, Phys. Rev., 113 (1964) 1537.

41. J.J. Leventhal, J.D. Earl, H.H. Harris, Phys. Rev. Lett., 35 (1975) 719.

42. G.H. Bearman, J.D. Earl, R.J. Pieper, H.H. Harris and J.J. Leventhal, Phys. Rev. A, 13 (1976) 1734.

43. J.D. Kelley, G.H. Bearman, H.H. Harris and J.J. Leventhal, Chem. Phys. Lett., 50 (1977) 295.

44. J.D. Kelley, G.H. Bearman, H.H. Harris and J.J. Leventhal, J. Chem. Phys., 68 (1978) 3345.

45. Ch. Ottinger and J. Simonis, Chem. Phys., 28 (1978) 97.

46. J.L. Barrett and J.J. Leventhal, J. Chem. Phys., 71 (1979) 4015.

47. H. Obase, M. Tsuji and Y. Nishimura, Chem. Phys. Lett., 105 (1984) 214.

48. H. Sekiya, M. Tsuji and Y. Nishimura, J. Chem. Phys., 87 (1987) 325.

49. G. Comtet, P.G. Fournier and B. Lassier-Govers, Chem. Phys., 101 (1986) 299.

50. M. Hamdan and A.G. Brenton, Int. J. Mass Spectrom. Ion Proc., 88 (1989) 309.

51. A.R. Lee, C.S. Enos and A.G. Brenton, Int. J. Mass Spectrom. Ion Proc., 124 (1993) 85.

52. D. Dowek, D. Dhuicq, J. Pommier, Vy Ngoc Tuan, V. Sidis and M. Barat, Phys. Rev. A, 24 (1981) 2445.

53. Y. Sato, M. Kikuchi and H. Inouye, Phys. Rev. A, 25 (1982) 3376.

54. E.Y. Kamber, A.G. Brenton, J.H. Beynon and J.B. Hasted, J. Phys. B: At., Mol. Phys., 18 (1985) 933.

55. D. Mathur, R.G. Kingston, F.M. Harris and J.H. Beynon, J. Phys. B: At., Mol. Phys. 19 (1986) L575.

56. D. Mathur, R.G. Kingston, F.M. Harris, A.G. Brenton and J.H. Beynon, J. Phys. B: At., Mol. Phys., 20 (1987) 1811.

57. T.F. Moran and J.B. Wilcox, J. Chem. Phys., 68 (1978) 2855.

58. A. Russek, Physica, 48 (1970) 165.

59. J. Durup, in K. Ogata and T. Hayakawa (ed), Recent Developments in Mass Spectrometry, Univ. Park Press, Baltimore, Maryland, 1970, p.921.

60. W.S. Koski, Adv. Chem. Phys., 30 (1975) 185.

61. J. Los and T.R. Govers, in R.G. Cooks (ed), Collision Spectroscopy, Plenum Press,

1978, Ch.6.

62. J.W. McConkey and J.M. Woolsey, J. Phys. B: At., Mol. Phys., 2 (1969) 529.

63. G.I. MacKay, J.P. Anglesey and R.E. March, Can. J. Chem., 50 (1972) 2516.

64. A. O'Keefe and J.R. McDonald, Chem. Phys., 103 (1986) 425.

65. J. Glosik, A.B. Raksit, N.D. Twiddy, N.G. Adams and D. Smith, J. Phys. B: At., Mol. Phys., 11 (1978) 3365.

66. H. Böhringer, M. Durup-Ferguson, D.W. Fahey, F.C. Fehsenfeld and E.E. Ferguson, J. Chem. Phys., 79 (1983) 4201.

67. C.J. Reid, J.Phys. B: At., Mol., Opt. Phys., 25 (1992) 4249.

68. P.H. Doolittle, R.I. Schoen and K.E. Schubert, J. Chem. Phys., 49 (1968) 5108.

69. B.R. Turner, J.A. Rutherford and D.M.J. Compton, J. Chem. Phys., 48 (1968) 1602.

70. P.H. Krupenie, J. Phys. Chem. Ref. Data 1 (1972) 423.

71. R.H. Hughes and D.K.W. Ng, Phys. Rev., 136 (1964) A1222.

72. S.N. Ghosh, Y. Sahai and K.K. Bhutani, Indian J. Pure Appl. Phys., 10 (1972) 296.

73. J.H. Birely, Phys. Rev. A., 11 (1975) 79.

74. H.H. Harris, M.G. Crowley and J.J. Leventhal, Chem. Phys. Lett., 29 (1974) 540.

75. G.H. Bearman, J.D. Earl, H.H. Harris, P.B. James and J.J. Leventhal, Chem. Phys. Lett., 44 (1976) 471.

76. J.H. Moore, Jr., J. Chem. Phys., 55 (1971) 2760.

77. J.T. Park, F.D. Schowengerdt and D.R. Schoonover, Phys. Rev. A, 3 (1971) 679.

78. M. Rincon, N.J. Kirchner and M.T. Bowers, Int. J. Mass Spectrom. Ion Proc., 86 (1988) 369.

79. M. Hamdan and A.G. Brenton, Int. J. Mass Spectrom. Ion Proc., 84 (1988) 203.

80. M. Hamdan and A.G. Brenton, J. Phys. B: At., Mol., Opt. Phys., 22 (1989) 2289.

81. C.S. Enos, A.R. Lee and A.G. Brenton, Org. Mass Spectrom., 26 (1991) 389.

82. A.R. Lee, C.S. Enos and A.G. Brenton, Chem. Phys., 150 (1991) 275.

83. A.R. Lee, C.S. Enos and A.G. Brenton, J. Mol. Spectrosc., 156 (1992) 461.

84. A.R. Lee, C.S. Enos and A.G. Brenton, Chem. Phys. Lett., 194 (1992) 118.

85. J.E. Hesser, J. Chem. Phys., 48 (1968) 2518.

86. J.H.D. Eland, Int. J. Mass Spectrom. Ion Phys., 9 (1972) 397.

87. J.A.R. Samson and J.L. Gardner, J. Geophys. Res., 78 (1973) 3663.

88. M. Bloch and D.W. Turner, Chem. Phys. Lett., 30 (1975) 344.

89. S.W. Jørgensen and G. Sørensen, J. Chem. Phys., 62 (1975) 2550.

90. R.C. Dunbar and D.W. Turner, Chem. Phys., 57 (1981) 377.

91. D.L. Judge, G.S. Bloom and A.L. Morse, Can. J. Phys., 47 (1969) 489.

92. T.S. Wauchop and H.P. Broida, J. Geophys. Res., 76 (1971) 21.

93. D. Gauyacq, C. Larcher and J. Rostas, Can. J. Phys., 57 (1979) 1634.

94. D. Gauyacq, M. Horani, S. Leach and J. Rostas, Can. J. Phys., 53 (1975) 2040.

95. P. Misra, D.W. Ferguson and K.N. Rao, J. Mol. Spectrosc., 125 (1987) 54.

96. C.J. Reid, Int. J. Mass Spectrom. Ion Proc., 101 (1990) 35.

97. M.A. Coplan and J.E. Mentall, J. Chem. Phys., 58 (1973) 4912.

98. M.J. Haugh and J.H. Birely, J. Chem. Phys., 60 (1974) 264.

99. H. Bregman-Reisler and J.P. Doering, Chem. Phys. Lett., 27 (1974) 199.

100. J.H. Birely and P.A. Johnson, J. Chem. Phys., 62 (1975) 4854.

101. H. Bregman-Reisler and J.P. Doering, J. Chem. Phys., 62 (1975) 3109.

102. J.H. Moore, Jr., J. Geophys. Res., 80 (1975) 3727.

103. W. Sim and M. Haugh, J. Chem. Phys., 65 (1976) 1616.

104. J.E. Parker, R.G. Milner and A.M. Robertson, Int. J. Mass Spectrom. Ion Phys., 24 (1977) 429.

105. W.J. Griffiths and F.M. Harris, Int. J. Mass Spectrom. Ion Proc., 87 (1989) 349.

106. C.A.F. Johnson and J.E. Parker, Chem. Phys., 111 (1987) 307.

107. R.W.B. Pearce and A.G. Gaynon, The Identification of Molecular Spectra, 4th ed., Chapman and Hall, London, 1978.

108. S. Bashkin and J.O. Stoner, Jr., Atomic Energy Levels and Grotrian Diagrams Vol. II, North-Holland Publishing Co., N.Y., 1975.

109. A. Michael, P. Misra, A. Farah and V. Kushawaha, J. Phys. B: At., Mol. Opt. Phys., 25 (1992) 2343.

110. M. Carre, Physica, 41 (1969) 63.

111. K. Johnson, I. Powis and C.J. Danby, Chem. Phys., 70 (1982) 329.

112. H. Bredohl, I. Dubois and F. Melen, J. Mol. Spectrosc. 98 (1983) 495.

113. M.C. Blanchette, J.L. Holmes and F.P. Lossing, Org. Mass Spectrum. 22 (1987) 701.

114. J.L. Holmes, P.M. Mayer and A.A. Mommers, Int. J. Mass Spectrom. Ion Proc., in press.

115. J.L. Holmes and P.M. Mayer, Org. Mass Spectrom., in press.

116. J.L. Holmes and P.M. Mayer, Org. Mass Spectrom., in preparation.

Chapter 5

Organic Free Radical and Cation Thermochemistry

5.1 Introduction

Recent work from this laboratory [1,2] has clearly demonstrated that the use of electron impact induced dissociative ionization of selected molecules can lead to accurate values for the heat of formation of organic free radicals. The criteria necessary for the success of such experiments have been described in detail in section 3.5 [2]. In general, the work to date [1-4] has mostly centred upon free radicals for which results had been obtained by conventional kinetic studies of gas phase reactions [5] or equilibrium data measured by electron paramagnetic resonance spectroscopy [6]. The present work includes the evaluation of many previously unknown heats of formation of oxygen - containing free radicals and the examination of the effect of the cyano group on gas phase ion and neutral thermochemistry.

5.2 Oxygen - Containing Organic Free Radicals

5.2.1 Introduction

Inspection of the last detailed collection [7] of $\Delta_f H^\circ_{298}$ values for free radicals and related bond strengths shows a considerable lack of reliable data for oxygen-containing free radicals, and so the present work was undertaken.

5.2.2 Results and Discussion

Table 5.2.1 contains the results obtained for the radicals studied. Parent molecules

with heats of formation obtained from Benson additivity [9] have an estimated uncertainty in their heats of formation of ± 1 kcal mol^{-1}. The error for those molecules listed in Pedley, et. al. [9] is typically better than ± 1 kcal mol^{-1}. The reproducibility of threshold energies for calibrant and sample gives an uncertainty in the AE value of ± 0.05 eV. The cation heats of formation have an uncertainty of ± 1 kcal mol^{-1}. The estimated error of the final $\Delta_f H°_{298}$ given in the Table is ± 3 kcal mol^{-1}. Agreement among the values obtained for the heat of formation of a radical generated from more than one precursor was generally good, with the largest range being 3.7 kcal mol^{-1} for $^{\bullet}C(O)OCH_3$.

Table 5.2.1

Experimentally Determined Appearance Energies, AE, of Counter Ions, Y^+, from Precursors, RY; Calculated $\Delta_f H°_{298}$ of Product Radicals, $R^{\bullet}$, (estimated uncertainty ± 3 kcal mol^{-1}), and Bond Strengths, D(R-H)[a]

	$R^{\bullet}$	Y^+	$\Delta_f H°_{298}$ $(RY)^b$	$\Delta_f H°_{298}$ $(Y^+)^c$	AE (Y^+)		$\Delta_f H°_{298}$ $(R^{\bullet})$
1.	CH_2CH_2OH	CH_3CO	-93.0	156	10.20		-13.8
2.		$(CH_3)_2C$	-81.0	166	10.14		-13.2
3.		CH_3OCHCH_3	-102.0	132	9.56		-13.5
						ave	-13.5
	$\Delta_f H°_{298}(RH)^g$= -56.2	D(R-H) = 94.8					
4.	CH_3CHOH	CH_3CHOH	-112.0	139	10.26		-14.4
5.		CH_2NH_2	-57.1	178	9.56		-14.6
						ave	-14.5
	$\Delta_f H°_{298}(RH)^g$= -56.2	D(R-H) = 93.8					
6.	$CH_2CH_2CH_2OH$	CH_3CO	-97.7	156	10.30		-16.2
7.		CH_3CHOH	-111.0	139	10.16		-15.7
						ave	-16.0
	$\Delta_f H°_{298}(RH)^g$= -61.0	D(R-H) = 97.1					

8.	$CH_2CH(OH)CH_3$	CH_3CHOH	-115.5	139	10.02		-23.4
9.		$(CH_3)_2COH$	-125.0	119	9.60		-22.6
						ave	-23.0

$\Delta_fH°_{298}(RH)^9$= -65.2 D(R-H) = 94.3

10. $CH_2C(OH)(CH_3)_2$	$(CH_3)_2COH$	-133.0	119	9.40		-35.2

$\Delta_fH°_{298}(RH)^9$= -74.7 D(R-H) = 91.6

11. CH_3CHCH_2OH	CH_2OH	-104.0	168	10.98		-18.8

$\Delta_fH°_{298}(RH)^9$= -61.0 D(R-H) = 94.3

12. $(CH_3)_2COH$	$(CH_3)_2COH$	-128.0	119	9.60		-25.6

$\Delta_fH°_{298}(RH)^9$= -65.2 D(R-H) = 91.7

13. $HOCHCH_2OH$	$(CH_3)_3C$	-120.0	166	10.12		-52.6

$\Delta_fH°_{298}(RH)^9$= -92.6 D(R-H) = 92.1

14. $CH_2C(O)OH$	$(CH_3)_3C$	-129.0	166	10.12		-61.6

$\Delta_fH°_{298}(RH)^9$= -103.4 D(R-H) = 93.9

15. $CH_2C(O)OCH_3$	$(CH_3)_3C$	-124.0	166	10.04		-58.5
16.	CH_3CO	-138.0	156	10.30		-56.5
					ave	-57.5

$\Delta_fH°_{298}(RH)^9$= -98.4 D(R-H) = 93.0

17. $CH_2OCH_2CH_3$	$CH_3CH_2OCH_2$	-99.0	145	10.12		-10.6

$\Delta_fH°_{298}(RH)^9$= -51.7 D(R-H) = 93.2

18. C(O)OH	CH_3CO	-127.0	156	10.28		-45.9
19.	$(CH_3)_2CH$	-115.0	192	11.28		-46.9
20.	CH_2Cl	-104.0[9]	227[91]	12.34		-46.4
21.	CH_3OCH_2	-134.0	157	10.68		-44.7
					ave	-46.0

$\Delta_fH°_{298}(RH)^9$= -90.5 D(R-H) = 96.6

22. $C(O)OCH_3$	$(CH_3)_2CH$	-110.0	192	11.42		-38.6
23.	$(CH_3)_3C$	-118.1[9]	166	10.64		-38.7
24.	CH_3CO	-122.0	156	10.24		-41.9
25.	CH_3OCH_2	-129.0	157	10.74		-38.3
26.	CH_3CHOH	-141.0	139	10.32		-42.0
					ave	-39.9

	$\Delta_fH°_{298}(RH)^9$= -85.0	D(R-H) = 97.2				
27. HO_2	$(CH_3)_3C$	-58.8[9]	166	9.90		3.5
	$\Delta_fH°_{298}(RH)^{10}$= -32.6	D(R-H) = 88.2				
28. $(CH_3)_3COO$	$(CH_3)_3C$	-83.4[9]	166	9.72		-25.2
	$\Delta_fH°_{298}(RH)^9$= -58.8	D(R-H) = 85.7				
29. HC(O)O	$(CH_3)_3C$	-112.0	166	10.42		-37.7
30.	CH_3OCH_2	-125.0	157	10.60		-37.6
					ave	-37.7
	$\Delta_fH°_{298}(RH)^9$= -90.5	D(R-H) = 104.7				
31. $CH_3C(O)O$	C_2H_5	-106.1[9]	216	11.74		-51.4
32.	CH_3OCH_2	-138.0	157	10.54		-51.9
					ave	-51.7
	$\Delta_fH°_{298}(RH)^9$= -103.4	D(R-H) = 103.8				

a) all values in kcal mol^{-1} except AE (eV)
b) all values from Benson additivity unless otherwise specified
c) all values from ref. 10 unless otherwise stated

Table 5.2.2 contains the alternative pathways for the formation of the desired counter ion which are the closest thermochemical competitors with the simple bond cleavage (refer to sec. 3.5.4 for a discussion of competitive dissociations). For example, in 1-3, the energy requirement for the production of neutral fragments HĊO and CH_4 is lower than for any other neutral pair of total elemental composition $C_2H_5O^+$ ($\Sigma\Delta_fH°_{298}$ values [10] are HĊO + CH_4 = -7.1 kcal mol^{-1}; H_2 + $^{\cdot}C_2H_3O$ = -6; $C_2H_3^{\cdot}$ + H_2O = 5.6; $CH_3^{\cdot}$ + CH_2O = 8.8; $H^{\cdot}$ + CH_3CHO = 12.5; C_2H_4 + $^{\cdot}OH$ = 21.8; $C_2H_5^{\cdot}$ + O = 87.6). The 3-hydroxypropyl radical, $^{\cdot}CH_2CH_2CH_2OH$ was formed from ionized 5-hydroxypentan-2-one (6). Loss of H_2O and $C_3H_5^{\cdot}$ yields a δ value (sec. 3.5.4, $\delta = \Sigma\ \Delta_fH°_{298}$(neutral losses) - $\Delta_fH°_{298}(R^{\cdot})$) of -2.9 kcal mol^{-1}. It was necessary, therefore, to measure the appearance

energy of the intermediate ion $[C_5H_{10}O_2 - H_2O]^{+\cdot}$, m/z 84. The result showed that the minimum energy barrier for the alternative pathway was greater than that for the desired reaction by at least 0.4 eV. The compound 1,4-pentanediol (7), another 3-hydroxypropyl radical precursor, also exhibits this reaction, losing $C_3H_5^{\cdot}$ first. Again, the AE of the intermediate ion $[C_5H_{12}O_2 - C_3H_5^{\cdot}]^+$, m/z 63, was found to be greater than that of the desired fragment ion at m/z 45. The isomeric radical, $CH_3\dot{C}HCH_2OH$, is produced from 2-methyl-1,3-propanediol (11), whose molecular ion was observed in its MIKE spectrum to lose $CH_3\dot{C}O$ followed by CH_4 resulting in a δ of -4.0. An appearance energy of the intermediate ion at m/z 47, $[C_2H_7O]^+$, showed that this process could not compete with the desired simple bond cleavage. The only exception was item 13 in Table 5.2.1, for which the energy barrier to consecutive losses of H_2O and $CH_3\dot{C}O$ was found to be 0.54 eV less than that of the bond cleavage forming $HO\dot{C}HCH_2OH$, leaving some doubt as to the reliability of the new value.

For 22-26, which form the $^{\cdot}C(O)OCH_3$ radical, none of the normal mass spectra of the parent molecules contains a peak due to loss of carbon dioxide and only one, 22, contains a peak due to methyl loss. However, the ion formed by methyl loss from methyl isobutyrate (22), m/z 87, does not lose CO_2, negating the alternative pathway. In the case of $HC(O)O^{\cdot}$, the ester HC(O)O-t-Bu (29) has neither $[M-H]^+$ or $[M-CO_2]^{+\cdot}$ in its normal mass spectrum. This precludes the stated alternative pathway (see Table 5.2.2). Only a weak loss of 44 da. was observed in the MIKE spectrum of the $[M-H]^+$ ion from methoxymethylformate (30). The initial barrier to $H^{\cdot}$ loss (typically quite large) should be sufficient to preclude this pathway from competition with the desired bond cleavage.

Ethyl acetate (31) has neither $[M-CH_3]^+$ nor $[M-CO_2]^{+\cdot}$ in its normal mass spectrum, eliminating their competition with the desired bond cleavage. The normal mass spectrum of methoxymethylacetate (32) has a peak at $[M-15]^+$ but not at $[M-44]^{+\cdot}$. Methyl loss from the molecular ion was not observed to be a metastable process, thus eliminating this alternative pathway from competition with the simple bond cleavage.

Table 5.2.2

Lowest Energy Alternative Processes Producing Counter Ions, Y^+

Reaction	Neutral,N_1	$\Delta_f H°_{298}(N_1)$[a,10]	Neutral,N_2[b]	$\Delta_f H°_{298}(N_2)$[a,10]	δ[a]
1,2,3	HCO	10.7	CH_4[c]	-17.8	+6.4
4,5	HCO	10.7	CH_4	-17.8	+7.4
6,7	H_2O[d]	-57.8	C_3H_5[c]	39.0	-2.8[e]
	C_3H_5[d]	39.0	H_2O[c]	-57.8	-2.8[e]
	CH_3CO[d]	-6.0	CH_4	-17.8	-7.8[f]
8,9[g]	C_3H_5[d]	39.0	H_2O[c]	-57.8	+3.5
	H_2O[d]	-57.8	C_3H_5[c]	39.0	+3.5
	CH_3CO[d]	-6.0	CH_4	-17.8	-1.6[f]
10	C_4H_7[d]	29.0	H_2O[c]	-57.8	+4.8
11	CH_3CO[d]	-6.0	CH_4[c]	-17.8	-4.0[e]
12[g]	CH_3CO	-6.0	CH_4	-17.8	+1.8[h]
13	H_2O[d]	-57.8	CH_3CO[c]	-6.0	-10.2
14	CO_2	-94.1	CH_3[c]	34.8	+2.3
15,16[g]	CH_3CO	-6.0	CH_2O[c]	-26.0	+25.5
	C_3H_3O[d]	17.0	H_2O	-57.8	+16.7[i]
17	CH_3[d]	34.8	CH_3CHO[c]	-39.6	+6.0
	CH_3CO[d]	-6.0	CH_4	-17.8	-13.0[f]
	H_2O[d]	-57.8	C_3H_5	39.0	-8.0[f]
18-21	H	52.1	CO_2	-94.1	+3.8
22-26	CH_3	34.8	CO_2	-94.1	-19.4[j]
	CO_2	-94.1	CH_3	34.8	-19.4[j]
27	H	52.1	O_2	0.0	+48.6
28	$(CH_3)_3C$	11.0	O_2	0.0	+36.2
29,30	H	52.1	CO_2	-94.1	-4.1[j]

	CO_2	-94.1	H	52.1	-4.1[j]
31,32	CH_3	34.8	CO_2	-94.1	-7.8[k]
	CO_2	-94.1	CH_3	34.8	-7.8[k]

a) kcal mol^{-1}; b) all intermediate ions were observed in the normal mass spectrum, unless otherwise stated; c) neutral loss observed in MIKE spectrum of intermediate ion; d) neutral loss observed in MIKE spectrum of parent ion; e) AE(intermediate ion) > $AE(Y^+)$ by at least 9 kcal mol^{-1}; f) intermediate ion does not yield Y^+; g) counter ion Y^+ observed in MI mass spectrum of parent ion; h) neither neutral loss was observed to be a metastable process; i) neither possible intermediate ion was observed in the normal mass spectra of 23-26; only $[M-CH_3]^+$ was observed in the normal mass spectrum of 22 (see text); j) neither possible intermediate ion was observed in the normal mass spectrum of 29; for discussion of 30, see text; k) neither possible intermediate ion was observed in the normal mass spectrum of 31; only $[M-CH_3]^+$ observed in normal mass spectrum of 32 (see text)

Before discussing the results in detail, some remarks must be made concerning the heats of formation of the neutral diols used in this study (Table 5.2.1, (4),(7)-(13)). A significant problem arises with the 1,3-diols. In this work we used $\Delta_fH^\circ_{298}$ values calculated by additivity rather than those available from, or based on, experimental values found in the most recent compilation [9]. Of the nine alkane diols in ref. 9, except for 1,3-propanediol, 1,3-butanediol, and 2,3-butanediol, the $\Delta_fH^\circ_{298}$ values agree with additivity based values to within 1 kcal mol^{-1}. For the first two diols above, the reference values are 3 kcal mol^{-1} more positive than those calculated by additivity. It is difficult to see how such discrepancies can arise, there being no obvious anomaly, such as a suspect ΔH°_{vap} value [9], and no likely physicochemical explanation (e.g. based on molecular geometry or H-bonding effects) comes to mind. Gardner and Hussain [11], in the original calorimetric work, noted that $\Delta_fH^\circ_{298}$ of 1,3-propanediol appeared to be too high by ~ 4 kcal mol^{-1}. However, like us, they could find no obvious explanation. Thus, for the diols

(8)-(11) in Table 1, the $\Delta_f H°_{298}$(RY) values could be estimated by modifying the experimentally derived values [9] for 1,3-propanediol, using appropriate additivity terms for methyl substitution. This would give $\Delta_f H°_{298}$ values greater by +3 kcal mol^{-1} than those from additivity alone. If the additivity based values are incorrect then this may manifest itself in anomalously low C-H bond strengths for (8)-(11) (see later discussion).

For 2,3-butanediol (4), the experimental $\Delta_f H°_{298}$ is 4.7 kcal mol^{-1} more negative than the additivity based value. The experimental $\Delta H°_{vap}$ [9] appears to be too low when compared with all of the other diols, having a Trouton's constant of 31 e.u. (cal mol^{-1} K^{-1}) compared with 34.5 e.u for $(CH_2OH)_2$ and 33.3 e.u. for $CH_3CH(OH)CH_2OH$, but this does not suffice to explain the 4.7 kcal mol^{-1} difference. A value of -112.0 kcal mol^{-1} was selected, slightly more negative than the additivity result, -111.0 kcal mol^{-1}. As will be seen, this does not produce an anomaly in the thermochemical data discussed below.

It is now appropriate to compare the present data with values from the literature and to discuss the significance of new values.

A previous attempt [12] at estimating the heat of formation of the 2-hydroxyethyl radical assumed a bond strength, D(R-H), equal to that in ethane (100.7 kcal mol^{-1} [13]) yielding a value for $\Delta_f H°_{298}(HOCH_2CH_2^{\bullet})$ of -7.5 kcal mol^{-1}. McMillen and Golden [7] list a value of 94 ± 2 kcal mol^{-1} for the bond strength which is in excellent agreement with the present value of 94.8 kcal mol^{-1}. For $CH_3\dot{C}HOH$, a previous determination from this laboratory [3] of the heat of formation gave -17.7 kcal mol^{-1}, in poor agreement with the value listed by McMillen and Golden [7], -15.2 kcal mol^{-1}. We have modified the heat of formation of the precursor molecule $CH_3CH(OH)CH(OH)CH_3$ (4) (see above discussion

on diol thermochemistry) resulting in a $\Delta_f H°_{298}(CH_3\dot{C}HOH)$ of -14.4 kcal mol^{-1}, in close agreement with the value obtained from $CH_3CH(OH)CH_2NH_2$, -14.6 kcal mol^{-1}. Both values are now in good agreement with that in ref. 7. Two separate experimental determinations of $\Delta_f H°_{298}$ ($(CH_3)_2\dot{C}OH$) by Benson [14,15], using the iodine abstraction method, gave -27 kcal mol^{-1} for the heat of formation and 90.5 kcal mol^{-1} for D(H-C(OH)$(CH_3)_2$), in good agreement with our values of -25.6 and 91.7 kcal mol^{-1}. The heat of formation of the 2-hydroxypropyl radical, $^{\bullet}CH_2CH(OH)CH_3$, was estimated from group additivity [16] to be -18.8 kcal mol^{-1}, 4.2 kcal mol^{-1} higher than our value of -23.0 kcal mol^{-1}.

The heat of formation of the resonance stabilized carboxymethyl radical (14) has been estimated from semi-empirical calculation [17] to be -59.1 kcal mol^{-1}, and from trends in experimentally determined $^{\bullet}CH_2OR$ heats of formation [18] to be -58.1 kcal mol^{-1}, both in reasonable agreement with our result of -61.6 kcal mol^{-1}.

Mozurkewich et. al. [19] used a modified version of RRKM theory to calculate rate constants and barrier heights for the reaction $HO^{\bullet} + CO \rightleftharpoons {}^{\bullet}C(O)OH \rightarrow H^{\bullet} + CO_2$. This gave a heat of formation for $^{\bullet}C(O)OH$ of -50.7 kcal mol^{-1}, and D(H-C(O)OH) = 91.9 kcal mol^{-1}. More recently a value of -53.2 ± 0.6 kcal mol^{-1} was derived from a photoionization mass spectrometry study [20]. This result was based upon a new determination of $\Delta_f H°_{298}(C(O)OH)^+$ = 143 kcal mol^{-1} and the ionization energy of the radical generated by the reaction of $F^{\bullet}$ with formic acid. This leads to a lower strength for the above bond, 90.1 kcal mol^{-1}. Our result of $\Delta_f H°_{298}$ = -46.0 kcal mol^{-1} gives a considerably higher value for the bond strength, 96.6 kcal mol^{-1}. Ab initio calculations,

at the 6-311G**//MP3 level, by Tse [21] on the reaction of HO˙ + CO yield a significantly higher value for the heat of formation of ˙C(O)OH, -36.5 kcal mol^{-1}, with a barrier to fragmentation to HO˙ + CO of 2.8 kcal. Calculations by Schatz et. al. [22] gave -41.6 kcal mol^{-1} but they modified this value to -51.1 kcal mol^{-1} following consideration of experimental data from the literature. Thus there is poor agreement between the above values for $\Delta_fH^\circ_{298}$(˙C(O)OH). The difference between the present results and the $\Delta_fH^\circ_{298}$ of Ruscic et. al. [20], 6.5 kcal mol^{-1}, is difficult to rationalize, particularily since our value is based on four independent measurements which lie within a narrow range, -46.0 ± 1.1 kcal mol^{-1}. Our results do agree with a recent value by Schwarz and Dodson [23], -47.0 kcal mol^{-1}, estimated from the reduction potential of $CO_2^{\cdot-}$ in aqueous solution. Note that we find for the closely related radical, ˙C(O)OCH$_3$, $\Delta_fH^\circ_{298}$ = -39.9 kcal mol^{-1} and a bond strength similar to that for formic acid, D(H-C(O)OCH$_3$) = 97.2 kcal mol^{-1}.

McMillen and Golden [7] list $\Delta_fH^\circ_{298}$(˙C(O)OCH$_3$) = -40.4 kcal mol^{-1} and 92.7 kcal mol^{-1} for D(H-C(O)OCH$_3$). However, these values are not mutually compatible; the quoted radical heat of formation, -40.4 kcal mol^{-1}, combined with the reliable heat of formation of HC(O)OCH$_3$, -85.0 kcal mol^{-1}, gives a bond strength of 96.7 kcal mol^{-1}. It would appear that the -40.4 kcal mol^{-1} value is a misprint!

The heat of formation of HC(O)O˙ was determined by Nishimura, et.al. [24], to be -40 ± 6 kcal mol^{-1} from the appearance energy of CH_3^+ from methylformate, 13.27 ± 0.24 eV. It is in fair agreement with the present result of -37.7 kcal mol^{-1}, but the AE value will certainly be inaccurate; the reaction leading to CH_3^+ is the sixth fragmentation in ascending energy for methyl formate and so kinetic and competitive shifts will be

significant. Semi-empirical calculations [25a] estimate $\Delta_f H°_{298}(HC(O)O^{\cdot})$ = -35.1 kcal mol^{-1}. The calculations by Schatz [22] give a value of -31.1 kcal mol^{-1}, modified to -42.2 kcal mol^{-1}, again by reference to experimental data.

The present results for the heat of formation of the $CH_3C(O)O^{\cdot}$ radical, -51.7 kcal mol^{-1}, and $D(H\text{-}O(O)CCH_3)$, 103.8 kcal mol^{-1}, are in reasonable agreement with those in ref. 7, -49.6 kcal mol^{-1} and 105.8 kcal mol^{-1}. Semi-empirical and local spin density (LCGTO-NLDA) calculations [25a,b] estimate the heat of formation to be -44.0 kcal mol^{-1} and -55.6 kcal mol^{-1} respectively.

McMillen and Golden [7] list a value for the heat of formation of $HO_2^{\cdot}$ of 2.5 kcal mol^{-1}, corresponding to 87.2 kcal mol^{-1} for D(H-OOH). Fisher and Armentrout [26] have recently reported $\Delta_f H°_{298}(HO_2^{\cdot})$ to be 3.8 ± 1.2 kcal mol^{-1} and D(H-OOH) to be 88.4 kcal mol^{-1}, from guided ion beam mass spectrometric studies of the reaction of O_2^+ with CH_4. Our values of 3.5 and 88.2 kcal mol^{-1} are in excellent agreement with this result, as well as with that suggested by Shum and Benson [27], 3.5 kcal mol^{-1}, in a critical analysis of available data. For the t-butylperoxy radical $(CH_3)_3COO^{\cdot}$, Heneghan and Benson [28] reported a heat of formation of -20.7 kcal mol^{-1} and $D(H\text{-}OOC(CH_3)_3)$ of 89.4 kcal mol^{-1} from a direct measurement of the equilibrium constant for $Br^{\cdot}$ + t-$C_4H_9O_2H$ ⇌ t-$C_4H_9O_2^{\cdot}$ + HBr and an estimate for $\Delta S°$. Our results are lower, -25.2 and 85.7 kcal mol^{-1}. Recalling that the AE method, due to kinetic shift and reverse activation energy, gives at worst upper limits for the radical heats of formation, the value obtained by Heneghan and Benson may be too high, possibly arising from uncertainty in $\Delta_f H°_{298}$(t-BuOOH). There are remarkably few [9] values for $\Delta_f H°_{298}$(ROOH), making it impossible to check for

consistency among them.

5.2.3 Thermochemical conclusions

Table 5.2.3 contains a comparison of the bond strengths found for the alcohols, D(R-H), with those of the corresponding alkane, D(A-H).

Table 5.2.3

A Comparison of Bond Strengths of Hydroxy Substituted (position X with respect to the bond in question) Alkyl Radicals, R$^{\bullet}$, With Those From the Corresponding Alkyl Radical, A$^{\bullet}$[a]

A$^{\bullet}$	$\Delta_fH°_{298}$ (A$^{\bullet}$)[b]	$\Delta_fH°_{298}$ (AH)[9]	D(A-H)[c]	R$^{\bullet}$	X	$\Delta_fH°_{298}$ (R$^{\bullet}$)[d]	$\Delta_fH°_{298}$ (RH)[9]	D(R-H)	Δ
CH_3	35.1[44]	-17.8	105	$HOCH_2$	α	-5.7[3]	-48.2	94.6	-10.4(a)
CH_3CH_2	27.8	-20.1	100.0	$HOCH_2CH_2$	β	-13.5	-56.2	94.8	-5.2(b)
$CH_3CH_2CH_2$	22.7	-25.0	99.8	$CH_3CH(OH)CH_2$	β	-23.0	-65.2	94.3	-5.5(c)
				$HOCH_2CH_2CH_2$	γ	-16.0	-61.0	97.1	-2.7(d)
$(CH_3)_2CH$	19.1	-25.0	96.2	CH_3CHCH_2OH	β	-18.8	-61.0	94.3	-1.9(e)
$(CH_3)_2CHCH_2$	15.8	-32.1	100.0	$(CH_3)_2C(OH)CH_2$	β	-35.2	-74.7	91.6	-8.4(f)

a) all values kcal mol^{-1}; b) from ref. 1 unless otherwise specified; c) uses $\Delta_fH°_{298}(H^{\bullet})$ = 52.1 kcal mol^{-1}; d) this work unless otherwise specified

The differences between the bond strengths are given by Δ = D(R-H) - D(A-H). Most of the heats of formation of the alkyl radicals (A$^{\bullet}$) used in the comparison were those determined in earlier work [1], values which compared extremely well with those reported by Griller and Castelhano [6], all values agreeing within the estimated experimental errors. The trend in the bond strengths in going from primary (~ 100 kcal mol^{-1}, except for methane) to secondary (96-7 kcal mol^{-1}) to tertiary (~ 94 kcal mol^{-1}) is evident from both works. For (a), where the OH group replaces hydrogen α to a primary

C-H bond, the C-H bond strength is lowered by 10.4 kcal mol^{-1}. The difference (Δ), for a given C-H bond type, is approximately halved for each carbon atom farther away from the bond that the substituent is placed. Thus, β-substitution decreases the strength of a primary bond by ~ 5 kcal mol^{-1} (b,c), while γ-substitution decreases the bond strength by only ~ 2.7 kcal mol^{-1} (d). The bond strength in H-$CH_2C(OH)(CH_3)_2$ is quite low at 91.6 kcal mol^{-1}, indicating a reduction of 8.4 kcal mol^{-1} (f). There is no clear reason why it should be different from the other two β-OH substituted analogues (b,c). The effect on a secondary C-H bond strength is about half that on a primary bond, as β-hydroxy substitution only weakens the bond by 1.9 kcal mol^{-1}, as opposed to 5 kcal mol^{-1} for primary bonds.

If the experimental values [9] for the heats of formation of 1,3-propanediol and 1,3-butanediol are accurate, then it is necessary to add +3 kcal mol^{-1} to the values obtained using additivity terms. If this applies to the similar molecules in Table 5.2.1, it is necessary to add +3 kcal mol^{-1} to the heats of formation of (8)-(10). The resulting radical heats of formation, $\Delta_fH°_{298}(^{\cdot}CH_2CH(OH)CH_3)$ = -20.0 kcal mol^{-1}, $\Delta_fH°_{298}$ $(^{\cdot}CH_2C(OH)(CH_3)_2)$ = -32.2 kcal mol^{-1}, and $\Delta_fH°_{298}(CH_3\dot{C}HCH_2OH)$ = -15.8 kcal mol^{-1}, give bond strengths of 97.3, 94.6, and 97.3 kcal mol^{-1} respectively. The first two values indicate a lowering of the primary C-H bond strength due to β-OH substitution by 2.5 and 5.2 kcal mol^{-1} respectively. The former value is even less than the observed effect of γ-substitution, 2.7 kcal mol^{-1}! Also, D(H-$CH(CH_3)CH_2OH$) = 97.3 kcal mol^{-1} means the secondary C-H bond strength has been <u>increased</u> by 1.1 kcal mol^{-1} over the simple alkane C-H bond strength. We would argue that these anomalous results justify our choice of the

neutral $\Delta_f H°_{298}$ values from additivity.

There is also a trend in the heats of formation and bond strengths for consecutive methyl substitution on the $^{\bullet}CH_2OH$ radical. The heats of formation of $^{\bullet}CH_2OH$, -5.7 kcal mol^{-1}, $CH_3\dot{C}HOH$, -14.5 kcal mol^{-1}, and $(CH_3)_2\dot{C}OH$, -25.6 kcal mol^{-1} are separated by ~ 10 kcal mol^{-1}. From a study of anion reduction potentials in solution, Schwarz and Dodson [23] derived $\Delta_f H°_{298}$ values for all three of these radicals, each about 3 kcal mol^{-1} lower than the present results, leading to higher bond strengths. The bond strengths, D(R-H), which follow from our values are 94.6, 93.8, and 91.7 kcal mol^{-1} respectively. The decrease in bond strength in going from a primary to a tertiary C-H bond in these alcohols parallels the trend in alkanes, but to a lesser degree.

This work has been published [29].

5.3 Cyano - Substituted Radical Cation Thermochemistry

5.3.1 Introduction

The purpose of this communication is to give a general review of the cyano functionality in gas phase ion and neutral thermochemistry, with emphasis upon the behaviour of the -CN group in the presence of a positive charge. There are two possibilities for the interaction of a -CN group with the charge centre of an ion. Either the cyano group directly participates in the charge centre, involving itself in the delocalized charge to a significant extent (π or conjugative effect), or it acts only as an inductive electron withdrawing group (due to the δ^+ C≡N δ^- dipole), separate from the

charge centre (σ effect). The two cases are extreme but useful starting points, allowing the results to be discussed in terms of the degree to which the -CN group behaves as one or the other in a given ion.

The investigation was directed by studying, 1) semi-empirical calculations, 2) cationic heats of formation and 3) neutral molecule ionization energies. Semi-empirical calculations (MNDO) were performed in order to understand the charge distribution in the four general types of radical cations described here, namely saturated radical cations, double and triple bond containing radical cations and aromatic ring containing radical cations. The focus of the calculations was to determine whether a charge bearing -CN group or an uncharged, σ- electron withdrawing -CN was the better representation. The calculated result was a mixture of the two. The degree of such mixing was reflected in the effect of the -CN group on cationic heats of formation. The change in $\Delta_f H^\circ_{298}$ of a cation upon substitution of -H with -CN was investigated for radical cations in the four above classes. The vehicle for comparing this change in heat of formation was designated Δ, which equals $\Delta_f H^\circ_{298}(R\text{-}CN^{+\bullet}) - \Delta_f H^\circ_{298}(R\text{-}H^{+\bullet})$, and, as described below, was always a positive quantity. A constant positive value of Δ for all of the ions studied would be consistent with an inductive electron withdrawing -CN group. It would destabilize the ion by a fixed amount, independent of the nature of the charge centre. On the other hand, if acting as a π donor, then its effect might be expected to vary depending on both the functional groups in the ion and the particular extent to which charge is delocalized to the -CN group.

Examining ionization energies (IE) allows the effect of the -CN group on both the

neutral molecule and the radical cation to be determined simultaneously. Any increase or decrease in ionization energy can be explained by relating it to the corresponding behaviour in the neutrals and ions. An increase in IE over the -H substituted analogue means that the -CN group destabilizes the ion more than the corresponding neutral, a result consistent with a predominantly σ-electron withdrawing group. A σ-electron withdrawing group has a greater impact on a cation's $\Delta_f H^\circ_{298}$ than on that of the neutral since a shift in electron density will be more significant to the ion's stability than to that of the neutral. A decrease in IE means that the ion has been destabilized to a lesser degree than the corresponding neutral. This would be expected of an ion in which the -CN group participated to a large extent in the charge centre, adding a stabilizing factor due to conjugation.

All of the observed results can be explained according to the above discussion. The behaviour of the -CN group has been likened to a halogen in organic chemistry; however, in thermochemistry, it will be shown that its behaviour is decidedly unlike halogens. Rather, it serves only to raise the heat of formation of ions and radicals relative to their -H counterparts and does not interact strongly with the charge centre.

Also presented are new thermochemical measurements for six species. The electron impact appearance energy technique was used to determine the heats of formation of cyanoketene, the benzoyl cyanide and benzoyl acetonitrile radical cations and the cyanoacetyl cation. The heats of formation of the cyanoketene radical cation and the cyanoacetyl radical were also estimated.

5.3.2 Experimental

Appearance energy (AE) measurements in this study were performed on a Kratos MS-902 S mass spectrometer by M. Vasseur as part of his fourth year project in Honours Chemistry at the University of Ottawa. The technique employed has been described elsewhere [30]. All compounds were commercially available and used without further purification. The AE determinations on t-butyl cyanoacetate and methyl cyanoacetate were calibrated with the metastable dissociation of diethylether,

$$CH_3CH_2OCH_2CH_3 + e^- \rightarrow CH_3CH_2OCH_2CH_3^{+\bullet} + 2e^- \rightarrow CH_3CH_2OCH_2^+ + CH_3^\bullet + 2e^-$$

which has a known AE, 10.26 eV [31]. Ionization energies (IE) for benzoyl cyanide and benzoyl acetonitrile were calibrated using the IE of benzene as a standard, IE = 9.25 eV [10].

AMPAC MNDO Ver. 3.0 calculations [32] were performed on a personal computer.

5.3.3 Results and Discussion

The following is a summary of the available data for -CN substituted odd electron cations. Only limited data were available for even electron cations (protonated species and fragment ions) and they were of poor quality. However, an assortment of molecular orbital calculations [33-38] indicate that for α-CN substituted even electron cations, resonant charge delocalization is only significant for $^+CH_2CN$. For higher homologues, the

inductive electron withdrawing nature of the -CN group dominates, destabilizing the cations relative to their -H substituted analogue. There has been an attempt to connect these results with the magnitude of the rate retarding nature of -CN in solution chemistry [39,40]. It must be emphasized that there are few experimental even electron cation heats of formation and free radical ionization energies to support these findings. Data for -CN substituted radical anions are reasonably abundant but those for the unsubstituted analogues are not. For these reasons, only -CN substituted radical cations are treated in this section. A discussion of -CN substituted even electron cations is presented in sec. 5.4.

Identifying the Charge Centre in Radical Cations

Semi-empirical MNDO calculations were performed on a selection of the radical cations in this study in order to determine where the charge resided, Table 5.3.1.

Table 5.3.1

Distribution of Charge in R-CN$^{+\cdot}$ as Calculated by MNDO

-R	% Charge on -R	% Charge on -CN
$-CH_3$	63	37
$-CH_2CH_3$	84	16
$-CH_2CH_2CH_3$	94	6
-CH=CH2	92	8
$-CH_2CH=CH_2$	110	-10 (partially negative)
-C≡CH	70	30
$-C\equiv CCH_3$	77	23
-C≡CF	71	29
-C≡CCl	77	23
-C≡CBr	79	21

-C≡CI	83	17
$-C_6H_5$	106	-6 (partially negative)

As can be seen from Table 5.3.1, for ions other than $CH_3CN^{+\bullet}$, the -CN group does not participate greatly in the charge centre. Thus, the effect of the cyano group on ionization energy and cationic heat of formation appears to be dominated by its σ-electron withdrawing nature. With this in mind, a review of the thermochemistry of cyano-substituted radical cations can be made.

Saturated Radical Cations

The heats of formation of nine -CN substituted radical cations were compared with their -H substituted analogues, Table 5.3.2.

Table 5.3.2

-CN Substitution in Saturated Radical Cations[a]

R-H	$\Delta_fH°_{298}$(ion) kcal mol^{-1}	IE eV	R-CN	$\Delta_fH°_{298}$(ion) kcal mol^{-1}	IE eV	Δ kcal mol^{-1}
CH_4	271	12.62	CH_3CN	299	12.2	+28
			$CH_2(CN)_2$	(356)	12.7	2 x +43
			$C(CN)_4$	(482)	13.9	4 x +53
$CHCl_3$	237	11.37	CCl_3CN	(294)	11.9	+57
CHF_3	154	13.86	CF_3CN	200	13.9	+46
CH_3CH_3	245.6	11.52	CH_3CH_2CN	285	11.8	+39
$CH_3CH_2CH_3$	227.5	10.95	$CH_3CH(CN)CH_3$	(266)	11.3	+38.5

				$CH_3CH_2CH_2CN$	(266)	11.2	+38.5
cyclo-C_3H_6	240		9.86	cyclo-C_3H_5CN	280	10.3	+40

a. all values from ref.10. Values in parentheses were so in ref.10.

The effect of substituting -CN for -H , $\Delta = \Delta_fH°_{298}(R\text{-}CN^{+\bullet}) - \Delta_fH°_{298}(R\text{-}H^{+\bullet})$, was approximately constant at 41 ± 2 kcal mol^{-1}. The three exceptions, $C(CN)_4^{+\bullet}$, $CCl_3(CN)^{+\bullet}$, and $CH_3CN^{+\bullet}$ were left out of this average. The first two have potentially unreliable $\Delta_fH°_{298}$ values since they involved an estimated neutral $\Delta_fH°_{298}$. The anomaly for $CH_3CN^{+\bullet}$ may be explained by a change in charge site. When IE values of -CN substituted species were compared with their unsubstituted analogues, it was found that the cyano group raises the ionization energy of all except CH_4, Table 5.3.2. Holmes and Lossing [41] found that a plot of IE vs 1/n for a homologues series of molecules produced a straight line with slope indicative of the nature of the functional group. If treated similarly, data for -CN substituted molecules yields a line with slope greater than that for the unsubstituted alkanes and much greater than that observed for halo-substituted alkanes, Figure 5.3.1. Thus, the cyano functionality has made it more difficult to ionize the molecule, consistent with what is expected from an inductive electron withdrawing group. The exception is IE(CH_3CN), which lies below IE(CH_4). In $CH_3CN^{+\bullet}$, almost 40% of the positive charge is centred on the -CN group (Table 5.3.1), reducing its destabilizing σ-electron withdrawing nature. Thus the heat of formation of the cation is raised by an amount less than the other cations in Table 5.3.1, resulting in a Δ of only + 28 kcal mol^{-1}. Also, the increase in cationic $\Delta_fH°_{298}$ is less than the increase observed for the neutral,

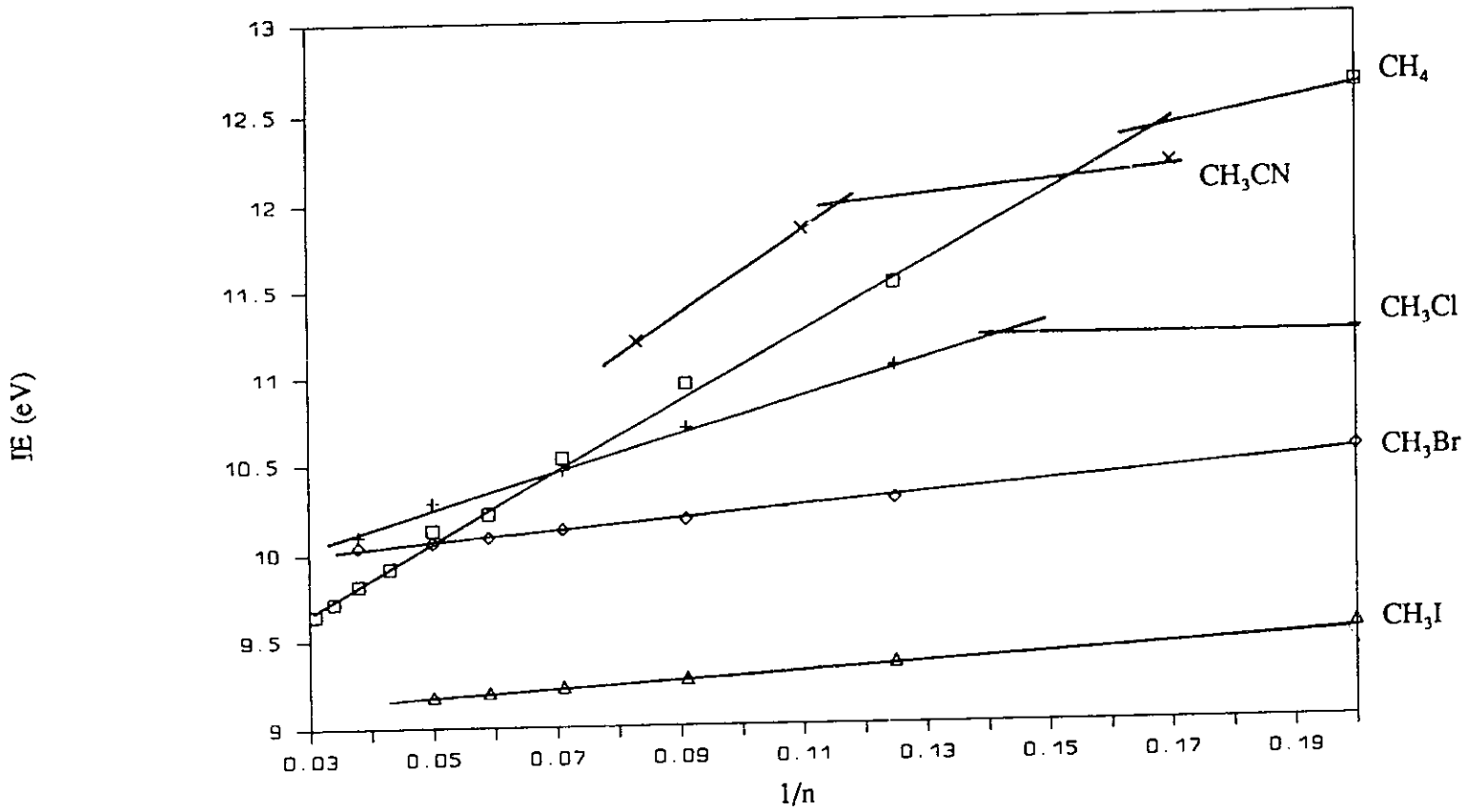

Figure 5.3.1. Plot of IE vs 1/n for saturated radical cations with substituent -H, -CN, -Cl, -Br and -I, where n equals the number of atoms in each ion.

$\Delta_f H°_{298}(CH_3CN)$ - $\Delta_f H°_{298}(CH_4)$ = 35.8 kcal mol^{-1} [10], leading to a decrease in IE compared with IE(CH_4).

Double Bond Containing Radical Cations

Table 5.3.3 shows the effect on cationic heats of formation when -CN replaces -H in double bond containing ions. Generally, there is a 43 ± 3 kcal mol^{-1} increase in $\Delta_f H°_{298}$

Table 5.3.3

-CN Substitution in Double Bond Containing Radical Cations[a]

R-H	$\Delta_f H°_{298}$(ion) kcal mol^{-1}	IE eV	R-CN	$\Delta_f H°_{298}$(ion) kcal mol^{-1}	IE eV	Δ kcal mol^{-1}
$CH_2=CH_2$	256	10.51	$CH_2=CHCN$	296	10.9	+40
			$CH(CN)=CHCN$	(338)	11.2	2 x +41
			$C(CN)_2=CHCN$	(390)	11.6	3 x +45
$CH_3CH=CH_2$	229	9.73	$CH_2=CHCH_2CN$	273	10.2	+44
			$CH_2=C(CN)CH_3$	269	10.3	+40
			$CH(CN)=CHCH_3$	(≤27[illegible])	10.2	≤+43
$CH_2=C=O$	210	9.61	$C(CN)_2=C=O$	(300)	10.6	2 x +45
$CH_2=C=S$	(242)	8.77	$C(CN)_2=C=S$	(339)	9.9	2 x +49

a. all values from ref.10. Values in parentheses were so in ref.10.

with the addition of a cyano substituent. This value is similar to that obtained for saturated radical cations. Moreover, the change in IE, ΔIE, resulting from mono substitution appears to be largely independent of the position of the -CN group, Table 5.3.3, ΔIE ≈ 10 ± 2 kcal mol^{-1}. Thus, the -CN functionality only increases the ionization

energy of the alkene but does not change the site of ionization itself. These results are also consistent with a predominantly σ-electron withdrawing -CN group and the typical charge distribution for these types of ions shown in Table 5.3.1.

Triple Bond Containing Radical Cations

Unfortunately there is a severe lack of data for these ions, as can be seen from Table 5.3.4, which includes all available values.

Table 5.3.4

-CN Substitution in Triple Bond Containing Radical Cations[a]

R-H	$\Delta_f H°_{298}$(ion) kcal mol^{-1}	IE eV	R-CN	$\Delta_f H°_{298}$(ion) kcal mol^{-1}	IE eV	Δ kcal mol^{-1}
HC≡CH	317.4	11.40	HC≡CCN	352	11.64	+35
FC≡CH	285	11.26	FC≡CCN	(305)	11.51	+20
ClC≡CH	305	10.58	ClC≡CCN	334	10.95	+29
BrC≡CH	297	10.31	BrC≡CCN	(350)	10.71	+53
CH_3C≡CH	283.5	10.36	CH_3C≡CCN	(329)	10.78	+45.5
			IC≡CCN	(347)	10.18	

a. all values from ref.10. Values in parentheses were so in ref.10.

The effect of the cyano substituent, Δ, does not appear to be so constant as in the previous two classes. A plot of IE vs substituent (Figure 5.3.2) revealed two discontinuous lines of closely similar shape. Thus for all these compounds, the -CN group raises the ionization energy, independent of the other functionality. Using this data it was also possible to estimate the IE for I-C≡C-H, ~9.8 eV. This value may also be arrived at by considering the increase in IE between CH_2=CHX and HC≡CX (X = Br, Cl) [10]. Note

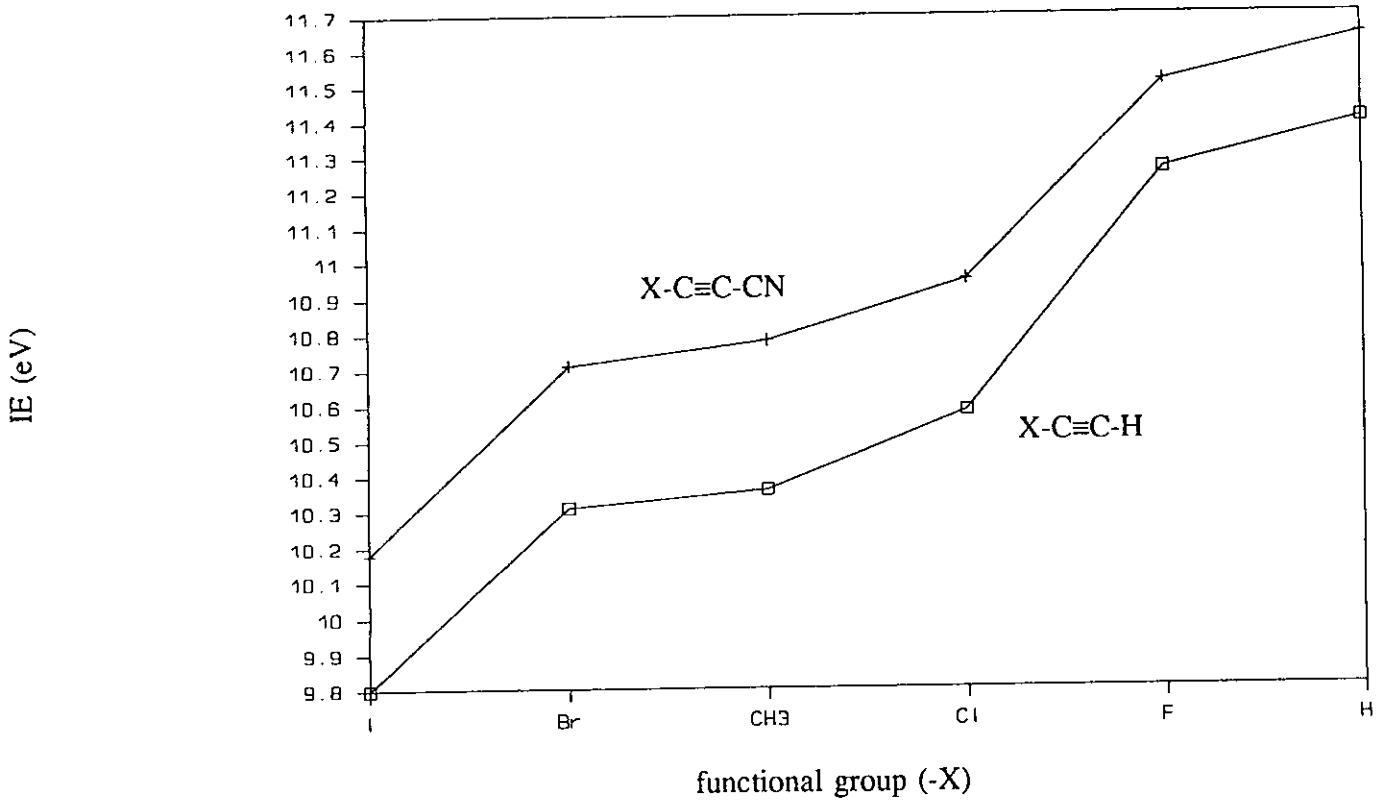

Figure 5.3.2. Plot of IE vs substituent for triple bond containing radical cations with either -H or -CN substituent.

that for H-C≡C-$CN^{+\bullet}$, the -CN group carries considerable charge (Table 5.3.1) and thus its σ- electron withdrawing nature is decreased, Δ being +35 kcal mol^{-1} (similar to that observed for $CH_3CN^{+\bullet}$ above). The value of Δ returns to +45 kcal mol^{-1} in CH_3-C≡C-$CN^{+\bullet}$, where the -CN group carries less charge (Table 5.3.1).

Aromatic Ring Substituted Radical Cations

The influence of replacing -H with -CN on substituted and unsubstituted benzenes is shown in Table 5.3.5. The data have been organized according to the type of substituent on the ring, be it electron withdrawing or donating, or if -CN substitution

Table 5.3.5

-CN Substitution in Benzene Ring Containing Radical Cations[a]

Ring Functionality	$\Delta_f H°_{298}$(ion) kcal mol^{-1}	IE eV	-CN subst.	$\Delta_f H°_{298}$(ion) kcal mol^{-1}	IE eV	Δ kcal mol^{-1}
H- (benzene)	233.2	9.25	-CN	274	9.6	+41
			1,2-diCN	316	9.9	2x +41.5
			1,3-diCN	322	10.2	2x +44.5
			1,4-diCN	318	10.1	2x +42.5
electron withdrawing groups						
NO_2-	243	9.86	m-CN	286	10.3	+43
			p-CN	283	10.2	+40
HC(O)-	210	9.49	p-CN	≤258	≤10.1	≤ +48
HOC(O)-	148	9.47	p-CN	193	10.0	+45
$CH_3C(O)$-	194	9.29	p-CN	≤237	≤9.8	≤ +40
electron donating groups						
F-	184.4	9.20	o-CN	231	9.8	+46.6
			m-CN	231	9.8	+46.6

				p-CN	229	9.7	+44.6
NH_2-		198	7.72	m-CN	252	8.6	+54
				p-CN	240	8.2	+42
CH_3-		215	8.82	o-CN	259	9.4	+44
				m-CN	259	9.3	+44
				p-CN	258	9.3	+43
CH_3O-		173	8.21	p-CN	213	8.6	+40
$(CH_3)_2N$-		118	7.12	p-CN	230	7.6	+42
n-C_4H_9-		198	8.69	m-CN	254	9.8	+56
				p-CN	261	10.1	+63
t-C_4H_9-		194	8.64	p-CN	229	8.8	+35
side chain substitution							
H-	,-CH_3	215	8.82	-CH_2CN	260	9.3	+45
	-C(O)H	210	9.49	-C(O)CN	256	9.9	+46[b]
	-$C(O)CH_3$	194	9.29	-$C(O)CH_2CN$	237	9.5	+43[b]
Cl-	,m-CH_3	208	8.83	m-CH_2CN	256	9.5	+48
	p-CH_3	205	8.69	p-CH_2CN	255	9.4	+50
CH_3-	,p-CH_3	158	8.44	p-CH_2CN	248	9.2	+49
CH_3O-	,p-CH_3	158	7.90	p-CH_2CN	209	8.8	+51
NO_2-	,p-CH_3	224	9.40	p-CH_2CN	274	10.1	+50

a. all values from ref.10 except where noted.
b. this work.

occurs on a side chain. Unfortunately, most of the cationic $\Delta_fH°_{298}$ values were obtained using "estimated" values for the neutral $\Delta_fH°_{298}$ and an ionization energy determined from onsets in photoelectron and photoionization spectra without, however, detailed investigations of the threshold regions themselves [10], giving rise to uncertainties in both quantities in Table 5.3.5. However, the results do show that the effect of -CN substitution

on $\Delta_f H^\circ_{298}$ values is independent of the other ring substituents and similar to that observed for the other ions discussed above. A plot of IE vs substituent, Figure 5.3.3, is similar to that found for the triple bond containing molecules, Figure 5.3.2, in that the general progression of IE values in para -H substituted rings is closely followed in para -CN substituted analogues. A similar trend is evident for the side chain substituted rings, Table 5.3.5. There is an anomaly in Figure 5.3.3 coinciding with 3-cyano butylbenzene. Note that the IE value for the m- substituted analogue, Table 5.3.5, is also considerably higher than expected from the overall trend in the figure. These IE values deserve to be confirmed.

The Thermochemistry of -CN Substitution in Neutral Molecules

Several neutral molecule group additivity terms in Benson's scheme [8] involve the cyano substituent. These have been revised and new terms introduced by Chu et. al. [42]. Two deserve attention. The first concerns the additivity term C_t-(CN) [≡C-CN group]. The current value for this term is 63.8 kcal mol^{-1} [42]. However, there are two sources for this, cyanoethyne and dicyanoethyne, which have $\Delta_f H^\circ_{298}$ values of 84 kcal mol^{-1} [10] and 126.5 kcal mol^{-1} [9] respectively. These two heats of formation lead to values for the additivity term C_t-(CN) of 57.1 and 63.3 kcal mol^{-1} respectively. The discrepancy between these therefore lends uncertainty to the assigned value which was determined only from dicyanoethyne [42].

The second uncertainty is for the term C_d-(C)(CN) [$=C<^{CN}_{C-}$ group] for which the reference value is 39.2 kcal mol^{-1} [8]. An inspection of available data shows that the only

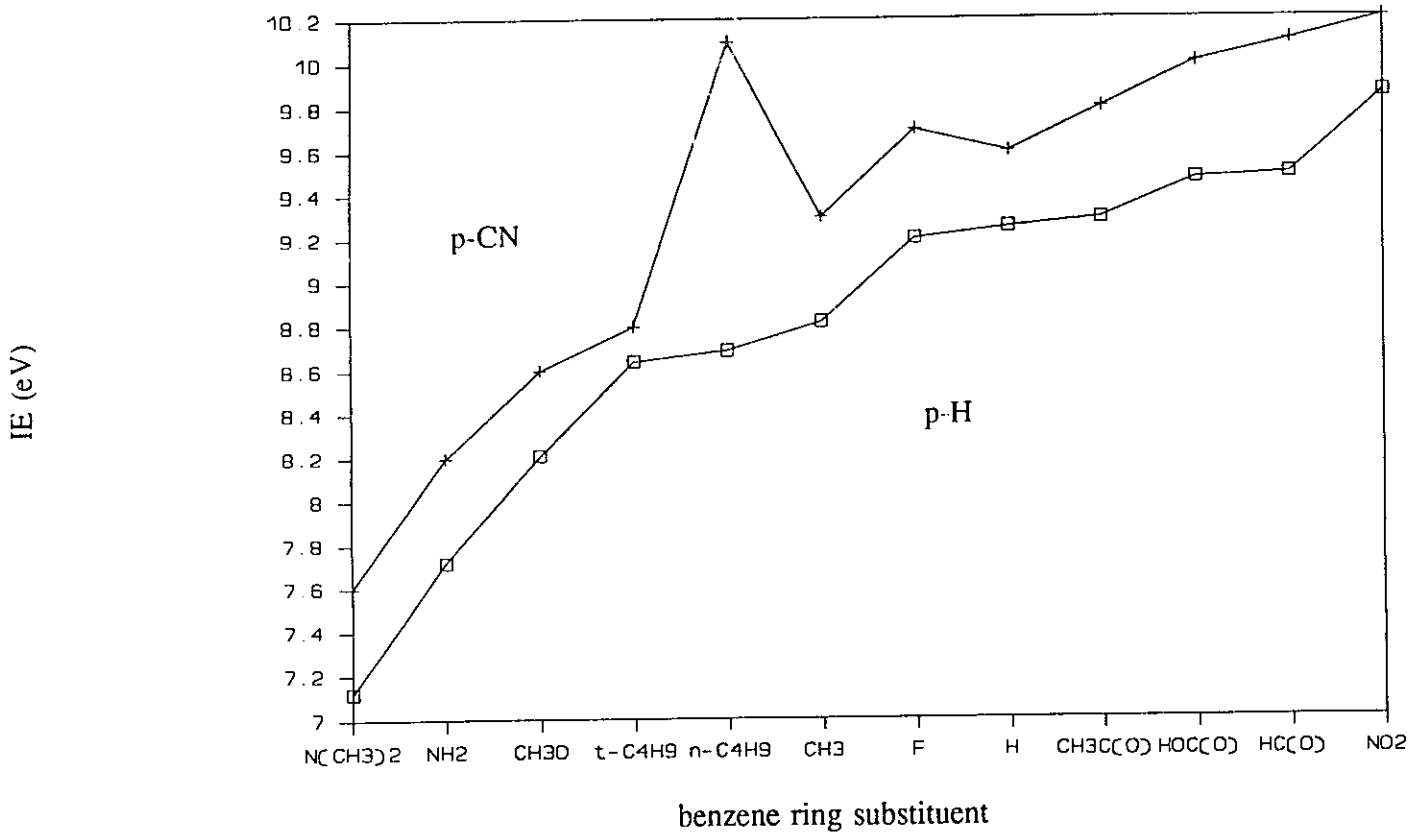

Figure 5.3.3. Plot of IE vs substituent for aromatic ring containing radical cations with either para-H or para-CN substituent.

compound with a measured heat of formation which yields this term is CH_2=C(CH_3)CN. The measured $\Delta_fH^\circ_{298}$, 31 kcal mol^{-1} [10], yields a value for the additivity term of 35 kcal mol^{-1}, significantly lower than the above value. The present value of 35 kcal mol^{-1} is recommended.

New thermochemical determinations for four cyano substituted species will now be described.

The Ionization Energy of Cyanoketene, CH(CN)=C=O

This is the first determination of the $\Delta_fH^\circ_{298}$ of the neutral cyanoketene molecule and its corresponding molecular ion. The EI mass spectrum of t-butyl cyanoacetate contains a base peak at m/z 59 corresponding to protonated acetone, has no molecular ion, and has m/z 126, $[M\text{-}CH_3]^+$, as the highest mass observed. The ion m/z 126 has a single metastable decomposition to m/z 59, and so was an appropriate choice for the determination of the heat of formation of neutral cyanoketene. The formation of neutral cyanoketene was confirmed by the presence of a peak at m/z 67 in the collision induced dissociative ionization (CIDI) mass spectrum [43] of m/z 126. The appearance energy for the formation of protonated acetone from metastable ions of m/z 126 was determined to be 11.4 ± 0.1 eV. The AE is the enthalpy of the overall process,

$$CH_2(CN)C(O)OC(CH_3)_3 + e^- \rightarrow (CH_3)_2COH^+ + CH(CN)=C=O + CH_3^\cdot + 2e^-$$

m/z 59

and so the heat of formation of the neutral cyanoketene molecule was calculated using

the equation:

$$AE(m/z\ 59) = \Delta_fH^\circ_{298}(CH(CN)=C=O) + \Delta_fH^\circ_{298}((CH_3)_2COH^+) + \Delta_fH^\circ_{298}(CH_3^\bullet) - \Delta_fH^\circ_{298}(CH_2(CN)C(O)OC(CH_3)_3)$$

$\Delta_fH^\circ_{298}$(cyanoketene) was found to be 24 ± 5 kcal mol^{-1} using $\Delta_fH^\circ_{298}((CH_3)_2COH^+)$ = 117 kcal mol^{-1} [10], $\Delta_fH^\circ_{298}(CH_3^\bullet)$ = 35.1 kcal mol^{-1} [44] and $\Delta_fH^\circ_{298}(CH_2(CN)C(O)OC(CH_3)_3)$ = -86.5 ± 3 kcal mol^{-1}. The derived heat of formation is 35 kcal mol^{-1} higher than that of unsubstituted ketene, in excellent agreement with what is expected for the difference between $\Delta_fH^\circ_{298}$(RCN) and $\Delta_fH^\circ_{298}$(RH), 32 kcal mol^{-1} [9].

The heat of formation of t-butyl cyanoacetate was estimated using the group additivity principle. However, there is no reference value for the required additivity term [8], C-(H)$_2$(CN)(CO). Therefore, it was necessary to estimate this group contribution from available thermochemical data. The molecule benzoyl acetonitrile, Ph-C(O)CH$_2$CN, has a $\Delta_fH^\circ_{298}$ of 16.8 kcal mol^{-1} [9]. It can be broken into the groups C-(H)$_2$(CN)(CO) + CO-(C)(C$_B$) + 5 x C$_B$-(H) + C$_B$-(CO). The values for the latter three are -31.3, 16.5 and 4.2 kcal mol^{-1} respectively [8]. Thus, the value for C-(H)$_2$(CN)(CO) is 27.4 kcal mol^{-1}. With this new term, it was possible to calculate the heat of formation of t-butyl cyanoacetate to be -86.5 ± 3 kcal mol^{-1}.

In order to determine the ionization energy of cyanoketene, the $\Delta_fH^\circ_{298}$ of the molecular ion is also required. Unfortunately, no precursor molecule was found which gave an ion at m/z 67 (cyanoketene radical cation) of sufficient intensity to measure its appearance energy directly and hence evaluate the heat of formation of the cyanoketene ion. However, from the above discussion on ionic heats of formation, it was noted that,

for double bond containing ions, -CN substitution raised the heat of formation by ~43 kcal mol^{-1}, Table 5.3.3. This can be used to estimate $\Delta_fH^\circ_{298}(CH(CN)=C=O^{+\cdot})$ using $\Delta_fH^\circ_{298}(CH_2=C=O^{+\cdot})$. The heat of formation of the ketene radical cation is 210 kcal mol^{-1} [10] which yields $\Delta_fH^\circ_{298}(CH(CN)=C=O^{+\cdot}) = 253 \pm 3$ kcal mol^{-1}.

Thus, the ionization energy of cyanoketene can be calculate from the equation

$$IE(CH(CN)=C=O) = \Delta_fH^\circ_{298}(CH(CN)=C=O^{+\cdot}) - \Delta_fH^\circ_{298}(CH(CN)=C=O)$$

to be 229 ± 6 kcal mol^{-1} or 9.93 ± 0.26 eV. The only previous estimation of the ionization energy of cyanoketene was by Bock et. al. [45] who measured the band maximum in the photoelectron spectrum of cyanoketene obtained from the pyrolysis of cyanoacetylchloride at 920K, giving a vertical IE of 10.07 eV, which is only an upper limit to the desired adiabatic IE.

The Heats of Formation of the Benzoyl Cyanide and Benzoyl Acetonitrile Radical Cations

The ionization energies of benzoyl cyanide, $C_6H_5C(O)CN$, and benzoyl acetonitrile, $C_6H_5C(O)CH_2CN$, were measured to be 9.89 ± 0.09 eV and 9.54 ± 0.09 eV respectively. The heats of formation of both neutral molecules can be found in a recent compilation of neutral molecule thermochemistry [9] and are 28.1 ± 1.0 kcal mol^{-1} and 16.8 ± 1.0 kcal mol^{-1} respectively. By adding these neutral $\Delta_fH^\circ_{298}$ values to the corresponding ionization energy, the heats of formation of the two radical cations were calculated, $\Delta_fH^\circ_{298}$(benzoyl cyanide$^{+\cdot}$) = 256 ± 2 kcal mol^{-1} and $\Delta_fH^\circ_{298}$(benzoyl acetonitrile$^{+\cdot}$) = 237 ± 2 kcal mol^{-1} (see also Table 5.3.5).

The Heat of Formation of the Cyanoacetyl Ion, $CH_2(CN)CO^+$

The appearance energy for the formation of the cyanoacetyl ion from methyl cyanoacetate was measured to be 11.45 ± 0.09 eV.

$$CH_3OC(O)CH_2CN + e^- \rightarrow CH_3O^{\cdot} + CH_2(CN)CO^+ + 2e^-$$

m/z 68

The heat of formation of the cyanoacetyl ion was calculated to be 198 ± 3 kcal mol^{-1} from the equation

$$AE(m/z\ 68) = \Delta_fH^\circ_{298}(CH_3O^{\cdot}) + \Delta_fH^\circ_{298}(CH_2(CN)CO^+) - \Delta_fH^\circ_{298}(CH_3OC(O)CH_2CN)$$

and using the values for $\Delta_fH^\circ_{298}(CH_3O^{\cdot})$ = 3.7 kcal mol^{-1} [10] and $\Delta_fH^\circ_{298}(CH_3OC(O)CH_2CN)$ estimated from group additivity [8], -62 ± 3 kcal mol^{-1} . The structure of the neutral fragment was assumed to be $CH_3O^{\cdot}$ resulting from the simple bond cleavage in the ionized ester. There is no peak in the MIKE spectrum of the molecular ion related to this dissociation and so there is no evidence favoring a complex rearrangement which might lead to formation of the thermochemically more stable radical $^{\cdot}CH_2OH$ [46]. Comparing this value to that for the -H substituted analogue CH_3CO^+, $\Delta_fH^\circ_{298}$ = 156 kcal mol^{-1} [10], the effect of -CN substitution is to raise the heat of formation by 42 kcal mol^{-1}, similar indeed to the results observed for radical cations discussed above.

Comparing ionization energies of -H, -halo and -CN substituted acetyl radicals, Table 5.3.6, reveals again that the -CN group does not play a role similar to the halogens in the neutral or the ion.

Table 5.3.6

Thermochemistry of -H, -Cl, -Br, -I and -CN Substituted Acetyl Radicals and Ions

R˙	$\Delta_f H°_{298}(R˙)$ kcal mol^{-1}	$\Delta_f H°_{298}(R^+)$ kcal mol^{-1}	IE(R˙)[a] eV
CH_3CO	-5.7[b]	156[c]	7.01
$ClCH_2CO$	-6 ± 2[b]	169 ± 2[d]	7.59 ± 0.15
$BrCH_2CO$	+3 ± 2[b]	179 ± 6[d]	7.63 ± 0.35
ICH_2CO	+15 ± 1[b]	187 ± 2[d]	7.46 ± 0.15
$NCCH_2CO$	+32 ± 1[b]	198 ± 3[e]	7.20 ± 0.15

a. $IE(R˙) = \Delta_f H°_{298}(R^+) - \Delta_f H°_{298}(R˙)$.
b. estimated, see discussion and ref. 93.
c. ref. 10.
d. ref. 92
e. this work.

The -CN substituent raises the ionization energy by raising the heat of formation of the ion slightly more than that of the radical, 42 and 38 kcal mol^{-1} respectively.

The heats of formation of the radicals in Table 5.3.6 were estimated in the following way. Group additivity terms $C-(H)_2(CO)(Cl)$, $C-(H)_2(CO)(Br)$, $C-(H)_2(CO)(I)$ and $C-(H)_2(CO)(CN)$ were calculated from the known heats of formation of chloroacetic acid [9], bromoacetone [9], iodoacetone [9] and benzoyl acetonitrile [9] (see discussion of $\Delta_f H°_{298}$(cyanoketene)) to be -11 ± 2, -2 ± 2, +10 ± 1 and +27 ± 1 kcal mol^{-1} respectively. These values were in turn used to estimate the heats of formation of chloroacetaldehyde, -40 ± 2 kcal mol^{-1}, bromoacetaldehyde, -31 ± 2 kcal mol^{-1}, iodoacetaldehyde, -19 ± 1 kcal mol^{-1}, and cyanoacetaldehyde, -2 ± 1 kcal mol^{-1}, the errors reflecting those for the reference $\Delta_f H°_{298}$ values [9]. The heat of formation of acetaldehyde

is accurately known, -39.6 ± 0.1 kcal mol^{-1} [9]. A constant C-H bond dissociation enthalpy (BDE) of 86 kcal mol^{-1} [7] for the process

$$XCH_2C(O)H \rightarrow XCH_2CO^{\cdot} + H^{\cdot} \qquad X = H, Cl, Br, I, CN$$

was assumed. The heats of formation of the radicals were calculated from the equation

$$86 \text{ kcal mol}^{-1} = \Delta_fH^\circ_{298}(XCH_2CO^{\cdot}) + \Delta_fH^\circ_{298}(H^{\cdot}) - \Delta_fH^\circ_{298}(XCH_2C(O)H) \quad X = H, Cl, Br, I, CN$$

using $\Delta_fH^\circ_{298}(H^{\cdot})$ = 52.1 kcal mol^{-1} [10] and the $\Delta_fH^\circ_{298}(XCH_2C(O)H)$ values derived above. Although the heat of formation of the acetyl radical is listed as -6 kcal mol^{-1} [10], it was raised slightly by the use of the above bond dissociation. A difference of 1 or 2 kcal mol^{-1} in BDE does not significantly change the observed trend in IE. The derived thermochemistry may not be exact but the trends observed should be reliable.

5.3.4 Thermochemical conclusions

From the investigation of ionization energies of molecules and heats of formation of ions, it is evident that the cyano functionality has a predictable effect on the thermochemistry of neutral molecules, radical cations, even electron cations and neutral radicals, although more data for the latter two are required for a detailed study. The cyano group has been shown to increase the heats of formation of several classes of radical cations by 42-44 ± 3 kcal mol^{-1}, which may prove useful in predicting the heats of formation of -CN containing organic ions. A similar result has been observed for an even electron cation and its neutral radical, cyanoacetyl, the thermochemistry of which were determined. All of this shows that the -CN group acts predominantly as an inductive

electron withdrawing group and does not greatly participate in charge delocalization of the cationic centre.

This work has been published [47].

5.4 Cyano - Substituted Even Electron Cations

5.4.1 Introduction

Recently there has been considerable interest in the role of the cyano group in positively charged organic reaction intermediates [48-52]. Results from solution phase studies of reaction kinetics [48-50] have indicated that the rate of a reaction in which the intermediate cation was α-substituted with -CN was reduced less than when the intermediate was -CN substituted β to the charge site. The rate reduction was also much less than expected when compared with other electron withdrawing substituents, such as $-CF_3$ [53]. This behaviour was proposed to arise from significant delocalization of the charge to the -CN group in α-substituted cations:

$$R_2C^+\text{-}C{\equiv}N \leftrightarrow R_2C{=}C{=}N^+$$

I II

The ^{13}C and ^{15}N NMR spectra [51,52] of the diphenylcyanomethyl cation in FSO_3H/SO_2ClF indicated shielding factors characteristic of a C-N double bond, and was interpreted as evidence for structure II above, i.e. both mesomeric forms of the charge centre were important.

To investigate such effects in the dilute gas phase (i.e. in the absence of solvent

influences), the thermochemistry of the six species $^{\cdot}CH_2CN$, $^{+}CH_2CN$, $CH_3\dot{C}HCN$, $CH_3{}^{+}CHCN$, $(CH_3)_2\dot{C}CN$ and $(CH_3)_2{}^{+}CCN$ have been considered in detail. The present work includes new appearance energy (AE) determinations of $\Delta_fH^\circ_{298}$ for $^{\cdot}CH_2CN$ and $^{+}CH_2CN$ and ionization energies (IE) of $CH_3\dot{C}HCN$ and $(CH_3)_2\dot{C}CN$. The revised thermochemistry was used to explore π-delocalization in each species, and to discuss the predictability of properties of -CN substituted free radicals and even-electron cations.

5.4.2 Results and Discussion

$^{+}CH_2CN$ and $^{\cdot}CH_2CN$

a) Theory

Results from solution chemistry [48-52] have prompted a number of theoretical investigations of the structure of the $^{+}CH_2CN$ ion [37,54-58]. The many calculated values for the C-C and C-N bond lengths, bond orders and charge distributions are similar and consistent with a resonance delocalized cation.

One method for studying the effect of a functionality on an ionic or radical centre is to calculate the energy change, ΔE, in an "isodesmic" reaction, such as (1).

$$^{+}CH_2CN + CH_4 + \Delta E \rightarrow CH_3CN + {}^{+}CH_3 \qquad (1)$$

Low levels of theory, which may overestimate resonance delocalization, give a positive value of ΔE in (1), i.e. the -CN group stabilizes the ionic centre relative to -H indicating that π- delocalization of the charge compensates for the destabilizing inductive electron withdrawing effect typically assigned to the -CN group. Higher levels of theory predict a negative ΔE for (1), a net destabilization of the charge centre relative to -H. This result

implies little π-delocalization to -CN, even though the calculated C-N and C-C bond lengths in the ion are consistent with a π-delocalized structure.

Detailed investigations of the potential surface of $C_2H_2N^+$ ions [57,58] revealed three structures occupying minima, $^+CH_2CN$, $^+CH_2NC$ and the cyclic structure $\overline{HC\text{-}CHN}^+$. The highest levels of theory used in these investigations indicated that the most stable form of the ion is the cyclic structure, with $^+CH_2CN$ and $^+CH_2NC$ both slightly higher in energy by ~ 13 kcal mol^{-1}. The barriers to their isomerization to the cyclic structure were found to be ~ 34 kcal mol^{-1} for $^+CH_2NC$ and 54 kcal mol^{-1} for $^+CH_2CN$ [58]. These barriers lie well below the lowest dissociation limit for the ion, to $HCCN^{+\bullet}$ and $H^\bullet$, ~ 130 kcal mol^{-1} above $^+CH_2CN$.

Interest in the cyanomethyl radical, $^\bullet CH_2CN$, has not been as widespread as in its cation. Theoretical calculations [59-64] have centred on determining the radical stabilization energy (RSE) of the -CN group compared to -H. The RSE can be equated to the calculated value of ΔE for the isodesmic reaction

$$^\bullet CH_2CN + CH_4 + \Delta E \rightarrow CH_3CN + {}^\bullet CH_3 \qquad (2)$$

These range from +11 kcal mol^{-1} and +12.5 kcal mol^{-1} to +5 kcal mol^{-1}, while experimental estimates of the stabilization energy in $^\bullet CH_2CN$ [65-69] are ~ +5.5 kcal mol^{-1}. All of these studies agree that -CN stabilizes the radical centre relative to -H, indicative of a π-delocalized structure.

b) Experiment

There have been three independent experimental evaluations of the heat of formation of the cyanomethyl radical, all from the kinetics of nitrile pyrolysis [65,66,69],

see Table 5.4.1.

Table 5.4.1

$\Delta_f H°_{298}(^{\cdot}CH_2CN)$ Derived from Kinetic Measurements

Workers	Pyrolysis	Year	$\Delta_f H°_{298}(^{\cdot}CH_2CN)$ kcal mol^{-1}	ref.
Hunt et. al.	CH_3CH_2CN	1965	50.3[a]	[65]
King and Goddard	$CH_3CH_2CH_2CN$	1975	58.5 ± 2.2	[66]
Trenwith	CH_3CH_2CN	1983	58.0	[69]

a) $\Delta_f H°_{298}(^{\cdot}CH_2CN)$ obtained using $\Delta_f H°_{298}(^{\cdot}CH_3)$ = 33.9 kcal mol^{-1} and $\Delta_f H°_{298}(CH_3CH_2CN)$ = 11.5 kcal mol^{-1}. If recent values of 35.1 kcal mol^{-1} [44] and 12.3 ± 0.1 kcal mol^{-1} [10] are used, $\Delta_f H°_{298}(^{\cdot}CH_2CN)$ = 49.9 kcal mol^{-1}.

Agreement is poor but the authors of the two most recent measurements have explained the possible sources of error in the earlier study [65]. Semi-empirical calculations [70,71] yielded values of $\Delta_f H°_{298}$ = 53-62 kcal mol^{-1}, while ab-initio results [72,73] were 58-59 kcal mol^{-1}, in good agreement with the later experimental values.

There have been several attempts to determine the heat of formation of $^{+}CH_2CN$ by the appearance energy (AE) method. The appearance energy for the formation of $^{+}CH_2CN$ from acetonitrile, CH_3CN, has been reported seven times [74-80], see Table 5.4.2.

Table 5.4.2

Appearance Energy Determinations for the Formation of $^{+}CH_2CN$ from CH_3CN

Workers	Ionization[a]	Year	AE($^{+}CH_2CN$) eV	ref.
McDowell and Warren	EI[b]	1952	14.30 ± 0.02	[74]
Pottie and Lossing	EI[b]	1961	14.28 ± 0.05	[75]
Franklin et. al.	EI[b]	1966	13.54 ± 0.08	[76]
Dibeler and Liston	PI	1968	14.01 ± 0.02	[77]
Heerma et. al.	EI[b]	1969	14.72	[78]
Allam et.al.	EI[b]	1982	14.75	[79]
Harland and McIntosh	EI[c]	1985	14.38 ± 0.04	[80]
(this work			13.94 ± 0.02)	

a) EI = electron impact, PI = photoionization
b) low energy resolution
c) near monoenergetic electrons

The resulting values for $\Delta_f H^\circ_{298}(^{+}CH_2CN)$ range from 276 kcal mol^{-1} to 303 kcal mol^{-1}, an alarming discrepancy. The problem is twofold. First, the electron impact measurements were performed using electron beams with a wide energy spread. The value determined by Dibeler and Liston [77], using monochromated photons, is probably the most reliable in Table 5.4.2, allowing the calculation of $\Delta_f H^\circ_{298}(^{+}CH_2CN)$ = 289 ± 1 kcal mol^{-1}, using $\Delta_f H^\circ_{298}(H^{\cdot})$ = 52.1 kcal mol^{-1} [10] and $\Delta_f H^\circ_{298}(CH_3CN)$ = 18.0 ± 0.2 kcal mol^{-1} [10].

However, regardless of the accuracy of the measured AE, there is still uncertainty with regard to the heat of formation of acetonitrile, CH_3CN. Over the years the value for $\Delta_f H^\circ_{298}(CH_3CN)$ has fallen from 20.9 kcal mol^{-1} [81] and 19.2 kcal mol^{-1} [82] to 18.0 ± 0.2 kcal mol^{-1} [10] and 15.4 ± 1.7 kcal mol^{-1} [9]. Any appearance energy determination

involving acetonitrile therefore suffers from this imprecision. The value listed in the most recent compilation [10], 18.0 ± 0.2 kcal mol^{-1} was used in this study for the following reason. The difference in $\Delta_fH°_{298}$ between CH_3-X and CH_3CH_2-X is ~ 7 kcal mol^{-1} and between CH_3CH_2-X and $(CH_3)_2CH$-X is ~ 8 kcal mol^{-1} (X = -OH, -Cl and $-NH_2$ [10]). Using $\Delta_fH°_{298}(CH_3CN)$ = 18 ± 0.2 kcal mol^{-1} [10] with $\Delta_fH°_{298}(CH_3CH_2CN)$ = 12.3 ± 0.1 kcal mol^{-1} [10] and $\Delta_fH°_{298}((CH_3)_2CHCN)$ = 5.8 ± 0.2 kcal mol^{-1} [10] yields similar values, 6 and 6.5 kcal mol^{-1}.

The ionization energy of the cyanomethyl radical calculated from the above experimental values for $\Delta_fH°_{298}(^+CH_2CN)$ and $\Delta_fH°_{298}(^·CH_2CN)$ is 10.0 ± 0.1 eV; this value is discussed again with the present results, see below. The IE has been reported only once, by Pottie and Lossing [75], using the radical formed in the pyrolysis of $NCCH_2CH_2ONO_2$, $NCCH_2CH_2CN$ and $NCCH_2I$. The selected best value was 10.87 ± 0.05 eV, considerably higher than that obtained above. The ionization energy has been calculated by semi-empirical methods, 10.4 - 11.0 eV [83] while ab-initio calculation results [57] are significantly lower, 9.46-9.64 eV; this latter IE combined with the selected calculated value for $\Delta_fH°_{298}(^·CH_2CN)$, 58 kcal mol^{-1}, results in $\Delta_fH°_{298}(^+CH_2CN)$ of 280 kcal mol^{-1}. Using this value in the isodesmic reaction (1) together with experimental values for the other species results in a ΔE of +17 ± 2 kcal mol^{-1}, i.e., the -CN group stabilizes the ion relative to -H. This is very different from the negative values for ΔE calculated by the higher levels of ab-initio theory and reveals an inconsistancy between the two methods for theoretically evaluating ΔE.

c) Present results

Evident from the above discussion is a considerable uncertainty in the thermochemistry of $^{\cdot}CH_2CN$ and $^{+}CH_2CN$ and also therefore, in the degree of delocalization proposed to occur in both the radical and cation.

We have re-investigated the thermochemistry of $^{\cdot}CH_2CN$ and $^{+}CH_2CN$ by the appearance energy method using monoenergetic electrons and the experimental technique discussed and described in detail in sec. 3.5.

In order to determine for the first time $\Delta_fH°_{298}(^{\cdot}CH_2CN)$ by the appearance energy method, the AE of the corresponding fragment ion, Y^+, in the process

$$Y\text{-}CH_2CN + e^- \rightarrow Y\text{-}CH_2CN^{+\cdot} + 2e^- \rightarrow Y^+ + {}^{\cdot}CH_2CN + 2e^-$$

was measured. The two precursor molecules studied were 3-hydroxypropionitrile and methyl cyanoacetate. The results are summarized in Table 5.4.3.

Table 5.4.3

Determination of $\Delta_fH°_{298}(^{\cdot}CH_2CN)$ from AE Measurements

Precursor	Fragment, Y^+	AE(Y^+) eV		$\Delta_fH°_{298}(^{\cdot}CH_2CN)$ kcal mol^{-1}
$HOCH_2CH_2CN$	$HOCH_2^+$	10.84 ± 0.02		58.5 ± 3[a]
$CH_3OC(O)CH_2CN$	CH_3OCO^+	10.40 ± 0.02		57.8 ± 3[b]
			ave.	58.2 ± 3

a) determined using $\Delta_fH°_{298}(HOCH_2CH_2CN)$ = -23.5 kcal mol^{-1} [8] and $\Delta_fH°_{298}(HOCH_2^+)$ = 168 ± 2 kcal mol^{-1} [10].
b) determined using $\Delta_fH°_{298}(CH_3OC(O)CH_2CN)$ = -62 kcal mol^{-1} [8] and $\Delta_fH°_{298}(CH_3OCO^+)$ = 120 kcal mol^{-1} [84].

The structures of the fragment ions, Y^+, were confirmed by their collisional activation mass spectra to be $HOCH_2^+$ and CH_3OCO^+ [84]. The two values for $\Delta_fH°_{298}(^•CH_2CN)$ in Table 5.4.3 are in excellent agreement with those obtained by kinetic measurements [66,69]. The RSE calculated using the present value for $\Delta_fH°_{298}(^•CH_2CN)$, 58 ± 3 kcal mol^{-1}, and literature values for the other species in the equation (2) is + 13 ± 3 kcal mol^{-1}, similar to those obtained by theoretical calculation. From their reactions with methane, the corresponding RSE of the allyl radical, a fully delocalized species, is + 18 kcal mol^{-1}, while that of the localized ethyl radical is +5 kcal mol^{-1}. This indicates that there is significant but incomplete resonant delocalization of the radical centre in $^•CH_2CN$.

The appearance energy for the formation of $^+CH_2CN$ from acetonitrile has been redetermined in the present study to be 13.94 ± 0.02 eV. Using $\Delta_fH°_{298}(CH_3CN)$ = 18.0 ± 0.2 kcal mol^{-1} [10] and $\Delta_fH°_{298}(H^•)$ = 52.1 kcal mol^{-1} [10], $\Delta_fH°_{298}(^+CH_2CN)$ = 287 ± 1 kcal mol^{-1}, which suffers from the uncertainty in $\Delta_fH°_{298}(CH_3CN)$, but is similar to that obtained by using the AE of Dibeler and Liston [77]. The KER for the formation of m/z 40 (C_2,H_2,N^+) from metastable molecular ions was large, 141 meV, suggesting a large reverse activation energy (see sec. 3.4.2). Hence, this value for $\Delta_fH°_{298}(^+CH_2CN)$ was considered an upper limit to the true value.

Iodoacetonitrile, ICH_2CN, was also chosen as a precursor. The KER in the dissociation of the molecular ion to $^+CH_2CN$ + $I^•$ was small, ~ 4.5 meV, making iodoacetonitrile the preferred route to the cyanomethyl cation. The measured AE of m/z 40, 12.18 ± 0.02 eV, gave $\Delta_fH°_{298}(^+CH_2CN)$ = 291 ± 2 kcal mol^{-1} (using $\Delta_fH°_{298}(I^•)$ = 25.5 kcal mol^{-1} [10] and $\Delta_fH°_{298}(ICH_2CN)$ = 36 ± 2 kcal mol^{-1}). The heat of formation of

neutral iodoacetonitrile was derived both by examining the effect of -I substitution on small molecules (and hence CH_3CN) and the effect of -CN substitution on small molecules (and hence CH_3I) [10]. There is a 4 kcal mol^{-1} discrepancy between these two values. A study was made of the mass spectral characteristics of the C_2,H_2,N^+ ions produced from the four precursor molecules CH_3CN (I), ICH_2CN (II), CH_3NC (III) and $\overline{HC=CHNNN}H$ (IV). The mass spectrometry of the ions formed from I, III and IV were virtually identical, but the ions from ICH_2CN were found to be unique. We believe that only ICH_2CN produces $^+CH_2CN$ upon dissociative ionization and that the other three molecules yield a common ion, probably the lowest energy isomer, $\overline{HC\text{-}CHN}^+$ (see Appendix for 5.4 for a complete discussion of the mass spectrometry and thermochemistry of the C_2,H_2,N^+ family of isomers). The $\Delta_fH^\circ_{298}$ (C_2,H_2,N^+) obtained from CH_3CN is most likely a high upper limit to the heat of formation for this cyclic isomer. We have learned of new high level calculations (unpublished) which clearly establish the cyclic ion as the lowest energy isomer.

To determine the degree of charge delocalization in the cyanomethyl cation, our value for $\Delta_fH^\circ_{298}(^+CH_2CN)$ was used in isodesmic reaction (1). A value for ΔE of $+7 \pm 1$ kcal mol^{-1} was calculated using literature values for the other species in the reaction. The positive value for ΔE shows that the -CN functionality weakly stabilizes the ionic centre relative to -H, indicative of some delocalization of the charge in $^+CH_2CN$. This result agrees with that predicted by low levels of ab-initio theory in spite of their non-inclusion of electron correlation. Thus calculations which determined the appropriate unknown enthalpies of individual species in equation (1) [57,72] gave results essentially

in agreement with experiment (a positive ΔE). However the calculations which determined the overall enthalpy change produced negative ΔE values, differing from the former by as much as 15-30 kcal mol^{-1}. The discrepancy reveals an apparent shortcoming in the application of higher levels of theory to this case.

The IE of $^{\cdot}CH_2CN$ calculated from the present measurements of $\Delta_fH°_{298}(^{+}CH_2CN)$ and $\Delta_fH°_{298}(^{\cdot}CH_2CN)$ is 10.1 ± 0.2 eV. The ionization energy of $^{\cdot}CH_2CN$ formed in the pyrolysis of $NCCH_2CH_2ONO_2$ was re-measured using monoenergetic electrons, 10.30 ± 0.02 eV, close to our calculated value.

$CH_3\dot{C}HCN$ and $CH_3{}^{+}CHCN$

The heat of formation of the $CH_3\dot{C}HCN$ radical has been determined to be 50 ± 2 kcal mol^{-1} from analysis of the kinetics of the pyrolysis of propionitrile [85]. The degree of π-delocalization was estimated by calculating the energy change in the isodesmic reaction (3).

$$CH_3\dot{C}HCN + CH_3CH_3 + \Delta E \rightarrow CH_3CH_2CN + CH_3CH_2^{\cdot} \qquad (3)$$

Using $\Delta_fH°_{298}(CH_3CH_2CN)$ = 12.3 ± 0.1 kcal mol^{-1} [10], $\Delta_fH°_{298}(CH_3CH_2^{\cdot})$ = 27.8 ± 0.6 kcal mol^{-1} [1] and $\Delta_fH°_{298}(CH_3CH_3)$ = -20.1 ± 0.05 kcal mol^{-1} [10], ΔE was found to be +10 ± 2 kcal mol^{-1}. Alone, this value is of limited significance, but when compared with the value found for the localized secondary radical $(CH_3)_2CH^{\cdot}$ in place of $CH_3\dot{C}HCN$ in equation (3), ΔE = +0.6 kcal mol^{-1}, and the resonance stabilized radical CH_2=CH-$CH_2^{\cdot}$, ΔE = 14 kcal mol^{-1}, it was apparent that there is some delocalization of the radical centre

in $CH_3\dot{C}HCN$.

The ionization energy (IE) of $CH_3\dot{C}HCN$ was measured to be 9.25 ± 0.02 eV, the radical being formed by pyrolysis of $CH_3CH(I)CN$. A previous determination [75], 9.76 eV, was presumably a vertical ionization energy, while semi-empirical calculations [83] place it at 9.52 eV.

Combining the IE with the radical $\Delta_fH^\circ_{298}$ yielded a heat of formation of the CH_3^+CHCN ion of 263 ± 2 kcal mol^{-1}. The -CN group has been found to increase the heat of formation of radical cations by ~ +43 ± 3 kcal mol^{-1} [47, sec. 5.3]. If this result is extended to even electron cations, the heat of formation can be estimated by adding +43 kcal mol^{-1} to $\Delta_fH^\circ_{298}(CH_3CH_2^+)$ = 215.6 kcal mol^{-1} [10], yielding $\Delta_fH^\circ_{298}(CH_3^+CHCN)$ = 259 ± 3 kcal mol^{-1}, close to the above value.

We have made several attempts to determine $\Delta_fH^\circ_{298}(CH_3^+CHCN)$ by the appearance energy method, but without success. The difficulty was that the fragment ion generated was probably the isomer CH_2=CH-$^+$C=NH which has a much lower heat of formation of 220 kcal mol^{-1} [10], derived from the proton affinity of C_2H_3CN. It may well be impossible, therefore, experimentally to determine an AE value for CH_3^+CHCN because of facile isomerization of the precursor ion.

The energy change, ΔE, in isodesmic reaction (4), similar to that used for the radical, was calculated to be -15 ± 2 kcal mol^{-1}, using $\Delta_fH^\circ_{298}(CH_3CH_3)$ = -20.1 ± 0.05 kcal mol^{-1} [10], $\Delta_fH^\circ_{298}(CH_3CH_2CN)$ = 12.3 ± 0.1 kcal mol^{-1} [10] and $\Delta_fH^\circ_{298}(CH_3CH_2^+)$ = 215.6 ± 1.0 kcal mol^{-1} [10].

$$CH_3^+CHCN + CH_3CH_3 + \Delta E \rightarrow CH_3CH_2CN + CH_3CH_2^+ \quad (4)$$

Hence, the -CN group destabilizes the ion relative to -H. The delocalization of the charge in this ion is therefore greatly reduced compared to $^{+}CH_2CN$, ΔE = +10 kcal mol^{-1}. The result is similar to that observed for radical cations [47] and is in keeping with theoretical calculations [37,55,86,87]. The lack of π-delocalization means that the structural features of the ion and radical will not be significantly different, as was the case for the cyanomethyl radical and cation. Hence, the measured IE should be closer to the adiabatic IE.

$(CH_3)_2\dot{C}CN$ and $(CH_3)_2{}^{+}CCN$

The next in this series of -CN substituted species is the $(CH_3)_2\dot{C}CN$ radical and the $(CH_3)_2{}^{+}CCN$ ion. The heat of formation of the radical has been determined by reaction kinetics [67] to be 40 ± 2 kcal mol^{-1}.

To investigate the degree of delocalization in the radical, ΔE in isodesmic reaction (5) was calculated.

$$(CH_3)_2\dot{C}CN + (CH_3)_2CH_2 + \Delta E \rightarrow (CH_3)_2CHCN + (CH_3)_2\dot{C}H \qquad (5)$$

Using $\Delta_fH^\circ_{298}((CH_3)_2CH_2)$ = -25.0 ± 0.1 kcal mol^{-1} [10], $\Delta_fH^\circ_{298}((CH_3)_2CHCN)$ = 5.8 ± 0.2 kcal mol^{-1} [10] and $\Delta_fH^\circ_{298}((CH_3)_2\dot{C}H)$ = 19.1 ± 0.6 kcal mol^{-1} [1], a ΔE value of +10 ± 2 kcal mol^{-1} was obtained, the same as that for $^{\cdot}CH_2CN$ and $CH_3\dot{C}HCN$. The results are similar to those obtained by Barbe et.al. [88] and that calculated by Lien and Hopkinson [89].

The ionization energy of the radical formed upon pyrolysis of 2,2′-azoisobutyronitrile, $(CH_3)_2C(CN)N{=}NC(CH_3)_2CN$, was measured to be 8.48 ± 0.02 eV.

Semi-empirical calculations [83] give 8.88 eV while a reported vertical IE is 9.15 eV [75]. When our IE is added to the radical $\Delta_f H^\circ_{298}$, a heat of formation for $(CH_3)_2{}^+CCN$ was obtained, 236 ± 2 kcal mol^{-1}. If 43 ± 3 kcal mol^{-1} [47] is added to the heat of formation of the isopropyl cation, $\Delta_f H^\circ_{298}$ = 190.9 kcal mol^{-1} [10], an estimated value of 234 ± 3 kcal mol^{-1} results, similar to that found above.

Attempts to determine $\Delta_f H^\circ_{298}((CH_3)_2{}^+CCN)$ by the appearance energy method have also failed, presumably due to facile isomerization of the precursor ion in a manner similar to that which affected $AE(CH_3{}^+CHCN)$.

Isodesmic reaction (6) yields a ΔE of -14 ± 3 kcal mol^{-1}, using $\Delta_f H^\circ_{298}(C_3H_8)$ = -25.0 ± 0.1 kcal mol^{-1} [10], $\Delta_f H^\circ_{298}((CH_3)_2CHCN)$ = 5.8 ± 0.2 kcal mol^{-1} [10], $\Delta_f H^\circ_{298}((CH_3)_2{}^+CH)$ = 190.9 kcal mol^{-1} [10] and 234 ± 3 kcal mol^{-1} for the nitrile ion.

$$(CH_3)_2{}^+CCN + (CH_3)_2CH_2 + \Delta E \rightarrow (CH_3)_2CHCN + (CH_3)_2{}^+CH \qquad (6)$$

Again, the -CN group destabilizes the ionic centre relative to hydrogen, indicating that π-delocalization of the charge to the cyano group is minimal, a point supported by theory [37,55,86,87]. This also is in keeping with the measured IE being the adiabatic IE as argued for $CH_3\dot{C}HCN$.

5.4.3 Thermochemical conclusions

The above results are summarized in Table 5.4.4.

Table 5.4.4

Summary of Results for -CN Substituted Free Radicals and Even Electron Cations

R-CN	$\Delta_f H°_{298}$ (kcal mol^{-1})	ΔE (kcal mol^{-1})	π-delocalization?
$^{\cdot}CH_2CN$	58 ± 3	+13	Partial
$CH_3\dot{C}HCN$	50 ± 2 [85]	+10	Partial
$(CH_3)_2\dot{C}CN$	40 ± 2 [67]	+10	Partial
$^{+}CH_2CN$	291 ± 2	+7	Partial
$CH_3{}^{+}CHCN$	263 ± 2	-15	NO
$(CH_3)_2{}^{+}CCN$	236 ± 2	-14	NO

The above free radical thermochemistry allows the examination of the effect of -CH_3 substitution on a cyano-substituted radical centre and the corresponding α C-H bond strengths in nitriles.

R=				
	$^{\cdot}CH_2CN$	$\Delta_f H°_{298}$ =	58 ± 3 kcal mol^{-1}	D(R-H) = 92 ± 3 kcal mol^{-1}
	$CH_3\dot{C}HCN$		50 ± 2	90 ± 2
	$(CH_3)_2\dot{C}CN$		40 ± 2	86 ± 2

The average difference in $\Delta_f H°_{298}$, -9 ± 2 kcal mol^{-1} is the same as the value obtained for methyl substitution in alkyl radicals [8] and -OH substituted radicals [29], showing that substitution at a radical centre can be treated using standard additivity term values. The C-H bond strengths, D(R-H), evaluated using these enthalpies are 92, 90 and 86 kcal mol^{-1}. The decrease in bond strength going from 1° to 2° to 3° is similar to that for the 1°, 2° and 3° bonds in CH_3CH_2-H, $(CH_3)_2$CH-H and $(CH_3)_3$C-H, which have values of 100, 96 and 94 kcal mol^{-1} respectively [29]. The -CN group reduces the C-H bond strength by ~ 7 kcal mol^{-1} relative to -CH_3.

In the cations, the difference in heats of formation for successive methyl

substitution at the charge site are ca -28 kcal mol^{-1}, similar in magnitude to those observed between $\Delta_f H^\circ_{298}(X\text{-}^+CH_2)$, $\Delta_f H^\circ_{298}(X\text{-}^+CHCH_3)$ and $\Delta_f H^\circ_{298}(X\text{-}^+C(CH_3)_2)$ where X = HO-, H_2N-, CH_2=CH- and HC≡C- (all in the range -16 to -29 kcal mol^{-1}). It is also apparent from isodesmic reactions (1), (4) and (6) that methyl substitution diminishes π-delocalization of the charge to the -CN group. The same trend is observed for even electron cations with other functionalities (e.g. -OH for which the ΔE values calculated from analogous isodesmic reactions were +62, +41 and +34 kcal mol^{-1}) except that for -CN there is a sign change in ΔE with the addition of a single methyl group. It can be stated that the mesomeric form of these -CN substituted gas phase ions in which the charge is carried by nitrogen is significant only for cyanomethylium.

This work has been published [90].

Appendix for 5.4: Mass Spectrometry of C_2,H_2,N^+ Ions

Three stable structures for ions of composition C_2,H_2,N^+ (i.e., structures which reside in potential wells) have been identified by ab-initio calculations [57,58]:

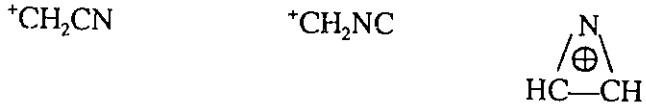

a *b* *c*

The calculations indicated that the lowest energy isomer was the cyclic ion *c*. The relative energies of the three, however, differed depending on the level of theory employed in the calculations. We set out to characterize these three ions by mass spectrometry. Four precursor molecules were chosen to produce these three isomers:

I II III IV

Originally, CH_3CN and ICH_2CN were chosen to produce the $^+CH_2CN$ ion (*a*), CH_3NC to give $^+CH_2NC$ (*b*) and 1-H-1,2,3-triazole (IV) to give the cyclic isomer (*c*). On first inspection a simple bond cleavage from the molecular ions of I, II and III should produce the desired C_2,H_2,N^+ ion, while a rearrangement must be involved in forming a C_2,H_2,N^+ ion from IV. This rearrangement might permit the lowest energy isomer *c* to be formed. Most of these suppositions turned out to be incorrect. Mass spectrometry and thermochemical determinations were combined to identify the C_2,H_2,N^+ ions formed from these four precursors. These results have implications for past experimental evaluations of the thermochemistry of *a* and *b* and are an excellent example of the importance of

mass spectrometry to the field of gas phase thermochemistry (and not only the reverse).

a) Making C_2,H_2,N^+ ions - The peak at m/z 40 (C_2,H_2,N^+) is a major signals in the mass spectra of I-IV. These are the source generated C_2,H_2,N^+ ions. The ions were also formed from metastable precursor ions in the 2FFR of the mass spectrometer (see sec. 3.2.2). Metastable molecular ions $I^{+\bullet}$ and $III^{+\bullet}$ lose $H^\bullet$, metastable $II^{+\bullet}$ ions lose $I^\bullet$ and metastable m/z 41 ions, formed by N_2 loss from $IV^{+\bullet}$ in the ion source, lose $H^\bullet$ to give ions of composition C_2,H_2,N^+. The KER in these dissociations were reflected in the measured $T_{0.5}$ values (see sec. 3.3.3).

$I^{+\bullet} - H^\bullet$	$T_{0.5}$ = 141 meV
$II^{+\bullet} - I^\bullet$	= 4.5 meV
$III^{+\bullet} - H^\bullet$	= 150 meV
$[IV - N_2]^{+\bullet} - H^\bullet$	= 146 meV

The large $T_{0.5}$ values for the fragmentations of $I^{+\bullet}$, $III^{+\bullet}$ and $[IV - N_2]^{+\bullet}$ suggest a significant barrier to the $H^\bullet$ loss from each, while the small $T_{0.5}$ for $I^\bullet$ loss from $II^{+\bullet}$ indicates that the process occurs near the thermochemical threshold (no barrier).

b) MIKE spectra of source generated C_2,H_2,N^+ ions - The C_2,H_2,N^+ ions from all four precursor molecules exhibited three peaks in their MIKE spectra, m/z 39 (- H), 38 (- H_2) and 28 (- C). However, these peaks were found to be extremely collision sensitive. Introducing only a trace amount of collision gas into one of the collision cells in the 2FFR produced pronounced increases in the intensity of all three peaks. Therefore, it was uncertain as to whether the peak intensities observed in the MIKE spectra were from true metastable processes or influenced by residual CID involving the background gas in the

2FFR of the instrument (pressure = 1 x 10^{-8} mbar). It was not possible to identify unique ion structures by comparing these MIKE spectra.

c) CID spectra of source generated C_2,H_2,N^+ ions - The He CID mass spectra (obtained in the 2FFR) of the source generated C_2,H_2,N^+ ions from the four precursor molecules are shown in Fig. 5.4.1. The spectra of the ions formed from I, III and IV are virtually identical, with only a small change in the m/z 26 : m/z 27 ratio to possibly distinguish them. The C_2,H_2,N^+ ion from II are quite different, exhibiting a much more intense peak at m/z 26 and almost no peak at m/z 27. This was the first indication that ions $I^{+\bullet}$, $III^{+\bullet}$ and $[IV - N_2]^{+\bullet}$ do not yield distinct C_2,H_2,N^+ ions.

d) NR spectra of source generated C_2,H_2,N^+ ions - The Xe/O_2 NR mass spectra of the source generated C_2,H_2,N^+ ions from the four precursor molecules are shown in Fig. 5.4.2. The spectra are almost identical, the only distinction being the abundance of re-ionized C_2,H_2,N^+ ions at m/z 40. The ion from II displays the largest recovery ion.

e) CID spectra of the NR recovery ions - The 3FFR CID spectra were obtained of the m/z 40 ions in the above NR experiments, Fig. 5.4.3. The four He CID spectra are identical, indicating that a common C_2,H_2,N^+ ion was formed in the reionization step of the NR experiment.

The relative energies of the radicals $^{\bullet}CH_2CN$ and $^{\bullet}CH_2NC$ were determined by the AE technique to be 58 ± 3 kcal mol^{-1} (see sec. 5.4.3) and 96 ± 3 kcal mol^{-1} respectively. The AE for the formation of CH_3OCO^+ from $CH_3OC(O)CH_2NC$ was measured to be 11.2 ± 0.02 eV, and $\Delta_fH^o_{298}(^{\bullet}CH_2NC)$ calculated using the heats of formation of CH_3OCO^+, 120 kcal mol^{-1} [84] and $CH_3OC(O)CH_2NC$, -40 kcal mol^{-1}. The heat of formation of methyl

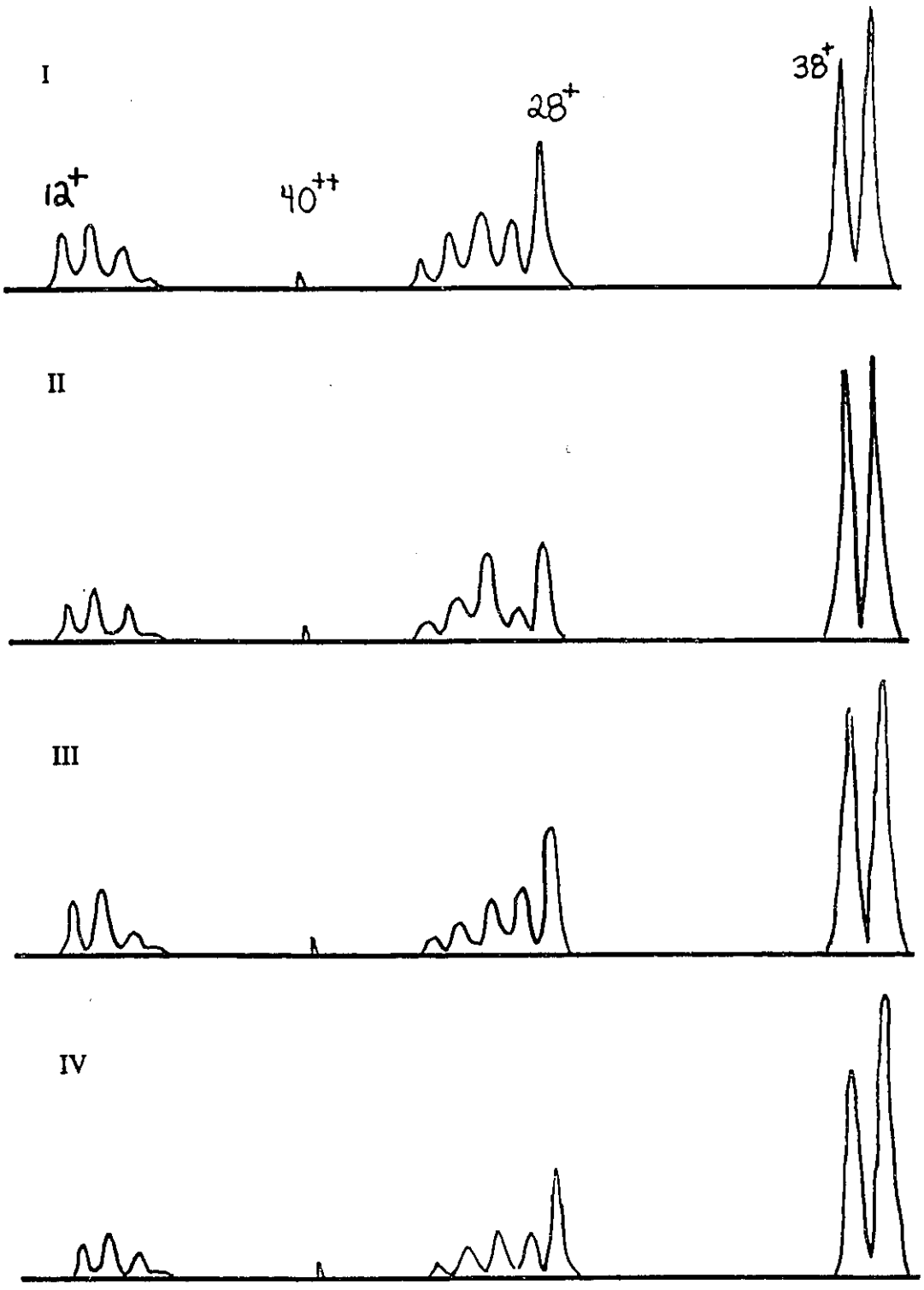

Fig. 5.4.1. 2FFR CID mass spectra (He, 90%T) of source generated C_2,H_2,N^+ ions from precursor molecules I-IV.

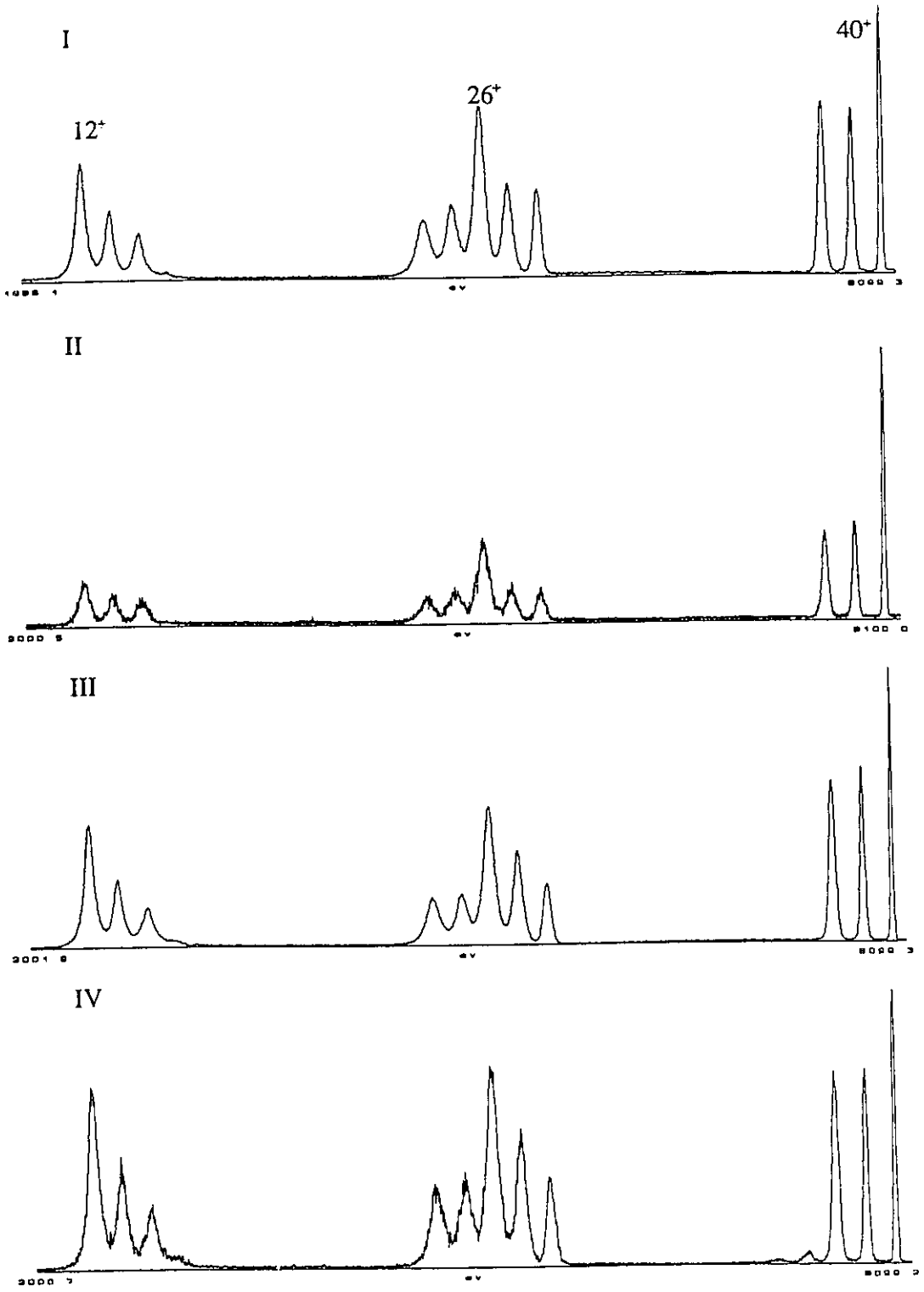

Fig. 5.4.2. NR mass spectra of source generated C_2,H_2,N^+ ions from precursor molecules I-IV. 2FFR, Xe (C1, 80%T), deflector +1000V, O_2 (C2, 80%T).

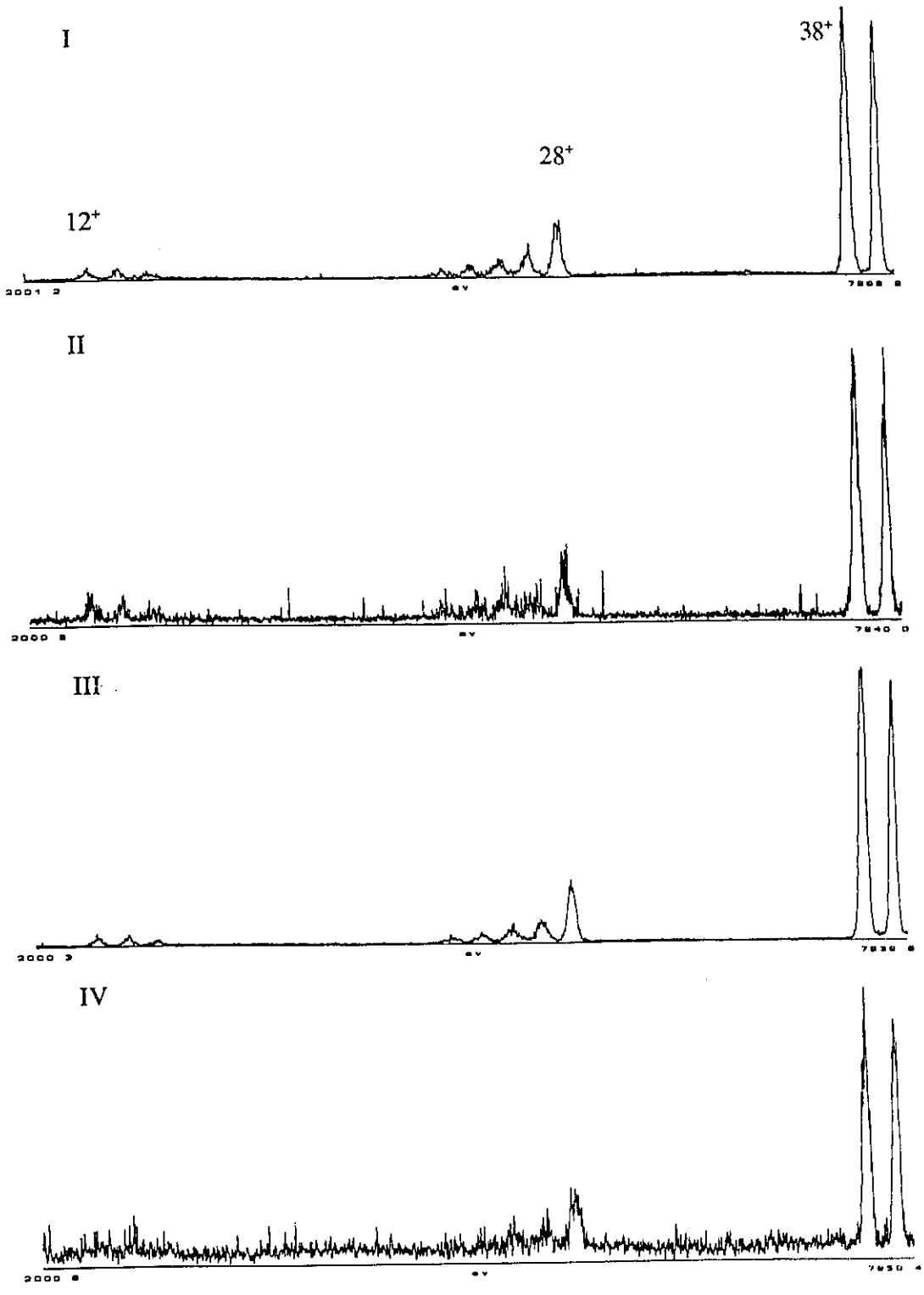

Fig. 5.4.3. 3FFR He CID mass spectra (He, 50%T) of m/z 40 recovery ions in 2FFR NR mass spectra of source generated C_2,H_2,N^+ ions from precursor molecules I-IV.

isocyanoacetate was estimated by group additivity [8]. However, the value for C-$(H)_2(CO)(NC)$ was unknown and had to be evaluated. The value for the term C-$(H)_2(C)(NC)$ was determined to be 44 kcal mol^{-1} from $\Delta_f H°_{298}(CH_3CH_2NC)$ = 33.8 kcal mol^{-1} [10]. Comparing the analogous cyano additivity terms, C-$(H)_2(C)(CN)$ = 22.5 kcal mol^{-1} [8] and C-$(H)_2(CO)(CN)$ = 27.4 kcal mol^{-1} [8], a difference of +5 kcal mol^{-1} results when (C) is replaced by (CO). Adding this difference to C-$(H)_2(C)(NC)$ yields a value for C-$(H)_2(CO)(NC)$ of 49 kcal mol^{-1}. This, along with the other standard additivity term values, results in $\Delta_f H°_{298}(CH_3OC(O)CH_2NC)$ = -40 kcal mol^{-1}.

The neutral counterpart of ion *c* is a three membered ring analogous to the cyclopropenyl radical. If this analogy extends to their thermochemistry, the cyclic $C_2,H_2,N^{\bullet}$ radical will have a heat of formation 23 kcal mol^{-1} higher than $^{\bullet}CH_2CN$, 81 kcal mol^{-1}.

Since EI using 70 eV electrons in the ion source of the mass spectrometer deposits considerable excess internal energy into the molecular ions, excitation which may ultimately affect the nature of the C_2,H_2,N^+ ions formed, attempts were made to produce C_2,H_2,N^+ fragment ions under conditions of low precursor excitation. The 11-12 eV EI generated molecular ions from I, II and IV give source generated C_2,H_2,N^+ ions whose He CID spectra were identical to those in Fig. 5.4.1. The C_2,H_2,N^+ ions were also formed from metastable precursor ions $I^{+\bullet}$-$III^{+\bullet}$ and $[IV - N_2]^{+\bullet}$ (see sec. 3.2.2). The C_2,H_2,N^+ ions in the 2FFR MIKE spectra of these metastable precursors were transmitted into the 3FFR where their He CID mass spectra were obtained, Fig. 5.4.4. The ions from $I^{+\bullet}$, $III^{+\bullet}$ and $[IV - N_2]^{+\bullet}$ have the same translational kinetic energy, 40/41 x 8 keV, while those from

metastable $II^{+\bullet}$ have only 40/167 x 8 keV. These latter ions will not undergo CID to the same extent as the former, higher kinetic energy ions. This is evident in the second CID spectrum in Fig. 5.4.4. The other three are identical and are also the same as those in Fig. 5.4.3. Thus, the C_2,H_2,N^+ ion formed from metastable $I^{+\bullet}$, $III^{+\bullet}$ and $[IV - N_2]^{+\bullet}$ is the same as that formed upon reionization of neutralized source generated C_2,H_2,N^+ ions from I, III and IV.

f) Thermochemistry of C_2,H_2,N^+ ions - The AEs for the formation of the C_2,H_2,N^+ ions from each precursor molecule were measured (see also sec. 5.4.2).

I	$CH_3CN + e^- \rightarrow C_2,H_2,N^+ + H^\bullet + 2e^-$	$AE \leq 13.94 \pm 0.02$ eV
II	$ICH_2CN + e^- \rightarrow C_2,H_2,N^+ + H^\bullet + 2e^-$	$AE = 12.18 \pm 0.02$ eV
III	$CH_3NC + e^- \rightarrow C_2,H_2,N^+ + H^\bullet + 2e^-$	$AE \leq 12.85 \pm 0.02$ eV
IV	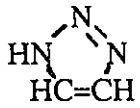 $+ e^- \rightarrow C_2,H_2,N^+ + N_2 + H^\bullet + 2e^-$	$AE \leq 11.50 \pm 0.02$ eV

The "≤" signs for the AEs from I,III and IV were assigned because of the large $T_{0.5}$ values for the dissociations (indicating a large barrier, sec. 3.5.2) and that a two step process is required from IV (see sec. 3.5.4). The $\Delta_fH^\circ_{298}(C_2,H_2,N^+)$ obtained from these AEs were:

I	$\Delta_fH^\circ_{298}(C_2,H_2,N^+)$	$\leq 287 \pm 1$ kcal mol^{-1}
II	"	$= 291 \pm 2$ kcal mol^{-1}
III	"	$\leq 285 \pm 1$ kcal mol^{-1}
IV	"	≤ 272 kcal mol^{-1}

using $\Delta_fH^\circ_{298}(CH_3NC) = 41.0 \pm 0.2$ kcal mol^{-1} [10] and $\Delta_fH^\circ_{298}$(1-H-1,2,3-triazole) = 59 kcal mol^{-1} [10].

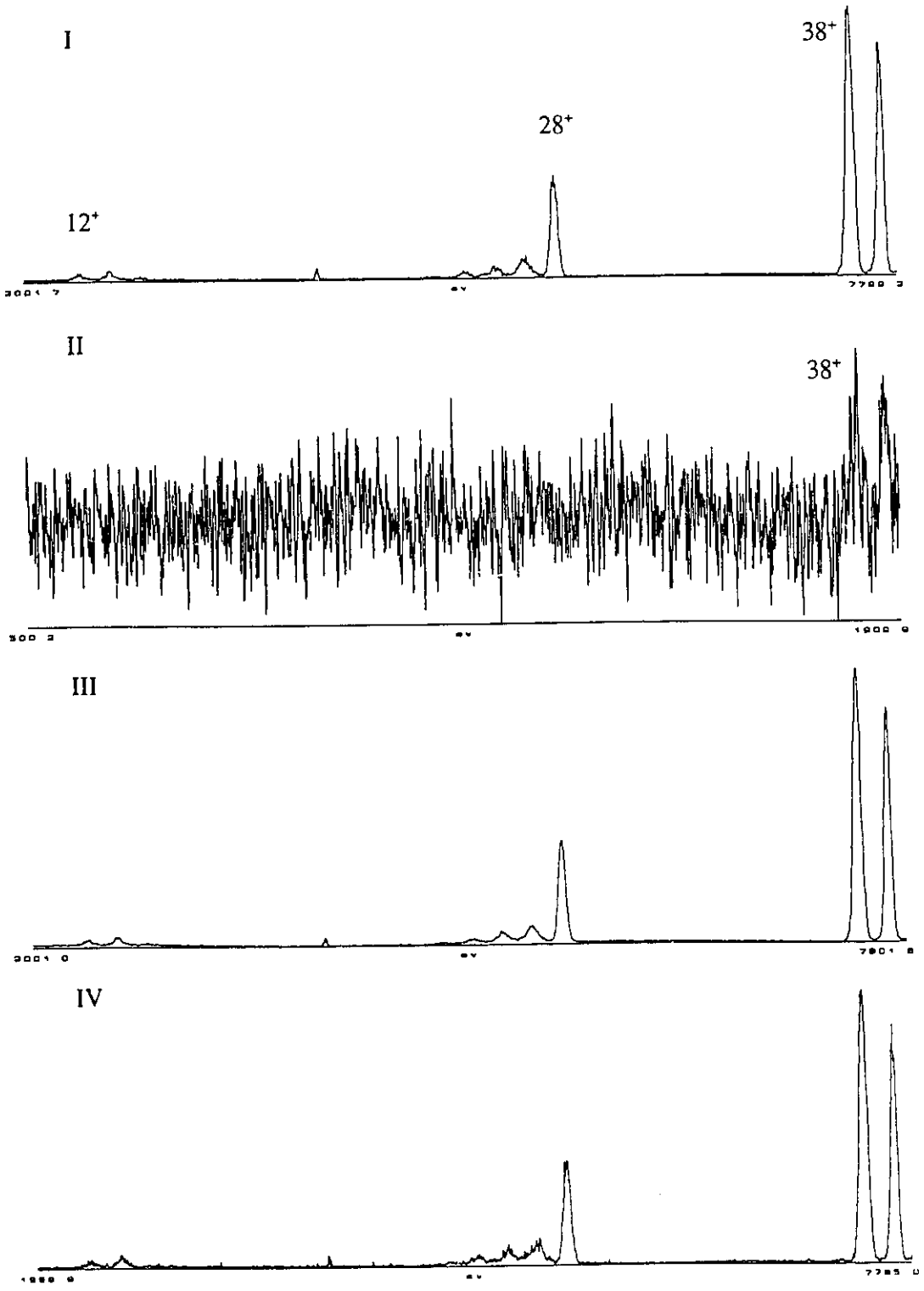

Fig. 5.4.4. 3FFR He CID mass spectra (He, 50%T) of m/z 40 ions in 2FFR MIKE spectra of metastable precursor ions from precursor molecules I-IV.

If I, III and IV produce the same C_2,H_2,N^+ ion, it must be the lowest energy isomer, the cyclic ion *c*, which has a heat of formation ≤ 272 kcal mol^{-1}. The high value for this ion obtained from I and III must be due to the large barrier to $H^\bullet$ loss and subsequent isomerization to the cyclic ion. This leaves the C_2,H_2,N^+ ion from ICH_2CN to be the linear $^+CH_2CN$ isomer having a heat of formation of 291 ± 2 kcal mol^{-1}. There is at least a 20 kcal mol^{-1} difference between the heats of formation of *a* and *c*.

g) Analogy to C_3,H_3^+ - The present series of C_2,H_2,N^+ ions is isoelectronic with the C_3,H_3^+ ions $^+CH_2C{\equiv}CH$ and cyclo-$C_3H_3^+$. It was found [93,94] that the linear isomer could only be made from $ICH_2C{\equiv}CH$, all other precursors gave the lower energy cyclic isomer. The KER measured for the production of these ions from a variety of metastable precursor ions exhibited two trends. The $T_{0.5}$ values from X-$CH_2C{\equiv}CH$ (X = Cl,Br,H) were large, > 63 meV while that from $ICH_2C{\equiv}CH$ was 5 meV. This is similar to the C_2,H_2,N^+ ions where the $T_{0.5}$ values were large from $I^{+\bullet}$, $III^{+\bullet}$ and $[IV\text{-}N_2]^{+\bullet}$ but small from $ICH_2CN^{+\bullet}$. Comparing their thermochemistry, we see a difference of 25 kcal mol^{-1} between $^+CH_2C{\equiv}CH$, $\Delta_fH^\circ_{298}$ = 282 kcal mol^{-1} [10] and cyclopropenium, $\Delta_fH^\circ_{298}$ = 257 kcal mol^{-1} [10], close to the difference for the two C_2,H_2,N^+ isomers.

h) Implications - There has been one previous investigation of the mass spectrometry of C_2,H_2,N^+ ions. Bursey et. al. [95] obtained He CID mass spectra (50%T, i.e., multiple collision conditions - see sec. 3.3.2) of the source generated C_2,H_2,N^+ ions from CH_3CN and CH_3NC. They also obtained the positive fragment ion CID spectra (charge reversal mass spectrometry) of the source generated C_2,H_2,N^- ions from both precursors. The results for the C_2,H_2,N^+ ions were similar to our own. The positive ion CID of source

generated C_2,H_2,N^- ions from acetonitrile (a double charge stripping event followed by fragmentation of the resulting C_2,H_2,N^+ ions) exhibited a m/z 24:25:26:27:28 ratio of 1:6:45:4:17, similar to the CID spectrum we obtained for the C_2,H_2,N^+ ions from iodoacetonitrile. Their discussion centred on how $^+CH_2CN$ ions from acetonitrile could rearrange to $^+CH_2NC$. They could not explain why the CID for the charge reversal produced different C_2,H_2,N^+ ions. We can now explain their results. The negative ions formed in the ion source were $^-CH_2CN$ and charge reversal formed distinctly $^+CH_2CN$. The C_2,H_2,N^+ ions formed from acetonitrile and isocyanomethane were actually the cyclic ion *c*, which also helps explain many of the fragmentation pathways.

The present results also mean that all previous determinations of $\Delta_fH°_{298}(^+CH_2CN)$ and $\Delta_fH°_{298}(^+CH_2NC)$ from CH_3CN and CH_3NC were inaccurate. A summary of the results is shown diagrammatically below.

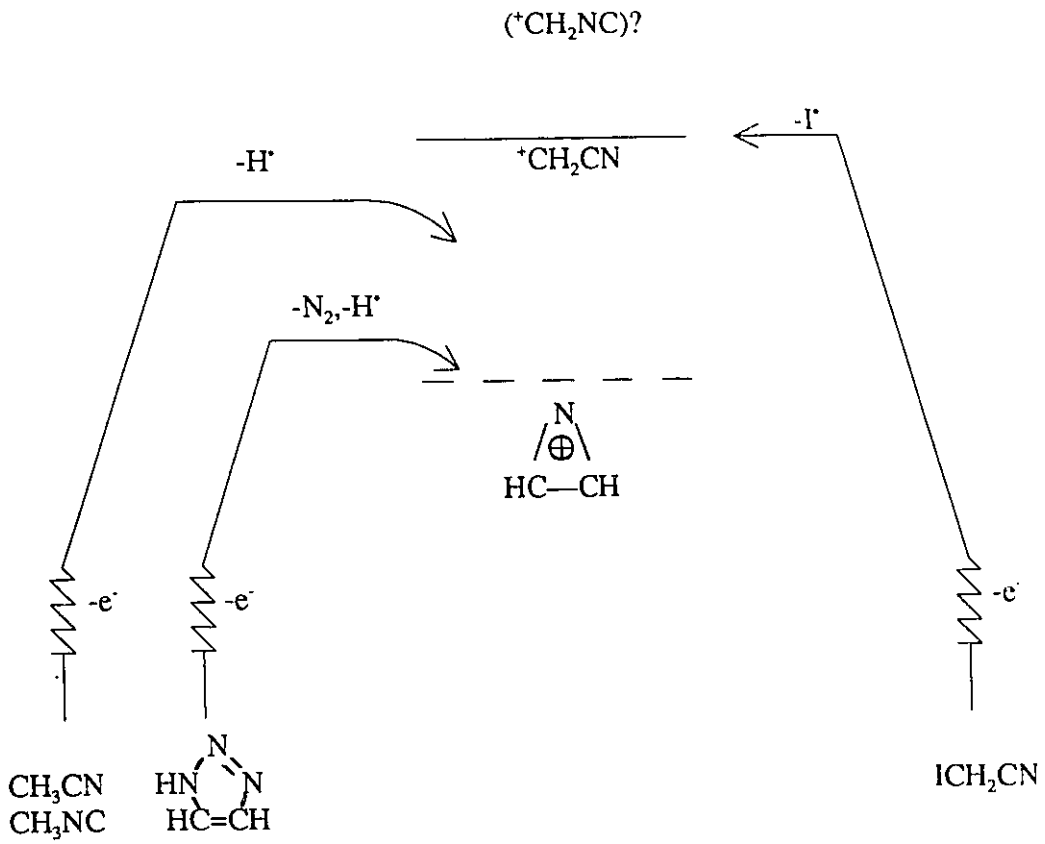

i) Conclusion - This relatively "simple" set of isomeric ions demonstrates the intimate connection between gas phase thermochemistry and mass spectrometry. It was only through extended experimental investigations that the system could be reasonably well understood.

References - Chapter 5

1. J.L. Holmes, F.P. Lossing and A. Maccoll, J. Am Chem. Soc., 110 (1988) 7339.

2. J.L. Holmes and F.P. Lossing, J. Am. Chem. Soc., 110 (1988) 7343.

3. J.L. Holmes and F.P. Lossing, Int. J. Mass Spectrom. Ion Phys., 58 (1984) 1133.

4. J.L. Holmes, F.P. Lossing and J.K. Terlouw, J. Am. Chem. Soc., 108 (1986) 1086.

5. E. Tschuikow-Roux and D.R. Salomon, J. Phys. Chem., 91 (1987) 699; E. Tschuikow-Roux, D.R. Salomon and S. Paddison, J. Phys. Chem., 91 (1987) 3037; E. Tschuikow-Roux and S. Paddison, Int. J. Chem. Kinet., 19 (1987) 15.

6. A.L. Castelhano and D. Griller, J. Am. Chem. Soc., 104 (1982) 3655.

7. D.F. McMillen and D.M. Golden, Ann. Rev. Phys. Chem., 33 (1982) 493.

8. S.W. Benson, Thermochemical Kinetics, 2nd ed. Wiley Interscience, New York, 1976.

9. J.B. Pedley, R.D. Naylor and S.P. Kirby, Thermochemical Data of Organic Compounds, 2nd ed. Chapman and Hall: New York, 1986.

10. S.G. Lias, J.E. Bartmess, J.F. Liebman, J.L. Holmes, R.D. Levin and W.G. Mallard, J. Phys. Chem. Ref. Data, Supp. 1 17 (1988).

11. P.J. Gardner and K.S. Hussain, J. Chem. Thermodynamics 4 (1972) 819.

12. C. Sosa and H.B. Schlegel, J. Am. Chem. Soc., 109 (1987) 7007.

13. A.T. Castelhano, P.R. Marriot and D. Griller, J. Am. Chem. Soc., 103 (1981) 4262.

14. D.M. Golden and S.W. Benson, Chem. Rev., 69 (1969) 125.

15. R. Walsh and S.W. Benson, J. Am Chem. Soc., 88 (1966) 3480.

16. A. Miyoshi, H. Matsui and N. Washida, J. Phys. Chem., 94 (1990) 3016.

17. I.M. Khudyakova and V.N. Burmistrov, Izvestiya Akademii Nauk SSSR, Seriya

Khimicheskaya, 1 (1977) 214.

18. V.M. Orlov, A.D. Misharev, V.V. Takhistov and I.I. Ryabinkin, Izvestiya Akademii Nauk SSSR, Seriya Khimicheskaya, 7 (1988) 1514.

19. M. Mozurkewich, J.J. Lamb and S.W. Benson, J. Phys. Chem., 88 (1984) 6435.

20. B. Ruscic, M. Schwarz and J. Berkowitz, J. Chem. Phys., 91 (1989) 6772; B. Ruscic, M. Schwarz and J. Berkowitz, J. Chem. Phys., 91 (1989) 6780.

21. J.S. Tse, private communication.

22. G.C. Schatz, M.S. Fitzcharles and L.B. Harding, Faraday Disc. Chem. Soc., 84 (1987) 359.

23. H.A. Schwarz and R.W. Dodson, J. Phys. Chem., 93 (1989) 409.

24. T. Nishimura, Q. Zha and G.G. Meisels, J. Chem. Phys., 87 (1987) 4589.

25. a) P. Bischof and G. Friedrich, J. Comput. Chem., 3 (1982) 486, b) E. Sicilia, F.P. Di Malo and N. Russo, J. Phys. Chem., 97 (1993) 528.

26. E.R. Fisher and P.B. Armentrout, J. Phys. Chem., 94 (1990) 4396.

27. L.G.S. Shum and S.W. Benson, J. Phys. Chem., 87 (1983) 3479.

28. S.P. Heneghan and S.W. Benson, Int. J. Chem. Kinet., 15 (1983) 815.

29. J.L. Holmes, F.P. Lossing and P.M. Mayer, J. Am. Chem. Soc., 113 (1991) 9723.

30. J.L. Holmes and P.C. Burgers, Org. Mass Spectrom., 17 (1982) 123.

31. F.P. Lossing, J. Am. Chem. Soc., 99 (1977) 7526.

32. M.J.S. Dewar and W. Thiel, J. Am. Chem. Soc., 99 (1977) 4907.

33. J.B. Moffat, Chem. Phys. Lett., 76 (1980) 304.

34. J.B. Moffat, Theochem., 17 (1984) 93.

35. D.A. Dixon, P.A. Charlier and P.G. Gassman, J. Am. Chem. Soc., 102 (1980) 3957.

36. M.N. Paddon-Row, C. Santiago and K.N. Houk, J. Am. Chem. Soc., 102 (1980) 6563.

37. D.A. Dixon, R.A. Eades, R. Frey, P.G. Gassman, M.L. Hendewerk, M.N. Paddon-Row and K.N. Houk, J. Am. Chem. Soc., 106 (1984) 3885.

38. Y.-D. Wu, W. Kirmse and K.N. Houk, J. Am. Chem. Soc., 112 (1990) 4557.

39. P.G. Gassman and J.J. Talley, J. Am. Chem. Soc., 102 (1980) 1214.

40. W. Kirmse and B. Goer, J. Am. Chem. Soc., 112 (1990) 4556.

41. J.L. Holmes and F.P. Lossing, Org. Mass Spectrom., 26 (1991) 537.

42. J.Y. Chu, T.T. Nguyen and K.D. King, J. Phys. Chem., 86 (1982) 443.

43. P.C. Burgers, J.L. Holmes, A.A. Mommers and J.K. Terlouw, Chem. Phys. Lett., 102 (1983) 1.

44. O. Dobis and S.W. Benson, Int. J. Chem. Kinet., 19 (1987) 691.

45. H. Bock, T. Hirabayashi and S. Mohmand, Chem. Ber., 114 (1981) 2595.

46. J.L. Holmes, C.E.C.A. Hop and J.K. Terlouw, Org. Mass Spectrom., 21 (1986) 776 and references therein; see also N. Heinrich, J. Schmidt, H. Schwarz and Y. Apeloig, J. Am. Chem. Soc., 109 (1987) 1317.

47. J.L Holmes, P.M. Mayer, M. Vasseur and P.C. Burgers, J. Phys. Chem., 97 (1993) 4865.

48. P.G. Gassman and T.T. Tidwell, Acc. Chem. Res., 16 (1983) 279 and references therein.

49. A.D. Allen, F. Shahidi and T.T. Tidwell, J. Am. Chem. Soc., 104 (1982) 2516.

50. W. Kirmse and B. Goer, J. Am. Chem. Soc., 112 (1990) 4556.

51. G.A. Olah, G.K. Surya Prakash and M. Arvanaghi, J. Am. Chem. Soc., 102 (1980) 6640.

52. G.A. Olah, M. Arvanaghi and G.K. Surya Prakash, J. Am. Chem. Soc., 104 (1982) 1628.

53. K.M. Koshy and T.T. Tidwell, J. Am. Chem. Soc., 102 (1980) 1216.

54. K.N. Houk, L.N. Domelsmith, R.W. Strozier and R.T. Patterson, J. Am. Chem. Soc., 100 (1978) 6531.

55. A.C. Hopkinson and M.H. Lien, Can. J. Chem., 63 (1985) 3582 and references therein.

56. F. Delbecq, J. Org. Chem., 49 (1984) 4838.

57. D.J. Swanton, G.B. Bacskay, G.D. Willett and N.S. Hush, J. Mol. Struct. (Theochem), 91 (1983) 313.

58. P.W. Harland, R.G.A.R. MacIagan and H.F. Schaefer III, J. Chem. Soc., Faraday Trans. 2, 85(3) (1989) 187.

59. A. Hinchliffe, J. Mol. Struct., 53 (1979) 147.

60. N.C. Baird, R.R. Gupta and K.F. Taylor, J. Am. Chem. Soc., 101 (1979) 4531.

61. D. Crans, T. Clark and P. von Rague Schleyer, Tetrahedron Lett., 21 (1980) 3681.

62. F. Delbecq, Chem. Phys. Lett., 99 (1983) 21.

63. D.J. Pasto, J. Am. Chem. Soc., 110 (1988) 8164 and references therein.

64. M. Lehd and F. Jensen, J. Org. Chem., 56 (1991) 884.

65. M. Hunt, J.A. Kerr and A.F. Trotman-Dickenson, J. Chem. Soc., (1965) 5074.

66. K.D. King and R.D. Goddard, Int. J. Chem. Kinet., 7 (1975) 837.

67. K.D. King and R.D. Goddard, J. Phys. Chem., 80 (1976) 546 and references therein.

68. Y. Gonen (Geliebter), L.A. Rajenbach and A. Horowitz, Int. J. Chem. Kinet., 9 (1977) 361.

69. A.B. Trenwith, J. Chem. Soc., Faraday Trans. 1, 79 (1983) 2755.

70. M.J.S. Dewar and H.S. Rzepa, J. Am. Chem. Soc., 100 (1978) 784.

71. M. Karelson, A.R. Katritzky and M.C. Zerner, J. Org. Chem., 56 (1991) 134.

72. G. Leroy, D. Peeters, C. Wilante and M. Khalil, Nouv. J. Chim., 4(6) (1980) 403.

73. G. Leroy, M. Sana and C. Wilante, J. Mol. Struct. (Theochem), 228 (1991) 37.

74. C.A. McDowell and J.W. Warren, Trans. Faraday Soc., 48 (1952) 1084.

75. R.F. Pottie and F.P. Lossing, J. Am. Chem. Soc., 83 (1961) 4737.

76. J.L. Franklin, Y. Wada, P. Natalis and P.M. Hierl, J. Phys. Chem., 70(7) (1966) 2353.

77. V.H. Dibeler and S.K. Liston, J. Chem. Phys., 48(10) (1968) 4765.

78. W. Heerma, J.J. de Ridder and G. Dijkstra, Org. Mass Spectrom., 2 (1969) 1103.

79. S.H. Allam, M.D. Migahed and A. El-Khodary, Egypt. J. Phys., 13(2) (1982) 167.

80. P.W. Harland and B.J. McIntosh, Int. J. Mass Spectrom. Ion Proc., 67 (1985) 29.

81. D.D. Wagman, W.H. Evans, V.B. Parker, I. Halow, S.M. Bailey and R.H. Schumm, MBS Tech. Note 270-3 U.S. Government Printing Office Washington, D.C. 20402 (1968).

82. S.W. Benson and H.E. O'Neal, "Kinetic Data on Gas Phase Unimolecular Reactions" NSRDS-NBS 21 U.S. Government Printing Office Washington, D.C. (1970)

83. H. Ichikawa and M. Ogata, Bull. Chem. Soc. Jpn., 47(10) (1974) 2591.

84. M.C. Blanchette, J.L. Holmes, C.E.C.A. Hop, F.P. Lossing, R. Postma, P.J.A. Ruttink

and J.K. Terlouw, J. Am. Chem. Soc., 108 (1986) 7589.

85. K.D. King and R.D. Goddard, J. Am. Chem. Soc., 97 (1975) 4504.

86. J.B. Moffat, Int. J. Quantum Chem., 19 (1981) 771.

87. M.H. Lien and A.C. Hopkinson, J. Mol. Struct. (THEOCHEM), 121 (1985) 1.

88. W. Barbe, H.-D. Beckhaus and C. Ruchardt, Chem. Ber., 116 (1983) 1042.

89. M.H. Lien and A.C. Hopkinson, J. Comput. Chem., 6 (1985) 274.

90. J.L. Holmes, F.P. Lossing and P.M. Mayer, Chem. Phys. Lett., 212 (1993) 134.

91. J.L. Holmes, F.P. Lossing and R.A. McFarlane, Int. J. Mass Spectrom. Ion Proc., 86 (1988) 209.

92. J.L. Holmes and M. Dakubu, Org. Mass Spectrom., 24 (1989) 461.

93. J.L. Holmes and F.P. Lossing, Can. J. Chem., 57 (1979) 249.

94. P.C. Burgers, J.L. Holmes, A.A. Mommers and J.E. Szulejko, J. Am. Chem. Soc., 106 (1984) 521.

95. M.M. Bursey, D.J. Harvan, C.E. Parker and J.R. Hass, J. Am. Chem. Soc., 105 (1983) 6801.

Claims To Original Research

1a) Design, manufacture and implementation of a novel collision cell for the observation, analysis and detection of photon emissions from projectile - target gas collisions in the VG ZAB-2F mass spectrometer. This apparatus allowed the aquisition of emission spectra from polyatomic projectile ions for the first time. Early work established the feasibility of performing this type of experiment on a commercial sector mass spectrometer [1,2].

1b) Monochromated emission spectra were obtained once a new field-free region was added to the mass spectrometer. Results for 8 keV $N_2^{+\bullet}$ [3], $O_2^{+\bullet}$ and $CO_2^{+\bullet}$ [4] were reported and formed the groundwork for our study of polyatomic projectile ions. Three $C_2,H_4,O^{+\bullet}$ isomers and two $C_2,H_5,Cl^{+\bullet}$ isomers (along with several of their fragment ions) were studied [5]. For the first time, detailed, quantitative information was obtained for polyatomic projectile - target gas collisions.

2a) The appearance energy technique (utilizing a monoenergetic electron beam) was used to determine the heats of formation of many organic free radicals and cations. Prior to this work very few heats of formation were known for free radicals with oxygen containing substituents. The $\Delta_fH^\circ_{298}$ values of seventeen oxygen containing free radicals were determined. This body of information allowed a discussion of the influence of -OH groups on bond strengths in alcohols and the additive nature of the effect on $\Delta_fH^\circ_{298}$ values of substitution on free radical centres [6].

2b) A discussion of the -CN group in radical cations [7] found that it behaves primarily as an inductive electron withdrawing group with no charge delocalization to the C≡N bond. The -CN group was found to raize the $\Delta_f H^\circ_{298}$ of radical cations by +43 ± 3 kcal mol^{-1} relative to their -H substituted analogues.

2c) A thermochemical study of the even electron cations and free radicals $^{+(\cdot)}CH_2CN$, $CH_3{}^{+(\cdot)}CHCN$ and $(CH_3)_2{}^{+(\cdot)}CCN$ was made [8,9], showing that the -CN group participates in π-delocalization of the radical site in all three radicals but only $^{+}CH_2CN$ undergoes π - delocalization of the charge.

[1] J.L. Holmes, P.M. Mayer and A.A. Mommers, "Emission of Radiation by Collisionally Activated Ions: A New Approach to Ion Structure Determination" J. Am. Chem. Soc., 113 (1991) 9405.

[2] J.L. Holmes, P.M. Mayer and A.A. Mommers, "The Collision-induced Emission of Radiation: Lifetimes of Excited States Formed in the Collision-induced Dissociation (CID) Processes and the Excitation of Target Gas Molecules" Org. Mass Spectrom., 27 (1992) 537.

[3] J.L. Holmes, P.M. Mayer and A.A. Mommers, "Photon Emissions from $N_2^{\cdot+}$ Ion Beam - Target Gas Collisions in a Modified Commercial Sector Mass Spectrometer" Int. J. Mass Spectrom. Ion Proc., in press.

[4] J.L. Holmes, P.M. Mayer, "Collision Induced Photon Emissions from 8 keV $O_2^{\cdot+}$ and $CO_2^{\cdot+}$ Ion Beams" Org. Mass Spectrom., submitted for publication.

[5] J.L. Holmes, P.M. Mayer, "Collision Induced Emission Spectra of Polyatomic Ions of Composition $C_2,H_4,O^{\cdot+}$ and $C_2,H_5,Cl^{\cdot+}$" -in preparation.

[6] J.L. Holmes, F.P. Lossing and P.M. Mayer, "Heats of Formation of Oxygen - Containing Organic Free Radicals from the Appearance Energy Measurements" J. Am. Chem. Soc., 113 (1991) 9723.

[7] J.L. Holmes, P.M. Mayer, M. Vasseur and P.C. Burgers, "The Effect of Cyano Substitution on the Heats

of Formation of Organic Ions and Neutrals" J. Phys. Chem., 97 (1993) 4865.

[8] J.L. Holmes, F.P. Lossing and P.M. Mayer, "The Effects of Methyl Substitution on the Structure and Thermochemistry of the Cyanomethyl Radical and Cation" Chem. Phys. Lett., 212 (1993) 134.

[9] J.L. Holmes and P.M. Mayer, "A Combined Mass Spectrometric and Thermochemical Examination of the C_2,H_2,N Family of Cations and Radicals" -in preparation.